
THE UNIVERSITY OF QUEENSLAND

AUSTRALIA

# Multifunctional Nanostructured Polymers for Improved $^{19}$F MRI

Kewei Wang

*A thesis submitted for the degree of Doctor of Philosophy at*

*The University of Queensland in 2014*

Australian Institute for Bioengineering and Nanotechnology (AIBN) and

Centre for Advanced Imaging (CAI)

## Abstract

Magnetic resonance imaging (MRI) has significantly enhanced clinical diagnosis of disease due to a number of advantages, such as high resolution, rich information content that can be derived from a single scan, its non-invasive nature, no limitation on tissue penetration depth and the lack of radiation burden that is often encountered when other imaging modalities are utilised. In recent years $^{19}F$ MRI has gained renewed attention as an increasingly important MRI technique, mainly due to the commercial availability of high field scanners (up to 16.4 T in the preclinical setting). $^{19}F$ has comparable nuclear magnetic resonance (NMR) properties as $^{1}H$, including large gyromagnetic ratio (40.03 MHz $T^{-1}$, 94% relative to $^{1}H$), high sensitivity (83% relative to $^{1}H$) and 100% natural abundance. An essentially attractive feature of $^{19}F$ MRI is the absence of confounding background signal because there is no endogenous $^{19}F$ NMR-detectable fluorine in the body. Hence $^{19}F$ MRI is a highly quantitative technique and naturally relies on the presence of $^{19}F$–containing imaging agents to generate an image. However, $^{19}F$ MRI is not routinely used in clinical mainly because of the lack of suitable contrast agents.

In the past few years, partly-fluorinated polymers have been considered as excellent candidates for $^{19}F$ MRI contrast agents due to the diverse architecture and functionality of polymers. However, understanding the relationship between molecular structure, NMR properties and imaging performance remains a challenging task. In addition, it is still a minimally explored field for the development of multifunctional agents, such as biologically-responsive $^{19}F$ agents (“smart” agents) and $^{19}F$ MRI-incorporating multimodal imaging agents. To tackle these challenges, this thesis aims to study the design of next-generation polymeric $^{19}F$ MRI agents by developing a fundamental understanding of multifunctional polymers with different molecular architectures and components for selective $^{19}F$ MRI, multimodal molecular imaging, improved $^{19}F$ MRI, and theranostics.

The first approach adopted for achieving high $^{19}F$ mobility was by distributing and separating the $^{19}F$ segments in a hyperbranched structure. In Chapter 2, star-like polymers with a hyperbranched core and hydrophilic arms were synthesised using the arm-first approach by reversible addition─fragmentation chain transfer (RAFT) polymerisation. The core was composed of units of 2,2,2-trifluoroethyl acrylate (TFEA), 2-(dimethylamino)ethyl methacrylate (DMAMEA) and ethylene glycol dimethacrylate (EGDMA), while the arms consisted of brush-like homopolymers of poly(ethylene glycol) methyl ether methacrylate (PEGMA). The chemical structure and composition of the polymers were characterised to obtain detailed information about the molecular structure. The pH-responsiveness of particle size was also investigated by dynamic light scattering (DLS) and cryo-transmission electron microscopy (cryo-TEM). The $^{19}F$ NMR properties, such as

$^{19}$F signal intensity, spin-lattice ($T_1$) relaxation time and spin-spin ($T_2$) relaxation time were examined in solutions of different pH. Finally the imaging performance of the polymers at different pH was evaluated by *in vitro* $^{19}$F MRI.

As the $T_2$ relaxation time is sensitive to the chemical environment of $^{19}$F nuclei, the influence of polymer architecture on imaging performance was then studied. Chapter 3 describes the development of core crosslinked star (CCS) polymers and these materials were compared to the star-like hyperbranched polymers described in Chapter 2. The CCS polymers were constructed of a biodegradable core and block copolymers as arms. In contrast to the polymers described in Chapter 2, the $^{19}$F units were positioned within the block copolymer arms by the RAFT copolymerisation of 2,2,2-trifluoroethyl methacrylate (TFEMA) and DMAEMA using PPEGMA as a macroCTA. The pH-responsiveness of $^{19}$F NMR properties was characterised, and the biodegradability were evaluated. The capability of the CCS polymers for selective $^{19}$F MRI was assessed in solutions of different pH. The change in imaging properties of different polymer architectures were also compared and discussed.

In order to expand the possible application of polymeric imaging agents, multifunctional hyperbranched polymers were synthesised for computed tomography (CT)/$^{19}$F MRI bimodal molecular imaging. In Chapter 4, hyperbranched polymers containing units of 2-(2',3',5'-triiodobenzoyl)ethyl methacrylate (TIBMA) and PEGMA were synthesised by RAFT polymerisation and were chain extended with TFEA and PEGMA. The biodegradability was studied in the presence of reducing agents. Nanoparticles were formed and characterised by DLS and TEM techniques. The radio-opacity of these polymers was assessed by *in vitro* CT experiments, and the MRI performance was evaluated by $^{19}$F MRI. The material showed good imaging potential in both modalities pointing towards a new class of multimodal imaging agents.

In order to systematically study the relationship between molecular structure and imaging performance, segmented highly-branched polymers (SHBPs) were synthesised by self-condensing vinyl polymerisation via the RAFT process (RAFT SCVP). Chapter 5 describes the synthesis of a polymerisable chain transfer agent (CTA) that was used for the copolymerisation of fluoro monomers and PEG-based monomers. A series of SHBPs with different compositions and degrees of branching (DBs) were synthesised and thoroughly characterised. The $^{19}$F NMR properties were strongly affected by the sequence distribution of fluorinated units, type of polymer backbone and degree of branching. As a result, SHBPs consisting of statistical copolymer segments with acrylate backbones were excellent candidates for imaging due to a single $^{19}$F signal, long $T_2$ relaxation times and high $^{19}$F contents. The SHBPs could be all imaged or selectively imaged by $^{19}$F MRI using

different pulse sequences by taking advantage of the differences in relaxation times, demonstrating the tuneable and selective imaging performance through tailoring the structure and composition of the SHBPs.

Finally, Chapter 6 describes the synthesis of star polymers with a polyhedral oligomeric silsesquioxanes (POSS) core and eight partly-fluorinated arms. Here the aim was to investigate how to combine $^{19}$F MRI with drug delivery by designing a platform possessing $^{19}$F-containing polymers and POSS cages. A macroCTA having eight CTA molecules attached to a POSS core was synthesised and used for the synthesis of star polymers by the R-group approach. The arms were composed of statistical copolymers consisting of TFEA and PEGA. Star polymers having different arm lengths were prepared and characterised. The particle size and $^{19}$F NMR properties were studied by DLS and $^{19}$F NMR, respectively. Finally the imaging performance was preliminarily evaluated by calculating the theoretical $^{19}$F MRI intensities and comparing with the previous imaging results.

In summary, this thesis studies the development of multifunctional nanostructured polymers as contrast agents for $^{19}$F MRI-related molecular imaging and theranostics using the RAFT technique. The molecular level understanding gained in this work provides useful guidance for the future design of highly-efficient $^{19}$F MRI contrast agents.

**Declaration by author**

This thesis is composed of my original work, and contains no material previously published or written by another person except where due reference has been made in the text. I have clearly stated the contribution by others to jointly-authored works that I have included in my thesis.

I have clearly stated the contribution of others to my thesis as a whole, including statistical assistance, survey design, data analysis, significant technical procedures, professional editorial advice, and any other original research work used or reported in my thesis. The content of my thesis is the result of work I have carried out since the commencement of my research higher degree candidature and does not include a substantial part of work that has been submitted to qualify for the award of any other degree or diploma in any university or other tertiary institution. I have clearly stated which parts of my thesis, if any, have been submitted to qualify for another award.

I acknowledge that an electronic copy of my thesis must be lodged with the University Library and, subject to the policy and procedures of The University of Queensland, the thesis be made available for research and study in accordance with the Copyright Act 1968 unless a period of embargo has been approved by the Dean of the Graduate School.

I acknowledge that copyright of all material contained in my thesis resides with the copyright holder(s) of that material. Where appropriate I have obtained copyright permission from the copyright holder to reproduce material in this thesis.

**Publications during candidature**

Peer-reviewed papers

Wang, K. W., Peng, H., Thurecht, K. J., Puttick, S., and Whittaker, A. K. Biodegradable Core Crosslinked Star Polymer Nanoparticles as F-19 MRI Contrast Agents for Selective Imaging. Polymer Chemistry, 2014, 5, 1760-1771.

Wang, K. W., Peng, H., Thurecht, K. J., Puttick, S., and Whittaker, A. K. pH-Responsive Star Polymer Nanoparticles: Potential F-19 MRI Contrast Agents for Tumour-Selective Imaging. Polymer Chemistry, 2013, 4, 4480-4489.

Conference proceedings

Wang, K. W., Peng, H., Thurecht, K. J., Puttick, S., and Whittaker, A. K. pH−Responsive Star Polymer Nanoparticles as Selective $^{19}$F MRI Contrast Agents. NanoBio Australia 2014, July, 2014, Brisbane, Australia. (Poster)

Wang, K. W., Peng, H., Thurecht, K. J., Puttick, S., and Whittaker, A. K. Biodegradable Core Cross-linked Star Polymer Nanoparticles as $^{19}$F MRI Contrast Agents for Selective Imaging. ChinaNANO 2013, September, 2013, Beijing, China. (Oral)

Wang, K. W., Peng, H., Thurecht, K. J., Puttick, S., and Whittaker, A. K. pH−Responsive Star Polymer Nanoparticles as Selective $^{19}$F MRI Contrast Agents. ChinaNANO 2013, September, 2013, Beijing, China. (Poster)

Wang, K. W., Peng, H., Thurecht, K. J., Puttick, S., and Whittaker, A. K. pH-Responsive Star Polymer Nanoparticles as Selective $^{19}$F MRI Contrast Agents. 34$^{th}$ APS, July, 2013, Darwin, Australia. (Oral)

Wang, K. W., Peng, H., Thurecht, K. J., and Whittaker, A. K. Synthesis of pH-Responsive Hyperbranched Polymers and Their Application as $^{19}$F MRI Contrast Agents. 33$^{th}$ APS, February, 2012, Hobart, Australia. (Poster)

**Publications included in this thesis**

Wang, K. W., Peng, H., Thurecht, K. J., Puttick, S., and Whittaker, A. K. pH-Responsive Star Polymer Nanoparticles: Potential F-19 MRI Contrast Agents for Tumour-Selective Imaging. Polymer Chemistry, 2013, 4, 4480-4489.– incorporated as Chapter 2.

| Contributor | Statement of contribution |
|---|---|
| Wang, K. W. | Design and experiments (60%)<br>Characterisation and interpretation of data (45%)<br>Drafting and writing (45%) |
| Peng, H. | Design and experiments (10%)<br>Characterisation and interpretation of data (10%)<br>Drafting and writing (10%) |
| Thurecht, K. J. | Design and experiments (10%)<br>Characterisation and interpretation of data (10%)<br>Drafting and writing (10%) |
| Puttick, S. | Design and experiments (10%)<br>Characterisation and interpretation of data (10%)<br>Drafting and writing (5%) |
| Whittaker, A. K. | Design and experiments (10%)<br>Characterisation and interpretation of data (25%)<br>Drafting and writing (30%) |

Wang, K. W., Peng, H., Thurecht, K. J., Puttick, S., and Whittaker, A. K. Biodegradable Core Crosslinked Star Polymer Nanoparticles as F-19 MRI Contrast Agents for Selective Imaging. Polymer Chemistry, 2014, 5, 1760-1771. – incorporated as Chapter 3.

| Contributor | Statement of contribution |
|---|---|
| Wang, K. W. | Design and experiments (60%)<br>Characterisation and interpretation of data (45%)<br>Drafting and writing (45%) |
| Peng, H. | Design and experiments (10%)<br>Characterisation and interpretation of data (10%)<br>Drafting and writing (10%) |
| Thurecht, K. J. | Design and experiments (10%)<br>Characterisation and interpretation of data (10%)<br>Drafting and writing (10%) |
| Puttick, S. | Design and experiments (10%)<br>Characterisation and interpretation of data (10%)<br>Drafting and writing (5%) |
| Whittaker, A. K. | Design and experiments (10%)<br>Characterisation and interpretation of data (25%)<br>Drafting and writing (30%) |

**Contributions by others to the thesis**

The author acknowledges the following individuals who have contributed to this thesis:

Prof. Andrew K. Whittaker for contributing to the conception, design, characterisation and interpretation of data, and critically revising the thesis.

Dr. Kristofer J. Thurecht for contributing to the conception, design, characterisation and interpretation of data, and critically revising the thesis.

Dr. Hui Peng for contributing to the conception, design, characterisation and interpretation of data, and critically revising the thesis.

Dr. Simon Puttick for contributing to the design and operation of MRI and CT experiments and interpretation of the imaging results.

**Statement of parts of the thesis submitted to qualify for the award of another degree**

None.

## Acknowledgements

First and foremost I would like to thank my PhD supervisors, Prof. Andrew Whittaker, Dr. Kris Thurecht and Dr. Hui Peng, for their continuous support and encouragement throughout my PhD study. Their enthusiasm and patience have helped me enjoy my research, and their passion and dedication have inspired me to work professionally and think critically.

I would also like to acknowledge the Australian Government, The University of Queensland, and Australian Institute for Bioengineering and Nanotechnology for the generous financial support (IPRS, UQCent, UQAdv and AIBN Top-Up).

I would like to express thanks to Dr. Simon Puttick for his kind help with $^{19}F$ MRI and CT experiments. Without his expertise and patience, the evaluation of the materials for bioimaging in this thesis would not have come true.

I would also like to thank the people who kindly offered me technical and instrumental assistance during my study. A big thank you goes out to Ms. Lynette Lambert and Dr. Gregory Pierens for their training and assistance with NMR instruments. I want to thank Dr. Meiliana Siauw for her generous help with TEM experiments and DSC training. I also acknowledge the cryo-TEM help from Mr. Garry Morgan. I also appreciate the CT help from Dr. Karine Mardon. I must thank Ms. Cheryl Berquist for giving me access to the Zetasizer in the Nanomac Lab, and I would like to thank Prof. Michael Monteiro for allowing me to use the GPC instruments in his lab. A special mention goes out to Dr. Ekaterina Strounina for her kind help with solid state NMR.

I am indebted to Dr. Ken Goh, Dr. Anguang Yu, Dr. Huey Wen Ooi and Dr. Craig Bell for their help during my laboratory work. I have learned quite a few synthetic skills by talking to them or watching them work beside the fumehoods. I also want to thank all the Whittaker Group members for their help. I would like to thank the AIBN and CAI for the state-of-the-art facilities and enjoyable research environment. A special thank you also goes out to my Master supervisor, Prof. Guojian Wang, for his kind concern and helpful advice on my study and career.

I would like to express my gratitude to all my friends who have been there throughout my study for their encouragement, support and patience. My thanks also go out to tea and coffee (in no particular order) for keeping me energetic in the ordinary days and cheering me up in those long and tough days.

I would like to thank my grandmother, my parents and my sister for their eternal love, understanding and continuous support. You are the reason why I have made it this far. Lastly, I would like to thank my girlfriend, Sophia, for her love, understanding, patience, encouragement, support and friendship.

**Keywords**

RAFT polymerisation, star polymers, hyperbranched polymers, pH-responsive polymers, partly-fluorinated polymers, molecular imaging, magnetic resonance imaging, computed tomography.

**Australian and New Zealand Standard Research Classifications (ANZSRC)**

ANZSRC code: 030306, Synthesis of Materials, 60%
ANZSRC code: 030301, Chemical Characterisation of Materials, 20%
ANZSRC code: 100709, Nanomedicine, 20%

**Fields of Research (FoR) Classification**

FoR code: 0303, Macromolecular and Materials Chemistry, 80%
FoR code: 1007, Nanotechnology, 20%

# Table of Contents

# List of Figures

# List of Tables

# List of Schemes

# List of Abbreviations

| | |
|---|---|
| 3D | three-dimensional |
| ACVA | 4,4’-azobis(4-cyanovaleric acid) |
| AIBN | 2,2′-azobis(2-methylpropionitrile) |
| ATRP | atom transfer radical polymerisation |
| BMA | butyl methacrylate |
| CAs | contrast agents |
| CCS | core-crosslinked star |
| CT | computed tomography |
| CTA | chain transfer agent |
| DB | degree of branching |
| DCC | N,N’-dicyclohexylcarbodiimide |
| DCM | dichloromethane |
| DEAEMA | 2-(diethylamino)ethyl methacrylate |
| $D_h$ | hydrodynamic diameter |
| DLS | dynamic light scattering |
| $Đ_M$ | molar-mass dispersity |
| DMAEA | 2-(dimethylamono)ethyl acrylate |
| DMAEMA | 2-(dimethylamino)ethyl methacrylate |
| DMAP | 4-(dimethylamino)pyridine |
| DMF | N,N-dimethylformamide |
| DOX | doxorubicin |
| DP | degree of polymerisation |
| DSC | differential scanning calorimetry |
| DSDMA | bis(2-methacryloyl)oxyethyl disulfide |
| DTT | DL-dithiothreitol |
| EDC | N-(3-dimethylaminopropyl)-N′-ethylcarbodiimide hydrochloride |
| EGDMA | ethylene glycol dimethacrylate |
| FLASH | fast low-angle shot |
| FTIR | fourier transform infrared |
| GPC | gel permeation chromatography |
| GSH | glutathion |
| HBPs | hyperbranched polymers |

| | |
|---|---|
| HEMA | 2-hydroxyethyl methacrylate |
| LCST | lower critical solution temperature |
| MAA | methacrylic acid |
| MALLS | multi angle laser light scattering |
| MECP | (S)-2-(Methacryloyloxy)ethyl 4-cyano-4-(((propylthio)carbonothioyl)thio)pentanoate |
| MEHQ | 4-Methoxyphenol |
| MRI | magnetic resonance imaging |
| MRS | magnetic resonance spectroscopy |
| MWCO | molecular weight cut off |
| NMR | nuclear magnetic resonance |
| NPs | nanoparticles |
| PBS | phosphate buffered saline |
| PEG | polyethylene glycol |
| PEGA | poly(ethylene glycol) methyl ether acrylate |
| PEGMA | poly(ethylene glycol) methyl ether methacrylate |
| PFC | perfluorocarbon |
| PFOB | perfluorooctylbromide |
| PLGA | poly(lactic-co-glycolic acid) |
| PMAA | poly(methacrylic acid) |
| POSS | polyhedral oligomeric silsesquioxanes |
| RAFT | reversible addition─fragmentation chain transfer |
| RARE | rapid acquisition with relaxation enhancement |
| ROI | region of interest |
| RP | repeating unit per branch |
| SCVP | self-condensing vinyl polymerisation |
| SHBPs | segmented hyperbranched (or highly-branched) polymers |
| SNR | signal-to-noise ratio |
| SPETC | single photon emission computed tomography |
| $T_1$ | longitudinal (spin-lattice) relaxation time |
| $T_2$ | transverse (spin-spin) relaxation time |
| *t*BMA | *tert*-butyl methacrylate |
| TCEP | tris(2-carboxyethyl)phosphine hydrochloride |
| TE | echo time |

| | |
|---|---|
| TEA | triethylamine |
| TEM | transmission electron microscopy |
| TFEA | 2,2,2-trifluoroethyl acrylate |
| TFEMA | 2,2,2-trifluoroethyl methacrylate |
| $T_g$ | glass transition temperature |
| THF | tetrahydrofuran |
| TIBMA | 2-(2',3',5'-triiodobenzoyl)ethyl methacrylate |
| TR | repetition time |

# CHAPTER 1

# INTRODUCTION

Modern medical science has benefitted enormously from the rapid development of diagnostic techniques, such as optical imaging, magnetic resonance imaging (MRI), X-ray imaging, computed tomography (CT), positron emission tomography (PET), single photon emission computed tomography (SPECT) and ultrasonography. With the help of these techniques, a vast range of diseases can be detected accurately and treated effectively.

Despite these advances, cancer related diseases, which have become increasingly problematic worldwide, still present large challenges today. It has been well-recognised that early and accurate diagnosis of cancer is crucial for successful treatment. As a key imaging modality, MRI has been widely implemented in the clinic for the diagnosis of cancerous tissues because it can produce high quality images of internal organs and tissue without providing a radiation burden.[1, 2]

## 1.1 Magnetic Resonance Imaging

As an indispensable medical diagnostic technique, MRI generates images by collecting and analysing the signals from certain types of isotopes in magnetic fields. This technique features images with high spatial resolution, especially for soft tissues, as well as not being hindered by tissue penetration limitations. Unlike other imaging modalities such as X-ray imaging, CT and PET, MRI is well known for its non-invasive and non-destructive nature because this technique does not rely on potentially harmful ionising radiation. Owing to these unique advantages, MRI has been extensively applied as a powerful medical diagnostic tool for visualising either the whole body or specific tissue by providing qualitative or quantitative three-dimensional (3D) anatomical images.

Based on the principles of nuclear magnetic resonance (NMR), a variety of nuclei which have odd number of protons (or neutrons) can be employed for MRI, including $^{1}H$, $^{13}C$, $^{19}F$, $^{23}Na$, $^{31}P$, etc.[3, 4] These isotopes exhibit nuclear magnetic resonance under an external magnetic field due to their non-zero magnetic moment. The NMR properties of several isotopes are listed in Table 1-1. Although all these isotopes are theoretically suitable for MRI, $^{1}H$ and $^{19}F$ have been the most commonly studied and practically utilised nuclei because both of them possess large gyromagnetic ratio, high sensitivity and rich natural abundance among all the candidates.

**Table 1-1** NMR properties of a few selected isotopes.[5]

| Nucleus | Spin | Gyromagnetic ratio, $\gamma/2\pi$ (MHz/T) | Sensitivity (%) | Natural abundance (%) | Biological abundance (% of mass) |
|---|---|---|---|---|---|
| $^{1}$H | 1/2 | 42.576 | 100 | 99.985 | 10 |
| $^{2}$H | 1 | 6.536 | 0.965 | 0.015 | 0.0015 |
| $^{3}$He | 1/2 | -32.434 | 44 | 0.000138 | – |
| $^{7}$Li | 3/2 | 16.546 | 29 | 92.5 | 0.0003 |
| $^{13}$C | 1/2 | 10.705 | 1.59 | 1.10 | 0.198 |
| $^{14}$N | 1 | 3.077 | 0.101 | 99.634 | 3.0 |
| $^{15}$N | 1/2 | -4.316 | 0.104 | 0.366 | 0.011 |
| $^{17}$O | 5/2 | -5.772 | 2.91 | 0.048 | 0.025 |
| $^{19}$F | 1/2 | 40.053 | 83.4 | 100.0 | 0.004 |
| $^{23}$Na | 3/2 | 11.263 | 9.25 | 100.0 | 0.15 |
| $^{31}$P | 1/2 | 17.235 | 6.63 | 100.0 | 1.0 |
| $^{39}$K | 3/2 | 1.987 | 0.051 | 93.26 | 0.23 |
| $^{43}$Ca | 7/2 | 2.865 | 0.640 | 0.135 | 0.002 |
| $^{129}$Xe | 1/2 | -11.78 | 2.12 | 26.4 | – |

### 1.1.1 $^{1}$H MRI Contrast Agents

Since the pioneering work in the 1970s,[6-8] proton magnetic resonance imaging ($^{1}$H MRI) has advanced rapidly and has been the dominant MRI in routine clinical scans. Basically, there are two reasons why $^{1}$H MRI has been the most prominent MRI. First, $^{1}$H has those aforementioned intrinsic advantageous NMR characteristics that ensure strong signals. For another, $^{1}$H is abundant in water and fat in living organisms, making the tissues readily visualised by $^{1}$H MRI. As the relaxation times of $^{1}$H differ in various environments, $^{1}$H MRI is able to distinguish different tissues. Moreover, $^{1}$H MRI can also be used to differentiate tumour tissue from healthy tissue based on the difference in relaxation times.[6] Nonetheless, $^{1}$H MRI often fails to provide unambiguous images due to insufficient differences (contrast) in relaxation times between normal and diseased states.

Apart from utilising higher magnetic field strengths, introducing contrast agents (CAs) is another feasible way to improve the image contrast and obtain accurate and reliable information from MRI scans.[9] CAs have been used in MRI to alter the longitudinal relaxation time ($T_1$) and transverse relaxation time ($T_2$) of the protons in surrounding water molecules, thus enhancing the image contrast for specific tissues.[10] Based on their effects on imaging, $^1$H MRI CAs can be divided into two categories, i.e., positive agents (producing positive image contrast) and negative agents (generating negative image contrast). In general, positive agents are often based on lanthanides (mostly gadolinium Gd(III) chelates) that can reduce $T_1$ of the surrounding water protons, while negative agents are mainly represented by superparamagnetic iron oxide nanoparticles (SPIONs) which can shorten $T_2$ of the neighbouring water protons.[1, 11] As two representative $^1$H MRI CAs, Gd(III)- and SPIONs-based CAs are introduced in Sections 1.1.1.1 and 1.1.1.2, respectively.

#### 1.1.1.1 $T_1$ Contrast Agents

As pioneers of Gd(III)-based CAs, small molecule gadolinium Gd(III) chelates have been the most commonly administrated CAs in the clinic, accounting for more than 30% of MRI scans.[12] As illustrated in Figure 1-1, a number of Gd(III) chelate-based CAs are commercially available for clinical MRI scans because of their high paramagnetism, effective contrast enhancement, relatively high stability and inertness, etc.[11] Owing to their small size, these CAs can achieve rapid equilibration between intravascular and interstitial space as well as being able to often reach usually inaccessible tissue after intravascular injection,[1, 11, 13] facilitating the diagnosis of a variety of diseases including diseases of central nervous system (CNS) where there is breakage of blood-brain-barrier (BBB) and neurodegenerative diseases.[14-18] Nevertheless, Gd(III) chelate-based CAs suffer from several drawbacks, such as short blood circulation time, relatively low relaxivity and non-selectivity.[11, 13] These shortcomings greatly limit their applications in both clinical MRI scans and biomedical research.

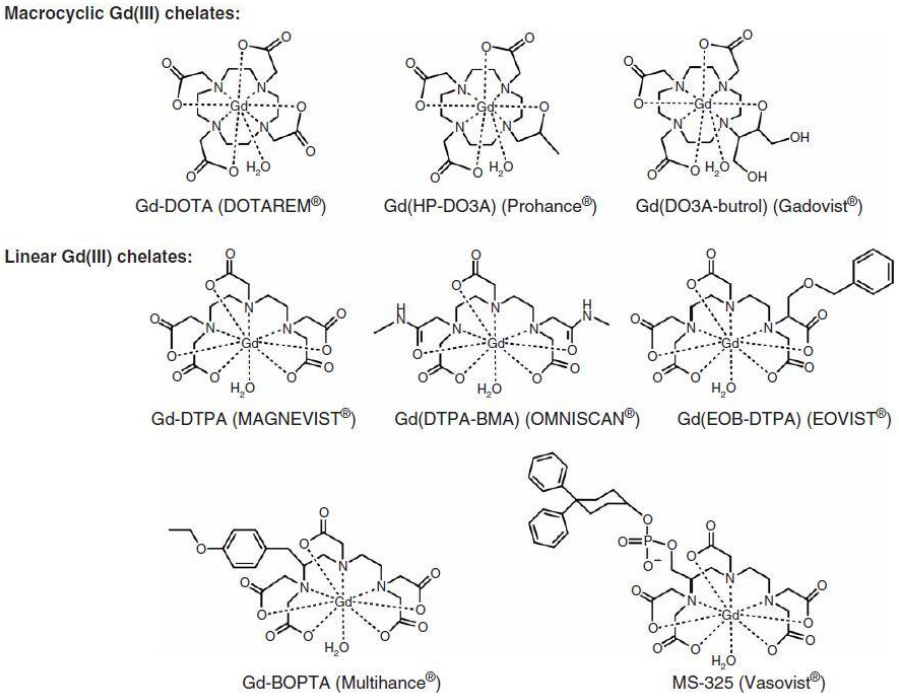


**Figure 1-1** Chemical structures of the commercial Gd(III) chelates used in clinical MRI as CAs. Adapted from Zhou *et al*.[11]

To overcome these challenges, macromolecular Gd(III) contrast agents have been designed and by conjugating Gd(III) chelates to macromolecules. Compared with their small molecule counterparts, macromolecular Gd(III) CAs possess several inherent advantages because of their complex structures and unique properties. For example, macromolecular Gd(III) CAs have higher relaxivity owing to the slower molecular tumbling caused by their larger size, potentially reducing the clinical dosage.[11, 19] In addition, since the renal excretion is reduced, the blood circulation time is prolonged, resulting in favourable pharmacokinetics and imaging timing.[19, 20] Besides, the numerous functionalities existing in macromolecules allow for further chemical modifications which can introduce biodegradability, targeting or environmentally-responsive properties to the CAs.[21] Furthermore, macromolecular Gd(III) CAs are prone to accumulate in tumour tissue sites with leaky vasculature *via* enhanced permeability and retention (EPR), thus the diagnosis of tumour tissue is improved and the imaging time window is enlarged.[22, 23]

Over the past two decades, a wide variety of macromolecular materials have been chosen for the fabrication of macromolecular Gd(III) CAs, including linear polymers,[24-37] star polymers,[26, 38] hyperbranched and dendritic polymers,[26, 38-52] proteins, liposomes, micelles and capsids,[53-57] etc. To meet the increasing demand of specific applications, considerable efforts have been dedicated to the development of 'smart' macromolecular Gd(III) CAs, such as biodegradable,[25, 29, 30, 32, 42] stimuli-

responsive[54, 58-61] and tumour-targeting[34, 46, 51] CAs. The great diversity of structure offered by macromolecular Gd(III) CAs allows control by rational design of size, relaxivity and customisable properties

Overall, Gd(III)-based CAs have been well studied, established and commercialised, and they are currently playing an essential role in clinical MRI scans. However, safety issues need to be taken into consideration even for commercial products. Free Gd(III) ion is known to be toxic on accumulation in bones, liver and spleen and disrupt physiological $Ca^{2+}$ signalling.[2, 13, 21] Therefore stability is a priority for the design of Gd(III)-based CAs to avoid the release of free Gd(III) ions from CAs compounds. Last but not least, detailed investigations are needed for a better understanding of the new Gd(III) CAs, and these include studies on pharmacokinetics, clearance from the human body, long-term toxicity as well as reproducible preparations.

#### 1.1.1.2 $T_2$ Contrast Agents

Iron oxides, which are ferrites consisting of maghemite ($Fe_2O_3$) or magnetite ($Fe_3O_4$), have been serving as another group of $^1$H MRI CAs for over three decades.[62] Unlike Gd(III) chelates, iron oxide compounds mainly increase the rate of $T_2$ relaxation ($R_2$, $1/T_2$) by shortening the $T_2$ of the nearby protons, providing negative images for $T_2$-weighted MRI, albeit in some cases they can also be used as $T_1$ CAs. With the rapid advances in nanotechnology, nano-sized iron oxides have attracted increasing attention as $^1$H MRI CAs, and include superparamagnetic iron oxide nanoparticles (SPIONs) and ultra-small superparamagnetic iron oxide nanoparticles (USPIONs).[63-66] Similar to Gd(III) based CAs, there have been a number of commercial SPIONs that gained regulatory approvals for clinical MRI, as listed in Table 1-2.

**Table 1-2** Details of important commercial SPIONs-based $^1$H MRI CAs.[66]

| Brand | Coating agent | Size (nm) | Application | Company |
|---|---|---|---|---|
| Endorem® Feridex® | Dextran T10 | 120-180 | Liver imaging, cellular labelling | Guerbet，Advanced Magnetics (Current name AMAG Pharma) |
| Sinerem® Combidex® | Dextran T10, T1 | 15-30 | Metastatic lymph node imaging, blood pool agent, cellular labelling | Guerbet，Advanced Magnetics (Current name AMAG Pharma) |
| Lumirem® Gastromark® | Silicon | 300 | Oral gastrointestinal imaging | Guerbet，Advanced Magnetics (Current name AMAG Pharma) |
| Resovist® | Carboxydextran | 60 | Liver imaging, cellular labelling | Schering |
| Supravist® | Carboxydextran | 21 | Blood pool agent, cellular labelling | Schering |
| Ferristene Abdoscan® | Sulphonated styrene-divinylbenzene copolymer | 3500 | Oral gastrointestinal imaging | GE-Healthcare |

Besides these conventional CAs, there is still growing interest in the synthesis of multifunctional CAs. Historically, iron oxide nanoparticles (NPs) have been synthesised *via* diverse methods, such as chemical coprecipitations, microemulsions, sol-gel syntheses, sonochemical reactions, hydrothermal reactions, etc.[65, 67] By the combination of these synthetic techniques and surface modifications, CAs with customised morphology, size, composition, and property can be designed and used for more specific or complicated applications.[68] In recent years, there has been a trend toward the development of next-generation SPIONs-based CAs that have multifunctional characteristics and can be exploited for a variety of applications, such as tumour-targeted imaging,[69-73] multimodal imaging[74-77] and theranostics.[78-80]

Through careful design, SPIONs with tailored properties have been developed and actively studied in biomedical research. Despite this, there are several problems to be addressed. For example, although SPIONs can be prepared *via* a number of methods following different mechanisms, reproducible, cost-effective and scalable synthesis still remains a tough goal, in particular for industrial manufacturing.[65] In addition, attaching specific molecules onto the SPIONs by surface chemistry has already been extensively studied, but the precise control over the density and species of the functional groups remains challenging, resulting in the fact that the CAs often vary from batch to batch.[81] Furthermore, more functions give rise to more complicated systems, hence the pharmacokinetics, biodistribution, cytotoxicity as well as the relationship between particle characteristics and relaxivity need to be thoroughly studied and established.[65] It could be expected that a better fundamental understanding of properties would pave the way to accurate diagnosis and successful treatment of cancer diseases using multifunctional SPIONs-based CAs.

### 1.1.2 $^{19}$F MRI Contrast Agents

$^{19}$F MRI was introduced only four years later than $^{1}$H MRI in 1977 by Holland *et al.*[82] As listed in Table 1-1, $^{19}$F nuclei have fairly comparable properties to $^{1}$H, including spin 1/2, large gyromagnetic ratio (only 6% lower than $^{1}$H), high sensitivity (83% relative to $^{1}$H) and virtually 100% of natural isotopic abundance. These characteristics naturally make $^{19}$F another suitable candidate for MRI. Furthermore, the most attractive feature is the physiological rarity of $^{19}$F, which can eliminate the unwanted background in imaging because the concentration of endogenous $^{19}$F nuclei in body is negligible and barely detectable by $^{19}$F MRI.[83, 84] Owing to this intrinsic advantage, $^{19}$F MRI is highly selective and quantitative when contrast agents (CAs) are employed.

In the past four decades, tremendous effort has been dedicated to the development of $^{19}$F MRI CAs, which can be categorised as $^{19}$F salts, $^{19}$F-containing small molecules, perfluorocarbon (PFC) emulsions and $^{19}$F-containing macromolecules.[83-86] The design of $^{19}$F MRI CAs has been facilitated by the nature of $^{19}$F. For instance, unlike the radioactive $^{18}$F used for PET, $^{19}$F is a stable isotope, easing both the preparation of CAs and procedures for imaging. Additionally, fluorine atoms are usually incorporated to the CAs in the form of highly-stable carbon-fluorine covalent bonds, thus reducing the risk of loss (or decomposition) of imaging moieties which may potentially occur with Gd(III) chelates.[84] Moreover, $^{19}$F can exist in numerous organic compounds ranging from small molecules to macromolecules, offering more opportunities for the development of $^{19}$F CAs.

As reviewed by Yu *et al.*,[87] quite a few $^{19}$F-containing small molecules have been exploited as reporters and sensors for the detection of changes of biological conditions (e.g. pH, metal ions and oxygen content) as well as the study of drug metabolism. However, in the following sections, perfluorocarbons (PFCs) and partially-fluorinated polymers will be introduced given that they represent two major categories of $^{19}$F MRI CAs.

#### 1.1.2.1 Perfluorocarbons (PFCs) as $^{19}$F MRI Contrast Agents

Perfluorocarbons (PFCs) are synthetic organic molecules (typically alkanes and their derivatives) for which all hydrogen atoms are replaced by fluorine atoms.[85] PFCs can be divided into five types based on their chemical structure including aromatic and unsaturated PFCs, saturated linear PFCs, saturated ring system PFCs, perfluoroamines and perfluoroethers.[86] A number of typical PFCs are illustrated in Figure 1-2. Owing to their unusual chemical structures, PFCs have several unique properties, such as highly hydrophobicity and lipophobicity, low surface tension, low intermolecular cohesion, chemical inertness and low cytotoxicity.[86] A number of these characteristics make them suitable candidates for various biological applications.

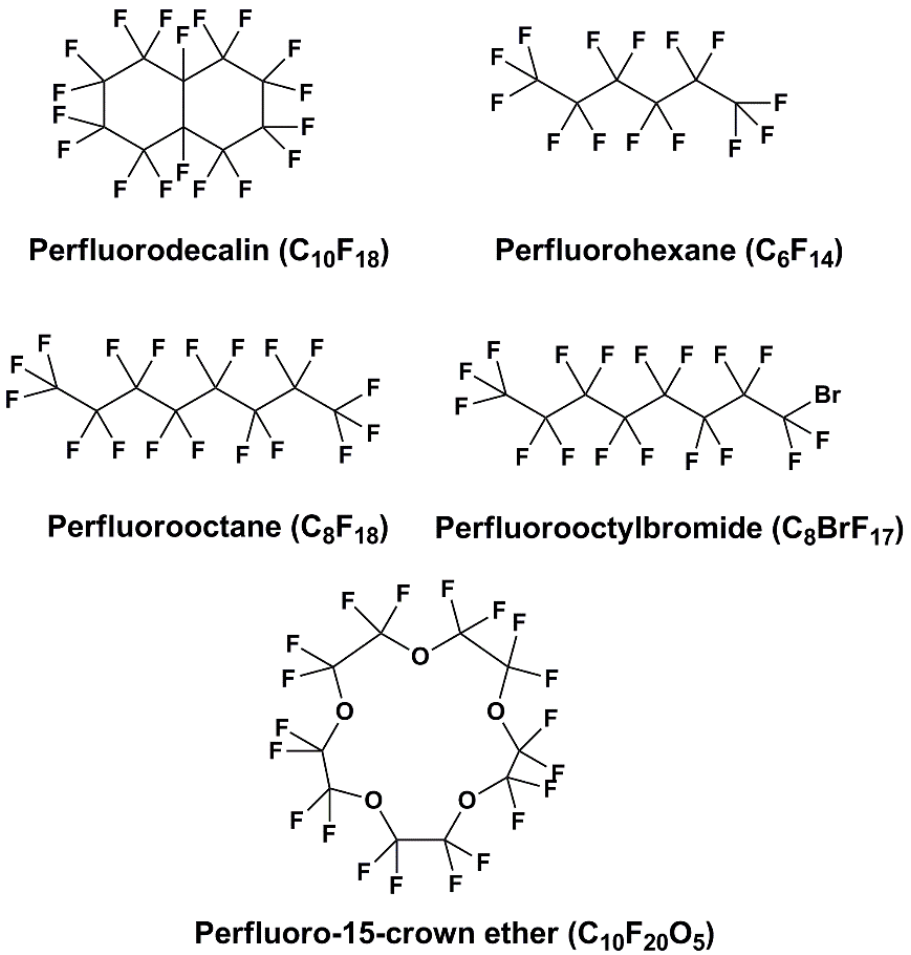


**Figure 1-2** Chemical structures of some typical PFCs.[86]

PFCs were initially explored as blood substitutes in the 1960s and 1970s due to their excellent capacity for carrying oxygen.[88, 89] In recent years, PFCs have been used as CAs for ultrasonography owing to their micro-bubble-forming capability.[90, 91] Since the appearance of $^{19}$F MRI in 1977, PFCs have attracted considerable attention as $^{19}$F MRI CAs.[83, 86, 87, 91, 92] PFCs possess quite a few advantages as $^{19}$F MRI CAs: (1) PFCs have a high $^{19}$F content that is required for generating an intense $^{19}$F signal; (2) PFCs are inert due to the stable carbon-fluorine bond, hence they can tolerate harsh preparation conditions (e.g. emulsification) as well as avoid undesired reactions with other compounds;[92] (3) PFCs have already been extensively used as blood substitutes, so their biological properties such as biodistribution and biocompatibility have been well investigated and documented.[91, 92]

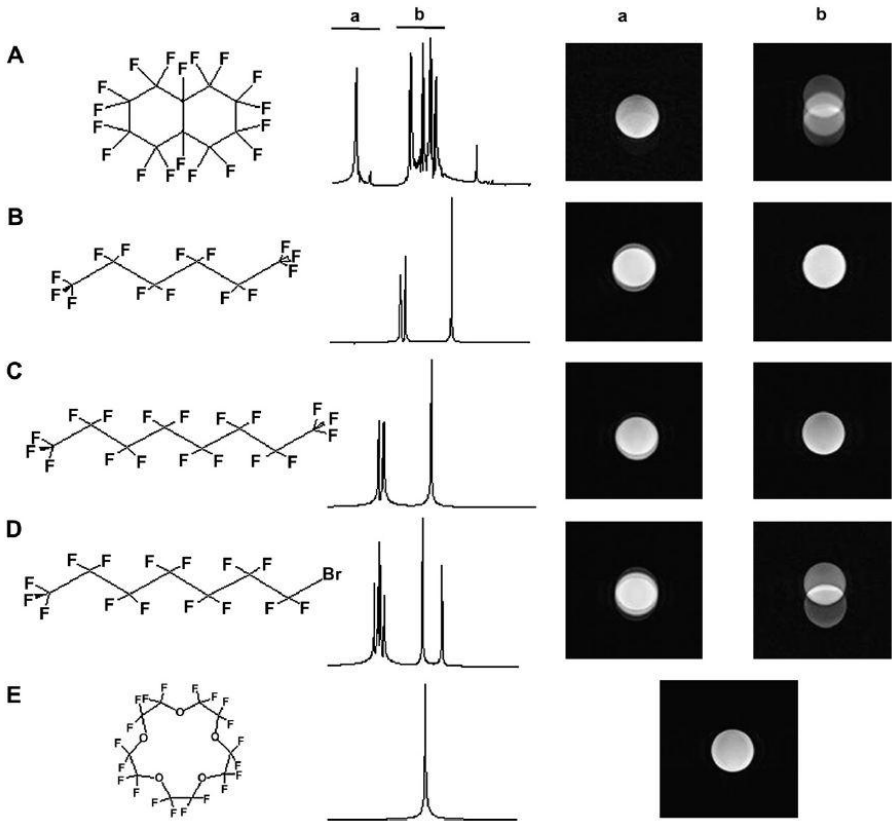


**Figure 1-3** Chemical structures of five representative PFCs and their $^{19}F$ NMR spectra and MRI images. Clearly, non-identical $^{19}F$ atoms in PFCs (A─D) show multiple peaks in $^{19}F$ NMR spectra and thus result in images with ghost artefacts. In contrast, chemically-equivalent $^{19}F$ nuclei in a symmetric structure (E) display only a single resonance peak in $^{19}F$ NMR and no artefacts in the images. Adapted from Srinivas *et al*.[93]

To be successful $^{19}F$ MRI CAs, PFCs should fulfil two criteria: (1) a symmetric structure for single and narrow $^{19}F$ resonance to avoid reduced detection sensitivity and chemical shift imaging artefacts;[85, 86] (2) a short $T_1$ to minimise scanning time and long $T_2$ to increase imaging quality.[86] The importance of identical $^{19}F$ nuclei for $^{19}F$ MRI has been pointed out in previous studies,[93] and is also illustrated in Figure 1-3. A single and sharp resonance from symmetric PFCs is favourable for $^{19}F$ MRI as it can avoid the use of selective MRI pulse sequences, and thus provide images with no ghost artefacts as well as maximised signal-to-noise ratio (SNR).[86, 93]

PFCs are highly hydrophobic and lipophobic and therefore they are normally formulated into stable emulsions, in particular nanoemulsions, for biological applications. Through high energy processing such as microfluidisation or sonication, PFC nanoemulsions with size of 20~500 nm have been prepared by using small amounts of surfactants.[86] For human use, PFC nanoemulsions must be stable and non-toxic. It is well known that surfactants play an essential role in the

fabrication of PFC nanoemulsions since they affect both the stability and biocompatibility. Therefore, biocompatible phospholipids and Pluronic F68$^{TM}$ (BASF) which are two effective surfactants have been commonly chosen for the preparation of PFC nanoemulsions.[94] The latter is a triblock copolymer of poly(ethylene oxide)-*block*-poly(propylene oxide)-*block*-poly(ethylene oxide) (PEO-*b*-PPO-*b*-PEO) that has been approved by the FDA for many applications.[95, 96] However, it was also suggested that the stability of PFC nanoemulsions was mostly determined by the structure of the PFCs rather than the type of surfactant, and PFCs having longer chain lengths or larger molecular weights are preferred to form emulsions with higher stability.[97, 98] Therefore, the stability of PFC nanoemulsions remains a relatively complicated issue which needs more detailed investigations before certain rules are established.

PFCs can introduced to specific tissues after *ex vivo* incubation with cells, while they can also be introduced *via* direct intravenous injection or oral administration.[87, 99] Generally, there are two ways that PFCs can act as $^{19}$F MRI CAs. First, PFCs can be introduced as an exogenous $^{19}$F source to be directly visualised and quantified by $^{19}$F MRI owing to the absence of background $^{19}$F signal. For example, PFCs have been extensively used as $^{19}$F MRI CAs for cell tracking and labelling[100-112] as well as imaging of diseased tissue.[99, 113-118] Second, since the relaxation times of $^{19}$F nuclei can be affected by environmental factors such as oxygen content, PFCs have been employed as probes to monitor these changes in biological tissues. As noted earlier, PFCs were first developed as blood substitutes because of their high oxygen-loading capacity. The rate of $T_1$ relaxation ($R_1 = 1/T_1$) is linearly related to the partial pressure oxygen ($p$O$_2$) for some types of PFCs and can also be affected by temperature and magnetic field, whereas it is barely sensitive to other conditions such as pH and $CO_2$.[87, 119] By making use of this feature, PFCs can be used as sensors for the measurement of $p$O$_2$ in different tissues including oximetry in tumour tissue under the conditions of fixed magnetic fields and temperatures.[120-127]

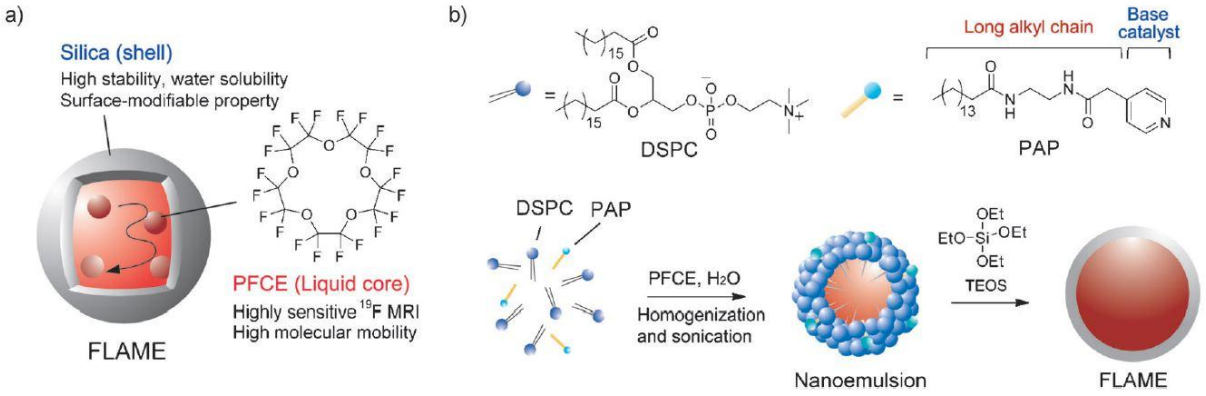


**Figure 1-4** Schematic illustration of the synthesis of PFCE/silica core-shell nanoparticles (FLAME) a) Structure and functions of FLAME and b) Synthetic routes for FLAME. Adapted from Matsushita *et al.* [128]

Owing to their chemical inertness, the application of PFCs has been restricted by the lack of sites for chemical modification. In an attempt to tackle this problem, considerable effort has been devoted to the fabrication of PFC-based multifunctional NPs for multimodal molecular imaging. By introducing a coating layer around the PFC emulsion particles, functional moieties can be attached to or incorporated in the coating materials which can be polymeric, inorganic or lipidic materials. Pisani *et al.*[129] fabricated core-shell structured microparticles/nanoparticles comprised of liquid perfluorooctylbromide (PFOB) as the core and biocompatible and biodegradable poly(lactic-co-glycolic acid) (PLGA) as the shell. The multifunctional particles, with tunable size and shell thickness, were evaluated as bimodal CAs for *in vivo* ultrasound imaging and *in vitro* $^{19}$F MRI. Lim *et al.*[130] synthesised IRDye800-coated nanoemulsions as bimodal CAs, which were used for the *in vitro* and *in vivo* labelling and imaging of dendritic cells by $^{19}$F MRI and near-infrared (NIR) fluorescence imaging. As illustrated in Figure 1-4, Matsushita *et al.*[128] developed core-shell NPs by coating perfluoro-15-crown-5-ether (PFCE) emulsion particles with a silica shell, which was further conjugated with reporter proteins and polyethylene glycol (PEG) chains. Such biocompatible and water-dispersible NPs were assessed as $^{19}$F MRI CAs for *in vitro* monitoring of gene expression in living cells and *in vivo* imaging tumour tissue as well. Bae *et al.*[117] encapsulated PFCE and Rhodamine with lipids and then conjugated folate molecules onto the lipid layer. The as-formed bimodal NPs were used for both fluorescence imaging and $^{19}$F MRI with tumour-targeting.

Finally, PFCs and other $^{19}$F-containing small molecules have been extensively explored as $^{19}$F MRI CAs for a broad range of biological implementations. The progress achieved in the last three decades confirms the great potential of $^{19}$F MRI as a prominent imaging modality. In spite of

numerous efforts, $^{19}$FMRI have not been routinely used in the clinic mainly due to the lack of efficient and reliable CAs. In light of the extremely high $^{19}$F loading, there seems to be no doubt that PFCs are effective candidates for $^{19}$F MRI CAs. However, the stability of PFC emulsions is a major issue because the emulsion can be slowly destabilised and decomposed due to the unavoidable process of Ostwald ripening, which is a molecular diffusion phenomenon of the gradual growth of larger particles at the expense of smaller ones.[86] Moreover, the relatively large size (100~250 nm) hampers a number of applications such as visualising the vasculature and cell labelling because of the impermeability of capillaries to particles of this size. Furthermore, although $^{19}$F MRI takes advantage of the minimal endogenous back ground signal, a sufficient concentration of $^{19}$F nuclei in the target voxel is required to generate an adequate signal. One feasible way to overcome this is to functionalise PFCs with targeting moieties so that they accumulate in desired tissues to enhance the signal intensity. Despite a few successful examples, the functionalisation of PFCs remains an elusive goal owing to the chemical inertness and the complicated process of emulsification. Therefore, further innovative work on the development of CAs is required for the maturation and clinical application of $^{19}$F MRI.

#### 1.1.2.2 Partly-Fluorinated Polymers as $^{19}$F MRI Contrast Agents

After decades of development of PFC CAs, virtually no candidate has received regulatory approval for clinic use, due in large part to the obstacles discussed in the last section. In recent years, partly-fluorinated polymers have drawn increasing attention as alternative $^{19}$F MRI CAs. Compared to small molecules and inorganic materials, polymers have considerable intrinsic advantages as CAs for molecular imaging, such as high diversity depending on monomer type, molecular weight, tacticity and topology, long circulation time owing to large size and complex chemical structure, capability to carry functional sites for incorporating multimodal imaging modalities, targeting moieties and therapeutic agents, etc.[131] In recent years, the precise synthesis of polymers with tailored architectures and functionalities has been achieved by controlled polymerisation techniques,[132, 133] facilitating the development of partly-fluorinated polymers for $^{19}$F MRI. A broad class of $^{19}$F-containing polymers, in which the $^{19}$F nuclei are usually incorporated through the copolymerisation of $^{19}$F-containing monomers, have been developed as $^{19}$F MRI CAs for both diagnosis and cancer therapy. Based on the polymer topology these can be classified as linear polymers, dendritic polymers, hyperbranched polymers, and other polymers.

#### 1.1.2.2.1 Linear Polymer CAs

Linear homopolymers have simple structures, and are relatively facile to synthesise and easy to control over a wide composition range. Mehta *et al.* reported an early study on $^{19}$F MRI probes based on partly-fluorinated linear polymers.[134] In their work, polylysine, a cationic polymer that is preferentially internalised by tumour cells, was modified with $^{19}$F-containing molecules (S-ethyltrifluorothioacetate and trifluoroacetamidosuccinic anhydride) at the sites of reactive amino groups. The resulting $^{19}$F-containing polymers showed a single sharp peak in the $^{19}$F NMR spectrum and thus had the potential to be $^{19}$F MRI CAs, although the authors did not demonstrate their utility in MRI.

Amphiphilic block copolymers have been applied in numerous fields because they can form various ordered structures *via* self-assembly processes.[135] Peng *et al.* pioneered the study of partly-fluorinated amphiphilic block copolymers as $^{19}$F MRI CAs.[136, 137] As displayed in Figure 1-5, amphiphilic block copolymers of poly(acrylic acid)-*b*-poly(*n*-butyl acrylate-*co*-2,2,2-trifluoroethyl (meth)acrylate) (PAA-*b*-P(*n*BA-*co*-TFE(M)A) were synthesised *via* atom transfer radical polymerisation (ATRP). The block copolymers were self-assembled into stable micelles with diameter of 20~45 nm in water or water/organic mixed solvents. After that the NMR and imaging properties of the micelles were evaluated by $^{19}$F NMR and MRI, respectively. It was found that the choice of $^{19}$F-containing monomer played a vital role in imaging performance. Acrylate backbones with a lower glass transition temperature ($T_g$) (in the bulk state) exhibited higher flexibility than methacrylate backbones, and therefore they have $^{19}$F nuclei with higher mobility and longer $T_2$ relaxation times which resulted in better imaging properties. In addition, the solvent was another key parameter because it not only determined the morphology and structure of the micelles but also affected the rigidity of the micelle core. Overall, this work revealed for the first time the potential of partly-fluorinated block polymers as $^{19}$F MRI CAs, and also elucidated a number of important criteria for the design of successful CAs.

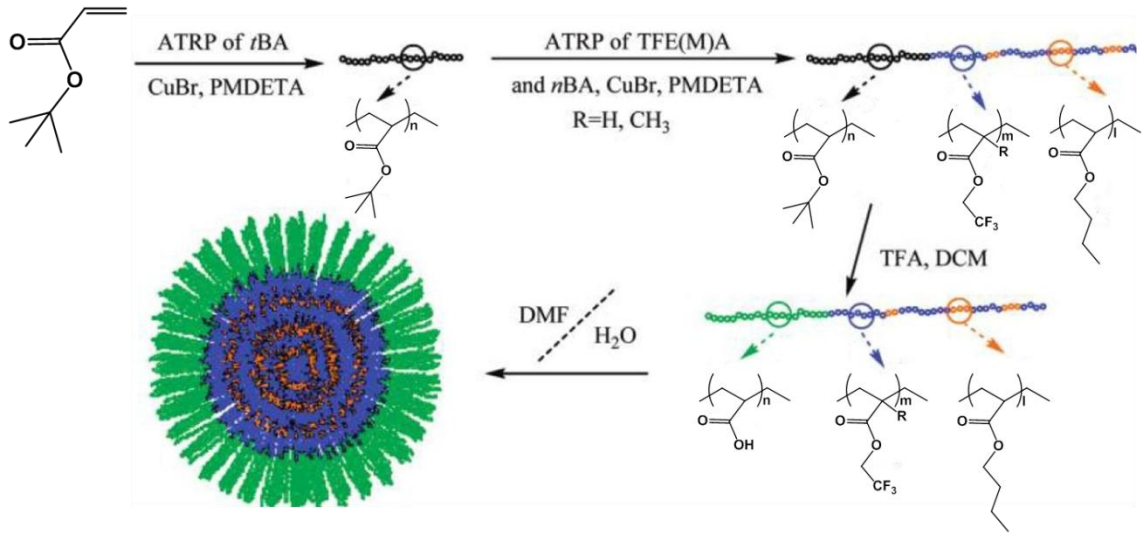


**Figure 1-5** Synthetic route for amphiphilic block copolymers PAA-*b*-P(*n*BA-*co*-TFE(M)A). Adapted from Peng *et al*.[137]

Following this work, Nurmi *et al.* developed block and statistical copolymers consisting of TFEMA and 2-(dimethylamino)ethyl methacrylate (DMAEMA) units as $^{19}$F MRI CAs.[138] The statistical copolymers P(TFEMA-*co*-DMAEMA) and block copolymers PTFEMA-*b*-P(TFEMA-*co*-DMAEMA) displayed pH-responsiveness owing to the existence of DMAEMA segments which were introduced to modulate the confirmation of copolymer chains in solution. Larger micelle sizes and longer $T_2$ relaxation times of $^{19}$F were observed at low solution pH because of the protonation of DMAEMA segments, which increased the hydrophilicity of P(TFEMA-*co*-DMAEMA) chains and accordingly enhanced the mobility of the $^{19}$F nuclei in the corona. Moreover, the NMR properties were found to be related to polymer composition, salt concentration and polymer concentration. Therefore Nurmi *et al.* demonstrated that achieving high mobility of the $^{19}$F nuclei and high $^{19}$F content was necessary for superior imaging performance, and this was consistent with the findings reported by Peng *et al*.[137] Furthermore, this work also presented a straightforward method to modulate the relaxation times of $^{19}$F by simply copolymerising $^{19}$F-containing monomer with a pH-responsive monomer.

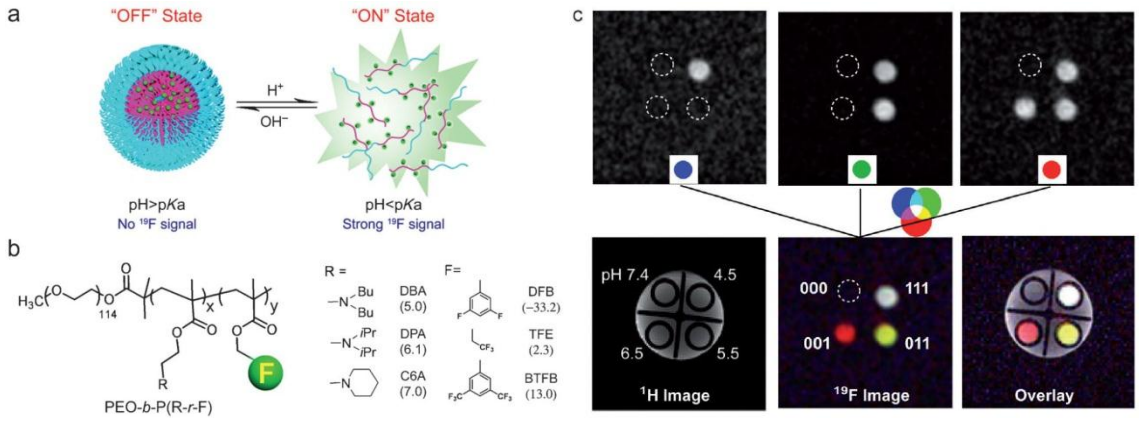


**Figure 1-6** (a) Schematic illustration for ON/OFF regulations of the $^{19}$F MRI probes based on partly-fluorinated amphiphilic block copolymers. (b) Chemical structures of the block copolymers. (c) $^{19}$F MRI images of the mixed polymer probes in solutions of different pH. The 'barcode map' concept was employed to realise pH readout by encoding each voxel with an activation barcode through the combination of $^{19}$F NMR and MRI. Adapted from Huang *et al*.[139]

Using a similar concept, Huang *et al.* have recently designed pH-responsive $^{19}$F MRI probes with tuneable ON/OFF transitions.[139] A series of amphiphilic block copolymers were synthesised through ATRP, comprised of PEO as the first block and copolymers of tertiary amine/ammonium monomers and $^{19}$F-containing monomers as the second block. As shown in Figure 1-6 (a) and (b), the hydrophilicity of the $^{19}$F-containing segments could be tuned by adjustment of the pH owing to the protonation and deprotonation of the tertiary amine/ammonium segments, and hance the morphology was switchable between micelles and unimers. To be more specific, the $^{19}$F nuclei in the rigid micelle cores were not $^{19}$F NMR detectable due to restricted motion, whereas those in the flexible umimers were detectable because of enhanced mobility. By assigning each polymer with a certain 'barcode', these polymers can be used as multi-chromatic $^{19}$F NMR/MRI probes for quantitative pH measurement (Figure 1-3 (c)), indicating their future application in a number of pathological indications including cancer, inflammation and osteoporosis.

Very recently, Zhang et al. reported the RAFT synthesis of thermo- and ionic-responsive copolymers of PEGMA and TFEA.[140] Those water soluble copolymers displayed lower critical solution temperature (LCST) transitions only in salt solutions. The LCST property was dependent on the composition of polymers as well as the type of salt. In addition, the motion of protons was not only affected by the temperature of salt solutions but also related to their position in the polymer chains. Although the $^{19}$F NMR and MRI were not conducted, it could be expected that the $^{19}$F

resonance would exhibit the similar changes to those of protons. Therefore these linear copolymers can be used as dual responsive CAs for $^{19}$F MRI

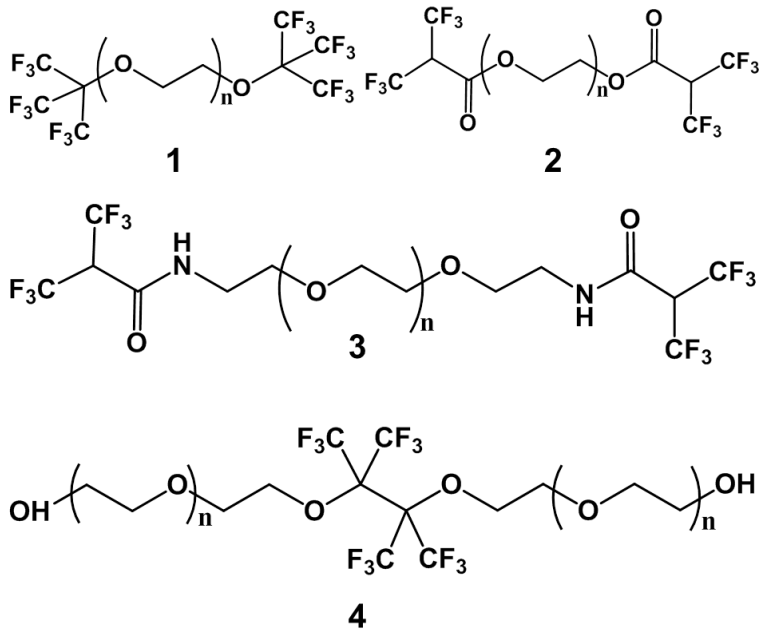


**Figure 1-7** Chemical structures of several partly-fluorinated polyethylene glycol (PEG) derivatives.[141-143]

In the past few years, CAs based on partly-fluorinated PEG have gained much attention.[141-143] Partly-fluorinated PEG derivatives were synthesised by end modification of linear PEG with perfluoro-alcohol such as perfluoro-*tert*-butyl alcohol and perfluoropinacol, and tested as $^{19}$F MRI CAs (Figure 1-7). These novel compounds exhibited several favourable properties, including simple chemical structures, high $^{19}$F content, hydrophilicity, a single $^{19}$F resonance, etc. However, the future exploration of these CAs may be limited by the lack of handles for chemical functionalisation and potentially very short blood circulation time.

The development of linear CAs has also been moving toward multimodal systems. Lu *et al.* designed a series of statistical linear copolymers consisting of the monomeric aggregation-induced emission (AIE) fluorophore, *N*-(2-hydroxypropyl) methacrylamide (HPMA), [2-(methacryloylxy)ethyl]trimethylammonium chloride (MATMA) and 2,2,2-trifluoehtyl methacrylate (TFEMA).[144] After self-assembling into micelles, these non-toxic and cell permeable polymers were exploited as CAs for fluorescence bioimaging and also showed feasibility for $^{19}$F MRI.

#### 1.1.2.2.2 Dendrimer CAs

Dendrimers are 'tree-like' macromolecules that have repeating branching units emanating from a central core.[145] In the past few years, dendrimers have been considered as an excellent platform for the design of $^{19}$F CAs.[85] Compared to linear polymers, dendrimers can accommodate a larger amount of chemically-identical $^{19}$F nuclei in one molecule, generating an enhanced single $^{19}$F signal. In addition, the increased hydrodynamic size can prolong the blood circulation time, facilitating a number of biological applications.

As a typical and commercially-available dendrimer, polyamidoamine (PAMAM) has been extensively chosen for the fabrication of $^{19}$F MRI CAs. As reported by Criscione *et al.*,[146] PAMAM was surface modified with heptafluororobutyric acid anhydride (HFAA), trifluoroacetic acid anhydride (TFAA) and pentafluoropropionic acid anhydride (PFAA), respectively. Through self-assembly process, the resulted partly-fluorinated PAMAM formed microparticles (0.7~3.3 μm) in water, which were pH-sensitive and utilised for controlled drug release. Moreover, the site-specific accumulation of the microparticles *in vivo* was also revealed by $^{19}$F MRI. This work confirmed the potential applications of partly-fluorinated PAMAM dendrimers as multifunctional $^{19}$F MRI CAs.

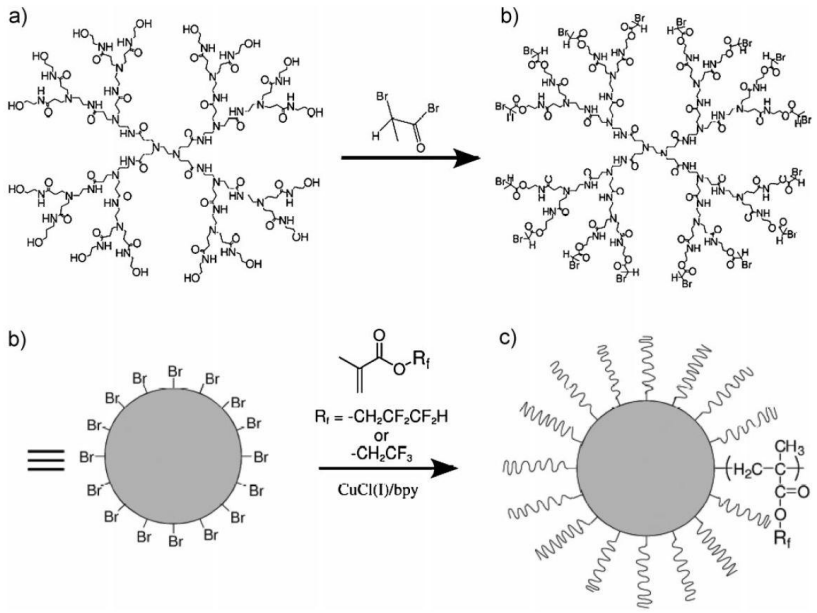


**Figure 1-8** Synthesis of partly-fluorinated star-like dendrimers *via* ATRP. (a) PAMAM-OH, (b) PAMAM-Br macroinitiator, and (c) partly-fluorinated star-like dendrimers. Adapted from Ogawa *et al.*[147]

Recently, controlled radical polymerisation has also been employed for the functionalisation of PAMAM. Ogawa *et al.* modified PAMAM with bromine end groups and then used these molecules

as macroinitiators for the polymerisation of 2,2,3,3-tetrafluoropropyl methacrylate (TFPMA) and TFEMA *via* ATRP (Figure 1-8).[147] Fluorinated star-like dendrimers with targeted degree of polymerisation (DP) and narrow molar-mass dispersity ($Đ_M$) were prepared, and they could form NPs in organic solvents with size of 2~25 nm. The $^{19}$F resonance of these NPs was also confirmed by $^{19}$F NMR, demonstrating their potential used as $^{19}$F MRI CAs. By extending this approach, Ogawa *et al.* later functionalised PAMAM with amphiphilic block copolymers of TFPMA and a zwitterionic monomer.[148] Interestingly, owing to the short $T_1$ (110~240 ms) and $T_2$ (8.4~13 ms), the as synthesised star-like dendrimers could be used for $T_1$-weighted $^{19}$F MRI by carefully selecting the repetition time (TR) and echo time (TE). More recently, Ogawa *et al.* functionalised PAMAM with amphiphilic statistical copolymers consisting of TFPMA and *tert*-butyl methacrylate (*t*BMA).[149] The P*t*BMA was then hydrolysed to poly(methacrylic acid) (PMAA) and converted into its sodium salt. The obtained dendrimers had a size of 12-25 nm and showed relatively short $T_1$ (400 ms) and long $T_2$ (70~80 ms), which were favourable for $^{19}$F MRI. The *in vitro* $^{19}$F MRI revealed that these NPs could be detected at very low polymer concentration (0.2 μM), while the *in vivo* $^{19}$F MRI visualised the accumulation of NPs in liver and kidneys of a rat with 10 min. These results indicated that the star-like dendrimers could be used as a new type of $^{19}$F MRI CAs. Nevertheless, the use of PTFPMA is not ideal because while it provides a high $^{19}$F content it also has multiple $^{19}$F NMR resonances.

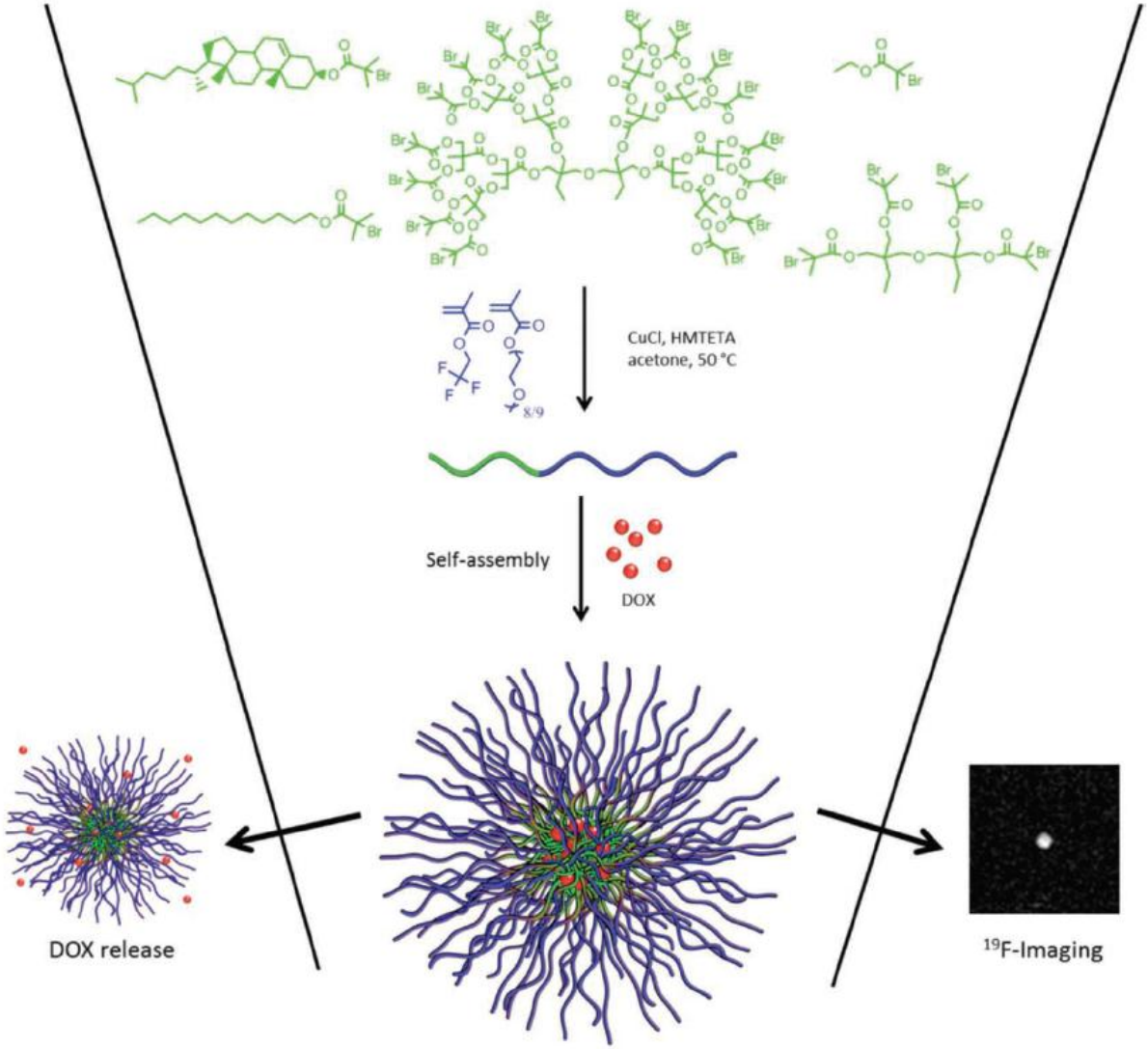


**Figure 1-9** Fabrication of theranostic NPs based on partly-fluorinated linear polymers and star-like dendrimers. Green colour stands for hydrophobic segments and blue colour represents hydrophilic segments. Adapted from Porsch *et al*.[150]

Owing to their 3D globular architecture and multiple functional groups, dendrimers have also been exploited for the development of theranostic agents. Porsch *et al.* prepared a series of $^{19}$F MRI CAs using ditrimethylolpropane (di-TMA)-based dendrimers (Figure 1-9).[150] Dendritic initiators of either 4 or 16 end groups were used to synthesise statistical copolymers consisting of TFEMA and poly(ethylene glycol) methyl ether methacrylate (PEGMA) units, resulting in star-like dendrimers composed of hydrophobic and dendritic cores and amphiphilic P(TFEMA-*co*-PEGMA) arms. NPs (6~9 nm) were formed through self-assembly in phosphate buffered saline (PBS), and were loaded with an anticancer drug doxorubicin (DOX). The DOX-loaded NPs could be taken up by breast cancer cells and showed dose-dependent toxicity. Moreover, these $^{19}$F-containing NPs were

visualised by $^{19}$F MRI in 10 min at a concentration of 10 mg/mL in PBS. Therefore, this work demonstrated an excellent example of $^{19}$F MRI-based theranostic system by using partly-fluorinated star-like dendrimers.

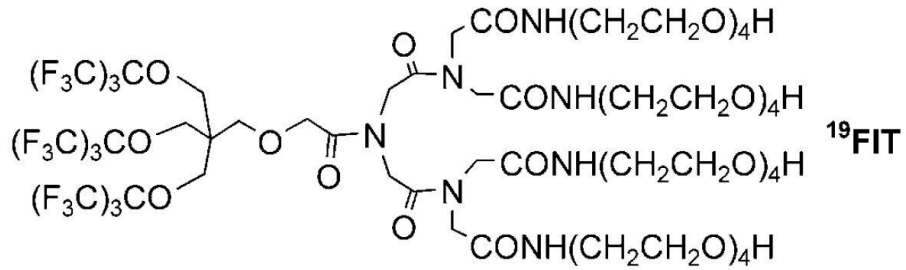


**Figure 1-10** Chemical structure of $^{19}$FIT. Adapted from Jiang *et al.*[151]

Apart from perfectly symmetrical dendrimers, partially symmetrical dendrimers comprised of two different hemispheres (dendrons) have also been designed for $^{19}$F MRI. $^{19}$FIT, a bispherical fluorocarbon molecule comprised of an H-spherical cone and a$^{19}$F-spherical cone, was developed as $^{19}$F MRI CAs by Jiang *et al.* (Figure 1-10).[151] Such structure could ensure high fluorine content while remaining water soluble. In addition, modification at the H-spherical cone did not affect the symmetry of the $^{19}$F atoms, avoiding unwanted multiple $^{19}$F resonances. The amphiphilic $^{19}$FIT molecule showed several outstanding properties, such as high $^{19}$F content (27.1 wt%), single $^{19}$F resonance, short $T_1$ (163 ms), non-toxicity and chemical stability. The *in vivo* imaging performance of $^{19}$FIT was demonstrated by whole body $^{19}$F MRI using mouse models at doses of 60 mmol/kg and 30 mmol/kg $^{19}$F. The molecules were initially visualised in several organs, but they were only detected in the bladder after 1-2 hours, indicating rapid excretion and an *in vivo* residence half-life time of about 0.5 day. It should be noted that the physicochemical properties of $^{19}$FIT could also be modulated by using fluorous mixture synthesis (FMS) to obtain dendrimers of multiple generations.[152]

As with PFC emulsions, the relaxation times of partly-fluorinated dendrimers can also be tuned by introducing Gd(III)-chelates. Huang *et al.* designed a dendrimer-based platform with $^{19}$F atoms around the periphery and Gd(III)-chelates conjugated nearby.[153] Owing to the existence of bifunctional Gd(III)-chelates, the $T_1$ was significantly shortened from 860 to 140 ms, reducing the scanning time without sacrificing the image quality. Moreover, the toxicity of these CAs could be effectively reduced by shielding the dendrimer surface with hydrophilic groups. The imaging performance was also confirmed by fast *in vivo* $^{19}$F MRI which showed that the CAs could be

detected in the rat at a comparably low dose (11.7 mmol/kg $^{19}$F). Therefore these fluorine-rich dendrimers are promising for molecular imaging using $^{19}$F MRI.

#### 1.1.2.2.3 Hyperbranched Polymer CAs

Hyperbranched polymers (HBPs) are a special class of dendritic polymers that have highly-branched, 3D globular structures. Unlike perfectly branched and monodisperse dendrimers, HBPs are relatively non-symmetric and irregular owing to the random distribution of dendritic, linear and terminal units along the polymer backbone.[154] Therefore, the synthesis of HBPs is much simpler and affordable than that of dendrimers, at a cost of perfect architecture.[155] HBPs have several unique properties, such as compact structure, low viscosity, high solubility and high functionality, and hence they have been widely investigated in the field of biomedicine.[154, 156, 157]

Du *et al.* reported HBP-based NPs as $^{19}$F MRI CAs.[158] First, HBPs with bromine or chlorine end groups were synthesised by a self-condensing vinyl (co)polymerisation. Then the HBPs were utilised as macroinitiators for the copolymerisation of TFEMA and *tert*-butyl acrylate. After hydrolysis, star-like polymers with a hydrophobic hyperbranched core and amphiphilic P(TFEMA-co-AA) arms were obtained and then self-assembled into micelles with a hydrodynamic diameter ($D_h$) of 20~25 nm. As characterised by $^{19}$F NMR, these micelles showed a single and narrow $^{19}$F signal and favourable $T_1$ (~500 ms) and $T_2$ (~50 ms). $^{19}$F MRI also confirmed the capability of these micelles as $^{19}$F CAs. However, the scanning time was quite long (13 hours) due to the relatively low $^{19}$F concentration (1~4 mM $^{19}$F). Therefore a higher $^{19}$F loading should be achieved for future $^{19}$F MRI applications. Using the same HBPs as platform, Du *et al.* developed a theranostic system.[159] Cascade blue, a fluorescence reporter, was incorporated into the amphiphilic arms by copolymerisation. The resulted micelles were used as drug carriers for the loading and releasing of DOX, and the high toxicity of DOX-loaded micelles to U87-MG-EGFRvIII-CBR cells was confirmed by MTT assays. Finally, the $^{19}$F signal from cell engulfed micelles was detected by $^{19}$F NMR. This study showed a successful example of mutilfunctional HBPs as theranostic agents for anticancer drug delivery, fluorescence imaging and $^{19}$F MRI.

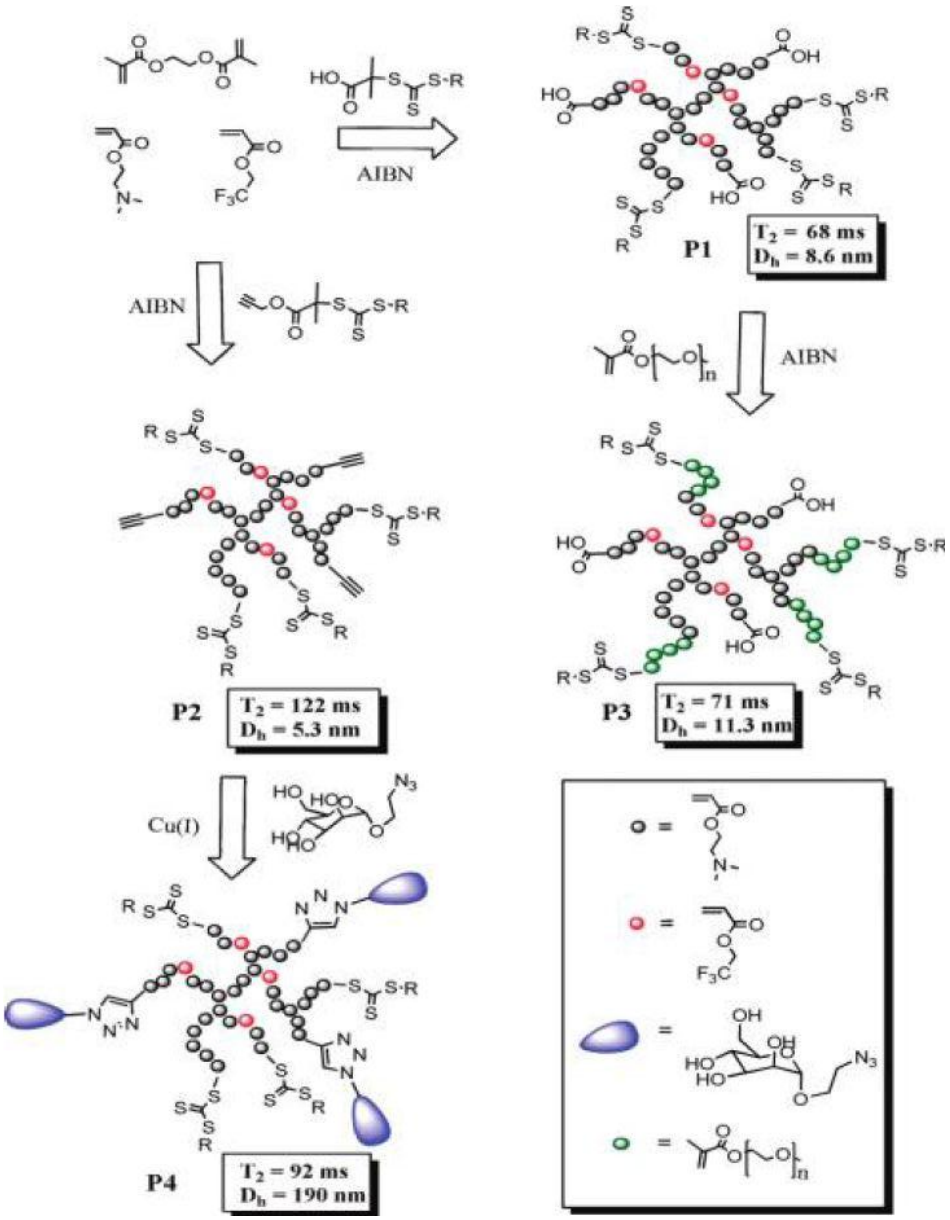


**Figure 1-11** Synthetic routes for partly-fluorinated HBPs with carboxyl acid (P1), alkyne (P2) and mannose (P3) end groups, respectively. Adapted from Thurecht *et al.*[160]

Although a variety of dendritic polymer-based CAs have been developed, the dendrimers and HBPs were usually utilised as 'core' materials. In those cases, $^{19}F$ nuclei were placed around the periphery of cores through surface functionalisation. Therefore the advantage of the 3D globular structure of HBPs has not been fully exploited. To further explore HBP materials, Thurecht *et al.* pioneered and detailed the synthesis of HBP-based CAs in which larger amounts of $^{19}F$ nuclei are placed with the 3D hyperbranched structure.[160] As displayed in Figure 1-11, partly-fluorinated HBPs were synthesised *via* RAFT copolymerisation of 2-(dimethylamono)ethyl acrylate (DMAEA) and 2,2,2-trifluoroethyl acrylate using a bifunctional monomer ethylene glycol dimethacrylate

(EGDMA) as a branching agent (crosslinker). Then the as-synthesised HBPs were used as macro chain transfer agents (CTAs) and chain extended with PEGMA to increase hydrophilicity and biocompatibility. The significance of such an innovative is profound. On one hand, the positioning of $^{19}$F nuclei within the 3D hyperbranched structure by direct copolymerisation not only increases the $^{19}$F loading but also improves the mobility of $^{19}$F as the association of $^{19}$F segments is prevented. On the other hand, RAFT polymerisation allows for the precise synthesis of HBPs with well-defined structures as well as the introducing various functional end groups. As a result, these novel HBP CAs formed NPs (~10 nm) in aqueous solution after chain extension with PEGMA, and they showed low cytotoxicity according to MTS assays. As measured by $^{19}$F NMR, these CAs had a $T_1$ of 480 ms and $T_2$ of 88 ms, which are preferable parameters for imaging. The imaging performance and excretion by kidneys were also observed by *in vivo* $^{19}$F MRI conducted on a mouse. Overall, this work proposed a new design concept for highly efficient and multifunctional HBP-based $^{19}$F CAs. Very recently Thurecht *et al.* furthered this work and developed a multimodal system for theranostic.[161] HBPs comprised of TFEA, PEGMA and EGDMA were synthesised *via* RAFT polymerisation using an alkyne-terminated CTA. Next the HBPs were labelled with fluorescence moieties (Rhodamine B and NIR-797) and also conjugated with a targeting molecule (folic acid). By combining highly sensitive optical imaging and high resolution $^{19}$F MRI, these multifunctional HBPs were evaluated as multimodal imaging agents *in vivo* and *in vitro* with very high targeting efficiency to B16 melanoma cells. Therefore this study demonstrated a powerful HBP-based platform by using robust synthetic techniques for advanced multimodal imaging.

#### 1.1.2.2.4 Other Polymer CAs

Apart from linear and dendritic polymers, other polymeric materials have also been chosen for the design of $^{19}$F MRI CAs, and these include proteins, nanogels and hydrogels.

Mehta *et al.* reported the early work on protein-based $^{19}$F MRI CAs.[162] Three proteins, serum albumin, γ-globulin and purified immunoglobulin (IgG), were conjugated with S-ethyl trifluorothioacetate molecules by reaction with the amino groups. The biocompatible partly-fluorinated proteins were examined by *in vivo* $^{19}$F magnetic resonance spectroscopy ($^{19}$F MRS), showing the potential for $^{19}$F MRI as intravascular CAs. Recently, Sun *et al.* developed lectin-based $^{19}$F MRI CAs for specific detection and imaging of glycoproteins.[163] When the $^{19}$F-labelled lectins were bound with glycoproteins, the $T_2$ of $^{19}$F was shortened due to the increased apparent molecular mass ($M_r$). By utilising this characteristic, these $^{19}$F-labelled lectins could be employed as ON/OFF

probes to distinguish glycoproteins from other small molecules saccharides on the basis of differences in their $M_r$.

Several types of $^{19}$F-containing nanogels have been prepared through crosslinking reactions. Oishi *et al.* synthesised partly-fluorinated nanogels that were comprised of PEG, TFEMA and 2-(diethylamino)ethyl methacrylate (DEAEMA) units.[164] Owing to the pH-responsiveness of DEAEMA segments, the $D_h$ of nanogels was highly dependent on the solution pH values. At low values of pH, the nanogels swelled and resulted in high $^{19}$F mobility, while they shrank and led to low $^{19}$F mobility at high pH. Consequently, the fluorine signal was detected only in acidic conditions, indicating that these nanogels were promising pH-sensitive drug carriers and tumour-specific $^{19}$F MRI CAs. Bailey *et al.* prepared a series of $^{19}$F-containing copolymer NPs in the presence of a crosslinker by free radical polymerisation.[165, 166] These NPs (200~500 nm) were formed through the copolymerisation of $^{19}$F-containing monomer, N-vinylformamide, and (1,5-N-vinylformamido) ethyl ether (crosslinker) using polyvinylpyrrolidone (PVP) as a surfactant. The abundant amide groups in the nanoparticles were hydrolysed to the corresponding amines for future conjugation of functional moieties. $^{19}$F NMR of the NPs using different $^{19}$F-containing monomers showed the potential of these NPs for $^{19}$F MRI.

More recently, Yang *et al.* reported a $^{19}$F-labelled injectable hyaluronic acid (HA) hydrogel for both $^{1}$H and $^{19}$F MRI.[167] HA hydrogel was synthesised by rapid carbazone reaction, and TFEA was attached to the hydrogel *via* orthogonal Michael addition to generate single $^{19}$F resonance. The shape and interior structure of the HA hydrogel was effectively imaged by a combination of $^{1}$H and $^{19}$F MRI, suggesting potential clinical applications of this biocompatible, injectable and MRI-trackable hydrogel.

In summary, the design of $^{19}$F MRI CAs has been facilitated by the vast range of polymers that possess a number of advantages such as flexible synthesis, numerous topologies, various kinds of functionalities, etc. Previous studies have provided new impetus to the development of $^{19}$F CAs using polymers. Recent progress has also spotlighted the prominence of hyperbranched polymers and dendrimers as versatile platforms for the fabrication of multifunctional theranostic systems. By applying multidisciplinary studies involving chemistry, biology and radiology, polymeric CAs have been emerging as the next-generation $^{19}$F MRI CAs for advanced molecular imaging and theranostics.

## 1.2 Reversible Addition–Fragmentation Chain Transfer (RAFT) Polymerisation

RAFT polymerisation, a powerful controlled radical polymerisation technique, was developed by CSIRO researchers in 1998.[168] The mechanism of RAFT polymerisation is described in Scheme 1-1.[169] At the beginning of a RAFT polymerisation, monomer is initiated by a radical to form a propagating radical ($P_n$•), which then undergoes chain transfer to the thiocarbonylthio compound [RSC(Z)=S] to generate a polymeric thiocarbonylthio compound [$P_n$SC(Z)=S] and a new radical (R•) after fragmentation of the intermediate radical. The new radical (R•) reacts with monomer to produce a new propagating radical ($P_m$•). Since the equilibrium between the active propagating radicals ($P_n$• and $P_m$•) and dormant polymeric thiocarbonylthio compound [$P_n$SC(Z)=S] is very fast, the chain growth is thus controlled to yield polymers with narrow molar mass distribution. At the end of polymerisation, the thiocarbonylthio functionality is retained in the final polymers. The sequence of addition–fragmentation equilibria minimises the chance of radical-radical termination and disproportionation which are two typical characteristics of free radical polymerisation, resulting in polymer chains with tightly defined degree of polymerisation.

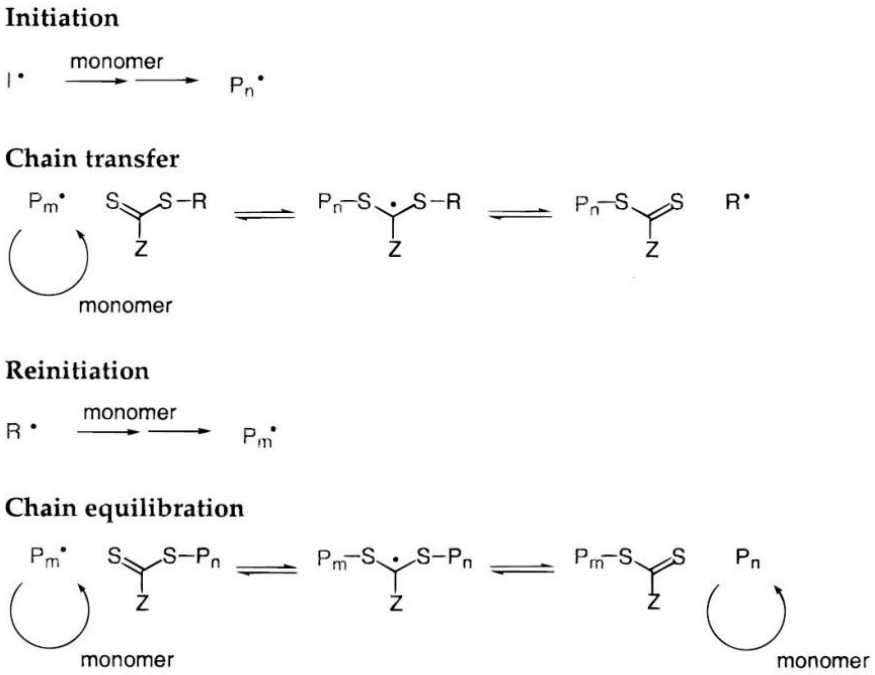


**Scheme 1-1** Mechanism of RAFT polymerisation. Adapted from Chong *et al*.[169]

According to the mechanism above, the use of chain transfer agent (CTA) [RSC(Z)=S] is a key component of RAFT polymerisation. Moreover, it should be stressed that the choice of CTA is of utmost important for RAFT polymerisation,[170] since each type of CTA is suitable for certain types

of monomers, as determined by the R and Z groups. In addition, the CTA also introduces end-group functionality to the polymers.

Owing to its convenience and versatility, the past fifteen years have witnessed a rapid growth in the use of RAFT polymerisation for the synthesis of a broad class of polymers with various structures and properties.[171-175] Due to the great depth and breadth of this field, the introduction of RAFT polymerisation is limited to the synthesis of linear, star and hyperbranched polymers that are commonly employed in the area of polymeric nanomedicine in the following sections.

### 1.2.1 Synthesis of Linear Polymers by RAFT Polymerisation

RAFT polymerisation is a robust and convenient protocol for the synthesis of different types of linear polymers, including homopolymers, statistical/gradient copolymers, alternating copolymers, and block copolymers, as has previously been comprehensively reviewed.[171-174] By carefully selecting the CTAs, RAFT polymerisation is versatile for a very wide range of monomers and tolerant of diverse synthetic conditions. In the past decade, the synthesis of nanostructured functional polymers using the RAFT process has been an intensively active research field.

RAFT polymerisation has been commonly exploited as a versatile synthetic tool for the synthesis of stimuli-responsive linear polymers, which are intellectual materials responsive to environmental changes.[176-178] Becer *et al.* synthesised a library of homopolymers and copolymers of methacrylic acid (MAA), mono(ethylene glycol) methyl ether methacrylate (MEOMA), di(ethylene glycol) methyl ether methacrylate ($MEO_2MA$), oligo(ethylene glycol) methyl ether methacrylate ($OEGMA_{475}$ and $OEGMA_{1100}$), and oligo(ethylene glycol) ethyl ether methacrylate ($OEGEMA_{246}$) *via* RAFT polymerisation,[179] The thermo-responsive behaviour of these polymers was investigated. It was found that the copolymers P(MAA-*co*-$OEGMA_{1100}$) had both pH- and thermo-responses at certain monomer ratios, though neither of the corresponding homopolymer exhibited LCST behaviour. Benoit *et al.* synthesised pH-responsive diblock copolymers PDMAEMA-*b*-P(DMAEMA-*co*-AA-*co*-BMA) by using a folate-conjugated CTA.[180] These diblock copolymers were utilised as tumour targeted-carriers for small interfering RNA (SiRNA) for *in vitro* gene knockdown. The cationic DMAEMA segments were employed for the binding and protection of siRNA as well as achieving pH-responsive endosomolytic behaviour. Roy *et al.* prepared block copolymers composed of 3-acrylamidophenylboronic acid (APBA) and *N*,*N*-dimethylacrylamide (DMA) *via* RAFT polymerisation.[181] As boronic acids are uniquely responsive to pH as well as diol concentration, the block polymers PAPBA-b-PDMA displayed pH- and sugar-responsiveness.

Unimer NPs (~7 nm) were observed at pH 10.7 (p$K_a$ ≈ 9) owing to the soluble anionic boronic acids units. However, when the pH was slowly reduced to 8.7, larger aggregates (~35 nm) were formed after dialysis because of the insoluble neutral boronic acids segments, and these aggregates were then disassembled into unimer NPs (~9 nm) again upon the addition of sugar due to the formation of soluble boronate esters. This study showed the first example of RAFT polymerisation of unprotected boronic acid monomers with pH- and sugar-responsive properties.

Recently, the RAFT technique has received increasing attention in the fabrication of nanostructures based on amphiphilic block copolymers. As mentioned in Section 1.1.2.2.1, amphiphilic block copolymers are attractive materials because they can form nano-sized micelles *via* self-assembly process in aqueous solution at concentrations above critical micelle concentration (CMC). However, the micelles disassemble when the concentration drops below CMC, e.g., dilution by bloodstream after intravenous administration.[182] One of the most common solutions to the disassembly is the development of shell/core cross-linked micelles.[177, 178, 183] Hales *et al.* reported shell-crosslinked vesicles based on block copolymers of poly($_{D,L}$-lactide) (PLA) and poly(*N*-isopropyl acrylamide) (PNIPAAm).[184] A macroCTA was synthesised *via* ring-opening polymerisation between $_{D,L}$-lactide and a hydroxyl-functionalised trithiocarbonate. Subsequently the macroCTA was chain extended with *N*-isopropyl acrylamide for the synthesis of PLA-*b*-PNIPAAm, which was further chain extended with a crosslinker hexanediol diacrylate to form shell-crosslinked particles (165~280 nm) in methanol. It was found that the thermal transition behaviour of the aggregates was significantly changed by the core crosslinking process, as revealed by turbidity study using UV spectroscopy. Using RAFT polymerisation, Duong *et al.* synthesised amphiphilic block copolymers composed of POEGMA, polystyrene (PS) and poly(3-isopropenyl-α,α-dimethylbenzyl isocyanate) (PTMI) (POEGMA-*b*-P(ST-*co*-TMI)), which were then self-assembled into micelles in aqueous solution and core-crosslinked using a platinum(IV)-containing difunctional amine.[185] These core-crosslinked micelles were stable in water but released the anticancer drug cisplatin slowly in the presence of reducing agent. In addition, cytotoxicity to A549 human lung cancer cells was revealed by *in vitro* experiments, suggesting the potential applications of these micelles as drug containers.

Apart from the self-assembly process after synthesis, RAFT polymerisation-induced self-assembly (PISA) has evolved as another useful methodology for the *in situ* fabrication of nano-objects based on block copolymers.[186, 187] Some monomers are soluble in water but their polymers are water insoluble, such as 2-hydroxypropyl methacrylate (HPMA) and 2-methoxyethyl acrylate (MEA).[188,

[189] Therefore, RAFT polymerisation of these monomers in aqueous solution using hydrophilic macroCTAs will gradually increase the hydrophobicity of the formed block copolymer chains, leading to the *in situ* formation of nanostructures (spherical micelles, vesicles, worms/rods, lamellae, etc) *via* self-assembly. For example, Sugihara *et al.* reported the systematic study of forming nano-objects by RAFT PSIA in aqueous solution.[188] As depicted in Figure 1-12, a hydrophiphilic macroCTA, poly(2-(methacryloyloxy)ethylphosphorylcholine) (PMPC), was synthesised by RAFT polymerisation, and then used as macroCTA for the polymerisation of HPMA. The resultant amphiphilic block copolymers were self-assembled *in situ* to form nano-objects with different morphologies depending on the chain length ratio of PMPC to PHPMA as well as total solid concentration. A detailed phase diagram was also proposed first time for such a system, enabling the future preparation of nano-objects *via* RAFT PSIA with predictable morphologies.

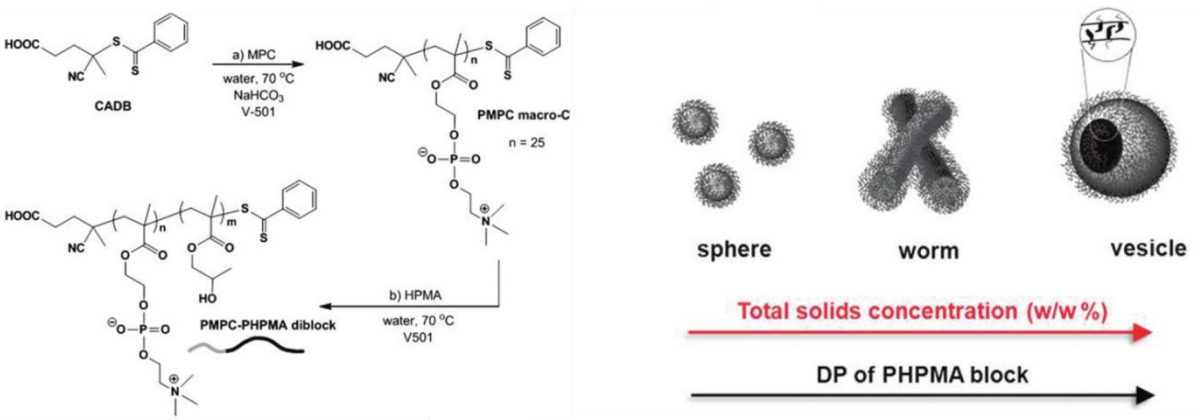


**Figure 1-12** Synthetic routes for PMPC-*b*-PHPMA block copolymers, and the transformation of morphology regulated by total solid concentration and DP of PHPMA block. Adapted from Sugihara *et al.*[188]

### 1.2.2 Synthesis of Star Polymers by RAFT Polymerisation

Star polymers, which are polymers having multiple linear polymer arms attached to a central core or point, have been extensively exploited for a variety of applications owing to their 3D globular structures and unique properties.[190] In the past decade, RAFT polymerisation has been proven to be a robust and versatile technique for the synthesis of star polymers. Basically, the synthesis of star polymers by RAFT polymerisation can be classified as 'core-first' and 'arm-first' techniques, as illustrated in Figure 1-13.[191-193]

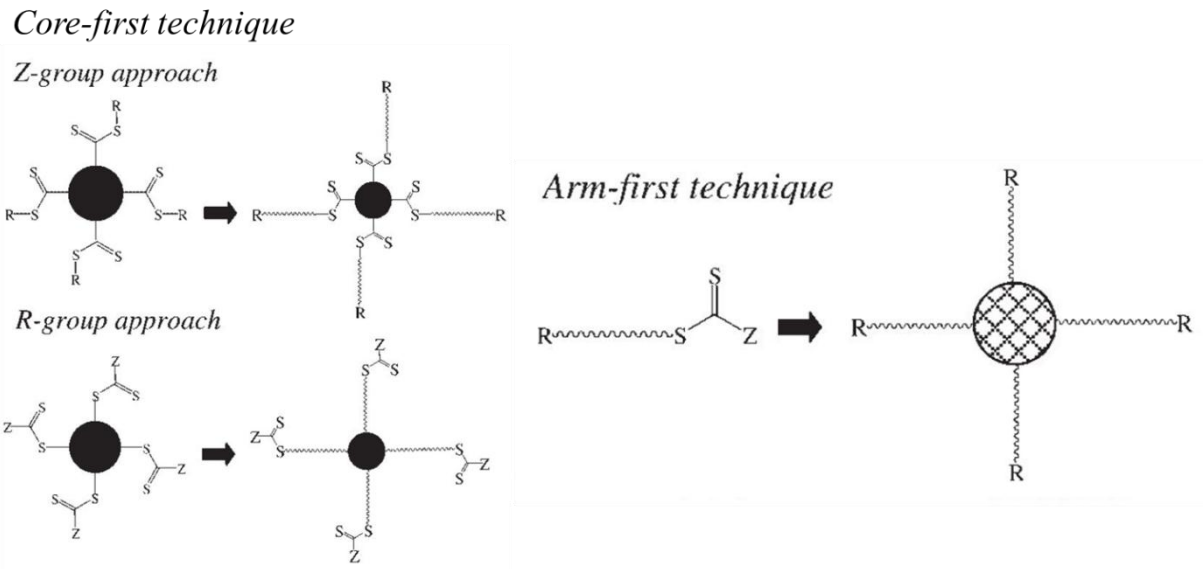


**Figure 1-13** Illustration of RAFT techniques for the synthesis of star polymers. Adapted from Barner *et al*.[192]

The 'core-first' technique includes the R-group and Z-group approaches. For the R-group approach, the CTA is attached to the core through the R-group. During RAFT polymerisation, the core acts as a macro-leaving group that carries multiple radicals, therefore one intrinsic drawback of this approach is unavoidable star-star coupling side reactions, which result in broadened molar mass distributions. Nonetheless, this problem could be alleviated, to some extent, by adopting the following strategies: (1) reducing the radical/CTA ratio in the system; (2) introducing a stable intermediate as a 'radical storage reservoir'; (3) minimising the CTA functionality on the core.[192] As an example, Chaffey-Millar *et al.* investigated the aforementioned design criteria for the RAFT synthesis of star polymers *via* the R-group approach.[194] As verified by simulated and experimental results, it was found that star-star coupling could be minimised by using retarded CTA with lower amount of arms and reduced concentration of free radical initiator.

For the Z-group approach, the CTA functionality is covalently anchored to the 'core' material, and the arm propagation proceeds nearby in the solution. Since the growing species are isolated from the core, star-star coupling can be effectively avoided, and the couplings between two living chains mainly account for the increased molar mass distributions. Therefore, compared with the R-group approach, this approach can produce well-defined star polymers with significantly narrower molar mass distributions. However, as the monomer conversion increases, the growing arms are becoming less accessible to the core due to steric effects, and these living chains are more likely to be terminated by chain-chain coupling to form dead polymers than to reach the core.[192] Even though,

the Z-group approach is an effective alternative to the R-group approach for the synthesis of well-defined star polymers with high yield. Liu *et al.* synthesised six-armed biodegradable star polymers using the Z-group approach. A hexa-functional CTA containing disulfide bond was prepared for the RAFT polymerisation for star polymers with arms of PS, poly(polyethylene glycol acrylate) (PEGA) and the PS-*b*-PEGA, respectively. Gel permeation chromatography (GPC) showed unimodal peaks for all the star polymers with $Đ_M$ below 1.3, confirming the advantage of the Z-group approach. Additionally, the six arms were successfully cleaved from the core the in the presence of reducing agents such as DL-dithiothreitol (DTT) and glutathione (GSH), indicating the potential use of this approach for the synthesis of well-defined star polymers with biodegradability.

Lately, growing attention has been given to the synthesis of star polymers *via* the arm-first method, which includes the synthesis of linear arms and attachment of the arms to a core through radical polymerisations, ring-open polymerisations, click chemistry, etc.[195] The main advantage of the arm-first technique is that it enables the synthesis of star polymers having a large number of arms with predesigned structures and compositions. Core-crosslinked star (CCS) polymers, which are representative products of the arm-first technique, have been increasingly attractive because of their facile synthesis by arm-first radical polymerisations using divinyl monomers as well as the unique properties resulting from their nano-sized architectures.[191] However, this technique produces star polymers with broad $Đ_M$ owing to side reactions of formation of intermediate radicals and core/chain shielding effects.[191] This can be overcome, to some degree, by carefully adjusting the polymerisation conditions. Ferreira *et al.* reported the optimisation of reaction parameters for the RAFT synthesis of CCS polymers.[196] CCS polymers were synthesised through the chain extension of a series of homopolymers and block copolymers with different crosslinkers *via* RAFT polymerisation. By adjusting the conditions (arm molecular weight, solvent, crosslinker type, reaction time), well-defined star polymers ($Đ_M$ < 1.2) were obtained with relatively high arm incorporation (> 90%). It was revealed that the solubility of the crosslinker was the key parameter for a successful synthesis. High arm incorporation was achieved using crosslinkers with poor solubility in the chosen solvent because of the possible nano-phase separation inducing compartmentalisation of the polymerisation. To some extent, this approach is related to the PISA process, as mentioned in Section 1.2.1.

An and coworkers have presented several examples of the synthesis of CCS polymers using RAFT aqueous dispersion polymerisation.[189, 197-202] For instance, CCS polymers were synthesised through the chain extension of PPEGMA macroCTA with MEA and a crosslinker poly(ethylene glycol)

diacrylate (PEGDA). This work featured the formation of amphiphilic block copolymer (PPEGMA-*b*-PMEA) micelles *via* PSIA as well as the subsequence core-crosslinking using PEGDA. As a result, CCS polymers with low $Đ_M$ (1.1~1.2) and small size (40~60 nm) were prepared at very high arm incorporation (~98%).[189] In the case of hydrophilic homopolymers as arms, crosslinker and spacing monomer played an essential role in the formation of well-defined CCS polymers. It was found that longer crosslinkers were helpful for forming CCS polymers due to the more flexible core, while hydrophobic spacing monomers could enhance the driving force to produce CCS polymers. Moreover, the arm incorporation was significantly reduced using arms with higher molecular weights owing to increased steric hindrance.[197]

### 1.2.3 Synthesis of Hyperbranched Polymers by RAFT Polymerisation

Hyperbranched polymers (HBPs) were previously synthesised mainly by step-growth polymerisation until Frechet *et al.* reported the synthesis of HBPs with irregular structures *via* self-condensing vinyl polymerisation (SCVP).[203] In the past few years, this concept has been extended to the synthesis of HBPs *via* RAFT polymerisation. Owing to the nature of the RAFT process, the HBPs produced in this way have more uniform structures and better defined properties.

Liu *et al.* pioneered the RAFT synthesis of HBPs about a decade ago.[204] HBPs were synthesised through the RAFT copolymerisation of MMA and crosslinker ethylene glycol dimethacrylate (EGDMA) using a dithiobenzoate CTA. The highly-branched structure was revealed by NMR and GPC analyses. Moreover, the HBPs were able to be further chain extended with styrene, confirming the living characteristic of the HBPs by RAFT polymerisation. This work opened an avenue to the controlled synthesis of HBPs *via* RAFT polymerisation, and a wide range of HBPs have been synthesised following this concept. However, the structure of the HBPs is greatly related to the experimental conditions such as the crosslinker/CTA ratio and monomer concentration, and sometimes unfavoured macroscopic gelation occurs.[205-207]

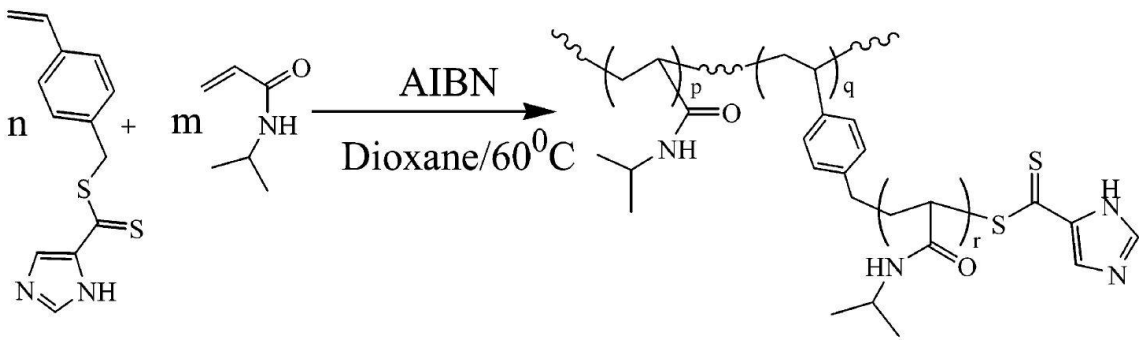


**Figure 1-14** Synthetic routes for highly-branched (co)polymers *via* RAFT SCVP. Adapted from Carter *et al.*[208]

RAFT SCVP, which utilises polymerisable CTAs to prepare HBPs in the absence of crosslinkers, seems to be a promising way to avoid gelation and obtain HBPs with relatively narrow $Đ_M$. Carter *et al.* present the earliest work on the synthesis of HBPs *via* RAFT SCVP.[208-210] As shown in Figure 1-14, a polymerisable CTA, 4-vinylbenzylimidazole dithioate was designed and copolymerised with NIPAM to form highly-branched polymers with low $Đ_M$ value. The characteristics of HBPs could be easily tuned by using different polymerisation parameters in particular NIPAM/CTA ratio. Later on, the method was extended to the synthesis of HBPs that contain segments of block copolymers or statistical copolymers for improved one-step protein purification.[210]

RAFT SCVP has been further exploited for the synthesis of HBPs with complex structure and multifunctionality. For example, Zhang *et al.* synthesised HBPs with adjustable degree of branching (DB) using a polymerisable trithiocarbonate by varying the monomer/CTA ratio, and they also used these HBPs for the synthesis of star polymers with a hyperbranched core.[211] By combing RAFT SCVP with other post modification techniques, the Gao group has recently developed a platform based on HBPs bearing multiple functional groups for fluorescence-related applications.[212-215]

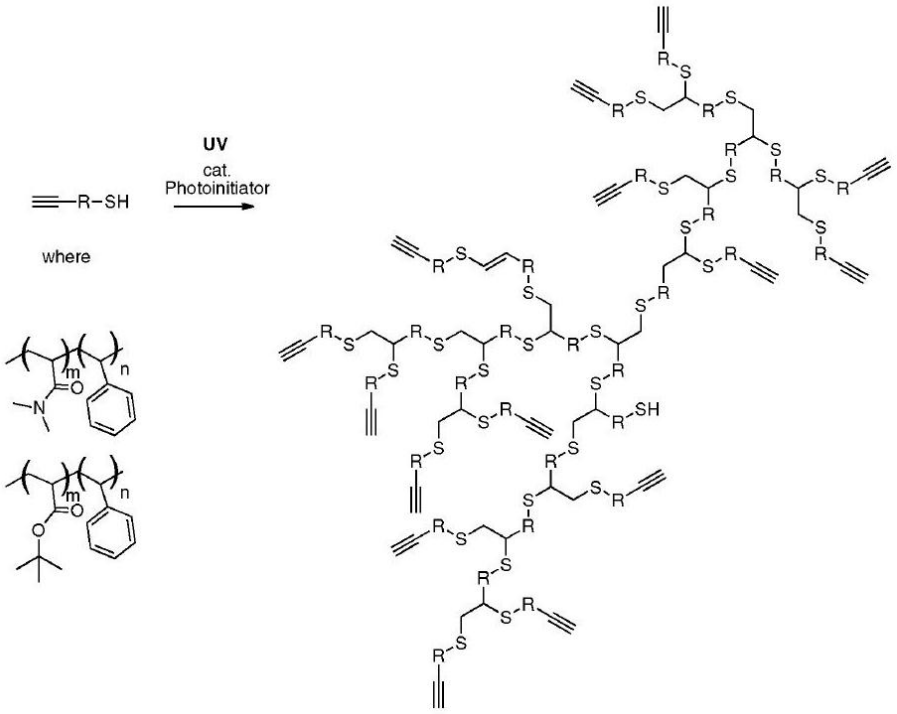


**Scheme 1-2** Synthesis of hyperbranched block copolymers *via* thiol-yne chemistry. Adapted from Konkolewicz *et al*.[216]

Very recently, HBPs have been synthesised through the combination of RAFT polymerisation and thiol-yne chemistry.[216, 217] Block polymers were first synthesised using an alkyne-terminated trithiocarbonate CTA *via* RAFT polymerisation. Then the trithiocarbonate groups were converted to thiol groups through aminolysis using isopropyl amine, followed by the photo-initiated thiol-yne reaction for the formation of HBPs. The HBPs were able to self-assemble into micelles in aqueous and showed pH-responsive behaviour. This innovative method broadened the synthetic techniques for HBPs with designable segmental characteristics and tuneable properties.

In conclusion, over a decade's research has proven that RAFT polymerisation is an extremely versatile and robust technique for the precise synthesis of a vast range of polymers. Owing to its excellent tolerance to a wide range of monomer types as well as polymerisation conditions, RAFT polymerisation has been a prominent and flexible toolbox for the synthesis of well-defined polymers with targeted architectures and desired properties for diverse applications.

## 1.3 Stimuli-responsive Imaging Agents

Stimuli-responsive polymers are polymers that have reversible physicochemical properties in response to the surrounding milieu.[218] Based on their special properties, they are also named 'smart polymers', 'intelligent polymers' or 'environmentally-sensitive polymers'.[219] The environmental conditions that stimuli-responsive polymers can respond to are generally classified as physical stimuli (temperature and light), chemical stimuli (pH and redox potential), and biological stimuli (enzymes and carbohydrates).[219, 220] In recent years, as emerging advanced materials, stimuli-responsive polymers have been playing an increasingly significant role in many fields in particular biomedical applications such as molecular imaging, drug/gene delivery, tissue engineering, etc.[221]

Stimuli-responsive agents are of special interest for molecular imaging and cancer therapy. For one thing, imaging performance can be reversely switchable in responsive to specific stimuli, enabling selective imaging of specific environments or areas. For another, the integration of stimuli-responsiveness to imaging agents is beneficial for the fabrication of multimodal agents for theranostics.[222]

pH-responsive polymers have been extensively exploited for the design of imaging agents to visualise acidic environments such as tumour tissues.[223, 224] As mentioned in Section 1.1.2.2, pH-responsive polymers that contain tertiary amines were utilised for the design of 'smart' $^{19}$F MRI CAs, which could be turned on and off based on the environmental pH.[139, 164] For example, Zhou *et al.* developed block copolymer-based micelles as pH-responsive agents for fluorescence imaging.[225] Block copolymers PEO-*b*-(PR-*co*-TMR) were synthesised, in which PR stands for segments containing tertiary amines and TMR are units incorporated with a pH-insensitive dye (tetramethyl rhodamine). At higher pH values, the PR-*co*-TMR block was hydrophobic, therefore the amphiphilic block copolymers were self-assembled to form micelles, quenching the fluorescent signals through mechanisms of Förster resonance energy transfer between TMR molecules (homo-FRET) and photo-induced electron transfer (PeT) from tertiary amines to TMR. In contrast, at lower pH values, the micelles were dissembled into separated chains, dramatically increasing the fluorescence emission because of the disassociated TMR units and the reduced PeT. Hence, by choosing different PR monomers, the fluorescence emission could be activated and deactivated at desired pH values, enabling the precise imaging of specific cells and tissues.

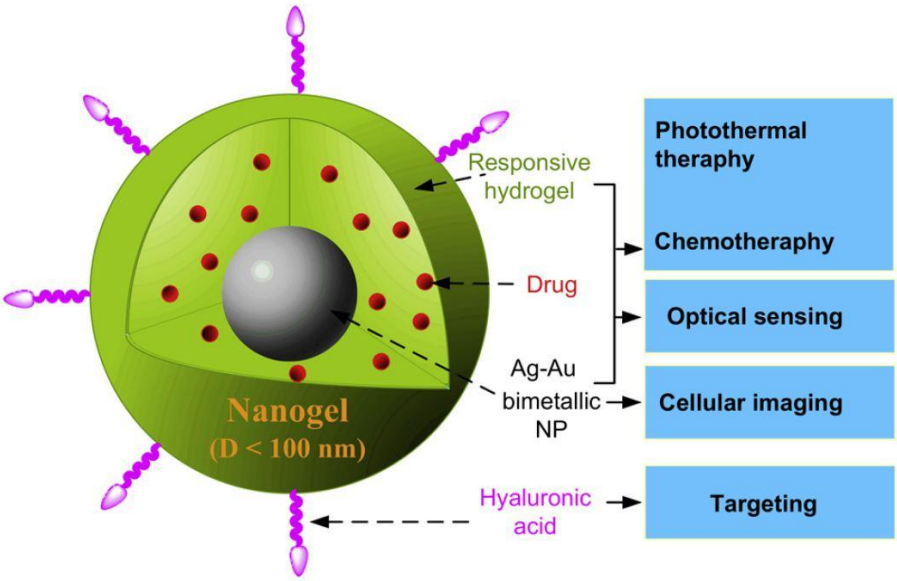


**Figure 1-15** Schematic illustration of the theranostic platform based on multifunctional core-shell NPs. Adapted from Wu *et al.*[226]

Thermo-responsive property has already been widely utilised for controlled release of drug molecules.[218] Recently, thermo-responsive imaging agents have been developed for cancer theranostics. As shown in Figure 1-15, Wu *et al.* reported a theranostic platform based on hybrid NPs, which were comprised of Ag-Au NPs as core and OEGMA-containing thermo-responsive gel as shell.[226] Fluorescent light was emitted from the bimetallic core, and the photoluminescence (PL) intensity was dependent on temperature with an ON/OFF switchable behaviour. In addition, these NPs were used as carriers for a hydrophilic anticancer drug temozolomide (TMA), and the drug release could be accelerated by either temperature increase of the local microenvironments or the heat generated by NIR irradiation. Furthermore, the NPs were also employed as effective photothermal agents without drug loading. The work presented multimodal NPs as targeted theranostic agents for fluorescence imaging, photothermal therapy and chemotherapy.

Imparting biodegradability to imaging agents can facilitate the clearance of NPs from the body as well as controlled drug release. Katz *et al.* prepared functional polymersomes using biodegradable diblock copolymers that were incorporated with both fluorescent and photocleavable moieties.[227] When exposed to UV, the polymersomes gradually collapsed, and a rapid release of biocytin was observed. Moreover, the polymersomes were visualised by fluorescence microscopy after incubation with immature dendritic cells. Hence this work developed a useful method for the preparation of biodegradable polymersomes based on block copolymers for both fluorescence imaging and UV-triggered drug delivery.

The desire for higher information content in imaging has led to the design of agents which are responsive to two or more stimuli. Mosaiab *et al.* designed pH- and thermo-responsive fluorescence imaging agents comprised of graphene oxide (GO) and graft copolymers (PEG-*g*-P(DMA-*co*-NIPAAm)) containing dye molecules borondipyrromethane.[228] Owing to the pH-responsiveness of PDMA and thermo-responsiveness of PNIPAAm, the fluorescence emission could be switched on only at low pHs and a lower temperature (25 $^{o}$C), whereas they were not able to be detected at above physiological pH and a higher temperature (37 $^{o}$C). Moreover, the NPs acted as DOX carriers with high loading efficiency (76.25%), and the drug release was much faster at pH 5.0 than that at pH 7.4. Thus these dual-responsive nanoparticles could be utilised for the detection of tumour tissues as well as controlled drug delivery.

Overall, tremendous effort has been devoted to the development of stimuli-responsive imaging agents, which have been increasingly attractive in nanomedicine and molecular imaging. For future clinical applications, detailed investigations on toxicity, biodistribution, and pharmacokinetics are to be carried out.

## 1.4 Multimodal Imaging Agents

The diverse modern imaging techniques play a vital role in both clinical diagnosis and biomedical research. However, the choice of imaging modalities is a common conundrum because each modality has its advantages and disadvantages, as summarised in Figure 1-16.[229] For example, optical imaging with high sensitivity lacks spatial resolution, whereas MRI with high spatial resolution has low sensitivity. Therefore, it is understandable that no single modality is sufficient to provide all the necessary information. In fact, clinical diagnosis often suffers from partial or ambiguous information when using single imaging modality.

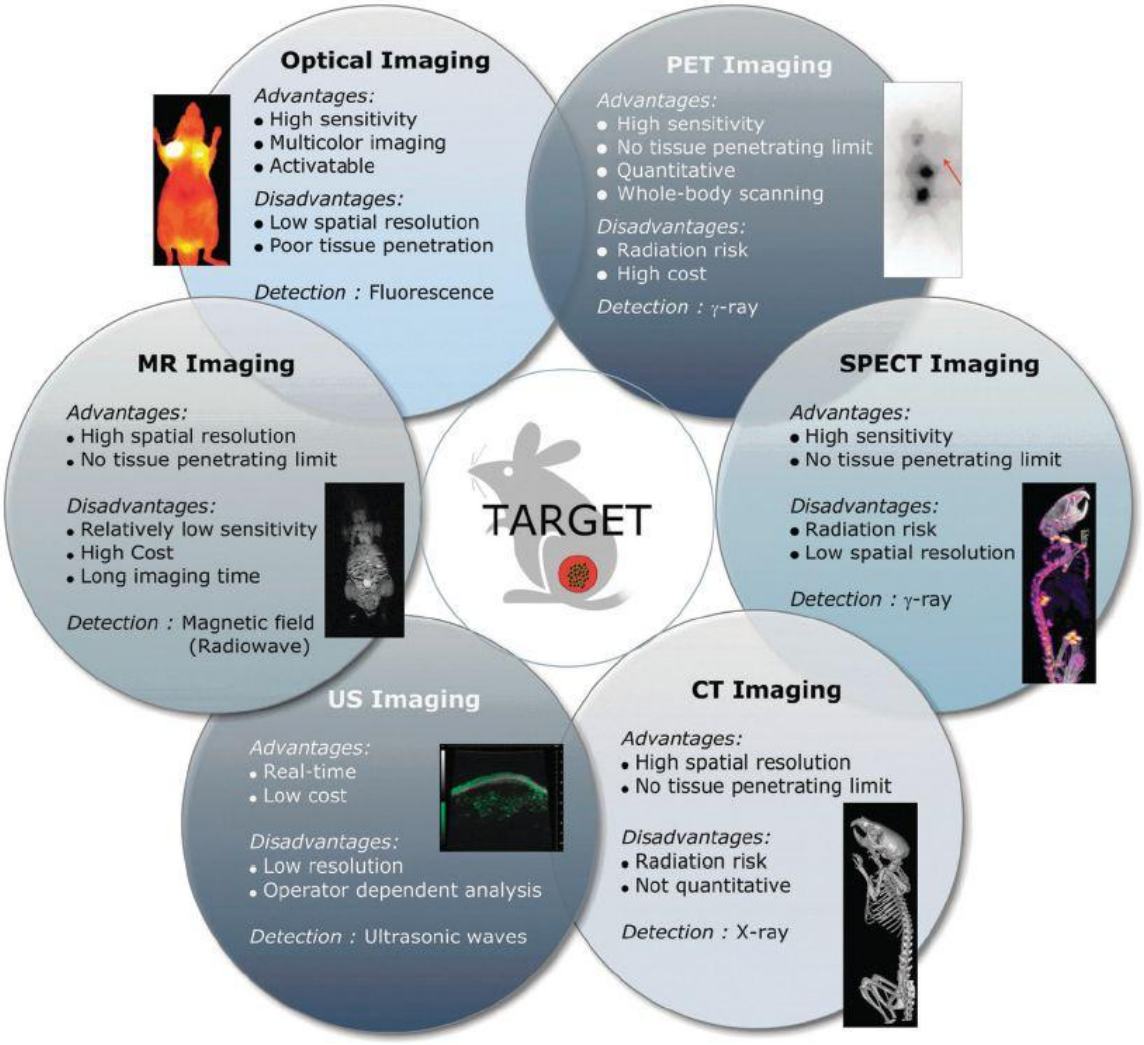


**Figure 1-16** A summary of the currently used modalities for molecular imaging. Adapted from Lee *et al.*[229]

To tackle this problem, the combination of two or more modalities has become a mainstream to obtain complementary information in molecular imaging.[131, 229-232] With the commercial appearance of multimodal fused instruments, there has been a surge in the development of multimodal molecular imaging agents, which has been greatly facilitated and accelerated by the rapidly advancing field of nanotechnology.[229, 231] As introduced in Section 1.1, MRI is a powerful and non-invasive imaging modality for producing 3D anatomical images with high resolution. The low sensitivity, a major problem of MRI, can be improved through multimodal imaging by combining MRI and other sensitive techniques, such as optical imaging, PET/SPECT, ultrasonography, etc.[131] Therefore, the development of imaging agents that contain both MRI and other imaging functionality is of great importance for multimodal molecular imaging.

Owing to their diverse architectures and functionalities, polymers have gained considerable attention as excellent materials for the construction of nano-sized multimodal imaging agents.[222, 233] The synergistic integration of different imaging moieties to a polymeric system can be achieved by a variety of approaches, including polymerisation, conjugation, non-covalent incorporation, etc. In addition, as introduced in Section 1.2, the size and structure of polymers can be precisely designed by employing controlled polymerisation techniques, providing robust and flexible methods for the design of polymeric agents with tuneable physicochemical and biological characteristics. Furthermore, the facile attachment and conjugation of other functionalities such as drug and targeting moieties to polymers allows for the fabrication of theranostic agents for both imaging and therapy.

The development of MRI/optical imaging agents is of great interest as these two modalities can produce images with both high resolution and sensitivity. Additionally, the wide class of fluorescent molecules adds more opportunities to the design of imaging agents. Howes *et al.* reported the preparation of MRI/optical imaging agents based on phospholipid micelles that were encapsulated with iron oxide nanoparticles and different hydrophobic conjugated polymers.[234] The bimodal imaging performance was examined by both fluorescence imaging and MRI. Successful cell uptake and low cytotoxicity were also observed. It should be highlighted that the two imaging moieties could be replaced by other commercial products. Therefore, this work presented a useful method for the preparation of MRI/optical imaging agents.

Star polymers and dendritic polymers are prefect candidates for multimodal imaging agents due to the 3D globular structure as well as abundant functionalities. Adkins *et al.* synthesised CCS star polymers *via* RAFT arm-first approach using PAA arms and a fluorescent crosslinker.[235] Then the

CCS polymers were conjugated with Gd(III) and Eu (III), followed by the further attachments with dopamine derivatives, cell penetrating units, and targeting moieties. High NMR relaxivities ($r_1$ = 85 mM $s^{-1}$, $r_2$ = 100 mM $s^{-1}$) were achieved, resulting in MRI with greatly enhanced contrast. Moreover, the *in vitro* uptake of CCS polymers by 3T3 mouse fibroblast cells was confirmed by confocal microscopy. These results demonstrated multifunctional CCS polymers as an outstanding platform for the design of MRI/optical imaging agents. As indicated before, multifunctional HBPs synthesised *via* RAFT polymerisation have been proven to be robust theranostic agents for both *in vitro* and *in vivo* $^{1}$H MRI/$^{19}$F MRI/optical imaging.[161] It should be emphasised that the overlay of both $^{1}$H MRI and $^{19}$F MRI allows imaging of the tissues as well as tracking of the CAs.

The combination of MRI and PET/SPECT can afford highly sensitive and quantitative imaging with temporal and spatial resolution.[236] Functional polymers have been attractive in the preparation of MRI-PET/SPECT bimodal imaging agents due to the facile conjugation with MRI moieties (SPIONs and Gd(III)-chelates) as well as radio-isotopes for PET/SPECT. Locatelli *et al.* reported the preparation of SPIONs/$^{68}$Ga/block copolymers hybrid nanoparticles as MRI/PET bimodal imaging agents.[237] SPIONs were encapsulated into micelles of PLGA-*b*-PEG block copolymers that had -COOH end groups. Then 2,2'-(7-(4-((2-aminoethyl)amino)-1-carboxy-4-oxobutyl)-1,4,7-triazonane-1,4-diyl) diacetic acid (NODA) molecules were attached to the surface of the as-formed hybrid NPs *via* the -COOH groups, followed by the chelation of $^{68}$Ga to NODA. These non-toxic radiolabelled SPIONs NPs were evaluated as imaging agents by both MRI and PET, demonstrating a successful example for the fabrication of MRI/PET bimodal imaging agents.

Polymers have been widely exploited as coating materials for the stabilisation of MRI-PET/SPECT imaging agents. de Rosales *et al.* developed $^{99m}$Tc-labelled SPIONs as MRI-PET/SPECT bimodal imaging agents.[238] $^{99m}$Tc-bisphosphonate chelates were attached to the surface of commercial SPIONs coated with dextran (Endorem/Feridx, liver MRI CAs). Although the $^{99m}$Tc-bisphosphonate chelates were proven to be conjugated directly with SPIONs rather than the dextran, the dextran layer was essential to stabilise the colloidal suspension. The capability of these NPs as imaging agents was tested and confirmed by MRI and SPECT-CT, and biodistribution studies revealed that NPs mainly accumulated in the liver and spleen. This work presented the first example of radiolabelled SPIONs as multimodal imaging agents.

Owing to their inherent nature, MRI and CT are more suited for imaging of soft and hard tissues, respectively. Therefore, the combination of MRI and CT seems promising as the information provided by each modality can complement each other. In recent years, the design of MRI/CT

bimodal imaging agents has been an emerging field. Kim *et al.* reported the preparation of hybrid nanoparticles coated with amphiphilic copolymer for MRI/CT bimodal imaging.[239] Using an emulsification process, oleylamine-stabilised hybrid Au-$Fe_3O_4$ NPs were encapsulated by amphiphilic statistical copolymers comprised of dodecyl methacrylate (DMA), methacrylic acid (MA) and PEGMA segments. Owing to the presence of Au and $Fe_3O_4$, these organic-inorganic hybrid NPs could be used for both CT and MRI. The excellent dual-imaging performance was confirmed by *in vivo* MRI/CT experiments on hepatoma-bearing mice, suggesting the potential application of these NPs as bimodal imaging agents for the diagnosis of hepatoma.

In conclusion, multimodal imaging is a continuously developing field that can greatly facilitate the accurate imaging and diagnosis by offering complementary information. Recently, the appearance of commercial fused instruments (e.g., MRI-PET) has significantly boosted the development of multimodal imaging agents. Polymers possess an almost infinite range of structural variations and the opportunity for multiple functionalities, and hence it could be foreseen that polymeric agents have the great potential to evolve as the next-generation multimodal imaging agents for improved theranostics.

## 1.5 Aims of This Project

Since its appearance in 1977, $^{19}$F MRI has been proven to be a prominent modality because it has almost zero background signal owing to the absence of appreciable endogenous fluorine in the body. By using molecular imaging CAs, $^{19}$F MRI provides not only the 3D anatomical images but also the specific location of CAs. Therefore it is a useful tool for a variety of biomedical applications, including cell labelling/tracking, tissue imaging, drug metabolism study, etc. Despite the attractive advantages, $^{19}$F MRI is not routinely used in clinical. The main impediment to clinical uptake is the lack of suitable CAs. After nearly four decades of research, few $^{19}$F MRI CAs have gained regulatory approval.

In recent years, polymeric $^{19}$F MRI CAs have been emerging as next-generation CAs. Thanks to controlled polymerisation techniques and conjugation chemistry, partly-fluorinated polymers with well-defined architectures and desired functionalities have been synthesised for $^{19}$F MRI as well as theranostics. As revealed by previous studies, two main design criteria for efficient polymeric CAs are high $^{19}$F loading and highly mobile $^{19}$F nuclei. More recent research has further demonstrated that partly-fluorinated HBPs are excellent candidates for $^{19}$F MRI because they can fulfil both criteria through rational chemical design. Moreover, owing to the abundant functionality, they are

preferred materials for fabricating multifunctional imaging agents for theranostics (e.g., $^{1}H/^{19}F$ MRI, fluorescence imaging, anticancer drug delivery, etc). Nevertheless, information on how imaging performance is determined by hyperbranched structure is dearth. For example, the influence of hyperbranched architecture and chain sequence distribution on $^{19}F$ MRI performance needs to be explored. In addition, stimuli-responsive CAs should be developed as they are increasingly important 'smart' CAs. Furthermore, the combination of $^{19}F$ MRI and other imaging modalities will certainly afford more opportunities to the area of multimodal molecular imaging.

Thus, the aims of this project are as follows.

1. to synthesise partly-fluorinated polymers with star and hyperbranched architectures as $^{19}F$ MRI CAs;
2. to study the influence of polymer architecture and chain sequence distribution on $^{19}F$ MRI performance;
3. to develop pH-responsive and partly-fluorinated polymers for selective imaging of diseased tissues
4. to design HBPs that contain both fluorine and iodine for $^{19}F$ MRI/CT bimodal molecular imaging;
5. to build up a robust RAFT polymerisation approach for partly-fluorinated HBPs as $^{19}F$ MRI CAs.
6. To gain a molecular level understanding for the design of highly-efficient $^{19}F$ MRI CAs.

In terms of these objectives, this thesis is divided into seven chapters. **Chapter 2** describes the RAFT synthesis of partly-fluorinated and pH-responsive star-like HBPs as 'smart' $^{19}F$ MRI CAs. These novel polymers were synthesised *via* the RAFT copolymerisation of TFEA, DMAEMA, and EGDMA (crosslinker) using PPPGMA homopolymers as macoCTAs. In such star-like system, the $^{19}F$ nuclei were positioned together with pH-responsive PDMAEMA segments within the hyperbranched core, which was shielded with hydrophilic and biocompatible PPEGMA arms. After forming nanoparticles by direct dissolution in aqueous solution, the pH-dependence of $D_h$ and NMR relaxation times ($T_1$ and $T_2$) were studied. Finally the $^{19}F$ NMR and MRI were conducted at different pH values. This work intends to establish a pH-responsive hyperbranched structure for 'smart' $^{19}F$ MRI CAs with ON/OFF property.

Following **Chapter 2**, it was hypothesised that the imaging performance would change by placing the $^{19}F$ nuclei exterior to the hyperbranched core. To investigate this further, **Chapter 3** explores

the capability of CCS polymers as $^{19}$F MRI CAs. Through RAFT aqueous dispersion polymerisation, CCS polymers were synthesised by using amphiphilic block copolymers PPEGMA-*b*-P(TFEMA-*co*-DMAEMA) as arms and a disulfide-containing bifunctional monomer DSDMA as crosslinker. The polymerisation kinetics were investigated. A series of CCS polymers with different $^{19}$F content were synthesised and the pH-dependence of $D_h$ and relaxation times ($T_1$ and $T_2$) studied. In order to verify the degradability, the CCS polymers were treated with reducing agents such as glutathione (GSH) and tris(2-carboxyethyl)phosphine hydrochloride (TCEP). Furthermore, the CCS polymers nanoparticles were evaluated by $^{19}$F NMR and MRI at four different pH values. The influence of polymer architecture on imaging performance was compared to those obtained in **Chapter 1**.

To further the application of $^{19}$F MRI, **Chapter 4** endeavours to develop HBP-based $^{19}$F MRI/CT bimodal imaging agents. Biodegradable HBPs containing iodine were synthesised *via* RAFT copolymerisation of an iodo-monomer, PEGMA and DSDMA. Then they were chain extended with TFEA and PEGMA to form star-like HBPs containing iodine in the hyperbranched core and fluorine in the arms. The polymer structure was comprehensively studied. The bimodal imaging performance was investigated by both $^{19}$F MRI and CT. To date, this study is the first example of polymeric $^{19}$F MRI/CT bimodal imaging agents.

According to both previous publications and our own experience, the RAFT synthesis of HBPs using crosslinkers is highly dependent on the experimental conditions. The structure can be affected by a number of factors, including crosslinker/monomer/CTA ratio, initiator/CTA ratio, monomer concentration, polymerisation time, solvent type, etc. Hence it is necessary to develop a more flexible methodology for the synthesis of HBP-based $^{19}$F MRI CAs. **Chapter 5** describes the investigation on RAFT self-condensing vinyl polymerisation (SCVP) for the synthesis of segmented and highly-branched polymers (SHBPs). A polymerisable trithiocarbonate CTA was designed for the RAFT process as well as formation of branching structure. A series of SHBPs consisting of TFE(M)A, PEG(M)A and CTA were synthesised. The polymerisation parameters, such as polymerisation time, monomer/CTA ratio, monomer concentration, were studied and optimised to produce well-defined SHBPs. SHBPs containing different types of monomers (acrylates and methacrylates) were prepared to study the influence of polymer backbone on the motion of fluorine nuclei. The relationship between fluorine content and fluorine mobility was also investigated by $^{19}$F NMR. In addition, the influence of degree of branching on fluorine mobility was studied. The tuneable and selective imaging performance of these SHBPs was examined by $^{19}$F

MRI, demonstration that RAFT SCVP is a robust way for the synthesis of SHBPs with tailored structures and imaging proterties.

To develop theranostic agents combing $^{19}$F MRI and drug delivery, **Chapter 6** explores the RAFT synthesis of star polymers with a polyhedral oligomeric silsesquioxanes (POSS) core and eight partly-fluorinated arms. Star polymer were synthesised by R-group approach us a macroCTA consisting a POSS core and eight CTA moieties for the copolymerisation of TFEA and PEGA. The synthetic conditions were investigated and optimised for well-defined star polymers with high yields. The molecular structure was characterised. The influence of arm length on fluorine mobility was analysed by $^{19}$F NMR. The potential $^{19}$F MRI performance was preliminarily confirmed by comparing the theoretical imaging intensities with the previous results. Such star polymers were promising theranostic agents for $^{19}$F MRI and drug delivery.

Finally, **Chapter 7** provides a comparison of all the polymeric agents developed in this thesis as well as a summary of the findings reported in this thesis.

## 1.6 References


1. M. Bottrill, L. K. Nicholas and N. J. Long, *Chem Soc Rev*, 2006, **35**, 557-571.
2. C. F. G. C. Geraldes and S. Laurent, *Contrast Media Mol I*, 2009, **4**, 1-23.
3. V. Kuperman, *Magnetic resonance imaging: physical principles and applications*, Academic Press, 2000.
4. R. K. Harris, E. D. Becker, S. M. C. de Menezes, R. Goodfellow, P. Granger and I. U. P. A. Chemistry, *Magn Reson Chem*, 2002, **40**, 489-505.
5. R. Kraus Jr, M. Espy, P. Magnelind and P. Volegov, *Ultra-Low Field Nuclear Magnetic Resonance: A New MRI Regime*, Oxford University Press, 2014.
6. R. Damadian, *Science*, 1971, **171**, 1151-&.
7. P. C. Lauterbur, *Nature*, 1973, **242**, 190-191.
8. P. Mansfield, *J Phys C Solid State*, 1977, **10**, L55-L58.
9. R. B. Lauffer, *Chem Rev*, 1987, **87**, 901-927.
10. P. Caravan, J. J. Ellison, T. J. McMurry and R. B. Lauffer, *Chem Rev*, 1999, **99**, 2293-2352.
11. Z. X. Zhou and Z. R. Lu, *Wires Nanomed Nanobi*, 2013, **5**, 1-18.
12. M. Botta and L. Tei, *Eur J Inorg Chem*, 2012, 1945-1960.
13. A. M. Mohs and Z. R. Lu, *Expert Opin Drug Del*, 2007, **4**, 149-164.
14. M. Essig, N. Anzalone, S. E. Combs, A. Dorfler, S. K. Lee, P. Picozzi, A. Rovira, M. Weller and M. Law, *Am J Neuroradiol*, 2012, **33**, 803-817.
15. F. L. Giesel, A. Mehndiratta and M. Essig, *Eur Radiol*, 2010, **20**, 2461-2474.
16. A. Charil and M. Filippi, *J Neurol Sci*, 2007, **259**, 7-15.
17. D. H. Miller, R. I. Grossman, S. C. Reingold and H. F. McFarland, *Brain*, 1998, **121**, 3-24.
18. F. Barkhof, J. H. Simon, F. Fazekas, M. Rovaris, L. Kappos, N. de Stefano, C. H. Polman, J. Petkau, E. W. Radue, M. P. Sormani, D. K. Li, P. O'Connor, X. Montalban, D. H. Miller and M. Filippi, *Nat Rev Neurol*, 2012, **8**, 13-21.
19. J. B. Tang, Y. Q. Sheng, H. J. Hu and Y. Q. Shen, *Prog Polym Sci*, 2013, **38**, 462-502.
20. A. J. L. Villaraza, A. Bumb and M. W. Brechbiel, *Chem Rev*, 2010, **110**, 2921-2959.
21. G. L. Davies, I. Kramberger and J. J. Davis, *Chem Commun*, 2013, **49**, 9704-9721.
22. J. M. Bryson, J. W. Reineke and T. M. Reineke, *Macromolecules*, 2012, **45**, 8939-8952.
23. H. Kobayashi and M. W. Brechbiel, *Adv Drug Deliver Rev*, 2005, **57**, 2271-2286.
24. S. El Habnouni, B. Nottelet, V. Darcos, B. Porsio, L. Lemaire, F. Franconi, X. Garric and J. Coudane, *Biomacromolecules*, 2013, **14**, 3626-3634.

25. E. Schopf, J. Sankaranarayanan, M. N. Chan, R. Mattrey and A. Almutairi, *Mol Pharmaceut*, 2012, **9**, 1911-1918.
26. Y. Li, M. Beija, S. Laurent, L. vander Elst, R. N. Muller, H. T. T. Duong, A. B. Lowe, T. P. Davis and C. Boyer, *Macromolecules*, 2012, **45**, 4196-4204.
27. M. Grogna, R. Cloots, A. Luxen, C. Jerome, C. Passirani, N. Lautram, J. F. Desreux, M. Collodoro, M. C. De Pauw-Gillet and C. Detrembleur, *Polym Chem*, 2011, **2**, 2316-2327.
28. M. Grogna, R. Cloots, A. Luxen, C. Jerome, J. F. Desreux and C. Detrembleur, *J Mater Chem*, 2011, **21**, 12917-12926.
29. X. X. Wen, E. F. Jackson, R. E. Price, E. E. Kim, Q. P. Wu, S. Wallace, C. Charnsangavej, J. G. Gelovani and C. Li, *Bioconjugate Chem*, 2004, **15**, 1408-1415.
30. Y. Zong, J. Guo, T. Ke, A. M. Mohs, D. L. Parker and Z. R. Lu, *J Control Release*, 2006, **112**, 350-356.
31. G. P. Yan, M. L. Liu and L. Y. Li, *Bioconjugate Chem*, 2005, **16**, 967-971.
32. Z. R. Lu, D. L. Parker, K. C. Goodrich, X. H. Wang, J. G. Dalle and H. R. Buswell, *Magn Reson Med*, 2004, **51**, 27-34.
33. P. Lebduskova, J. Kotek, P. Hermann, L. V. Elst, R. N. Muller, I. Lukes and J. A. Peters, *Bioconjugate Chem*, 2004, **15**, 881-889.
34. G. P. Yan, R. X. Zhuo, Y. H. Yang, L. Y. Li, M. L. Liu and C. H. Ye, *J Bioact Compat Pol*, 2002, **17**, 139-151.
35. D. M. Corsi, L. Vander Elst, R. N. Muller, H. van Bekkum and J. A. Peters, *Chem-Eur J*, 2001, **7**, 64-71.
36. E. Toth, I. van Uffelen, L. Helm, A. E. Merbach, D. Ladd, K. Briley-Saebo and K. E. Kellar, *Magn Reson Chem*, 1998, **36**, S125-S134.
37. Y. Berthezene, V. Vexler, D. C. Price, J. Wisnerdupon, M. E. Moseley, K. P. Aicher and R. C. Brasch, *Invest Radiol*, 1992, **27**, 346-351.
38. Y. Li, S. Laurent, L. Esser, L. V. Elst, R. N. Muller, A. B. Lowe, C. Boyer and T. P. Davis, *Polym Chem*, 2014, **5**, 2592-2601.
39. M. Z. Ye, Y. Qian, J. B. Tang, H. J. Hu, M. H. Sui and Y. Q. Shen, *J Control Release*, 2013, **169**, 239-245.
40. J. Lim, B. Turkbey, M. Bernardo, L. H. Bryant, M. Garzoni, G. M. Pavan, T. Nakajima, P. L. Choyke, E. E. Simanek and H. Kobayashi, *Bioconjugate Chem*, 2012, **23**, 2291-2299.
41. P. J. Klemm, W. C. Floyd, C. M. Andolina, J. M. J. Frechet and K. N. Raymond, *Eur J Inorg Chem*, 2012, 2108-2114.

42. C. H. Huang, K. Nwe, A. Al Zaki, M. W. Brechbiel and A. Tsourkas, *Acs Nano*, 2012, **6**, 9416-9424.
43. K. Luo, G. Liu, B. He, Y. Wu, Q. Y. Gong, B. Song, H. Ai and Z. W. Gu, *Biomaterials*, 2011, **32**, 2575-2585.
44. L. A. Han, J. F. Li, S. X. Huang, R. Q. Huang, S. H. Liu, X. Hu, P. W. Yi, D. Shan, X. X. Wang, H. Lei and C. Jiang, *Biomaterials*, 2011, **32**, 2989-2998.
45. F. Fernandez-Trillo, J. Pacheco-Torres, J. Correa, P. Ballesteros, P. Lopez-Larrubia, S. Cerdan, R. Riguera and E. Fernandez-Megia, *Biomacromolecules*, 2011, **12**, 2902-2907.
46. W. L. Zhang, N. Li, J. Huang, J. H. Yu, D. X. Wang, Y. P. Li and S. Y. Liu, *J Appl Polym Sci*, 2010, **118**, 1805-1814.
47. C. C. Cyran, Y. J. Fu, H. J. Raatschen, V. Rogut, B. Chaopathomkul, D. M. Shames, M. F. Wendland, B. M. Yeh and R. C. Brasch, *J Magn Reson Imaging*, 2008, **27**, 581-589.
48. T. L. Kaneshiro, E. K. Jeong, G. Morrell, D. L. Parker and Z. R. Lu, *Biomacromolecules*, 2008, **9**, 2742-2748.
49. Y. J. Fu, H. J. Raatschen, D. E. Nitecki, M. F. Wendland, V. Novikov, L. S. Fournier, C. Cyran, V. Rogut, D. M. Shames and R. C. Brasch, *Biomacromolecules*, 2007, **8**, 1519-1529.
50. N. Sato, H. Kobayashi, A. Hiraga, T. Saga, K. Togashi, J. Konishi and M. W. Brechbiel, *Magn Reson Med*, 2001, **46**, 1169-1173.
51. S. D. Konda, M. Aref, S. Wang, M. Brechbiel and E. C. Wiener, *Magn Reson Mater Phy*, 2001, **12**, 104-113.
52. H. Kobayashi, N. Sato, S. Kawamoto, T. Saga, A. Hiraga, T. Ishimori, J. Konishi, K. Togashi and M. W. Brechbiel, *Magn Reson Med*, 2001, **46**, 457-464.
53. J. Min, H. Jung, H. H. Shin, G. Cho, H. Cho and S. Kang, *Biomacromolecules*, 2013, **14**, 2332-2339.
54. S. Figueiredo, J. N. Moreira, C. F. G. C. Geraldes, S. Aime and E. Terreno, *Bioorgan Med Chem*, 2011, **19**, 1131-1135.
55. A. Datta, J. M. Hooker, M. Botta, M. B. Francis, S. Aime and K. N. Raymond, *J Am Chem Soc*, 2008, **130**, 2546-2552.
56. L. S. Karfeld-Sulzer, E. A. Waters, N. E. Davis, T. J. Meade and A. E. Barron, *Biomacromolecules*, 2010, **11**, 1429-1436.
57. V. C. Pierre, M. Botta, S. Aime and K. N. Raymond, *J Am Chem Soc*, 2006, **128**, 9272-9273.
58. V. Catanzaro, C. V. Gringeri, V. Menchise, S. Padovan, C. Boffa, W. Dastru, L. Chaabane, G. Digilio and S. Aime, *Angew Chem Int Edit*, 2013, **52**, 3926-3930.
59. S. Okada, S. Mizukami and K. Kikuchi, *Bioorgan Med Chem*, 2012, **20**, 769-774.

60. Y. M. Li, Y. F. Qian, T. Liu, G. Y. Zhang and S. Y. Liu, *Biomacromolecules*, 2012, **13**, 3877-3886.
61. M. M. Ali, M. Woods, P. Caravan, A. C. L. Opina, M. Spiller, J. C. Fettinger and A. D. Sherry, *Chem-Eur J*, 2008, **14**, 7250-7258.
62. M. H. M. Dias and P. C. Lauterbur, *Magn Reson Med*, 1986, **3**, 328-330.
63. L. Li, W. Jiang, K. Luo, H. M. Song, F. Lan, Y. Wu and Z. W. Gu, *Theranostics*, 2013, **3**, 595-615.
64. N. Lee and T. Hyeon, *Chem Soc Rev*, 2012, **41**, 2575-2589.
65. S. Laurent, D. Forge, M. Port, A. Roch, C. Robic, L. V. Elst and R. N. Muller, *Chem Rev*, 2008, **108**, 2064-2110.
66. C. Corot, P. Robert, J. M. Idee and M. Port, *Adv Drug Deliver Rev*, 2006, **58**, 1471-1504.
67. A. K. Gupta and M. Gupta, *Biomaterials*, 2005, **26**, 3995-4021.
68. O. Veiseh, J. W. Gunn and M. Q. Zhang, *Adv Drug Deliver Rev*, 2010, **62**, 284-304.
69. Z. L. Wang, J. Zhu, Y. Y. Chen, K. M. Geng, N. Qian, L. Cheng, Z. W. Lu, Y. Pan, L. Guo, Y. G. Li and H. W. Gu, *Rsc Adv*, 2014, **4**, 7483-7490.
70. S. Mahajan, V. Koul, V. Choudhary, G. Shishodia and A. C. Bharti, *Nanotechnology*, 2013, **24**.
71. F. M. Kievit, Z. R. Stephen, O. Veiseh, H. Arami, T. Z. Wang, V. P. Lai, J. O. Park, R. G. Ellenbogen, M. L. Disis and M. Q. Zhang, *Acs Nano*, 2012, **6**, 2591-2601.
72. D. F. Liu, W. Wu, J. J. Ling, S. Wen, N. Gu and X. Z. Zhang, *Adv Funct Mater*, 2011, **21**, 1498-1504.
73. D. Cheng, G. B. Hong, W. W. Wang, R. X. Yuan, H. Ai, J. Shen, B. L. Liang, J. M. Gao and X. T. Shuai, *J Mater Chem*, 2011, **21**, 4796-4804.
74. T. B. Brismar, D. Grishenkov, B. Gustafsson, J. Harmark, A. Barrefelt, S. V. V. N. Kothapalli, S. Margheritelli, L. Oddo, K. Caidahl, H. Hebert and G. Paradossi, *Biomacromolecules*, 2012, **13**, 1390-1399.
75. S. Cavalli, D. Carbajo, M. Acosta, S. Lope-Piedrafita, A. P. Candiota, C. Arus, M. Royo and F. Albericio, *Chem Commun*, 2012, **48**, 5322-5324.
76. J. H. Lee, Y. W. Jun, S. I. Yeon, J. S. Shin and J. Cheon, *Angew Chem Int Edit*, 2006, **45**, 8160-8162.
77. E. J. Cha, E. S. Jang, I. C. Sun, I. J. Lee, J. H. Ko, Y. I. Kim, I. C. Kwon, K. Kim and C. H. Ahn, *J Control Release*, 2011, **155**, 152-158.
78. K. Hayashi, M. Nakamura, W. Sakamoto, T. Yogo, H. Miki, S. Ozaki, M. Abe, T. Matsumoto and K. Ishimura, *Theranostics*, 2013, **3**, 366-376.

79. C. Y. Wang, S. Ravi, G. V. Martinez, V. Chinnasamy, P. Raulji, M. Howell, Y. Davis, J. Mallela, M. S. Seehra and S. Mohapatra, *J Control Release*, 2012, **163**, 82-92.
80. J. Chen, M. Shi, P. M. Liu, A. Ko, W. Zhong, W. J. Liao and M. M. Q. Xing, *Biomaterials*, 2014, **35**, 1240-1248.
81. J. H. Gao, H. W. Gu and B. Xu, *Accounts Chem Res*, 2009, **42**, 1097-1107.
82. G. N. Holland, P. A. Bottomley and W. S. Hinshaw, *J Magn Reson*, 1977, **28**, 133-136.
83. J. Ruiz-Cabello, B. P. Barnett, P. A. Bottomley and J. W. Bulte, *Nmr Biomed*, 2011, **24**, 114-129.
84. J. C. Knight, P. G. Edwards and S. J. Paisey, *Rsc Adv*, 2011, **1**, 1415-1425.
85. Y. B. Yu, *Wires Nanomed Nanobi*, 2013, **5**, 646-661.
86. J. M. Janjic and E. T. Ahrens, *Wires Nanomed Nanobi*, 2009, **1**, 492-501.
87. J. X. Yu, V. D. Kodibagkar, W. N. Cui and R. P. Mason, *Curr Med Chem*, 2005, **12**, 819-848.
88. R. P. Geyer, *New Engl J Med*, 1973, **289**, 1077-1082.
89. L. C. Clark and F. Gollan, *Science*, 1966, **152**, 1755-&.
90. E. G. Schutt, D. H. Klein, R. M. Mattrey and J. G. Riess, *Angew Chem Int Edit*, 2003, **42**, 3218-3235.
91. R. Diaz-Lopez, N. Tsapis and E. Fattal, *Pharm Res-Dordr*, 2010, **27**, 1-16.
92. M. Srinivas, A. Heerschap, E. T. Ahrens, C. G. Figdor and I. J. M. de Vries, *Trends Biotechnol*, 2010, **28**, 363-370.
93. M. Srinivas, L. J. Cruz, F. Bonetto, A. Heerschap, C. G. Figdor and I. J. M. de Vries, *Biomaterials*, 2010, **31**, 7070-7077.
94. J. G. Riess, *Chem Rev*, 2001, **101**, 2797-2919.
95. L. E. Bromberg and E. S. Ron, *Adv Drug Deliver Rev*, 1998, **31**, 197-221.
96. M. L. Hans and A. M. Lowman, *Curr Opin Solid St M*, 2002, **6**, 319-327.
97. A. S. Kabalnov and E. D. Shchukin, *Adv Colloid Interfac*, 1992, **38**, 69-97.
98. M. G. Freire, A. M. A. Dias, M. A. Z. Coelho, J. A. P. Coutinho and I. M. Marrucho, *J Colloid Interf Sci*, 2005, **286**, 224-232.
99. S. Temme, F. Bonner, J. Schrader and U. Flogel, *Wires Nanomed Nanobi*, 2012, **4**, 329-343.
100. M. Srinivas, P. A. Morel, L. A. Ernst, D. H. Laidlaw and E. T. Ahrens, *Magn Reson Med*, 2007, **58**, 725-734.
101. A. V. Ratner, R. Hurd, H. H. Muller, B. Bradleysimpson, W. Pitts, D. Shibata, C. Sotak and S. W. Young, *Magn Reson Med*, 1987, **5**, 548-554.

102. Y. Takaoka, T. Sakamoto, S. Tsukiji, M. Narazaki, T. Matsuda, H. Tochio, M. Shirakawa and I. Hamachi, *Nat Chem*, 2009, **1**, 557-561.
103. E. T. Ahrens, R. Flores, H. Y. Xu and P. A. Morel, *Nat Biotechnol*, 2005, **23**, 983-987.
104. B. M. Helfer, A. Balducci, Z. Sadeghi, C. O'Hanlon, A. Hijaz, C. A. Flask and A. Wesa, *Cell Transplant*, 2013, **22**, 87-97.
105. H. Dewitte, B. Geers, S. Y. Liang, U. Himmelreich, J. Demeester, S. C. De Smedt and I. Lentacker, *J Control Release*, 2013, **169**, 141-149.
106. M. B. Kok, A. de Vries, D. Abdurrachim, J. J. Prompers, H. Grull, K. Nicolay and G. J. Strijkers, *Contrast Media Mol I*, 2011, **6**, 19-27.
107. M. Srinivas, L. J. Cruz, F. Bonetto, A. Heerschap, C. G. Figdor and I. J. M. de Vries, *Biomaterials*, 2010, **31**, 7070-7077.
108. B. P. Barnett, J. Ruiz-Cabello, P. Hota, R. Ouwerkerk, M. J. Shamblott, C. Lauzon, P. Walczak, W. D. Gilson, V. P. Chacko, D. L. Kraitchman, A. Arepally and J. W. M. Bulte, *Contrast Media Mol I*, 2011, **6**, 251-259.
109. J. Ruiz-Cabello, P. Walczak, D. A. Kedziorek, V. P. Chacko, A. H. Schmieder, S. A. Wickline, G. M. Lanza and J. W. M. Bulte, *Magn Reson Med*, 2008, **60**, 1506-1511.
110. K. C. Partlow, J. J. Chen, J. A. Brant, A. M. Neubauer, T. E. Meyerrose, M. H. Creer, J. A. Nolta, S. D. Caruthers, G. M. Lanza and S. A. Wickline, *Faseb J*, 2007, **21**, 1647-1654.
111. M. Srinivas, P. Boehm-Sturm, C. G. Figdor, I. J. de Vries and M. Hoehn, *Biomaterials*, 2012, **33**, 8830-8840.
112. P. Boehm-Sturm, L. Mengler, S. Wecker, M. Hoehn and T. Kallur, *Plos One*, 2011, **6**.
113. J. Pacheco-Torres, P. Lopez-Larrubia, P. Ballesteros and S. Cerdan, *Nmr Biomed*, 2011, **24**, 1-16.
114. R. P. Mason, P. P. Antich, E. E. Babcock, J. L. Gerberich and R. L. Nunnally, *Magn Reson Imaging*, 1989, **7**, 475-485.
115. A. Balducci, Y. Wen, Y. Zhang, B. M. Helfer, T. K. Hitchens, W. S. Meng, A. K. Wesa and J. M. Janjic, *Oncoimmunology*, 2013, **2**.
116. M. Q. Huang, P. H. Basse, Q. Yang, J. A. Horner, T. K. Hichens and C. Ho, *Magn Reson Imaging*, 2004, **22**, 645-652.
117. P. K. Bae, J. Jung, S. J. Lim, D. Kim, S. K. Kim and B. H. Chung, *Mol Imaging Biol*, 2013, **15**, 401-410.
118. R. F. Mattrey, M. A. Trambert, J. J. Brown, S. W. Young, J. N. Bruneton, G. E. Wesbey and Z. N. Balsara, *Radiology*, 1994, **191**, 841-848.

119. D. W. Zhao, L. Jiang and R. P. Mason, *Imaging in Biological Research, Pt B*, 2004, **386**, 378-418.
120. U. Noth, L. M. Rodrigues, S. P. Robinson, A. Jork, U. Zimmermann, B. Newell and J. R. Griffiths, *Int J Radiat Oncol*, 2004, **60**, 909-919.
121. P. Bornert, D. G. Norris, H. Koch, W. Dreher, H. Reichelt and D. Leibfritz, *Magn Reson Med*, 1993, **29**, 226-234.
122. H. P. Shukla, R. P. Mason, D. E. Woessner and P. P. Antich, *J Magn Reson Ser B*, 1995, **106**, 131-141.
123. H. P. Shukla, R. P. Mason, N. Bansal and P. P. Antich, *Magn Reson Med*, 1996, **35**, 827-833.
124. S. Laukemper-Ostendorf, A. Scholz, K. Burger, C. P. Heussel, M. Schmittner, N. Weiler, K. Markstaller, B. Eberle, H. U. Kauczor, M. Quintel, M. Thelen and W. G. Schreiber, *Magn Reson Med*, 2002, **47**, 82-89.
125. D. K. K. Kadayakkara, J. M. Janjic, L. K. Pusateri, W. B. Young and E. T. Ahrens, *Magn Reson Med*, 2010, **64**, 1252-1259.
126. S. Y. Liu, S. J. Shah, L. J. Wilmes, J. Feiner, V. D. Kodibagkar, M. F. Wendland, R. P. Mason, N. Hylton, H. W. Hopf and M. D. Rollins, *Magn Reson Med*, 2011, **66**, 1722-1730.
127. L. Lemaire, G. Bastiat, F. Franconi, N. Lautram, T. D. T. Dan, E. Garcion, P. Saulnier and J. P. Benoit, *Eur J Pharm Biopharm*, 2013, **84**, 479-486.
128. H. Matsushita, S. Mizukami, F. Sugihara, Y. Nakanishi, Y. Yoshioka and K. Kikuchi, *Angew Chem Int Edit*, 2014, **53**, 1008-1011.
129. E. Pisani, N. Tsapis, B. Galaz, M. Santin, R. Berti, N. Taulier, E. Kurtisovski, O. Lucidarme, M. Ourevitch, B. T. Doan, J. C. Beloeil, B. Gillet, W. Urbach, S. L. Bridal and E. Fattal, *Adv Funct Mater*, 2008, **18**, 2963-2971.
130. Y. T. Lim, Y. W. Noh, J. N. Kwon and B. H. Chung, *Chem Commun*, 2009, 6952-6954.
131. K. J. Thurecht, *Macromol Chem Phys*, 2012, **213**, 2567-2572.
132. D. J. Siegwart, J. K. Oh and K. Matyjaszewski, *Prog Polym Sci*, 2012, **37**, 18-37.
133. H. Kakwere and S. Perrier, *Polym Chem*, 2011, **2**, 270-288.
134. V. D. Mehta, P. V. Kulkarni, R. P. Mason, E. E. Babcock, A. Constantinescu and P. P. Antich, *Bioorg Med Chem Lett*, 1992, **2**, 527-532.
135. Y. Y. Mai and A. Eisenberg, *Chem Soc Rev*, 2012, **41**, 5969-5985.
136. H. Peng, K. J. Thurecht, I. Blakey, E. Taran and A. K. Whittaker, *Macromolecules*, 2012, **45**, 8681-8690.
137. H. Peng, I. Blakey, B. Dargaville, F. Rasoul, S. Rose and A. K. Whittaker, *Biomacromolecules*, 2009, **10**, 374-381.

138. L. Nurmi, H. Peng, J. Seppala, D. M. Haddleton, I. Blakey and A. K. Whittaker, *Polym Chem*, 2010, **1**, 1039-1047.
139. X. N. Huang, G. Huang, S. R. Zhang, K. Sagiyama, O. Togao, X. P. Ma, Y. G. Wang, Y. Li, T. C. Soesbe, B. D. Sumer, M. Takahashi, A. D. Sherry and J. M. Gao, *Angew Chem Int Edit*, 2013, **52**, 8074-8078.
140. C. Zhang, H. Peng and A. K. Whittaker, *J Polym Sci Pol Chem*, 2014, **52**, 2375-2385.
141. Y. Li, B. Thapa, H. Zhang, X. F. Li, F. H. Yu, E. K. Jeong, Z. G. Yang and Z. X. Jiang, *Tetrahedron*, 2013, **69**, 9586-9590.
142. S. Rossi, M. Benaglia, M. Ortenzi, E. Micotti, C. Perego and M. G. De Simoni, *Tetrahedron Lett*, 2011, **52**, 6581-6583.
143. C. Biaggi, M. Benaglia, M. Ortenzi, E. Micotti, C. Perego and M. G. De Simoni, *J Fluorine Chem*, 2013, **153**, 172-177.
144. H. G. Lu, F. Y. Su, Q. Mei, Y. Q. Tian, W. J. Tian, R. H. Johnson and D. R. Meldrum, *J Mater Chem*, 2012, **22**, 9890-9900.
145. J. Khandare, M. Calderon, N. M. Dagia and R. Haag, *Chem Soc Rev*, 2012, **41**, 2824-2848.
146. J. M. Criscione, B. L. Le, E. Stern, M. Brennan, C. Rahner, X. Papademetris and T. M. Fahmy, *Biomaterials*, 2009, **30**, 3946-3955.
147. M. Ogawa, S. Nitahara, H. Aoki, S. Ito, M. Narazaki and T. Matsuda, *Macromol Chem Phys*, 2010, **211**, 1369-1376.
148. M. Ogawa, S. Nitahara, H. Aoki, S. Ito, M. Narazaki and T. Matsuda, *Macromol Chem Phys*, 2010, **211**, 1602-1609.
149. M. Ogawa, H. Kataoka, S. Nitahara, H. Fujimoto, H. Aoki, S. Ito, M. Narazaki and T. Matsuda, *B Chem Soc Jpn*, 2012, **85**, 79-86.
150. C. Porsch, Y. N. Zhang, A. Ostlund, P. Damberg, C. Ducani, E. Malmstrom and A. M. Nystrom, *Part Part Syst Char*, 2013, **30**, 381-390.
151. Z. X. Jiang, X. Liu, E. K. Jeong and Y. B. Yu, *Angew Chem Int Edit*, 2009, **48**, 4755-4758.
152. Z. X. Jiang and Y. B. Yu, *J Org Chem*, 2010, **75**, 2044-2049.
153. Z. H. Huang, R. S. Sengar, A. Nigam, M. C. Abadjian, D. M. Potter, D. B. Grotjahn and E. C. Wiener, *Invest Radiol*, 2010, **45**, 641-654.
154. Y. F. Zhou, W. Huang, J. Y. Liu, X. Y. Zhu and D. Y. Yan, *Adv Mater*, 2010, **22**, 4567-4590.
155. B. I. Voit and A. Lederer, *Chem Rev*, 2009, **109**, 5924-5973.
156. M. Calderon, M. A. Quadir, S. K. Sharma and R. Haag, *Adv Mater*, 2010, **22**, 190-218.

157. H. B. Jin, W. Huang, X. Y. Zhu, Y. F. Zhou and D. Y. Yan, *Chem Soc Rev*, 2012, **41**, 5986-5997.

158. W. J. Du, A. M. Nystrom, L. Zhang, K. T. Powell, Y. L. Li, C. Cheng, S. A. Wickline and K. L. Wooley, *Biomacromolecules*, 2008, **9**, 2826-2833.

159. W. J. Du, Z. Q. Xu, A. M. Nystrom, K. Zhang, J. R. Leonard and K. L. Wooley, *Bioconjugate Chem*, 2008, **19**, 2492-2498.

160. K. J. Thurecht, I. Blakey, H. Peng, O. Squires, S. Hsu, C. Alexander and A. K. Whittaker, *J Am Chem Soc*, 2010, **132**, 5336-5337.

161. B. E. Rolfe, I. Blakey, O. Squires, H. Peng, N. R. B. Boase, C. Alexander, P. G. Parsons, G. M. Boyle, A. K. Whittaker and K. J. Thurecht, *J Am Chem Soc*, 2014, **136**, 2413-2419.

162. V. D. Mehta, P. V. Kulkarni, R. P. Mason, A. Constantinescu and P. P. Antich, *Bioconjugate Chem*, 1994, **5**, 257-261.

163. Y. Sun, Y. Takaoka, S. Tsukiji, M. Narazaki, T. Matsuda and I. Hamachi, *Bioorg Med Chem Lett*, 2011, **21**, 4393-4396.

164. M. Oishi, S. Sumitani and Y. Nagasaki, *Bioconjugate Chem*, 2007, **18**, 1379-1382.

165. M. M. Bailey, C. M. Mahoney, K. E. Dempah, J. M. Davis, M. L. Becker, S. Khondee, E. J. Munson and C. Berkland, *Macromol Rapid Comm*, 2010, **31**, 87-92.

166. M. M. Bailey, S. R. Kline, M. D. Anderson, J. L. Staymates and C. Berkland, *J Appl Polym Sci*, 2012, **126**, 1218-1227.

167. X. Yang, Y. Sun, S. Kootala, J. Hilborn, A. Heerschap and D. Ossipov, *Carbohyd Polym*, 2014, **110**, 95-99.

168. J. Chiefari, Y. K. Chong, F. Ercole, J. Krstina, J. Jeffery, T. P. T. Le, R. T. A. Mayadunne, G. F. Meijs, C. L. Moad, G. Moad, E. Rizzardo and S. H. Thang, *Macromolecules*, 1998, **31**, 5559-5562.

169. Y. K. Chong, T. P. T. Le, G. Moad, E. Rizzardo and S. H. Thang, *Macromolecules*, 1999, **32**, 2071-2074.

170. D. J. Keddie, G. Moad, E. Rizzardo and S. H. Thang, *Macromolecules*, 2012, **45**, 5321-5342.

171. G. Moad, E. Rizzardo and S. H. Thang, *Aust J Chem*, 2009, **62**, 1402-1472.

172. G. Moad, E. Rizzardo and S. H. Thang, *Aust J Chem*, 2006, **59**, 669-692.

173. G. Moad, E. Rizzardo and S. H. Thang, *Aust J Chem*, 2005, **58**, 379-410.

174. G. Moad, E. Rizzardo and S. H. Thang, *Polymer*, 2008, **49**, 1079-1131.

175. C. Boyer, M. H. Stenzel and T. P. Davis, *J Polym Sci Pol Chem*, 2011, **49**, 551-595.

176. S. Dai, P. Ravi and K. C. Tam, *Soft Matter*, 2009, **5**, 2513-2533.

177. A. W. York, S. E. Kirkland and C. L. McCormick, *Adv Drug Deliver Rev*, 2008, **60**, 1018-1036.
178. A. E. Smith, X. W. Xu and C. L. Mccormick, *Prog Polym Sci*, 2010, **35**, 45-93.
179. C. R. Becer, S. Hahn, M. W. M. Fijten, H. M. L. Thijs, R. Hoogenboom and U. S. Schubert, *J Polym Sci Pol Chem*, 2008, **46**, 7138-7147.
180. D. S. W. Benoit, S. Srinivasan, A. D. Shubin and P. S. Stayton, *Biomacromolecules*, 2011, **12**, 2708-2714.
181. D. Roy, J. N. Cambre and B. S. Sumerlin, *Chem Commun*, 2008, 2477-2479.
182. J. T. Wiltshire and G. G. Qiao, *Aust J Chem*, 2007, **60**, 699-705.
183. A. Rosler, G. W. M. Vandermeulen and H. A. Klok, *Adv Drug Deliver Rev*, 2001, **53**, 95-108.
184. M. Hales, C. Barner-Kowollik, T. P. Davis and M. H. Stenzel, *Langmuir*, 2004, **20**, 10809-10817.
185. H. T. T. Duong, V. T. Huynh, P. de Souza and M. H. Stenzel, *Biomacromolecules*, 2010, **11**, 2290-2299.
186. W. M. Wan and C. Y. Pan, *Polym Chem*, 2010, **1**, 1475-1484.
187. B. Charleux, G. Delaittre, J. Rieger and F. D'Agosto, *Macromolecules*, 2012, **45**, 6753-6765.
188. S. Sugihara, A. Blanazs, S. P. Armes, A. J. Ryan and A. L. Lewis, *J Am Chem Soc*, 2011, **133**, 15707-15713.
189. G. Y. Liu, Q. Qiu, W. Q. Shen and Z. S. An, *Macromolecules*, 2011, **44**, 5237-5245.
190. H. F. Gao, *Macromol Rapid Comm*, 2012, **33**, 722-734.
191. A. Blencowe, J. F. Tan, T. K. Goh and G. G. Qiao, *Polymer*, 2009, **50**, 5-32.
192. L. Barner, T. P. Davis, M. H. Stenzel and C. Barner-Kowollik, *Macromol Rapid Comm*, 2007, **28**, 539-559.
193. C. Barner-Kowollik, T. P. Davis and M. H. Stenzel, *Aust J Chem*, 2006, **59**, 719-727.
194. H. Chaffey-Millar, M. H. Stenzel, T. P. Davis, M. L. Coote and C. Barner-Kowollik, *Macromolecules*, 2006, **39**, 6406-6419.
195. A. Gregory and M. H. Stenzel, *Prog Polym Sci*, 2012, **37**, 38-105.
196. J. Ferreira, J. Syrett, M. Whittaker, D. Haddleton, T. P. Davis and C. Boyer, *Polym Chem*, 2011, **2**, 1671-1677.
197. C. L. Zhang, M. Miao, X. T. Cao and Z. S. An, *Polym Chem*, 2012, **3**, 2656-2664.
198. X. F. Shi, W. Zhou, Q. Qiu and Z. S. An, *Chem Commun*, 2012, **48**, 7389-7391.
199. G. Y. Liu, Q. Qiu and Z. S. An, *Polym Chem*, 2012, **3**, 504-513.

200. W. Q. Shen, Y. L. Chang, G. Y. Liu, H. F. Wang, A. N. Cao and Z. S. An, *Macromolecules*, 2011, **44**, 2524-2530.
201. Q. Qiu, G. Y. Liu and Z. S. An, *Chem Commun*, 2011, **47**, 12685-12687.
202. X. F. Shi, M. Miao and Z. S. An, *Polym Chem*, 2013, **4**, 1950-1959.
203. J. M. J. Frechet, M. Henmi, I. Gitsov, S. Aoshima, M. R. Leduc and R. B. Grubbs, *Science*, 1995, **269**, 1080-1083.
204. B. L. Liu, A. Kazlauciunas, J. T. Guthrie and S. Perrier, *Macromolecules*, 2005, **38**, 2131-2136.
205. J. Rosselgong, S. P. Armes, W. R. S. Barton and D. Price, *Macromolecules*, 2010, **43**, 2145-2156.
206. J. Rosselgong, S. P. Armes, W. Barton and D. Price, *Macromolecules*, 2009, **42**, 5919-5924.
207. R. Wang, Y. W. Luo, B. G. Li and S. P. Zhu, *Macromolecules*, 2009, **42**, 85-94.
208. S. Carter, B. Hunt and S. Rimmer, *Macromolecules*, 2005, **38**, 4595-4603.
209. S. Carter, S. Rimmer, R. Rutkaite, L. Swanson, J. P. A. Fairclough, A. Sturdy and M. Webb, *Biomacromolecules*, 2006, **7**, 1124-1130.
210. S. Carter, S. Rimmer, A. Sturdy and M. Webb, *Macromol Biosci*, 2005, **5**, 373-378.
211. M. J. Zhang, H. H. Liu, W. Shao, K. Miao and Y. L. Zhao, *Macromolecules*, 2013, **46**, 1325-1336.
212. J. Han, S. P. Li, A. J. Tang and C. Gao, *Macromolecules*, 2012, **45**, 4966-4977.
213. S. P. Li and C. Gao, *Polym Chem*, 2013, **4**, 4450-4460.
214. S. P. Li, J. Han and C. Gao, *Polym Chem*, 2013, **4**, 1774-1787.
215. Z. L. Weng, Y. C. Zheng, A. J. Tang and C. Gao, *Aust J Chem*, 2013, **67**, 103-111.
216. D. Konkolewicz, C. K. Poon, A. Gray-Weale and S. Perrier, *Chem Commun*, 2011, **47**, 239-241.
217. R. Barbey and S. Perrier, *Acs Macro Lett*, 2013, **2**, 366-370.
218. J. F. Mano, *Adv Eng Mater*, 2008, **10**, 515-527.
219. E. Cabane, X. Y. Zhang, K. Langowska, C. G. Palivan and W. Meier, *Biointerphases*, 2012, **7**.
220. J. M. Zhuang, M. R. Gordon, J. Ventura, L. Y. Li and S. Thayumanavan, *Chem Soc Rev*, 2013, **42**, 7421-7435.
221. M. A. C. Stuart, W. T. S. Huck, J. Genzer, M. Muller, C. Ober, M. Stamm, G. B. Sukhorukov, I. Szleifer, V. V. Tsukruk, M. Urban, F. Winnik, S. Zauscher, I. Luzinov and S. Minko, *Nat Mater*, 2010, **9**, 101-113.
222. H. Cabral, N. Nishiyama and K. Kataoka, *Accounts Chem Res*, 2011, **44**, 999-1008.

223. L. P. Zhu, P. P. Smith and S. G. Boyes, *J Polym Sci Pol Phys*, 2013, **51**, 1062-1067.
224. L. Wang and C. Li, *J Mater Chem*, 2011, **21**, 15862-15871.
225. K. J. Zhou, Y. G. Wang, X. N. Huang, K. Luby-Phelps, B. D. Sumer and J. M. Gao, *Angew Chem Int Edit*, 2011, **50**, 6109-6114.
226. W. T. Wu, J. Shen, P. Banerjee and S. Q. Zhou, *Biomaterials*, 2010, **31**, 7555-7566.
227. J. S. Katz, S. Zhong, B. G. Ricart, D. J. Pochan, D. A. Hammer and J. A. Burdick, *J Am Chem Soc*, 2010, **132**, 3654-3655.
228. T. Mosaiab, I. In and S. Y. Park, *Macromol Rapid Comm*, 2013, **34**, 1408-1415.
229. D. E. Lee, H. Koo, I. C. Sun, J. H. Ryu, K. Kim and I. C. Kwon, *Chem Soc Rev*, 2012, **41**, 2656-2672.
230. S. R. Cherry, *Annu Rev Biomed Eng*, 2006, **8**, 35-62.
231. A. Y. Louie, *Chem Rev*, 2010, **110**, 3146-3195.
232. L. E. Jennings and N. J. Long, *Chem Commun*, 2009, 3511-3524.
233. P. A. Jarzyna, A. Gianella, T. Skajaa, G. Knudsen, L. H. Deddens, D. P. Cormode, Z. A. Fayad and W. J. M. Mulder, *Wires Nanomed Nanobi*, 2010, **2**, 138-150.
234. P. Howes, M. Green, A. Bowers, D. Parker, G. Varma, M. Kallumadil, M. Hughes, A. Warley, A. Brain and R. Botnar, *J Am Chem Soc*, 2010, **132**, 9833-9842.
235. C. T. Adkins, J. N. Dobish, C. S. Brown, B. Mayrsohn, S. K. Hamilton, F. Udoji, K. Radford, T. E. Yankeelov, J. C. Gore and E. Harth, *Polym Chem*, 2012, **3**, 390-398.
236. H. F. Wehrl, M. S. Judenhofer, S. Wiehr and B. J. Pichler, *Eur J Nucl Med Mol I*, 2009, **36**, 56-68.
237. E. Locatelli, L. Gil, L. L. Israel, L. Passoni, M. Naddaka, A. Pucci, T. Reese, V. Gomez-Vallejo, P. Milani, M. Matteoli, J. Llop, J. P. Lellouche and M. C. Franchini, *Int J Nanomed*, 2012, **7**, 6021-6033.
238. R. T. M. de Rosales, R. Tavare, A. Glaria, G. Varma, A. Protti and P. J. Blower, *Bioconjugate Chem*, 2011, **22**, 455-465.
239. D. Kim, M. K. Yu, T. S. Lee, J. J. Park, Y. Y. Jeong and S. Jon, *Nanotechnology*, 2011, **22**.

# Chapter 2
# pH-Responsive Star-like Hyperbranched Polymers for Selective F-19 MRI

The key design criteria of polymeric $^{19}F$ MRI contrast agents are to achieve high $^{19}F$ content and highly mobile $^{19}F$ nuclei in aqueous solution. This chapter explores hyperbranched structures for the fabrication of $^{19}F$ MRI contrast agents. Star-like polymers with a hyperbranched core were synthesised using the arm-first approach by RAFT polymerisation. The fluorine-rich units were positioned in a three-dimensional (3D) hyperbranched structure, which was shielded by hydrophilic poly(ethylene glycol) brushes as arms. The mobility of the $^{19}F$ nuclei was expected to be enhanced through the separation of fluorinated segments by the hyperbranched structure. In addition, the mobility of the $^{19}F$ nuclei was expected to be dependent on the solution pH due to changes in polymer conformation regulated by the presence of pH-responsive segments. The star-like polymers could be imaged only in acidic environments, suggesting potential applications in the diagnosis of cancer diseases.

## 2.1 Introduction

Early and accurate detection of cancerous tissue is of crucial importance for successful treatment. As a key diagnostic modality, magnetic resonance imaging (MRI) has attracted considerable attention because of its non-invasive and non-destructive properties as well as its capability to provide high resolution images including three-dimensional images with detailed anatomic contrast.[1, 2] So far, MRI has been extensively studied and utilised for the detection, assessment and therapeutic monitoring of a variety of cancer diseases, such as prostate cancer, breast cancer, brain cancer, etc.[3] In the past few decades, $^{1}H$ MRI has been the dominant imaging modality in clinical MRI. However, due to the large background signal arising from the abundance of protons in human tissue, it is often difficult for $^{1}H$ MRI to generate unambiguous images and discriminate tumour tissue from the surrounding normal tissues, especially in the early stages of disease, and at the tumour margins.[4]

Since its first appearance in 1977,[5] $^{19}F$ MRI has been considered as a promising alternative to $^{1}H$ MRI because of the advantages of negligible $^{19}F$ background in the living body, high gyromagnetic ratio, favourable sensitivity and high natural abundance of $^{19}F$.[6, 7]

In many MRI examinations, contrast agents are required to improve the image quality or visualize specific body tissues. $^{1}$H MRI measures the abundant water molecules and hence provides high quality images.[8] To achieve the same image quality as $^{1}$H MRI, $^{19}$F MRI requires a high concentration of $^{19}$F nuclei in the targeted tissue area. For this reason, contrast agents with high content of detectable $^{19}$F nuclei are indispensable for $^{19}$F MRI. During the past few decades, tremendous effort has been devoted to the development of $^{19}$F MRI contrast agents. A range of $^{19}$F-containing compounds, from small molecules to polymers, have been designed and studied as candidate $^{19}$F MRI contrast agents.[8, 9]

Recently, $^{19}$F-containing polymers have been considered as a potentially new generation of $^{19}$F MRI contrast agents. Compared to their small molecule counterparts, polymeric agents have a number of favourable characteristics, such as potentially high loading of the NMR-active fluorine nuclei, versatile molecular structures and abundant possibilities for functionalisation. In recent years, a number of polymers have been synthesised and evaluated as $^{19}$F MRI contrast agents, including linear polymers,[10-13] polymeric nanogels[14, 15], dendrimers[16-19] and hyperbranched polymers.[20-22] Among these, water-soluble star polymers are especially advantageous owing to several features. First, they can form stable nanoparticles in aqueous solution without involving self-assembly processes and hence their stability is not compromised due to presence of a critical micelle concentration. Thus, unlike block copolymer micelles, star polymers will not suffer from potential problems arising from disassembly and collapse *in vivo*.[21] Secondly, in a three-dimensional branched or star structure, the $^{19}$F nuclei can be well separated thus maintaining high molecular mobility, ensuring long transverse relaxation times, the generation of a strong $^{19}$F signal and good MRI image quality.[22] Thirdly, the abundant functional groups in star polymers provide many possibilities for post-modification to satisfy various demands, such as conjugation with complementary imaging agents or targeting groups. In the past few years, the above aspects have been leading to a wave of interest in the fabrication of branched polymeric $^{19}$F MRI contrast agents.

More recently, the development of stimuli-responsive imaging agents has attracted significant interest.[9, 23, 24] Imaging agents sensitive to environmental conditions (pH, temperature, metal concentration, etc.), termed "smart" imaging agents, can be designed to be only visible (detectable) in specific circumstances. pH-Responsive imaging agents are especially attractive because of the well-known variation in pH in tissue types and in diseased tissue.[25, 26] Polymers that bear tertiary amino groups, such as poly 2-(dimethylamino)ethyl methacrylate (PDMAEMA) and poly 2-(diethylamino)ethyl methacrylate (PDEAEMA), have been widely exploited in various applications

as pH-responsive materials.[26] As a result of the protonation and deprotonation of the tertiary amino groups, these polymer chains can swell and shrink upon a change in pH across the p*K*a. Although a few examples have been reported,[11, 14, 18] there is still a dearth of data on the development of pH-responsive $^{19}$F MRI agents.

In this Chapter, we study the synthesis of pH-responsive and $^{19}$F-containing star-like polymers with a branched core and their potential application as "smart" $^{19}$F MRI contrast agents. First, poly(poly(ethylene glycol) methyl ether methacrylate) (PPEGMA) was synthesised by reversible addition-fragmentation chain transfer (RAFT) polymerisation. Then it was used as a macro chain transfer agent (macroCTA) for the copolymerisation of 2,2,2-trifluoroethyl acrylate (TFEA, $^{19}$F-containing monomer), 2-(dimethylamino)ethyl methacrylate (DMAEMA, pH-responsive monomer) and ethylene glycol dimethacrylate (EGDMA, cross-linker), forming star-like polymers with a branched core and PPEGMA brush arms. The star-like polymers were directly dissolved in phosphate-buffered saline (PBS, pH = 7.4) to form nanoparticles. The pH responsiveness was examined by measurement of particle size by cryo-transmission electron microscopy (cryo-TEM) and $^{19}$F spin-lattice ($T_1$) and spin-spin ($T_2$) relaxation times by $^{19}$F nuclear magnetic resonance ($^{19}$F NMR). Preliminary *in vitro* $^{19}$F MRI measurements confirmed a strong change in image intensity across the p*K*a.

An advantage of these star-like polymers compared with the hyperbranched platforms reported previously by our group[22, 27] is the ability to simply tune the core density through the arm-first method. This potentially provides greater control of the response of the imaging agent to an external stimulus, in this case a change in pH.

## 2.2 Experimental Section

### 2.2.1 Materials

All chemicals were purchased from Sigma-Aldrich unless otherwise stated. Poly(ethylene glycol) methyl ether methacrylate (PEGMA, $M_n$ = 475), 2-(dimethylamino)ethyl methacrylate (DMAEMA), 2,2,2-trifluoroethyl acrylate (TFEA), and ethylene glycol dimethacrylate (EGDMA) were passed through basic alumina columns to remove inhibitors prior to use. 2,2′-azobis(2-methylpropionitrile) (AIBN) was recrystallized twice from methanol before use. The RAFT agent, 4-cyano-4-(dodecylsulfanylthiocarbonyl)sulfanyl pentanoic acid (denoted as CTA), was synthesised according to a previously reported procedure.[28, 29] Dialysis tubing with molecular weight cut off

(MWCO) of 3.5 or 100 kDa was purchased from Thermo Fisher Scientific Inc. and Spectrum Laboratories Inc., respectively. PBS (1×) was prepared using PBS tablets purchased from AMRESCO. Milli-Q water was used for the preparation of aqueous solution and for dialysis of the polymers.

## 2.2.2 Synthesis

### 2.2.2.1 Synthesis of Alkyne-Terminated CTA (Alkyne-CTA)

CTA (1.70 g, 4.22 mmol), *N*-(3-dimethylaminopropyl)-*N′*-ethylcarbodiimide hydrochloride (EDC, 1.21 g, 6.31 mmol), 4-(dimethylamino)pyridine (DMAP, 0.77 g, 6.31 mmol ) were dissolved in 30 mL of dichloromethane (DCM) in a 50 mL round bottom flask and bubbled with nitrogen for 30 min in an ice bath. Propargyl alcohol (1.25 mL, 21.42 mmol) was injected drop-wise into the flask under nitrogen flow. After injection, the reaction was kept at 0 $^{o}$C for 1 h, and then stirred at room temperature overnight. Finally, the resultant brown solution was washed with 1 M HCl (4×50 mL) and brine (4×100 mL) in sequence, dried over $MgSO_4$ and then the solvent was removed by rotary evaporation, yielding a brownish-yellow oil. The structure was confirmed by $^{1}$H nuclear magnetic resonance ($^{1}$H NMR) (500 MHz, $\delta$, ppm, $CDCl_3$): 0.88 (t, 3H, C$\underline{H}_3CH_2CH_2$), 1.26 (br s, 18H, (C$\underline{H}_2$)$_9$), 1.69 (m, 2H, C$\underline{H}_2CH_2S$), 1.87 (s, 3H, C$\underline{H}_3$), 2.37-2.70 (m, 4H, C$\underline{H}_2C\underline{H}_2$-COO), 2.49 (t, H, $OCH_2C{\equiv}C\underline{H}$), 3.32 (t, 3H, $CH_2C\underline{H}_2S$), 4.70 (d, 2H, $OC\underline{H}_2C{\equiv}CH$). $^{13}$C NMR (125 MHz, δ, ppm, $CDCl_3$): 170.63 ($\underline{C}OOCH_2$), 118.87 ($\underline{C}N$), 75.20 ($\underline{C}{\equiv}CH$), 52.41(C$\equiv\underline{C}$H), 46.21 ($\underline{C}(CH_3)CN$)), 37.03 ($C(=O)CH_2\underline{C}H_2$), 33.62 ($C(=O)\underline{C}H_2CH_2$), 31.85, 29.56, 27.61, 24.81, 22.63 (overlapping $^{13}$C signals), 14.07 ($\underline{C}H_3CH_2CH_2$).

### 2.2.2.2 Synthesis of PPEGMA Macro-CTA by RAFT Polymerisation

PEGMA (9.5 g, 20 mmol), alkyne-CTA (0.441g, 1 mmol) and AIBN (32.8 mg, 0.2 mmol) were dissolved in 20 mL of toluene in a 50 mL round bottom flask equipped with a magnetic stirrer bar and sealed with a rubber septum. The solution was purged with nitrogen for 45 min in an ice bath, followed by being immersed in an oil bath thermostated at 70 $^{o}$C. Samples were removed at intervals using a gas-tight syringe for kinetic studies. After 180 min, the polymerisation was quenched by placing the flask in an ice bath and exposing to air for 5 min. The crude polymer solution was precipitated into hexane twice and then further purified by dialysed against water for 24 h using dialysis tubing with MWCO of 3.5 kDa. A yellowish viscous oil was obtained after freeze drying (5 g, yield: 86%). The molecular weights of the final product were determined by both gel permeation chromatography (GPC) and $^{1}$H NMR. GPC: $M_n$ = 8100, $M_w/M_n$ = 1.12. $^{1}$H NMR:

$M_n$ = 14,200, degree of polymerisation (DP) = 29.

#### 2.2.2.3 Synthesis of Star-like Polymers by RAFT Polymerisation using PPEGMA Macro-CTA

In a typical experiment, PPEGMA macroCTA (0.9 g, 0.061 mmol), TFEA (0.063 mL, 0.5 mmol), DMAEMA (0.253 mL, 1.5 mmol), EGDMA (0.094 mL, 0.5 mmol), and AIBN (3.28 mg, 0.02 mmol) were dissolved in 5 mL of tetrahydrofuran (THF) in a 25 mL flask equipped with a magnetic stirrer bar and sealed with a rubber septum. The flask was then deoxygenated by being purged with nitrogen for 15 min in an ice bath before it was placed in an oil bath thermostated at 70 $^{o}$C for 24 h. The polymerisation was stopped by immersing the flask in an ice bath and exposing the solution to air for 5 min. The crude polymer solution was precipitated into hexane twice and then purified by extensive dialysis in water (MWCO: 100 kDa) for 5 days to remove the small molecular weight impurities. A yellowish and viscous solid was obtained after freeze drying. Yield: 0.71 g, 55%.

#### 2.2.2.4 Preparation of Star-like Polymer Nanoparticles in PBS

Solutions of the star-like polymers were prepared by direct dissolution in PBS (pH = 7.4). Typically, 20 mg of the sample was dissolved in 20 mL of PBS, which was stirred for 2 h at room temperature (20 $^{o}$C) to form a clear solution. HCl and NaOH aqueous solution (both 1 M) were used to adjust the pH to desired values for further characterisation.

### 2.2.3 Characterisation

#### Gel Permeation Chromatography (GPC)

Molecular weights and molecular weight distributions were determined by GPC using a Waters Alliance 2690 Separations Module equipped with Waters 2414 Refractive Index (RI) Detector, Waters 2489 UV/Visible Detector, Waters 717 Plus Autosampler and Waters 1515 Isocratic HPLC Pump. Samples were dissolved in THF/triethylamine (95/5, v/v) and passed through 0.45 μm filters before each measurement. THF was used as mobile phase at a flow rate of 1 mL min$^{-1}$. The system was calibrated using polystyrene (PS) standards, to which the number average molecular weight ($M_n$) and weight average molecular weight ($M_w$) were referenced. For measuring absolute molecular weights of the star-like polymers, a multi angle laser light scattering (MALLS) detector (DAWN 8$^{+}$, Wyatt) was attached to the GPC, and the polymer sample solutions were eluted at a flow rate of 1 mg mL$^{-1}$ in THF. The refractive index increment, *dn*/*dc*, was calculated for each sample after measuring the refractive indices of a series of dilute polymer/THF solutions with a range of

concentrations, and was found to be around 0.055 ml $g^{-1}$ for the star-like polymers in THF at 25 $^{o}$C.

### $^{1}$H Nuclear Magnetic Resonance ($^{1}$H NMR)

$^{1}$H NMR analysis was performed on a Bruker Avance 500MHz spectrometer with either TXI5 or BBO5 probe at 25 $^{o}$C using an internal lock ($CDCl_3$) and referenced to the residual non-deuterated solvent ($CHCl_3$). A 90$^{o}$ pulse of either 7.85 or 13.7 μs was applied in all experiments, the relaxation delay was 4 s and the acquisition time was 3.9 s. Data were collected using a spectrum width of 5.5 kHz, 43k data points and 256 scans.

### $^{19}$F Nuclear Magnetic Resonance ($^{19}$F NMR)

All $^{19}$F NMR spectra were acquired at 470.55 MHz without $^{1}$H decoupling on a Bruker Avance 500 spectrometer using a 5 mm broadband inverse probe (BBI5) for which the inner coil was double-tuned for $^{19}$F and $^{1}$H. The samples were prepared by dissolving the star-like polymers in $H_2O/D_2O$ (90/10, v/v) at a concentration of 20 mg $mL^{-1}$. All measurements were performed at 25 $^{o}$C. A 90$^{o}$ pulse of 15.1 μs was applied in all measurements, the relaxation delay was 2 s and the acquisition time was 0.7 s. Data were collected using a spectrum width of 23 kHz, 32k data points and 128 scans.

$^{19}$F spin-spin relaxation times ($T_2$) were measured using the Carr-Purcell-Meiboom-Gill (CPMG) pulse sequence at 25 $^{o}$C. The samples were dissolved in $H_2O/D_2O$ (90/10, v/v) at a concentration of 20 mg $mL^{-1}$. The relaxation delay was 3 s and the acquisition time was 0.7 s. For each measurement, the echo times were from 2 to 770 ms and 15 points were collected, which could be described by exponential functions for the calculation of $T_2$.

$^{19}$F spin-lattice ($T_1$) relaxation times were measured using the standard inversion-recovery pulse sequence. For each measurement, the recovery times were from 2 ms to 3 s and 15 points were acquired. Values for the major peak at around -72.8 ppm are reported.

### $^{19}$F MRI

$^{19}$F MRI images were acquired at 376.5 MHz (9.4 T) on a Bruker BioSpec 94/30 USR small animal imaging system using a 40 mm internal diameter $^{1}$H/$^{19}$F volume coil. Star-like polymers were dissolved in PBS (20 mg $mL^{-1}$) and loaded in clear glass vials (8 × 30 mm, 0.75 mL), which were

then placed in a $^{1}H/^{19}F$ dual resonator 40 mm volume coil. Scan parameters were chosen to optimize acquisition for $^{19}F$ density contrast and minimize the effect of $T_1$ and $T_2$ on signal attenuation. RF basic frequency and RF pulse width and attenuation were calibrated manually. A multi slice multi echo (MSME) sequence acquiring a single echo per excitation was used (repetition time (TR) = 1000 ms, echo time (TE) = 6.2 ms, number of excitations (NEX) = 1024) with matrix (MTX) of 32 × 32 × 1 over a field of view (FOV) of 30 × 30 × 20 mm giving a total scan time of 9 h and 6 min.

**Cryo-Transmission Electron Microscopy (Cryo-TEM)**

Samples (20 mg $mL^{-1}$ in PBS at pH 6 and 9) were plunge frozen on C-flat holey carbon grids (Protochips, Raleigh, NC, USA) into liquid ethane using an FEI Vitrobot Mark 3 (FEI Company, Eindhoven, The Netherlands). The optimal blot time was 4 seconds, with the chamber maintained at 100% humidity at 4 ºC. Frozen/vitrified samples were viewed on a Technai T12 TEM (FEI Company) operating at 120 kV, and imaged at 30,000× magnification (8.4 electrons/$Å^2$) and 52,000× magnification (26 electrons/$Å^2$), using an FEI Eagle 4k CCD (FEI Company), and SerialEM image acquisition software.

## 2.3 Results and Discussion

### 2.3.1 Design Concept

It is well established that for spin-echo MR imaging, the intensity of the observed MRI signal in any volume element depends on the number of spins in that volume, and the relaxation times ($T_1$ and $T_2$), as described by the following equation.[30]

$$I \approx N(F)\exp\left(\frac{-\mathrm{TE}}{T_2}\right)\left[1-2\exp\left(\frac{-\left(\mathrm{TR}-\frac{\mathrm{TE}}{2}\right)}{T_1}\right)+\exp\left(\frac{-\mathrm{TR}}{T_1}\right)\right] \qquad (2\text{-}1)$$

In Equation (2-1), $I$ is the imaging intensity, $N(F)$ is the NMR detectable $^{19}F$ nuclei density, and TR and TE are the pulse sequence repetition time and echo delay times, respectively. Equation (2-1) informs that a long $T_2$ and short $T_1$ are required to achieve high MRI signal intensity. The spin-spin relaxation time, $T_2$, is determined by the strength of the dipolar coupling of the $^{19}F$ nuclei with near-neighbour fluorine and proton nuclei, and hence is sensitive to the spatial arrangement of the

nuclear spins and their relative mobility. We have previously demonstrated in studies of partially-fluorinated block copolymers that flexible fluorine segments with highly mobile $^{19}$F-containing groups result in longer $T_2$ relaxation times and higher imaging signal-to-noise ratios.[12, 31]

Polymeric $^{19}$F imaging agents are promising because of their advantageous chemical structure, e.g. high fluorine content, small size, multifunctional properties and numerous possibilities for functionalisation. However, the fluorinated segments tend to aggregate in aqueous solution due to their hydrophobic nature, and this can significantly restrict local modes of motion leading to a shortening of the $T_2$ relaxation times.[11, 12, 31] As described above this leads to poor MRI signal intensity. Therefore, to develop high performance imaging agents, it is necessary to prevent the association of the $^{19}$F nuclei.

Our approach to achieve the separation of the fluorinated monomers is by statistical terpolymerisation of TFEA with DMAEMA in the presence of the branching/crosslinking monomer EGDMA by the RAFT technique, generating star-like polymers with a hyperbranched core and hydrophilic poly(ethylene glycol) brushes as arms. The detailed synthetic methodology is illustrated in Scheme 2-1. The hyperbranched core contains DMAEMA and TFEA monomeric units, which provide pH-responsiveness and $^{19}$F signal, respectively. The EGDMA units act as crosslinking agents to form branched structures and assist to prevent the association of the TFEA monomers.[22] It is worth highlighting that the $^{19}$F-containing segments are well separated and dispersed in the 3D branched structure through the RAFT-controlled, statistical copolymerisation of the monomers, thus generating strong signal intensity.[22] The arms are comprised of PEGMA brush polymer chains, an approach commonly used in biomaterials because PEG is hydrophilic, biocompatible, and approved by the United States Food and Drug Administration (FDA) for human use.[32-37] Such water-soluble star-like polymers can form nanoparticles in aqueous solution directly, and no self-assembly procedure is needed, which greatly facilitates potential applications *in vivo*.

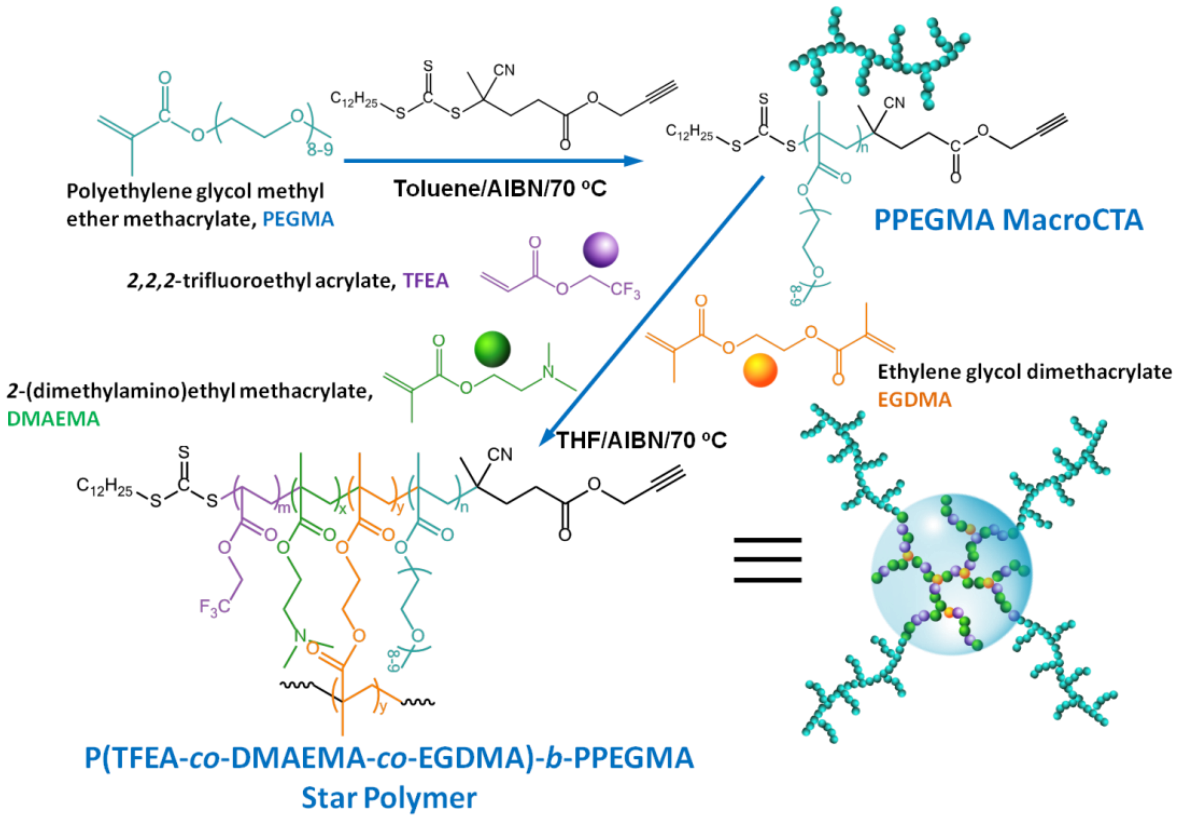


**Scheme 2-1** Schematic illustration of the synthesis of the star-like hyperbranched polymers.

### 2.3.2 Synthesis of PPEGMA Macro-CTA

Well-defined PPEGMA macro-CTA polymers were prepared by RAFT polymerisation.[38] The chain transfer agent (CTA) used here is an alkyne-terminated trithiocarbonate which has a tertiary cyanoalkyl R group (see Appendix A Figure A2.1 for the $^{1}$H and $^{13}$C NMR spectra), as shown in Scheme 2-1. As displayed in Figure 2-1 (A), the polymerisation exhibited pseudo-first-order kinetics, indicating that the radical concentration was constant. In addition, the $M_n$ measured by GPC in THF using a RI detector was linearly dependent on monomer conversion and the molar mass dispersity remained low at around 1.10 (Figure 2-1 (B)). Furthermore, as revealed in Figure 2-1 (C), the GPC traces with narrow $Đ_M$ also evolved toward high molecular weight (low retention time) with polymerisation time and monomer conversion. All the above results confirmed a well-controlled RAFT polymerisation of PEGMA.

It should be mentioned that another frequently used trithiocarbonate, S-1-dodecyl-S'-(α,α'-dimethyl-α"-acetic acid) trithiocarbonate, was also evaluated for the RAFT polymerisation of PEGMA. However, it showed poor control over the polymerisation, and bimodal GPC curves with broad molar mass distributions were observed, mainly caused by the low transfer coefficient of the

alkyl R leaving group (see Appendix A Figure A2.2). Normally, the choice of R group is very crucial for RAFT polymerisation of methacrylates,[39] and a guideline for the selection of proper RAFT agents has been proposed by Moad and co-workers.[40] Accordingly, trithiocarbonates with tertiary cyanoalkyl groups are good RAFT agents for the polymerisation of PEGMA, as has been demonstrated by these results.

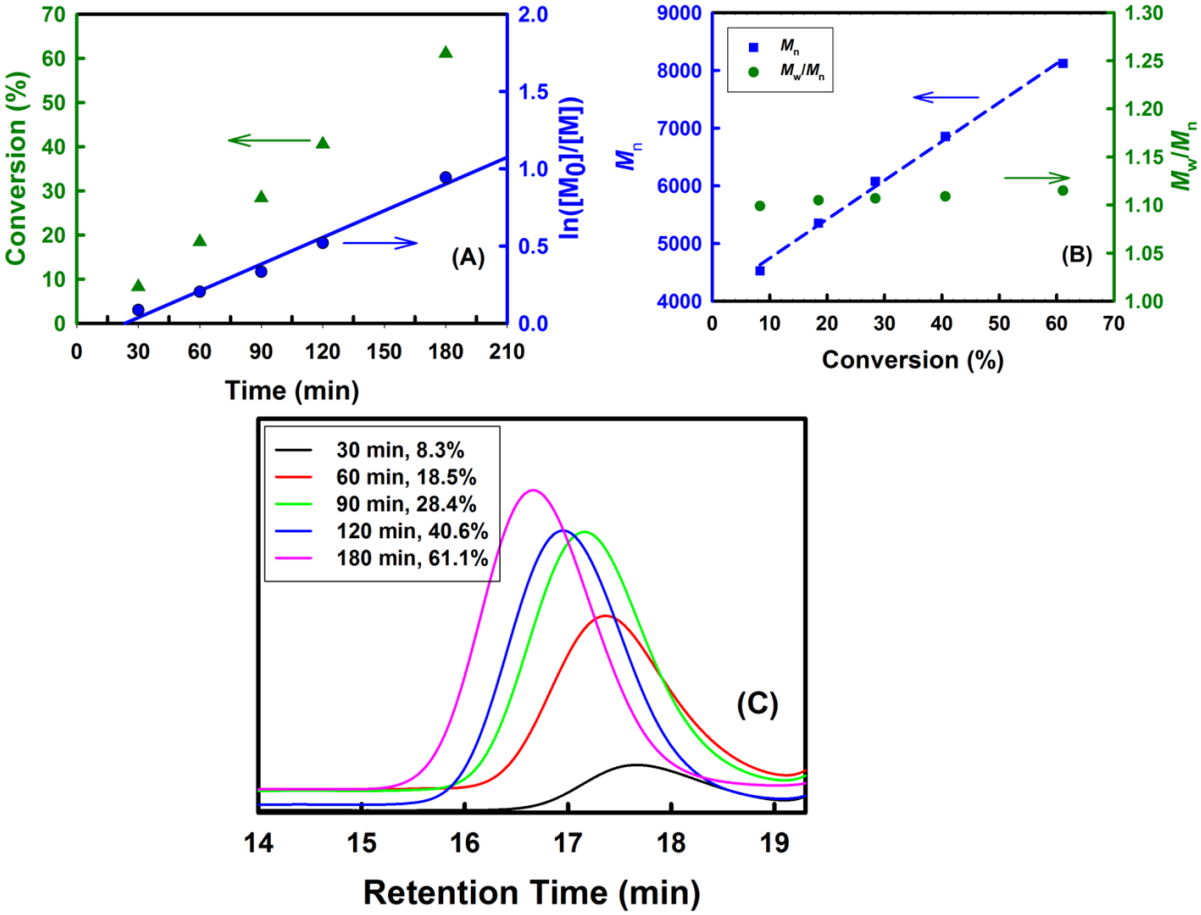


**Figure 2-1** RAFT polymerisation of PPEGMA RAFT-CTA. (A) Pseudo-first-order kinetic plot of the conversion of monomer to polymer. (B) Dependence of number average molecular weight ($M_n$, determined by GPC) and molar mass dispersity ($Đ_M$) on monomer conversion. (C) GPC traces during the polymerisation.

### 2.3.3 Synthesis of Star-like Polymers

PPEGMA of number-average molecular weight equal to 14,200 (by $^1$H NMR) was used as the macro-CTA for the synthesis of star-like polymers through chain extension with TFEA, DMAEMA and EDGMA at 70 $^o$C for 24 h. After polymerisation, the crude sample was collected by

precipitating the mixture into hexane. In Figure 2, a bimodal elution curve was obtained for the crude sample, with the major species eluting at a much shorter retention time compared to that of the macro-CTA, indicating the evolution from linear homopolymer to star-like polymer by the successful chain extension of PPEGMA macro-CTA.

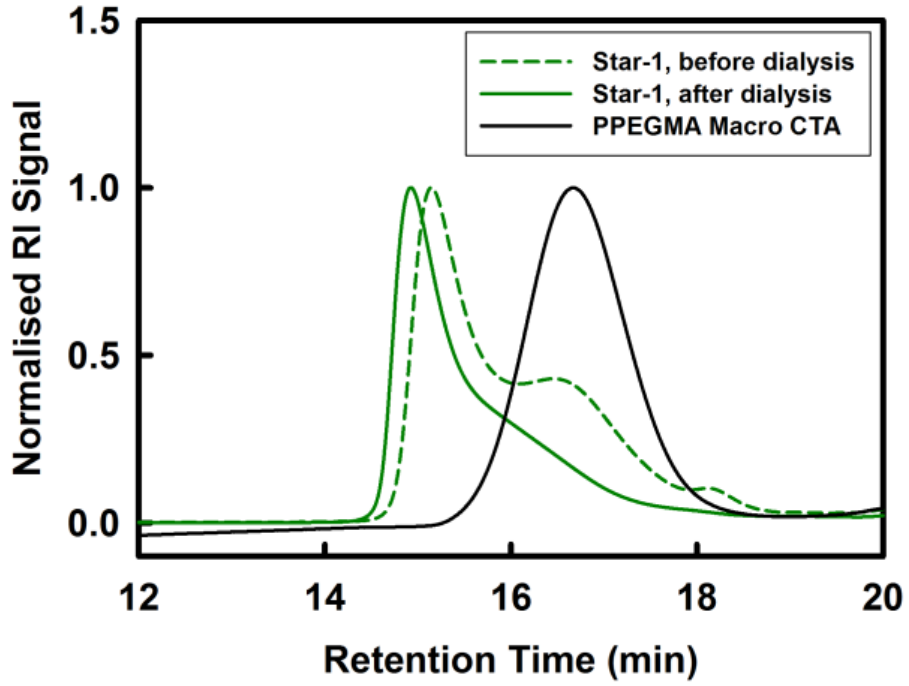


**Figure 2-2** GPC traces of the sample Star-1 before and after dialysis. [Macro-CTA]:[TFEA]:[DMAEMA]:[EGDMA]:[AIBN] = 1:4:28:8:0.2. Polymerised in THF at 70 $^{o}$C for 24 h, [monomer] = 0.5 M. See Appendix A Figure A2.3 for the GPC data of Star-2 and Star-3.

The star-like polymers were synthesised by an arm-first approach, and hence there may be linear chains remaining in the crude sample. This was confirmed by the observation of a shoulder peak at a retention time of 16.5 minutes in the GPC curve (dash line, Figure 2-2). In the synthesis of star polymers via the arm-first approach, the presence of linear residue precursors in the samples is unavoidable as some linear chains cannot be incorporated into the pre-formed hyperbranched cores due to steric hindrance during the formation of star-like polymers.[41] The crude polymers were further purified by extensive dialysis against water for 5 days using tubing with 100 kDa MWCO. After dialysis, most of the impurities having low molecular weights were removed, resulting in the purified star-like polymers having molar mass distributions of 1.5~1.6, as shown in Figure 2 and Table 2-1. This relatively broad molar mass distribution reveals that the samples are comprised of star-like polymers with cores of a range of degrees of branching, which is one characteristic of branched polymers synthesised using multi-functional monomers.[42-44] On the basis of the GPC

results, we conclude that star-like polymers were successfully synthesised through the chain extension of PPEGMA macro-CTA with TFEA, DMAEMA and EGDMA.

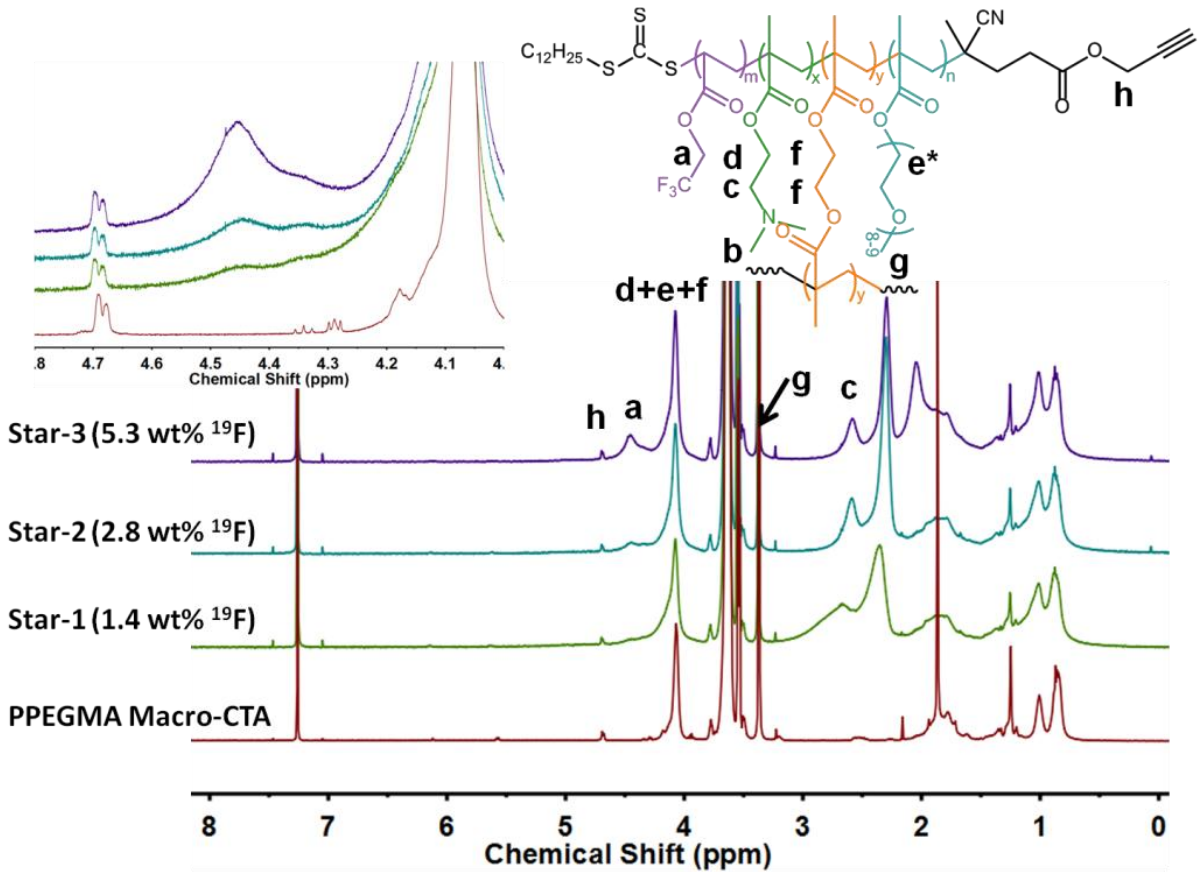


**Figure 2-3** $^{1}$H NMR spectra of the macro-CTA and star-like polymers in $CDCl_3$ at 25 $^{o}$C. (The letter 'e' represents the two protons of the $CH_2$ adjacent to the ester bond). The inset shows a magnification of the spectra between 4.0 and 4.8 ppm.

The as-synthesised star-like polymers with different TFEA molar fractions were characterised by $^{1}$H NMR (Figure 2-3). The characteristic peaks of TFEA (a) and DMAEMA (b, c, and d) are identified in the spectra, while they are absent in the spectrum of the macro-CTA, demonstrating the successful chain extension, in agreement with the GPC results. Star-like polymers with three different compositions were synthesised by varying the ratio of TFEA to DMAEMA, and the composition was determined by comparing ratios of the integrations of characteristic peaks of each monomer unit. As shown in the inset in Figure 2-3, the intensity of the peak for the protons of $CH_2$ adjacent to $CF_3$ becomes obviously stronger with an increase of TFEA in the feed. The fluorine content was from 1.4, to 5.3 wt% for the three star-like polymer samples. The detailed structural characteristics of the polymers are summarised in Table 2-1. As shown in Scheme 2-1, the as-

synthesised star-like polymers are expected to possess a hyperbranched core and PPEGMA arms. The branched core contains fluorinated units (TFEA) and pH-responsive (DMAEMA) monomers, thus it can be utilized to generate $^{19}$F NMR signals and will be pH-responsive. The PPEGMA bush polymer is hydrophilic and can shield the cytotoxic PDMAEMA component to enhance the biocompatibility of the nanoparticles.

**Table 2-1** Details of the structure of the star-like polymers.

| Sample | TFEA to DMAEMA Ratio[a] | $^{19}$F wt.%[a] | $M_n$ ($^1$H NMR)[a] | $M_n$ (RI)[b] | $Đ_M$[b] | $M_n$ (MALLS)[c] | $N_{arms}$[d] |
|---|---|---|---|---|---|---|---|
| PPEGMA | | - | 14,200 | 8,100 | 1.12 | - | - |
| Star-1 | 1:6.4 (1:7) | 1.4 | 20,500 | 18,000 | 1.6 | 225,000 | 11 |
| Star-2 | 1:3.5 (1:3) | 2.8 | 22,500 | 15,700 | 1.5 | 243,000 | 11 |
| Star-3 | 1:1.2 (1:1) | 5.3 | 21,400 | 13,800 | 1.5 | 76,000 | 3.6 |

[a] The experimental composition, fluorine content and $M_n$ of the samples were determined by $^1$H NMR. The feed ratios of TFEA to DMAEMA are provided in the brackets. [b] $M_n$ and molar mass distribution, $Đ_M$, were measured by GPC using RI detector and THF as eluent. [c] Absolute molecular weights were obtained using he GPC-MALLS technique. [d] The number of arms was calculated through the following equation: $N_{arms} = M_n$ (MALLS)/$M_n$ ($^1$H NMR), assuming that the hyperbranched structure was formed via intermolecular reaction of the linear chains rather than intramolecular reaction during the RAFT polymerisation.

### 2.3.4 Preparation and Properties of Nanoparticles of Star-like Polymer

Unlike block copolymer micelles that usually require a self-assembly process, water-soluble star polymers can readily form nanoparticles when dissolved in aqueous solution owning to the complex branched architecture in the cores and the presence of stabilizing PEGMA chains in the arms. This lack of a CMC is desirable for *in vivo* applications as it negates disassembly when the polymer concentration falls on dilution in the blood stream.[45]

Star-like polymer nanoparticles were formed by direct dissolution of the samples in PBS, and the morphology of the nanoparticles in solution was characterised by cryo-TEM. As shown in Figure 2-4, the nanoparticles exhibited spherical morphology with a diameter between 20 and 25 nm at pH 6, a size close to that reported from cryo-TEM images of a similar highly-branched polymer.[27] By contrast, only irregular particles with diameter of approximately 5 nm were observed at pH 9. This dramatic size change is attributed to the deprotonation and hence loss of charge of PDMAEMA units, which has a p*K*a of around 7.4-7.8.[46]

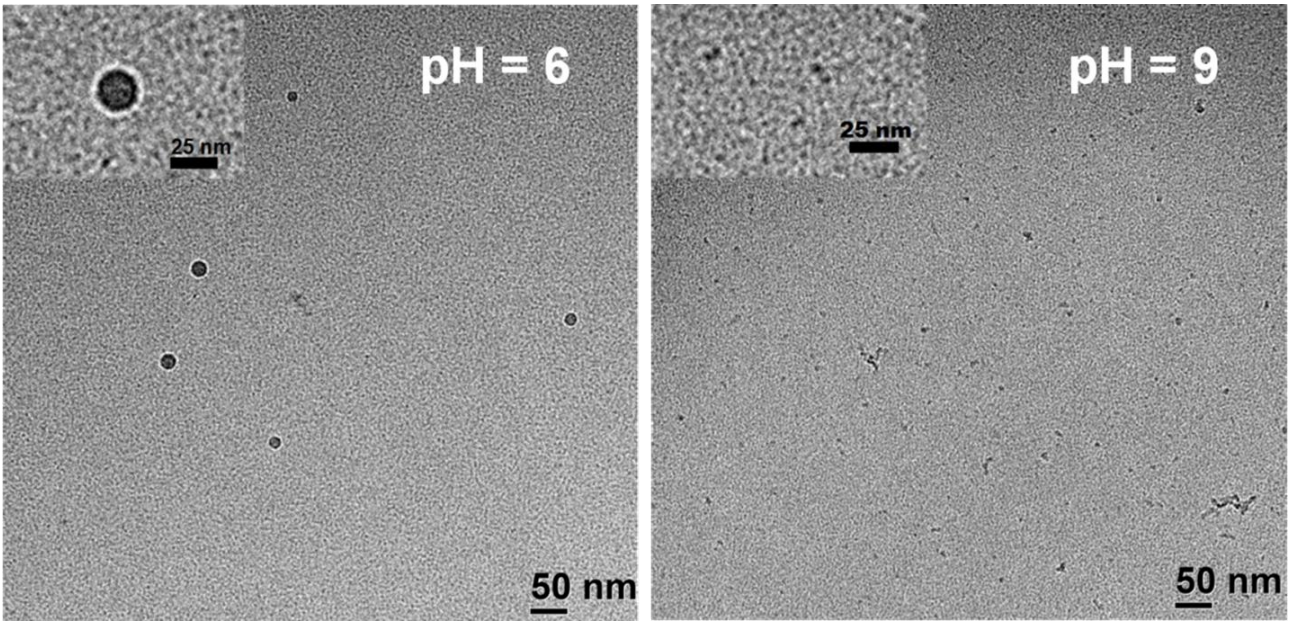


**Figure 2-4** Cryo-TEM images of frozen solutions of Star-1 at pH 6 and 9, respectively. Sample solutions were prepared by dissolving Star-1 in PBS (20 mg $mL^{-1}$).

When the environmental pH is below the p*K*a, the PDMAEMA chains tend to expand due to electrostatic repulsion between the charged chains (swollen state). In contrast, when the pH is above the p*K*a, the polymer chains are relatively compact (shrunken state). A number of previous studies on hyperbranched polymers containing PDMAEMA segments also demonstrated this dependence of polymer dimensions on the pH. [47-49]

These results demonstrate that nanoparticles with a branched core and PPEGMA shell were fabricated, and the particle size is highly dependent on the environmental pH, i.e. from 20-25 nm at pH 6 to approximately 10 nm at pH 9.

### 2.3.5 $^{19}$F NMR and MRI Studies

The $^{19}$F NMR of the star-like polymer nanoparticles was also investigated at a range of values of pH

from 4 to 9. The results of these measurements are displayed in Figure 2-5 (A). A major peak was observed at around -72.7 ppm, due to $^{19}F$ nuclei in the branched core of the particles, while the small peak at -76.6 ppm of very low intensity (<< 1%) can be assigned to residual fluorinated compounds (including monomer) in the sample. In Figure 2-5 (B), the intensity and width of the major peaks remained almost constant when the pH of the solution was below 7.4. However, this peak became broader and less intense when the pH was increased to above 7.4. This behaviour is clearly revealed in the magnified and superimposed spectrum (Figure 2-5 (C) and (D)). Based on these results, it can be concluded that the $^{19}F$ signal intensity is heavily dependent on the pH of the aqueous solution.

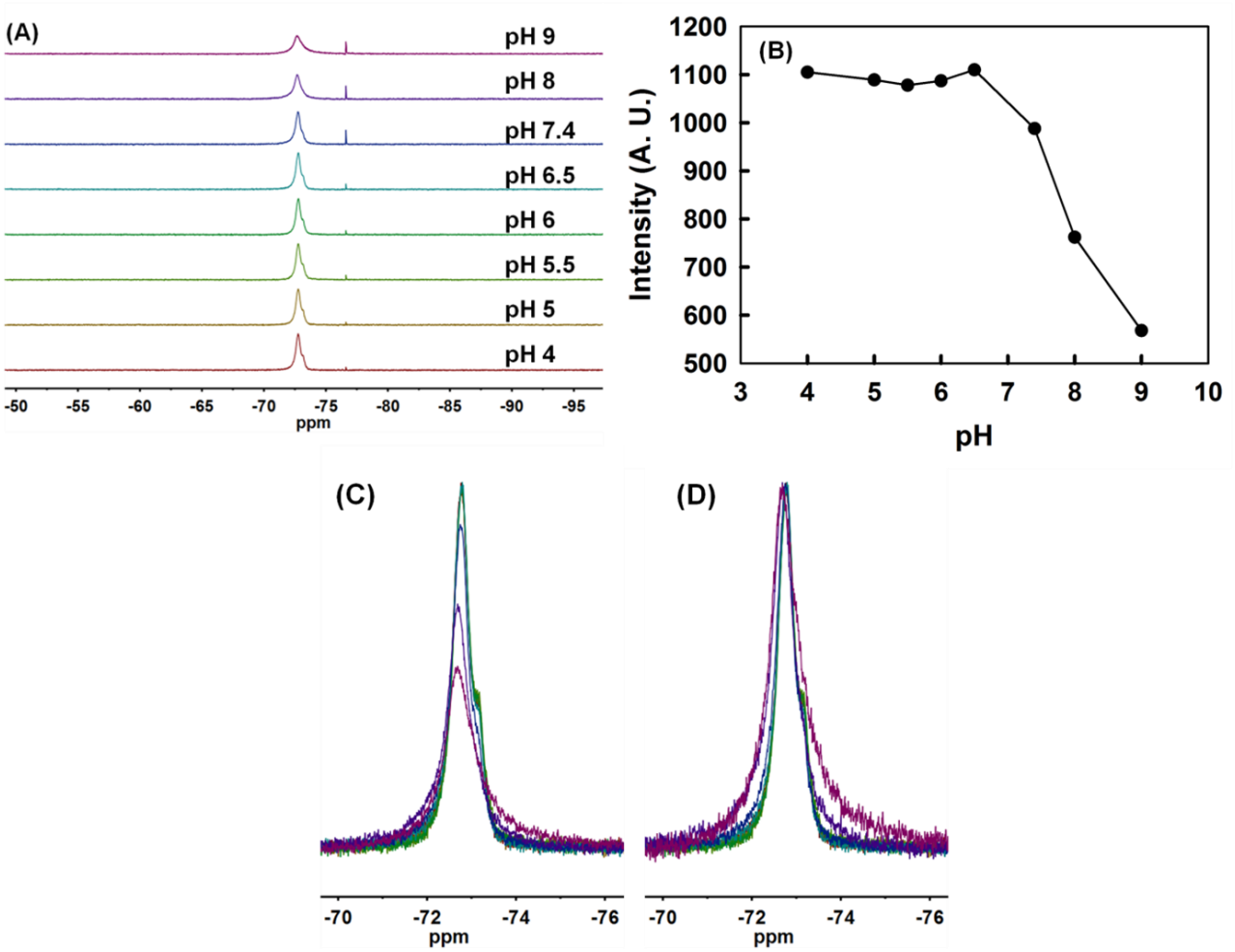


**Figure 2-5** $^{19}F$ NMR results for solutions of Star-1. (A) Stacked $^{19}F$ NMR spectra of Star-1 in PBS at different values of pH. (B) The dependence of integrated peak intensity on pH. (C) Superimposed $^{19}F$ NMR spectra of Star-1. (D) Superimposed and normalised $^{19}F$ NMR spectra of Star-1. Samples were dissolved in $H_2O/D_2O$ (90/10, v/v) at 20 mg $mL^{-1}$ for all $^{19}F$ NMR measurements.

According to Equation (2-1), the $^{19}F$ MR imaging performance depends on the number of $^{19}F$

nuclei (which remains constant) and the relaxation times ($T_1$ and $T_2$). These last two properties were measured by $^{19}$F NMR. As demonstrated previously,[11] long values of the transverse relaxation time, $T_2$, are required for acquiring images with good signal-to-noise ratio, while a short $T_1$ can reduce the MRI scan time. The $T_2$ relaxation times of the three star-like polymers were first measured at pH 5. As presented in Figure 2-6, Star-2 and Star-3 had measured values of $T_2$ of 15.7 and 13.0 ms, respectively, whereas Star-1 had a $T_2$ of 38.8 ms. We suggest that the relatively short $T_2$ of Star-2 and Star-3 can be attributed to the comparatively high $^{19}$F content, so that the probability of association of hydrophobic $^{19}$F segments in aqueous solution increased, resulting in reduced mobility of the fluorinated segments. In Figure 2-6, the $T_2$ of Star-1 was found to be highly dependent on pH and showed the same trend with pH as the NMR intensity. In contrast, the $T_1$ relaxation time was almost constant at approximately 450 ms, irrespective of pH. This indicates that the spectral density of motions in the 500 MHz frequency range was not affected by the change in polymer conformation. Previous studies of block copolymer micelles also showed that the $T_1$ relaxation time was less sensitive to changes in packing and conformation.[12]

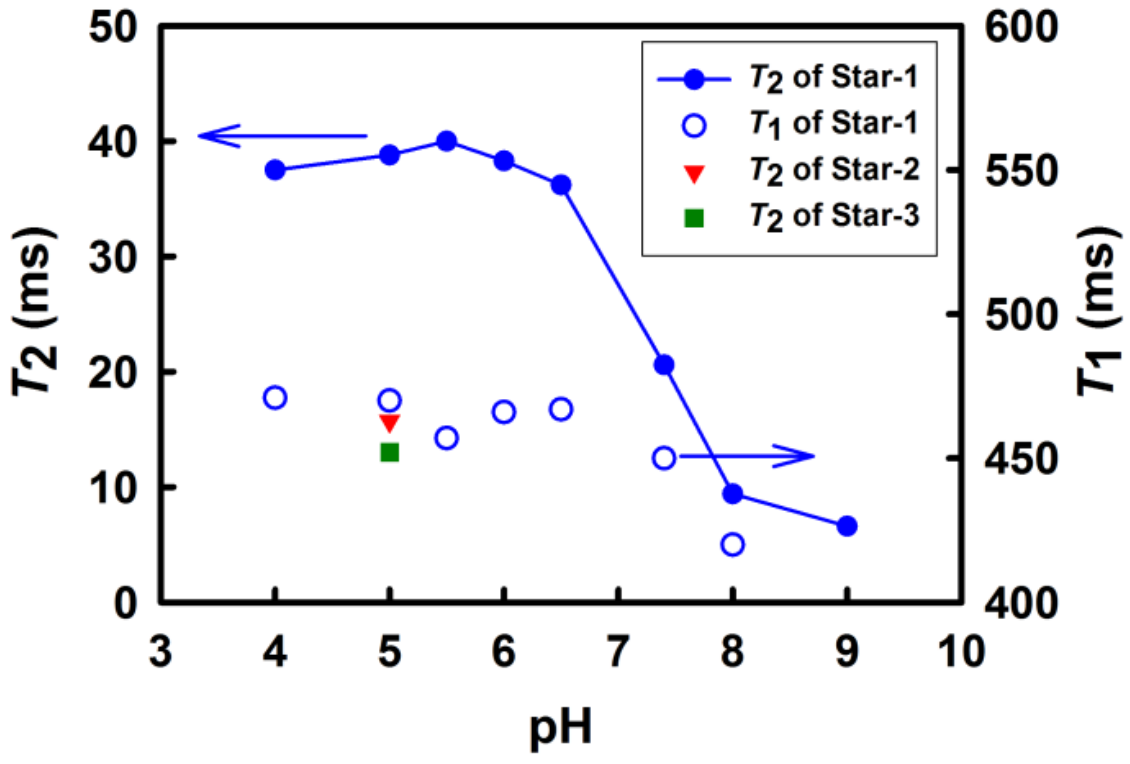


**Figure 2-6** Spin-lattice ($T_1$) and spin-spin ($T_2$) relaxation times of the star-like polymer nanoparticles in PBS at different values of pH.

The pH-responsiveness of $T_2$ can be utilized for the design of $^{19}$F MRI agents for the diagnosis of cancer diseases. The star-like polymer nanoparticles are expected to provide a weak $^{19}$F MR signal

at physiological pH of 7.4. However, tumour tissue has been reported to be more acidic than normal tissue, with an extracellular pH of 6.8-7.2.[50] Furthermore if these nanoparticles can be delivered and internalised by the target cells, the lysosomes exhibit a pH as low as 4.5[51] and a large change in NMR properties will be expected.

The potential of these molecules as imaging agents was demonstrated by $^{19}$F MRI of solutions of the three polymers in solutions of pH values equal to 6 and 9. In Figure 2-7, the $^{19}$F images (A) are on the left, and the $^{1}$H density images (B) of the same set of aqueous samples are displayed on the right to illustrate the location of the NMR tubes within the resonator. A very clear increase in intensity can be seen for all three star-like polymers in the acidic media. This is consistent with the dramatic change in spin-spin relaxation time reported in Figure 6 for one of the polymers, which in turn arises from the change in the dimensions of the hyperbranched core on change of pH. We conclude therefore that these star-like polymer nanoparticles have the potential to be applied as selective agents for the detection of changes in local pH *in vivo* as well as the identification of tumour tissue using whole body $^{19}$F MRI.

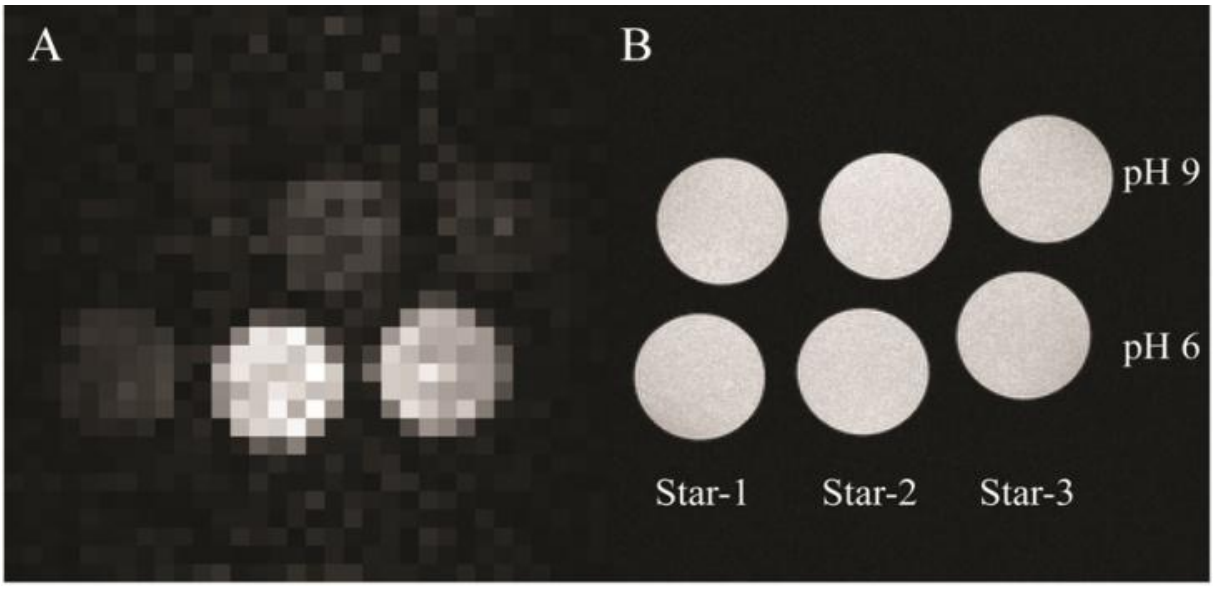


**Figure 2-7** (A) $^{19}$F image of 20 mg mL$^{-1}$ solutions of the star-like polymers in PBS acquired using a spin-echo sequence (TR = 1000 ms, TE = 6.2 ms, NEX = 1024, MTX = 32 × 32 × 1, FOV = 30 × 30 × 20 mm). The difference in signal intensity between polymers at pH 6 and pH 9 can clearly be seen. (B) $^{1}$H FLASH image used for localisation of the field of view.

## 2.4 Conclusions

In summary, a well-defined PPEGMA macro-CTA was synthesised through RAFT polymerisation. Subsequently, pH-responsive and $^{19}$F-containing star-like polymers were prepared through chain extension of the macro-CTA. The polymer nanoparticles consisted of a hyperbranched core and hydrophilic PPEGMA arms. Nanoparticles were formed by dissolving the star-like polymers in aqueous solution, and the particle size was found to be highly dependent on the pH. $^{19}$F NMR showed that the $T_2$ relaxation time was strongly related to both the $^{19}$F content and the pH of the polymer solution. A strong $^{19}$F signal and long $T_2$ were only observed under acidic conditions (pH values below 6.5), as a result of enhanced mobility of fluorinated segments. Above the p*K*a, the $T_2$ relaxation time was significantly reduced. Preliminary $^{19}$F MRI measurements of the particles in solution also show a strong dependence of imaging performance on pH and therefore demonstrate the potential for these star-like polymer nanoparticles as contrast agents for selective $^{19}$F MRI in the diagnosis of cancer tissue.

## 2.5 References


1. M. Bottrill, L. K. Nicholas and N. J. Long, *Chem Soc Rev*, 2006, **35**, 557-571.
2. A. M. Mohs and Z. R. Lu, *Expert Opin Drug Del*, 2007, **4**, 149-164.
3. K. Pinker, A. Stadlbauer, W. Bogner, S. Gruber and T. H. Helbich, *Eur J Radiol*, 2012, **81**, 566-577.
4. J. F. Dechent, L. Buljubasich, L. M. Schreiber, H. W. Spiess and K. Munnemann, *Phys Chem Chem Phys*, 2012, **14**, 2346-2352.
5. G. N. Holland, P. A. Bottomley and W. S. Hinshaw, *J Magn Reson*, 1977, **28**, 133-136.
6. M. Srinivas, A. Heerschap, E. T. Ahrens, C. G. Figdor and I. J. M. de Vries, *Trends Biotechnol*, 2010, **28**, 363-370.
7. W. Wolf, C. A. Presant and V. Waluch, *Adv Drug Deliver Rev*, 2000, **41**, 55-74.
8. J. Ruiz-Cabello, B. P. Barnett, P. A. Bottomley and J. W. Bulte, *Nmr Biomed*, 2011, **24**, 114-129.
9. J. C. Knight, P. G. Edwards and S. J. Paisey, *Rsc Adv*, 2011, **1**, 1415-1425.
10. S. Rossi, M. Benaglia, M. Ortenzi, E. Micotti, C. Perego and M. G. De Simoni, *Tetrahedron Lett*, 2011, **52**, 6581-6583.
11. L. Nurmi, H. Peng, J. Seppala, D. M. Haddleton, I. Blakey and A. K. Whittaker, *Polym Chem*, 2010, **1**, 1039-1047.

12. H. Peng, I. Blakey, B. Dargaville, F. Rasoul, S. Rose and A. K. Whittaker, *Biomacromolecules*, 2009, **10**, 374-381.
13. J. M. Janjic, M. Srinivas, D. K. K. Kadayakkara and E. T. Ahrens, *J Am Chem Soc*, 2008, **130**, 2832-2841.
14. M. Oishi, S. Sumitani and Y. Nagasaki, *Bioconjugate Chem*, 2007, **18**, 1379-1382.
15. M. M. Bailey, C. M. Mahoney, K. E. Dempah, J. M. Davis, M. L. Becker, S. Khondee, E. J. Munson and C. Berkland, *Macromol Rapid Comm*, 2010, **31**, 87-92.
16. M. Ogawa, S. Nitahara, H. Aoki, S. Ito, M. Narazaki and T. Matsuda, *Macromol Chem Phys*, 2010, **211**, 1369-1376.
17. M. Ogawa, S. Nitahara, H. Aoki, S. Ito, M. Narazaki and T. Matsuda, *Macromol Chem Phys*, 2010, **211**, 1602-1609.
18. J. M. Criscione, B. L. Le, E. Stern, M. Brennan, C. Rahner, X. Papademetris and T. M. Fahmy, *Biomaterials*, 2009, **30**, 3946-3955.
19. M. Ogawa, H. Kataoka, S. Nitahara, H. Fujimoto, H. Aoki, S. Ito, M. Narazaki and T. Matsuda, *B Chem Soc Jpn*, 2012, **85**, 79-86.
20. W. J. Du, Z. Q. Xu, A. M. Nystrom, K. Zhang, J. R. Leonard and K. L. Wooley, *Bioconjugate Chem*, 2008, **19**, 2492-2498.
21. W. J. Du, A. M. Nystrom, L. Zhang, K. T. Powell, Y. L. Li, C. Cheng, S. A. Wickline and K. L. Wooley, *Biomacromolecules*, 2008, **9**, 2826-2833.
22. K. J. Thurecht, I. Blakey, H. Peng, O. Squires, S. Hsu, C. Alexander and A. K. Whittaker, *J Am Chem Soc*, 2010, **132**, 5336-5337.
23. K. Mizusawa, Y. Ishida, Y. Takaoka, M. Miyagawa, S. Tsukiji and I. Hamachi, *J Am Chem Soc*, 2010, **132**, 7291-7293.
24. Y. Takaoka, T. Sakamoto, S. Tsukiji, M. Narazaki, T. Matsuda, H. Tochio, M. Shirakawa and I. Hamachi, *Nat Chem*, 2009, **1**, 557-561.
25. X. J. Ju, R. Xie, L. H. Yang and L. Y. Chu, *Expert Opin Ther Pat*, 2009, **19**, 683-696.
26. S. Dai, P. Ravi and K. C. Tam, *Soft Matter*, 2008, **4**, 435-449.
27. J. H. Tan, N. A. J. McMillan, E. Payne, C. Alexander, F. Heath, A. K. Whittaker and K. J. Thurecht, *J Polym Sci Pol Chem*, 2012, **50**, 2585-2595.
28. G. Moad, Y. K. Chong, A. Postma, E. Rizzardo and S. H. Thang, *Polymer*, 2005, **46**, 8458-8468.
29. S. H. Thang, Y. K. Chong, R. T. A. Mayadunne, G. Moad and E. Rizzardo, *Tetrahedron Lett*, 1999, **40**, 2435-2438.
30. R. E. Hendrick, *Magn Reson Imaging*, 1987, **5**, 31-37.

31. H. Peng, K. J. Thurecht, I. Blakey, E. Taran and A. K. Whittaker, *Macromolecules*, 2012, **45**, 8681-8690.
32. V. T. Huynh, P. de Souza and M. H. Stenzel, *Macromolecules*, 2011, **44**, 7888-7900.
33. H. Y. Cho, A. Srinivasan, J. Hong, E. Hsu, S. G. Liu, A. Shrivats, D. Kwak, A. K. Bohaty, H. J. Paik, J. O. Hollinger and K. Matyjaszewski, *Biomacromolecules*, 2011, **12**, 3478-3486.
34. A. H. Soeriyadi, G. Z. Li, S. Slavin, M. W. Jones, C. M. Amos, C. R. Becer, M. R. Whittaker, D. M. Haddleton, C. Boyer and T. P. Davis, *Polym Chem*, 2011, **2**, 815-822.
35. M. C. R. Tria, C. D. T. Grande, R. R. Ponnapati and R. C. Advincula, *Biomacromolecules*, 2010, **11**, 3422-3431.
36. Z. Zarafshani, T. Obata and J. F. Lutz, *Biomacromolecules*, 2010, **11**, 2130-2135.
37. J. P. Magnusson, S. Bersani, S. Salmaso, C. Alexander and P. Caliceti, *Bioconjugate Chem*, 2010, **21**, 671-678.
38. G. Moad, E. Rizzardo and S. H. Thang, *Polymer*, 2008, **49**, 1079-1131.
39. Y. K. Chong, J. Krstina, T. P. T. Le, G. Moad, A. Postma, E. Rizzardo and S. H. Thang, *Macromolecules*, 2003, **36**, 2256-2272.
40. G. Moad, E. Rizzardo and S. H. Thang, *Accounts Chem Res*, 2008, **41**, 1133-1142.
41. A. Blencowe, J. F. Tan, T. K. Goh and G. G. Qiao, *Polymer*, 2009, **50**, 5-32.
42. H. J. Yang, B. B. Jiang, W. Y. Huang, D. L. Zhang, L. Z. Kong, J. H. Chen, C. L. Liu, F. H. Gong, Q. Yu and Y. Yang, *Macromolecules*, 2009, **42**, 5976-5982.
43. B. L. Liu, A. Kazlauciunas, J. T. Guthrie and S. Perrier, *Macromolecules*, 2005, **38**, 2131-2136.
44. M. Semsarilar, V. Ladmiral and S. Perrier, *Macromolecules*, 2010, **43**, 1438-1443.
45. R. Trivedi and U. B. Kompella, *Nanomedicine*, 2010, **5**, 485-505.
46. P. van de Wetering, N. J. Zuidam, M. J. van Steenbergen, O. A. G. J. van der Houwen, W. J. M. Underberg and W. E. Hennink, *Macromolecules*, 1998, **31**, 8063-8068.
47. S. Z. Luo, M. C. Han, Y. H. Cao, C. X. Ling and Y. Y. Zhang, *Colloid Polym Sci*, 2011, **289**, 1243-1251.
48. J. H. Zhou, L. Wang, J. Z. Ma, J. J. Wang, H. J. Yu and A. G. Xiao, *Eur Polym J*, 2010, **46**, 1288-1298.
49. T. He, F. Di Lena, K. C. Neo and C. L. L. Chai, *Soft Matter*, 2011, **7**, 3358-3365.
50. L. E. Gerweck and K. Seetharaman, *Cancer Res*, 1996, **56**, 1194-1198.
51. S. Ganta, H. Devalapally, A. Shahiwala and M. Amiji, *J Control Release*, 2008, **126**, 187-204.

# Chapter 3

# Biodegradable Core Crosslinked Star Polymers for Selective F-19 MRI

In Chapter 2, star-like polymers were synthesised and evaluated as pH-responsive contrast agents for $^{19}$F MRI. In those polymers, the $^{19}$F nuclei were dispersed within a 3D hyperbranched core that was shielded by hydrophilic PEG brushes. The $^{19}$F signal intensity was highly dependent on the solution pH owing to the presence of pH-responsive PDMAEMA segments in the core. We hypothesise that the $^{19}$F NMR properties could also be affected by the spatial structure in which the $^{19}$F nuclei are positioned. In this chapter, star polymers with a densely crosslinked core and partly-fluorinated arms were designed and examined as pH-responsive contrast agents for $^{19}$F MRI. Compared with the star-like polymers in Chapter 2, the major difference is that the fluorine units are incorporated in the arms instead of the star core. Such a difference is expected to influence the $^{19}$F MRI performance.

## 3.1 Introduction

Magnetic resonance imaging (MRI), a commonly-used diagnostic modality, has proven to be an indispensable imaging technique since its first appearance in the early 1970s. Unlike other imaging procedures, in particular X-ray computed tomography (CT), MRI does not utilise ionizing radiation during image acquisition, and is therefore non-harmful to humans. $^{1}$H MRI in particular can provide spatial anatomical images with high quality and resolution, with contrast arising from differences in proton density and relaxation parameters. However, $^{1}$H MRI is intrinsically restricted by two factors. First, the abundant water molecules in the body generate strong background signals that make detection of small concentrations of particular tissue types or metabolites difficult. Secondly, the proton relaxation times in different tissues are often similar, resulting in poor image contrast.[1] To address these issues, tremendous effort have been devoted to the development of $^{1}$H MRI contrast agents. The principle classes of $^{1}$H MRI contrast agents include gadolinium-based chelates,[2-4] superparamagnetic iron oxide nanoparticles,[5, 6] manganese-based contrast agents,[7-11] and other lanthanide-based contrast agents.[12, 13] An alternative approach to improving image contrast is to consider other NMR-active nuclei, and $^{19}$F MRI has been considered to be an excellent option.

Shortly after the appearance of $^{1}$H MRI, the first example of $^{19}$F MRI was reported in 1977.[14] Compared to other candidates, such as $^{13}$C, $^{15}$N and $^{31}$P, the $^{19}$F nucleus exhibits a number of attractive properties, e.g. 100% natural abundance, high sensitivity (83% relative to $^{1}$H), large gyromagnetic ratio (40.03 MHz $T^{-1}$, 94% relative to $^{1}$H), and absence in the human body.[15-17] The physiological rarity of mobile fluorine nuclei in the body guarantees essentially no background signal during imaging and highlights the distinctive advantage of $^{19}$F MRI. $^{19}$F MRI naturally relies on the use of $^{19}$F-containing contrast agents, and a high concentration of $^{19}$F nuclei is preferred in the target voxel to provide adequate signal for the acquisition of good quality images. During the past few decades, perfluorocarbons (PFCs) have been extensively exploited as $^{19}$F MRI contrast agents because of their high fluorine content as well as chemical and biological inertness.[17-19] Due to their hydrophobicity, PFCs are normally formulated as emulsions for biological applications. Although a few PFC emulsions are commercially available for clinical use, this category of contrast agents has several drawbacks, such as emulsion stability, limited methods of functionalisation and long reticuloendothelial system (RES) clearance times.[20-22]

Recently, $^{19}$F MRI contrast agents based on polymers have been introduced by a number of groups. Several classes of polymeric agents have been developed and evaluated, including linear polymers,[23-28] hyperbranched polymers,[29, 30] dendrimers[31-34] and nanogels.[35] In Chapter 2, we suggested that polymeric $^{19}$F MRI agents should fulfil a list of criteria, i.e. high fluorine content, separation of fluorine segments, small particle size, low cytotoxicity and possibility for chemical modification of conjugation.[24, 25, 30] We are particularly interested in polymeric contrast agents that have highly-branched structures because these polymers have the potential to fulfil the aforementioned requirements. In these molecules, a high concentration of highly separated fluorine segments retains high flexibility, resulting in efficient averaging of the dipolar coupling and therefore ensures strong signal intensity in $^{19}$F MRI. On the other hand, the abundant functional groups in the polymers are especially favourable for subsequent functionalisation for specific applications.

In recent years ‘smart’ imaging agents, which are responsive to certain environmental conditions (pH, temperature, light, ionic strength, the presence of enzymes, redox potential, etc.), have elicited great scientific interest.[36-42] In particular it is well known that compared to normal tissues, cancerous tissues have a slightly acidic extracellular pH (6.7-7.1),[43] hence it has been suggested that they may be detected through selective imaging using contrast agents that can be triggered by a change in pH. The development of pH-responsive imaging agents has become an intensive research

field, and a variety of such imaging agents have been fabricated and show great potential for the early diagnosis of cancer diseases.[34, 44-50].

Core crosslinked (CCS) star polymers, which are composed of a number of arms and a crosslinker core, have a spherical 3D structure and possess unique properties. In the past several years, CCS star polymers synthesised by reversible-deactivation radical polymerisation (also referred to as controlled radical polymerisation) via the arm-first approach have been studied in detail.[51] Synthesis of CCS polymers via the arm-first method allows for the precise pre-design of arm precursors and can thus lead to star polymers with well-defined structures and compositions. In our previous study, star polymers with a branched core (composed of $^{19}$F-containing and pH-responsive units) and hydrophilic arms were prepared and utilised as selective $^{19}$F MRI contrast agents with the potential for the detection of diseased tissues.[52] Although a number of branched polymers bearing $^{19}$F nuclei have been developed as $^{19}$F MRI contrast agents, to the best of our knowledge, CCS polymers with fluorinated units in the arms have not been reported as $^{19}$F MRI agents. In this chapter we investigate the effect of placement of $^{19}$F nuclei and pH-responsive units in the block copolymer arms instead of in the branched core.

In this study, we aim to synthesise core crosslinked star (CCS) polymers as $^{19}$F MRI contrast agents via the arm-first approach by reversible addition-fragmentation chain transfer (RAFT) polymerisation. As illustrated in Scheme 3-1, the arms are block copolymers that contain 2,2,2-trifluoroethyl methacrylate (TFEMA) units to provide $^{19}$F NMR and MRI signal and 2-(dimethylamino)ethyl methacrylate (DMAEMA) segments to achieve pH-responsiveness. In addition, the cores are comprised of bis(2-methacryloyl)oxyethyl disulfide (DSDMA) crosslinked homopolymer, which is degradable in the presence of reducing agents. It is expected that the protonation and deprotonation of DMAEMA units in the copolymer arms in aqueous solution will not only influence the size of the nanoparticles but also alter the mobility of $^{19}$F nuclei in the TFEMA segments, resulting in the variations in signal intensity and relaxation times of $^{19}$F nuclei with pH. Moreover, selective imaging can be realised in $^{19}$F MRI by utilising the pH-responsiveness of the $^{19}$F relaxation times. Last but not least, since the CCS polymers have abundant disulfide bonds in the crosslinked core, the as-formed nanoparticles can be degraded by reducing agents such as dithiothreitol (DTT), tris(2-carboxyethyl)phosphine hydrochloride (TCEP) and glutathione (GSH),[53-55] and this biodegradability is especially desirable for future *in vivo* applications.

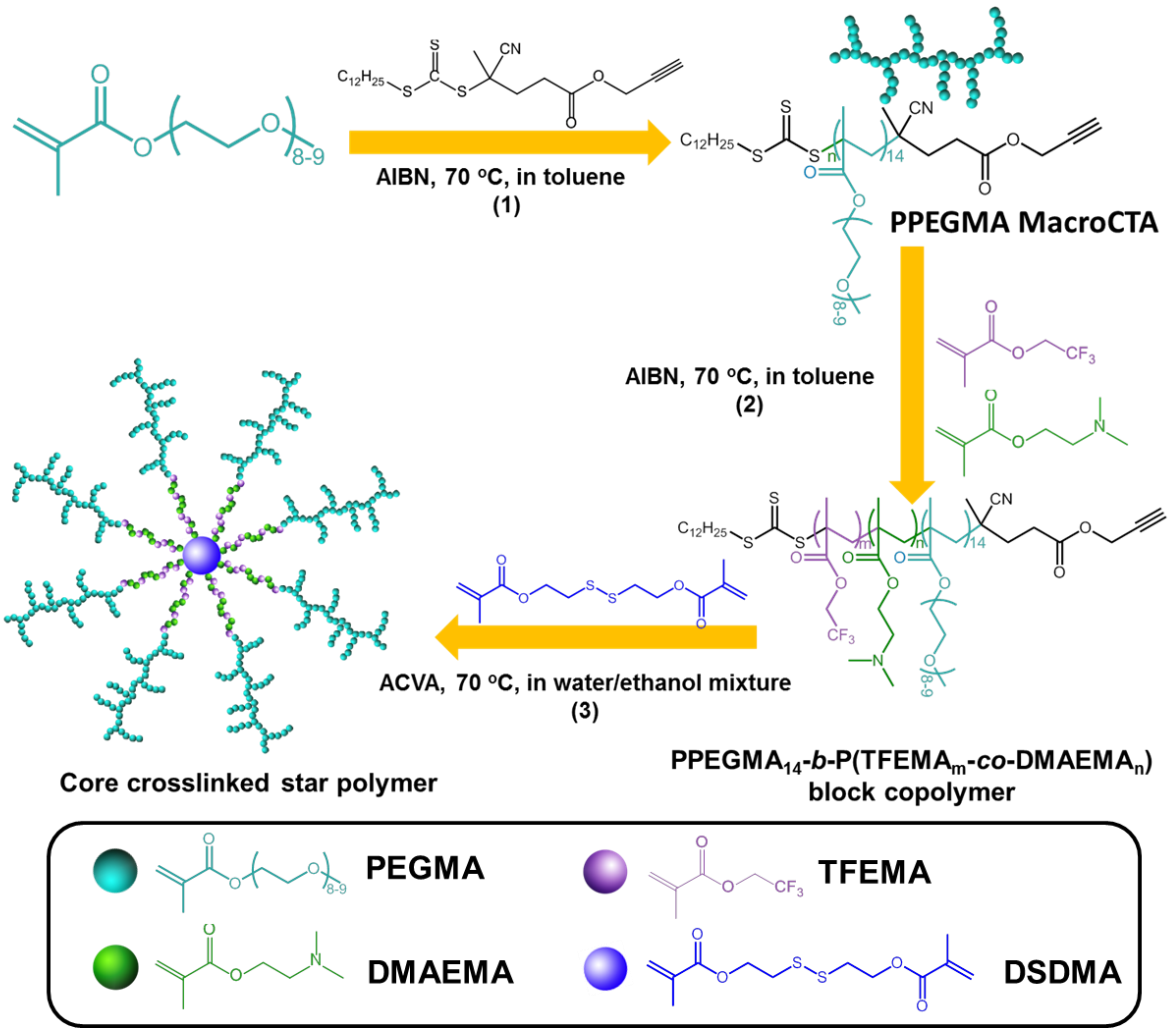


**Scheme 3-1** Schematic illustration of the synthesis of CCS polymers.

## 3.2 Experimental Section

### 3.2.1 Materials

All chemicals were purchased from Sigma-Aldrich unless otherwise stated. Poly(ethylene glycol) methyl ether methacrylate (PEGMA, *M*W = 475), 2-(dimethylamino)ethyl methacrylate (DMAEMA), 2,2,2-trifluoroethyl methacrylate (TFEMA), ethylene glycol dimethacrylate (EGDMA), butyl methacrylate (BMA) and 2-hydroxyethyl methacrylate (HEMA) were passed through basic alumina columns to remove inhibitors prior to use. The initiators, 2,2'-azobis(2-methylpropionitrile) (AIBN) and 4,4'-azobis(4-cyanovaleric acid) (ACVA) were recrystallised from ethanol twice before use. 4-Methoxyphenol (MEHQ), 4-(dimethylamino)pyridine (DMAP), triethylamine (TEA), N,N'-dicyclohexylcarbodiimide (DCC), tris(2-carboxyethyl)phosphine

hydrochloride (TCEP) and L-glutathione reduced (GSH) were used as received. The trithiocarbonate RAFT agent, 4-cyano-4-(dodecylsulfanylthiocarbonyl)sulfanyl pentanoic acid (denoted as CTA), was synthesised following a previously reported method.[56] Milli-Q water with a resistivity of 18.4 $M\Omega.cm^{-1}$ was used for the synthesis and purification of polymers and preparation of aqueous solutions. Tetrahydrofuran (THF), dichloromethane (DCM) and toluene were obtained from a solvent purification system (SPS) and used directly.

## 3.2.2 Synthesis

### 3.2.2.1 Synthesis of Alkyne-Terminated Chain Transfer Agent (alkyne-CTA)

The CTA (4.04 g, 10 mmol), propargyl alcohol (1.46 mL, 25 mmol) and DMAP (0.24 g, 2 mmol) were dissolved in 130 mL of DCM in a 250 mL flask, which was sealed with a rubber septum and then bubbled with argon for 30 min in an ice bath. Following this, DCC (4.13 g, 20 mmol) in 20 mL of DCM was injected dropwise into the flask. The reaction was kept in the ice bath and magnetically stirred for 2 h, followed by stirring at room temperature for 48 h. After the reaction, the mixture was filtered to remove the insoluble dicyclohexylurea precipitate. The filtrate was washed with water (100 mL × 2) and brine (100 mL × 2), and then dried over anhydrous $MgSO_4$. Finally, the solvent was removed by rotary evaporation, and the residual oil was further purified by flash column chromatography ($SiO_2$, gradient petroleum spirit/ethyl acetate, from 9/1 to 8/2), yielding a scarlet oil (3.7 g, 84% yield). $^1$H NMR (500 MHz, $\delta$, ppm, $CDCl_3$): 0.88 (t, 3H, $C\underline{H}_3CH_2CH_2$), 1.26 (br s, 18H, $(CH_2)_9$), 1.69 (m, 2H, $C\underline{H}_2CH_2S$), 1.87 (s, 3H, $C\underline{H}_3$), 2.37-2.70 (m, 4H, $C\underline{H}_2C\underline{H}_2$-COO), 2.49 (t, H, $OCH_2C{\equiv}C\underline{H}$), 3.32 (t, 3H, $CH_2C\underline{H}_2S$), 4.70 (d, 2H, $OC\underline{H}_2C{\equiv}CH$). $^{13}$C NMR (125 MHz, δ, ppm, $CDCl_3$): 170.63 ($\mathit{C}OOCH_2$), 118.87 ($\mathit{C}N$), 75.20 ($\mathit{C}{\equiv}CH$), 52.41(C≡$\underline{C}$H), 46.21 ($\underline{C}(CH_3)CN$)), 37.03 ($C(=O)CH_2\underline{C}H_2$), 33.62 ($C(=O)\underline{C}H_2CH_2$), 31.85, 29.56, 27.61, 24.81, 22.63 (overlapping $^{13}$C signals), 14.07 ($\underline{C}H_3CH_2CH_2$).

### 3.2.2.2 Synthesis of Poly PPEGMA macro-CTA

PEGMA (24 g, 50 mmol), alkyne-CTA (0.886 g, 2 mmol), AIBN (66 mg, 0.4 mmol) were dissolved in 50 mL of toluene in a 100 mL flask, which was sealed with a rubber septum and bubbled with argon for 1 h in an ice bath. Then the flask was immersed in an oil bath maintained at 70 $^{o}$C and magnetically stirred. At given intervals, samples were withdrawn using a gas-tight syringe for measurement of extent of conversion. After 180 min, the polymerisation was quenched by cooling the flask in an ice bath and exposing the solution to air. The crude solution was

precipitated into cold hexane 3 times and then dialysed against water for 2 days. After lyophilisation, a yellow oil was obtained. Yield: 11 g, 94%). GPC: $M_n$ = 7200, molar mass dispersity ($Đ_M$, $M_w/M_n$) = 1.12. $^1$H NMR: DP = 14, $M_n$ = 7100.

### 3.2.2.3 Synthesis of PPEGMA-b-P(TFEMA-co-DMAEMA) Block Copolymers

In a typical experiment, the macro-CTA (0.665 g, 0.094 mmol), TFEMA (0.144 mL, 1 mmol), DMAEMA (0.674 mL, 4 mmol) and AIBN (3.3 mg, 0.02 mmol) were dissolved in 4 mL of toluene. The solution was equally divided into 5 tubes, each of which was purged with nitrogen for 5 min in an ice bath before being placed in a 70 $^o$C oil bath. The tubes were opened and cooled to 0 $^o$C at various time intervals to allow measurement of conversion.

For the fully scaled-up synthesis, the macro-CTA (3.6 g, 0.51 mmol), TFEMA (0.771 mL, 5.4 mmol), DMAEMA (3.649 mL, 21.6 mmol) and AIBN (17.8 mg, 0.102 mmol) were dissolved in 22 mL of toluene in a 100 mL flask, which was sealed with a rubber septum and purged with nitrogen for 30 min in an ice bath. The flask was placed in a 70 $^o$C oil bath for 2.5 h, followed by being cooled to 0 $^o$C and exposed to air. The sample was purified by precipitation into cold hexane 3 times and dried under vacuum. A yellowish viscous solid was obtained. Yield: 4.86 g, 86%. The degree of polymerisation (DP) was calculated from $^1$H NMR, and the composition of the block copolymer was confirmed to be $PPEGMA_{14}$-b-($TFEMA_5$-co-$DMAEMA_{19}$) (10500 by $^1$H NMR), $Đ_M$= 1.21 (by GPC).

### 3.2.2.4 Synthesis of CCS Polymers Using EGDMA as Crosslinker

CCS polymers were synthesised by the arm-first approach through dispersion polymerisation. Typically, $PPEGMA_{14}$-b-($TFEMA_5$-co-$DMAEMA_{19}$) (0.210 g, 0.02 mmol), BMA (16 µL, 0.1 mmol), EGDMA (20 mg, 0.1 mmol) and ACVA (1.12 mg, 0.004 mmol) were added to a mixture of 2 mL ethanol and 2 mL water. The solution was stirred at room temperature for 30 min to form a clear solution, before being divided into 5 tubes containing stirrer bars. Each tube was sealed with a rubber septum, followed by being purged with nitrogen for 15 min in an ice bath. After that, the tubes were immersed in 70 $^o$C oil bath, and were opened at given time intervals for GPC and DLS analysis.

### 3.2.2.5 Synthesis of Bis(2-methacryloyl)oxyethyl Disulfide (DSDMA)

Degradable crosslinker DSDMA was synthesised using a published procedure,[57] with minor

modification. 2-Hydroxyethyl disulfide (7.7 g, 0.05 mol) and MEHQ (60 mg) were added to 150 mL DCM in a 500 mL flask, and a heterogeneous mixture was formed. Then methacryloyl chloride (20 mL, 0.2 mol) was added to the mixture. The flask was immersed in an ice/water bath and TEA was added drop-wise using a dropping funnel over 40 min. During addition of the TEA, a white precipitate was gradually formed. After the addition of TEA, the mixture was stirred at 0 $^{o}$C for another 30 min and then at room temperature for 24 h. After reaction, the mixture was filtered to remove the the insoluble triethylamine hydrochloride salt. Then the filtrate was washed with 1 M $NaHCO_3$ solution (150 mL × 3) and water (150 mL × 3), and the organic phase was dried over anhydrous $MgSO_4$ with 60 mg of MEHQ. After that, DCM was removed by rotary evaporation. The residual was purified by flash column chromatography ($SiO_2$, gradient hexane/ethyl acetate, from 90/10 to 60/40). A slightly yellowish oil was obtained and was stored in a freezer in dark. Yield: 8.9 g, 61%.

### 3.2.2.6 Synthesis of Biodegradable CCS Polymers Using DSDMA as Crosslinker

$PPEGMA_{14}$-b-($TFEMA_6$-co-$DMAEMA_{20}$) (0.216 g, 0.02 mmol), DSDMA (58 mg, 0.2 mmol) and ACVA (2.24 mg, 0.005 mmol) were added to a mixture of 2 mL ethanol and 2 mL water, which was then stirred at room temperature for 30 min to form a clear solution. After that the solution was divided equally to 4 tubes, and each tube was purged with nitrogen for 10 min in an ice bath. Finally the tubes were placed in a 70 $^{o}$C oil bath, and each tube was opened and cooled to 0 $^{o}$C periodically. GPC measurements were carried out for each sample to monitor the formation of CCS polymer.

For the scale-up synthesis, $PPEGMA_{14}$-b-($TFEMA_6$-co-$DMAEMA_{20}$) (2.16 g, 0.2 mmol), DSDMA (0.58 g, 2 mmol) and ACVA (22.4 mg, 0.05 mmol) were added to a mixture of 20 mL ethanol and 20 mL water in a 100 mL flask, which was then sealed with a rubber septum and purged with nitrogen for 45 in an ice bath. Then the flask was immersed in 70 $^{o}$C oil bath for 30 min. After polymerisation, the sample was purified using centrifugal filter units (Amicon Ultra-15, 100k) and then lyophilised.

### 3.2.2.7 Degradation of CCS Polymer by Reduction with TCEP

SP-1 (30 mg, $4.6\times 10^{-5}$ mmol) was dissolved in 6 mL of methanol in a 20 mL schlenk tube, which was then magnetically stirred and purged with Ar. After 30 min, TCEP (86 mg, 0.3 mmol) was added to the polymer solution under the protection of Ar. The solution was stirred at RT for 7 hours,

followed by the injection of pre-deoxygenated TEA (100 µL, 0.72 mmol) and MMA (200 µL, 1.87 mmol) to cap the formed thiol groups. After stirring at RT overnight, the reaction was stopped through exposure to air and an aliquot was withdrawn for GPC analysis.

#### 3.2.2.8 Degradation of CCS by Reduction with GSH

SP-1 (15 mg, $2.3 \times 10^{-5}$ mmol) was dissolved in 30 mL of PBS in a 100 mL flask and the pH was adjusted to 7.4 using 1 M NaOH solution. The flask was then sealed with a rubber septum and purged with Ar for 30 min, followed by the addition of GSH (92 mg, 0.3 mmol) under Ar flow. The solution was purged with Ar for another 30 min and stirred at 37 $^{o}$C. After 72 h, pre deoxygenated TEA (200 µL, 1.44 mmol) and HEMA (250 µL, 2.06 mmol) were injected to the flask to cap the thiol groups that were formed after reduction. After another 24 h the sample was freeze dried and subjected to GPC analysis.

### 3.2.3 Characterisation

#### Gel Permeation Chromatography (GPC)

Molecular weights and molecular weight distributions were determined by GPC using a Waters Alliance 2690 Separations Module equipped with Waters 2414 Refractive Index (RI) Detector, Waters 2489 UV/Visible Detector, Waters 717 Plus Autosampler and Waters 1515 Isocratic HPLC Pump. Samples were dissolved in THF/triethylamine (95/5, v/v) and passed through 0.45 µm filters before each measurement. THF was used as the mobile phase at a flow rate of 1 mL min$^{-1}$. The system was calibrated using polystyrene (PS) standards, to which the number average molecular weight ($M_n$) and weight average molecular weight ($M_w$) were referenced. Absolute molecular weights of the star polymers were measured by a triple detection GPC (Polymer Labs GPC50) equipped with dual angle laser light scattering detector, viscometer and differential refractive index detector. N,N-dimethylacetamide (DMAc, HPLC grade, containing 0.03 wt % LiCl) was used as the eluent at a flow rate of 1.0 mL min$^{-1}$. Separations were achieved using two PLGel Mixed B (7.8 × 300 mm) columns connected in series and held at a constant temperature of 50 $^{o}$C. The triple detection system was calibrated using a 2 mg mL$^{-1}$ PSTY standard (Polymer Laboratories, $M_w$ = 110 K, *dn/dc* = 0.16 mL g$^{-1}$ and IV = 0.5809). Samples of given concentrations were prepared in DMAc (containing 0.03 wt% LiCl) and passed through a 0.45 µm PTFE syringe filters prior to measurements. The absolute molecular weights and *dn/dc* values were determined by using Polymer Laboratories Multi Cirrus software based on the quantitative mass recovery technique.

**Nuclear Magnetic Resonance (NMR)**

$^{1}H$ NMR and $^{13}C$ NMR analysis were performed on a Bruker Avance 500 MHz spectrometer equipped with a BBO5 probe at 25 $^{o}C$ using an internal lock ($CDCl_3$) and referenced to the residual non-deuterated solvent ($CHCl_3$).

**Dynamic Light Scattering (DLS)**

DLS measurements were carried out on a Nanoseries Zetasizer (Malvern, UK) at 25 $^{o}C$. Sample solutions were prepared in PBS (1 mg $mL^{-1}$) at different pH values and passed through 0.45 µm filters prior to each measurement. Each hydrodynamic diameter was the average value of 5 runs. To minimise the influence of large aggregates, number averaged diameters are reported.

**$^{19}F$ Nuclear Magnetic Resonance ($^{19}F$ NMR)**

All $^{19}F$ NMR spectra were acquired at 470.55 MHz without $^{1}H$ decoupling on a Bruker Avance 500 spectrometer using a 5 mm broadband inverse probe (BBO5) for which the inner coil was double-tuned for $^{19}F$ and $^{1}H$. The samples were prepared by dissolving the star polymers in PBS/$D_2O$ (90/10, v/v) at a concentration of 20 mg $mL^{-1}$. All measurements were performed at 25 $^{o}C$. A 90$^{o}$ pulse of 15.1 µs was used in all measurements, the relaxation delay was 2 s and the acquisition time was 0.7 s. Data were collected using a spectrum width of 23 kHz, 32k data points and 128 scans.

$^{19}F$ spin-spin relaxation times ($T_2$) were measured using the Carr-Purcell-Meiboom-Gill (CPMG) pulse sequence at 25 $^{o}C$. The samples were dissolved in PBS/$D_2O$ (90/10, v/v) at a concentration of 20 mg $mL^{-1}$. The relaxation delay was 3 s and the acquisition time was 0.7 s. For each measurement, the echo times were from 2 to 770 ms and 15 points were collected, which could be described by exponential functions for the calculation of $T_2$.

$^{19}F$ spin-lattice ($T_1$) relaxation times were measured using the standard inversion-recovery pulse sequence. For each measurement, the recovery times were from 2 ms to 3 s and 15 points were acquired. Values for the major peak at around -72.6 ppm are reported.

**$^{19}F$ Magnetic Resonance imaging ($^{19}F$ MRI)**

Images of phantoms containing the solutions of the CSS particles were acquired on a Bruker BioSpec 94/30 USR 9.4 T small animal MRI scanner. CCS polymers were dissolved in PBS/$D_2O$ (90/10,v/v) to a concentration of 20 mg $mL^{-1}$ and loaded in clear glass vials (8 × 30 mm, 0.75 mL),

which were then placed in a $^{1}H/^{19}F$ dual resonator 40 mm volume coil. $^{1}H$ were acquired for localisation of the samples using a RARE sequence with an echo train length of 8 (TE = 28 ms, TR = 2 s, FOV = 40 × 40 × 1 mm, Matrix = 128 × 128 × 1). $^{19}F$ images were acquired in the same stereotactic space as the $^{1}H$ image using a RARE sequence with an echo train length of 8 (TE = 10 ms, effective TE = 40 ms, TR = 1 s, FOV = 40 × 40 × 30 mm, Matrix = 32 × 32 × 1) with a total acquisition time of 1 hour 8 minutes.

## 3.3 Results and Discussion

### 3.3.1 Synthesis of PPEGMA macroCTA

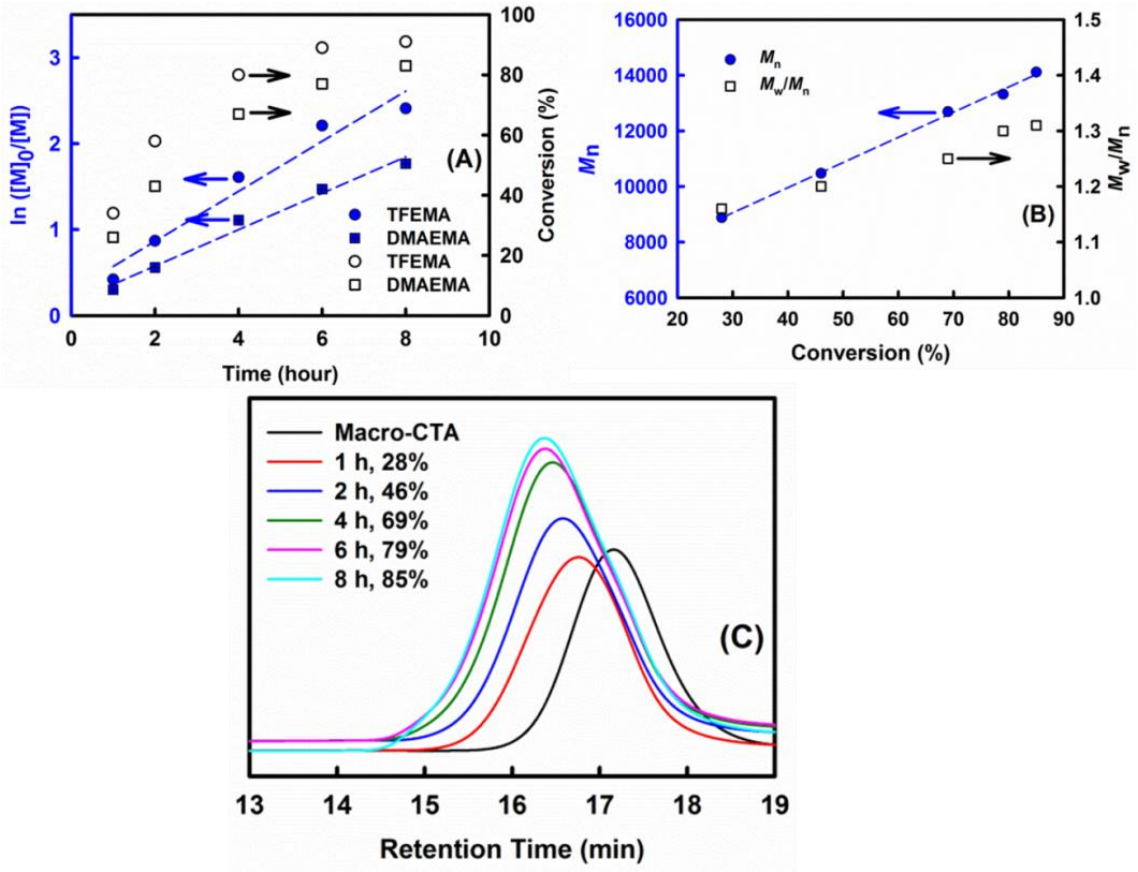


**Figure 3-1** RAFT polymerisation of TFEMA and DMAEMA using PPEGMA macro-CTA. (A) Pseudo-first-order kinetic plots of the polymerisation. (B) Dependence of number-average molecular weight ($M_n$, determined by GPC) and molar-mass dispersity ($Đ_M$) on the total monomer conversion. (C) GPC traces during the polymerisation.

A trithiocarbonate chain transfer agent, 4-cyano-4-(dodecylsulfanylthiocarbonyl)sulfanyl pentanoic acid, was first end functionalised with propargyl alcohol and subsequently used for the synthesis of

PPEGMA macro-CTA, as reported in our previous study.[52] The alkyne end group can offer the possibility of further modification of the CCS polymer through 'click' chemistry. Furthermore, the alkyne end group facilitates the calculation of the degree of polymerisation (DP) using $^1$H NMR owing to the well-resolved peak (~4.7 ppm) due to the protons in the methylene group adjacent to the alkyne group. PEGMA was chosen because of its hydrophilicity and biocompatibility. The kinetics of the synthesis of PPEGMA was investigated, and the results confirmed a well-controlled RAFT polymerisation (see Appendix B Figure A3.1). The PPEGMA so-formed (DP = 14, $M_n$ ($^1$H NMR) = 7100, $Đ_M$ = 1.12) was used as the macro-CTA in subsequent steps.

### 3.3.2 Synthesis of PPEGMA-b-P(TFEMA-co-DMAEMA) Block Copolymers

The as-synthesised PPEGMA macro-CTA was chain extended with TFEMA and DMAEMA for the synthesis of PPEGMA-b-P(TFEMA-co-DMAEMA). As displayed in Figure 1, the polymerisation rates of both TFEMA and DMAEMA exhibited pseudo-first-order kinetics throughout the polymerisation to above 80% conversion (Figure 3-1 (A)). In addition, the number-average molecular weight increased linearly with monomer conversion while the molar-mass dispersity ($Đ_M$) remained relatively low (Figure 3-1 (B)). Furthermore, in Figure 3-1 (C) the GPC curves also evolved from long retention time to short retention time with increase of reaction time and conversion. This confirms the successful synthesis of PPEGMA-b-P(TFEMA-co-DMAEMA) from the PPEGMA macro-CTA. To minimise the loss of trithiocarbonate end group, a monomer conversion of ~50% was targeted in the scale-up polymerisation. After purification, $PPEGMA_{14}$-b-($TFEMA_5$-co-$DMAEMA_{19}$) was obtained (denoted as Arm-1, $M_n$ = 10500 by $^1$H NMR, $Đ_M$ = 1.21). In order to prepare block copolymers with different compositions, Arm-2 ($PPEGMA_{14}$-b-($TFEMA_{11}$-co-$DMAEMA_{15}$, $M_n$ = 11300 by $^1$H NMR, $Đ_M$ = 1.20) and Arm-3 ($PPEGMA_{14}$-b-($TFEMA_{18}$-co-$DMAEMA_{10}$, $M_n$ = 11700 by $^1$H NMR, $Đ_M$ = 1.18) were then synthesised by varying the TFEMA/DMAEMA ratio and using the same polymerisation condition. The properties of the macro-CTA and block copolymers are summarised in Table 3-1.

**Table 3-1** Properties of the macro-CTA and arm precursors.

| Sample | $^{19}$F wt%[a] | $M_n$[b] (GPC) | $Đ_M$[b] | $M_n$[c] ($^1$H NMR) |
|---|---|---|---|---|
| Macro-CTA ($PPEGMA_{14}$) | - | 7200 | 1.12 | 7100 |
| Arm-1 ($PPEGMA_{14}$-*b*-($TFEMA_5$-*co*-$DMAEMA_{19}$) | 3.2 | 9200 | 1.24 | 10500 |
| Arm-2 ($PPEGMA_{14}$-b-($TFEMA_{11}$-co-$DMAEMA_{15}$) | 5.5 | 8900 | 1.20 | 11300 |
| Arm-3 ($PPEGMA_{14}$-b-($TFEMA_{18}$-co-$DMAEMA_{10}$) | 8.8 | 8900 | 1.18 | 11700 |

[a] Weight percentage of fluorine in the samples was determined by $^1$H NMR. [b] $M_n$ and $Đ_M$ were measured by GPC RI detector. [c] $M_n$ was calculated using the DP given by $^1$H NMR.

### 3.3.3 Synthesis of CCS Polymers by the Arm-first Approach via RAFT polymerisation

Recently, RAFT dispersion polymerisation has been exploited for the synthesis of CCS polymers by An and co-workers, and its benefits have been discussed and highlighted.[58-61] Compared to conventional homogeneous polymerisation in organic solvents, the heterogeneous polymerisation in aqueous solution can significantly reduce the polymerisation time due to an accelerated monomer consumption. Furthermore, the method can increase the yield of star polymer by facilitating the arm incorporation process. As the three block copolymers were all water soluble due to the presence of hydrophilic PPEGMA segments, RAFT dispersion polymerisation in water/ethanol mixture was introduced for the synthesis of CCS polymers.

The CCS polymers were synthesised through the chain extension of arm precursors with the crosslinker EGDMA. The polymerisation was carried out in water/ethanol mixture (50/50, v/v) at 70 $^o$C using ACVA as initiator. It was found that the polymerisation time played a pivotal role in the formation of CCS polymers. Figure 3-2 shows the GPC traces of the samples withdrawn at different polymerisation times during the dispersion polymerisation. As one can see in Figure 3-2 (A), although the peak of the arms became broader and started to shift toward shorter retention times, CCS polymer was not formed within 20 min. After 30 min, a peak appeared at retention time of 14.6 min and could be assigned to the CCS polymer owing to its larger hydrodynamic radius. Over the next 30 min the intensity of the CCS peak continued to increase while that of the linear

polymer peak at 16.2~17.0 decreased gradually, indicating the increasing arm incorporation and yield of CCS polymer. Interestingly, as shown in Figure 2 (B), the intensity of the CCS polymer peak decreased by half after 2 hours, and then continued to be diminished over the next 4 hours before it completely disappeared after 8 hours.

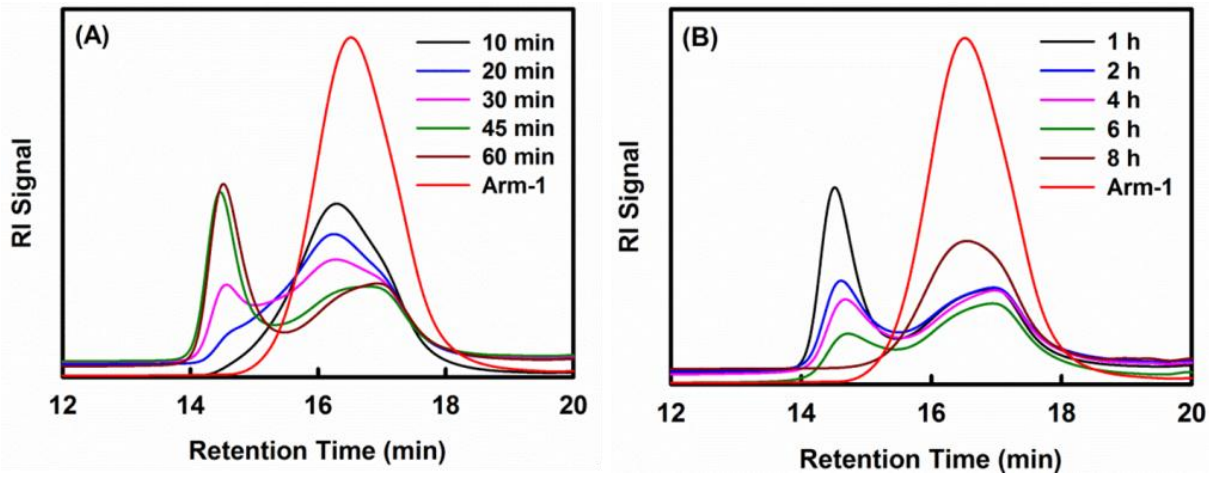


**Figure 3-2** GPC traces during the synthesis of CCS polymer using EGDMA as crosslinker by dispersion polymerisation. Condition: [Arm-1]/[BMA]/[EGDMA]/[ACVA] = 1/5/5/0.2, [arm-1] = 5 mM, in water/ethanol (50/50, v/v), 70 $^{o}$C.

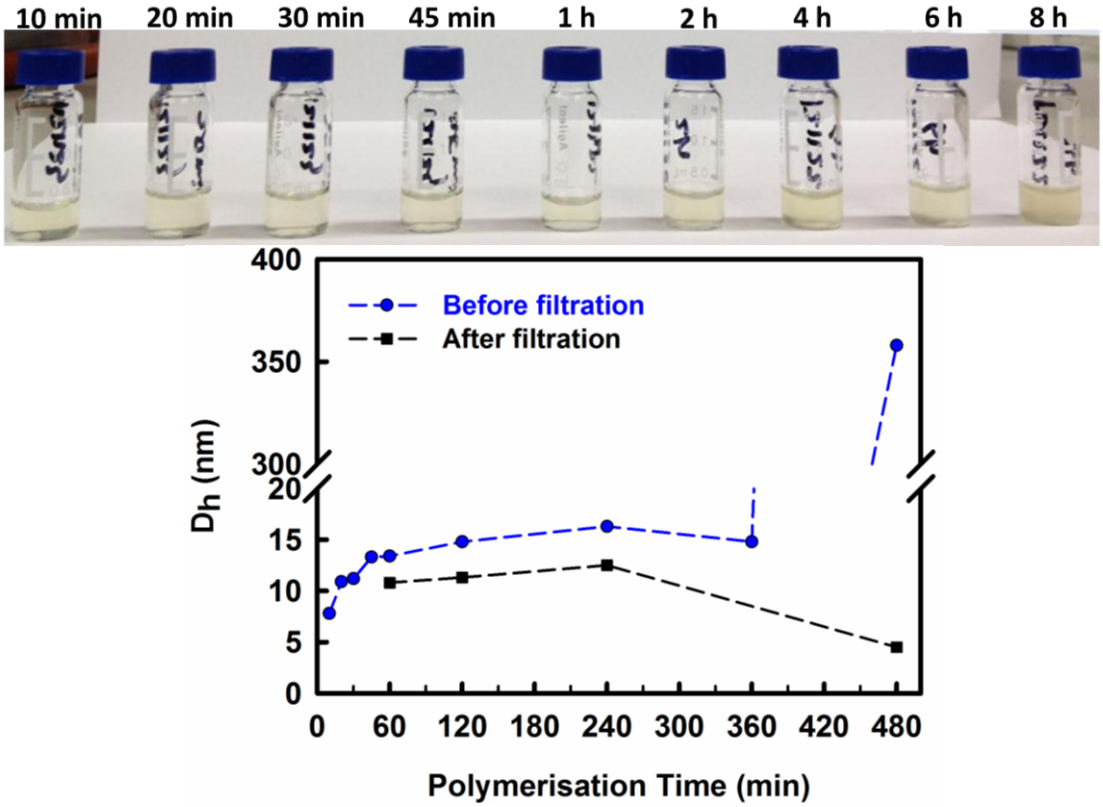


**Figure 3-3** Top: Digital photographs of the samples withdrawn at different time intervals during the synthesis of CCS polymer by RAFT dispersion polymerisation. The samples were at room temperature (~25 $^{o}$C). Bottom: DLS results of the samples at different polymerisation time before and after filtration using 450 μm syringe filters. Each size was the average of five measurements at 25 $^{o}$C.

Based on the GPC traces, the extent of formation of the CCS polymer through the chain extension of block copolymer with crosslinker reached a maximum after 1 h. However, due to monomer consumption and abundant vinyl groups in the core, after 1 h intermolecular coupling (or star-star coupling) started to dominate the polymerisation, and resulted in the formation of macroscopic gel particles, which consumed the as-formed CCS polymers and substantially reduced the CCS polymer yield. In support of this a digital photographs of the samples at increasing conversion demonstrates a change from clear solution to turbid dispersion (Figure 3-3 Top), confirming the gradual formation of larger and insoluble particles after 1 h. Furthermore, in Figure 3-3 (Bottom), the particle size (number averaged diameter) of the crude polymerisation solution increased significantly from 7.4 nm after 10 min to 13.4 nm after 1 h, slowly increased to 14.8 nm after 6 h before dramatically increasing to ~360 nm after 8 h After filtration, the particle size became smaller owing to the removal of large particles.

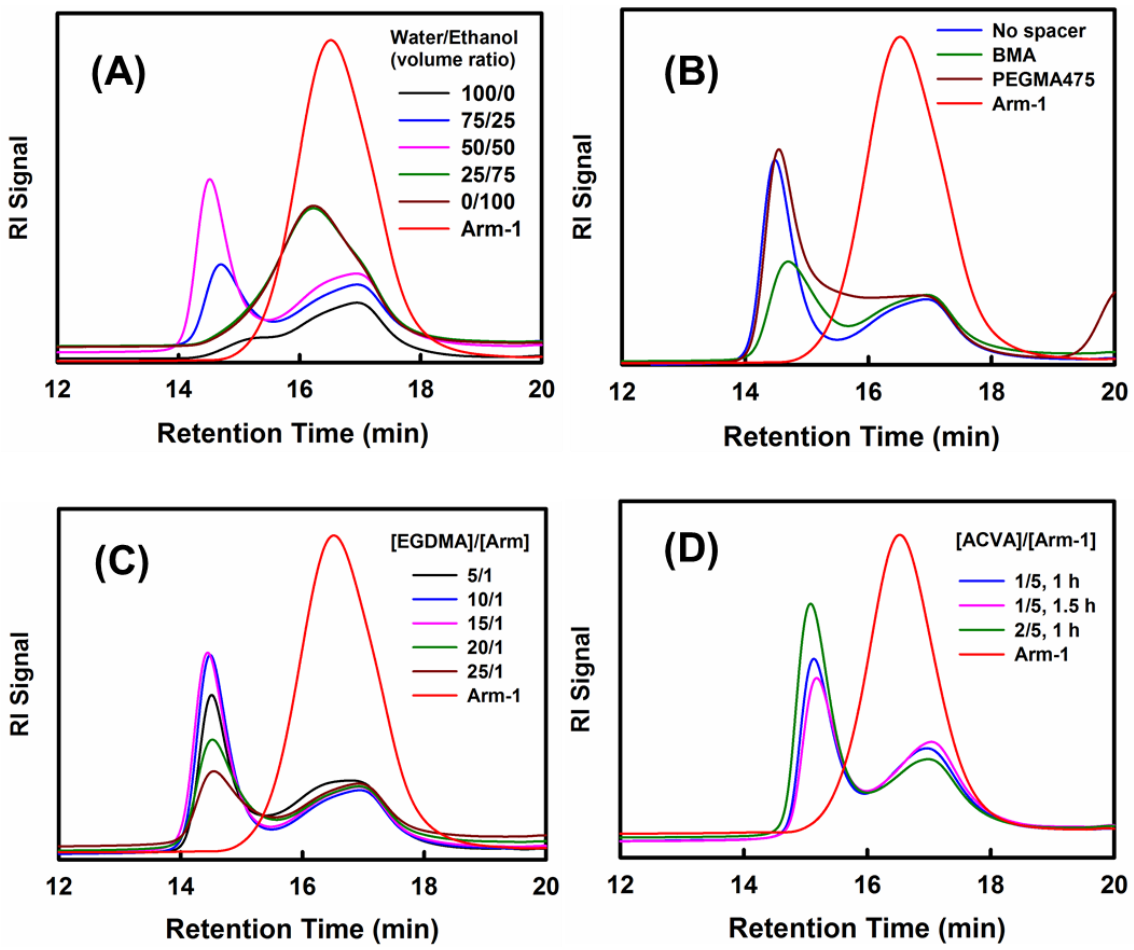


**Figure 3-4** GPC traces of CCS polymers synthesised at (A) different water/ethanol ratios, (B) with or without spacer monomers and (C) different EGDMA/arm ratios. Conditions: (A) [Arm-1]/[EGDMA]/[BMA]/[ACVA] = 1/5/5/0.2, [arm-1] = 5 mM, 70 $^{o}$C,1 h. (B) [Arm-1]/[EGDMA]/[Spacer]/[ACVA] = 1/10/10/0.2, [arm-1] = 5 mM, water/ethanol (50/50, v/v), 70 $^{o}$C, 1 h. (C) [Arm-1]/[ACVA] = 1/0.2, [arm-1] = 5 mM, water/ethanol (50/50, v/v), 70 $^{o}$C, 1 h. (D) [Arm-1]/[EGDMA] = 1/10, [arm-1] = 5 mM, water/ethanol (50/50, v/v), 70 $^{o}$C.

A number of other significant parameters in the polymerisation were also investigated. It was found that the water/ethanol ratio was a key factor since well-defined CCS polymers were only formed in water/ethanol (50/50, v/v) (Figure 3-4 (A)). This is understandable since a higher ethanol content in the polymerisation solvent (> 75 %) will result in homogeneous polymerisation; CCS polymers usually take much longer to form (typically 8~24 h) in organic solvents[62-65] than in conventional dispersion polymerisation. However, the arm precursor has poor solubility when the ethanol content is too low (< 50 %). Therefore a moderate water/ethanol ratio is required for a successful dispersion polymerisation, so that the starting reagents dissolve well while the CCS polymer has poor solubility. In addition, unlike other reports,[59, 60, 62] the use of the spacing monomer

did not improve the formation of CCS polymer (Figure 3-4 (B)). Moreover, the highest yield of CCS polymers was achieved when [EGDMA]/[arm-1] ratio was 10 or 15 (Figure 3-4 (C). As shown in Figure 3-4 (D), the CCS polymer yield was also increased by using a higher [ACVA]/[Arm-1] ratio (2/5). These results revealed that the arm-first synthesis of CCS polymer via RAFT dispersion polymerisation could be affected by a number of parameters and well-defined CCS polymers with high yield could be obtained by carefully selecting and controlling the polymerisation conditions.

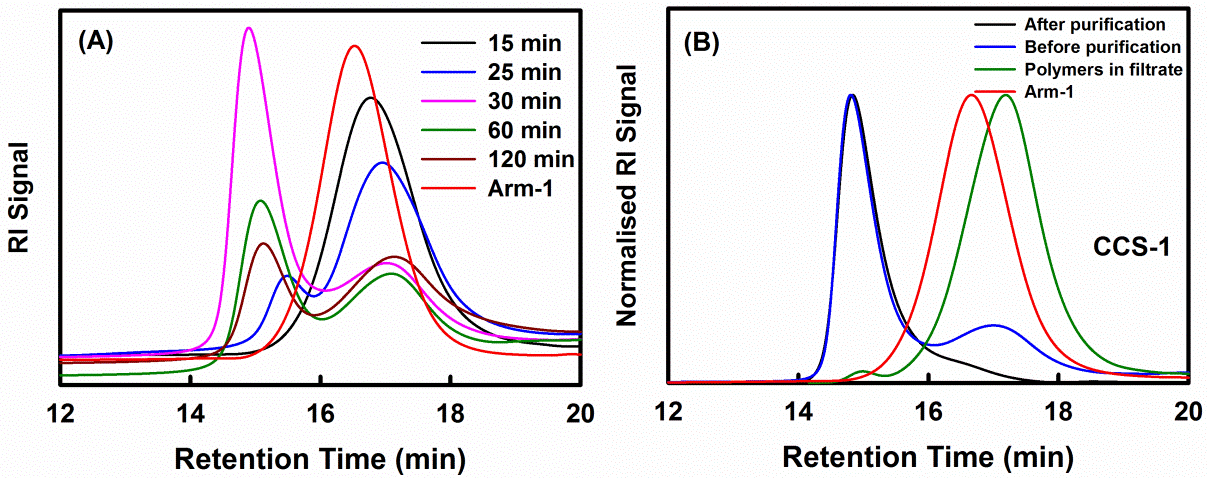


**Figure 3-5** GPC traces of CCS polymer synthesised using DSDMA as crosslinker. (A) GPC traces at different polymerisation time. (B) GPC traces of CCS polymer prepared after 30 min. Condition: [Arm-1]/[DSDMA]/[ACVA] = 1/10/0.4, [arm-1] = 5 mM, in water/ethanol (50/50, v/v), 70 $^{o}$C

A degradable crosslinker, bis(2-methacryloyl)oxyethyl disulfide (DSDMA), was then chosen for the synthesis the CCS polymers. As displayed in Figure 3-5 (A), well-defined CCS polymer can be synthesised within 30 min with the highest yield (74%). At longer reaction times star-star coupling became more significant, as evidenced by the decrease in the peak of CCS polymer. The as-synthesised CCS polymer (denoted as CCS-1) was purified using centrifugal filter units. In Figure 3-5 (B), one can see that most of the linear residues were removed after purification (black line).

The chemical structure of the arms and CCS polymers was characterised by $^{1}$H NMR. As shown in Figure 3-6 (A) and (C), all the characteristic peaks of monomer units are well assigned, indicating the successful synthesis of arms precursors and CCS polymers. After purification, the polymers in the filtrate (denoted as Filtrate-1) were also collected and analysed by GPC and $^{1}$H NMR. According to the GPC trace (green line), despite the presence of a small amount of CCS polymer (1.21%), the linear residues showed a smaller $M_n$ compared to that of Arm-1while its $Đ_M$ was as low as that of Arm-1. In addition, in the $^{1}$H NMR spectra (Figure 3-6 (B)), for Filtrate-1, the peak

intensity of the protons of the $CH_2$ adjacent to the trithiocarbonate considerably decreased compared with Arm-1, suggesting that the residual linear polymers had very low end group functionality. The structure of the residual polymer was confirmed to be $PPEGMA_{14}$-b-$P(TFEMA_3$-co-$DMAEMA_8)$ by $^1H$ NMR with $M_n$ of 8400. We therefore conclude that the residual linear polymer collected from the filtrate is block copolymer in which the trithiocarbonate end groups have been lost during the synthesis of the arm precursor. This implies that the loss of CTA functionality is inevitable in the synthesis of PPEGMA-*b*-P(TFEMA-*co*-DMAEMA) block copolymers even with low monomer conversions.

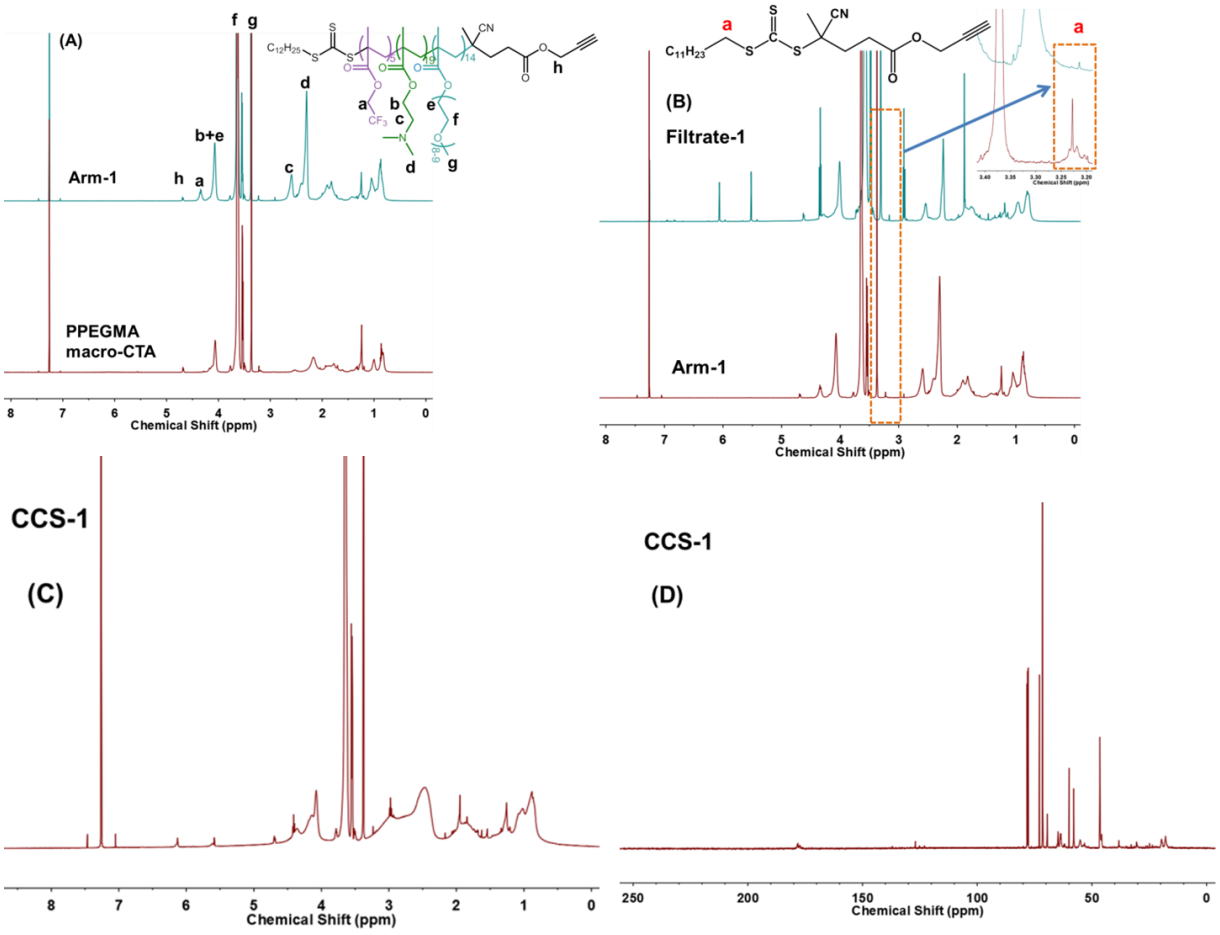


**Figure 3-6** (A), (B) and (C) 1H NMR spectra of macro-CTA, Arm-1, filtrate-1 and CCS-1. 'e' represents the two protons of the $CH_2$ adjacent to −COO− in PEGMA. (D) 13C NMR spectrum of CCS-1.

In Figure 3-6 (C), the peaks at 5.7 and 6 ppm were assigned to the unreacted vinyl groups that were likely to be in the periphery of the core. Nevertheless, the DSDMA units could not be fully detected due to the highly rigid nature of the core.[66] The $^{13}C$ NMR spectrum (Figure 3-6 (D))

further confirmed the absence of a peak at ~222 ppm from the trithiocarbonate carbons. It is well known that the increased dipolar couplings experienced in rigid cores of particles may prevent direct observation by solution-state NMR methods.

**Table 3-2** Details of the CCS polymers.

| Sample | $^{19}$F wt%[a] | $M_n$ (GPC)[b] | $Đ_M$[b] | Absolute MW[c] | $Đ_M$[c] | $N_{arms}$[d] |
|---|---|---|---|---|---|---|
| **CCS-1** | 2.3 | 32800 | 1.23 | 653,300 | 1.17 | 46 |
| **CCS-2** | 3.9 | 43300 | 1.19 | 482,500 | 1.07 | 31 |
| **CCS-3** | 6.1 | 28000 | 1.19 | 683,000 | 1.15 | 41 |

[a] Fluorine content in the samples was determined by $^1$H NMR.. [b] $M_n$ and $Đ_M$ of the crude CCS polymers were measure by GPC RI detector. [c] Absolute molecular weight and $Đ_M$ were measured by triple detection GPC. [d] Number of arms was calculated using a method described in Appendix B)

A range of CCS polymers with different compositions were prepared by using Arm-2 and Arm-3 for the synthesis of CCS-2 and CCS-3, respectively, and the resulting CCS polymers were purified using the same procedure described above for CCS-1. The GPC data of CCS-2 and CCS-3 are displayed in Appendix B Figure A3.2. The properties of the CCS polymers are listed in Table 3-2.

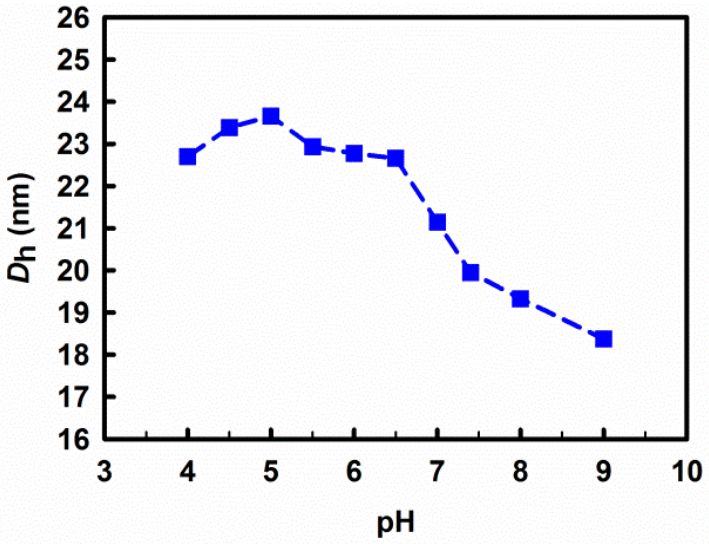


**Figure 3-7** Number-averaged diameter of CCS-1 in PBS (1 mg mL$^{-1}$) at different pH at 25 $^o$C.

The particle sizes of CCS-1 in PBS and at a range of pH values from 4 to 9 were measured by

DLS. As shown in Figure 3-7, the particle size was around 23 nm when the pH was below 6.5 and decreased progressively with an increase in pH and finally reached ~18 nm at pH 9. The change in particle size arises from the DMAEMA units present in the arms; PDMAEMA is well known as a pH-responsive polymer and has a p*K*a between 7.3~7.5. Specifically, in aqueous solution, the protonation of the tertiary amines below p*K*a renders the PDMAEMA segments charged and the chains undergo electrostatic repulsion, while on deprotonation above p*K*a the chains adopt a more contracted configuration. On the basis of the DLS results, the volume of CCS-1 nanoparticles at pH 9 was reduced by 53% compared to that at pH 5, indicating a significant dependence of particle size on environmental pH.

In addition, the protonation and deprotonation process was revealed by a change in zeta potential at different pHs. (see Appendix B Figure A3.4)

### 3.3.4 Degradation of CCS Polymer

Disulfide-containing crosslinkers have been frequently used for the preparation of degradable materials because the disulfide group can be cleaved to thiols by reducing agents.[67] As the core of the as-synthesised CCS polymer is comprised of PDSDMA homopolymer, it is expected that the core can be degraded when treated with reducing agents. The degradation of CCS-1 in methanol was first tested using TCEP as the reducing agent, and the GPC curve shifted to longer retention time after 7 hours while the $Đ_M$ was as low as that of Arm-1 (Figure 3-8 (A)), confirming the successful cleavage of the disulfide bonds in the core. It should be noted that the thiol groups in solution are very sensitive to oxygen and can form disulfide again when exposed to air. For example, after reduction of the CCS-1 with DTT in THF, samples were withdrawn periodically for GPC analysis, and the GPC curves of the degraded polymer shifted progressively to longer retention time and the $Đ_M$ became very large (39~98) owing to the re-formation of disulfide linkages in air (see Appendix B Figure A3.3). To avoid the re-formation of disulfides, after degradation the thiol groups were capped with MMA through based-catalysed Michael addition.[68, 69]

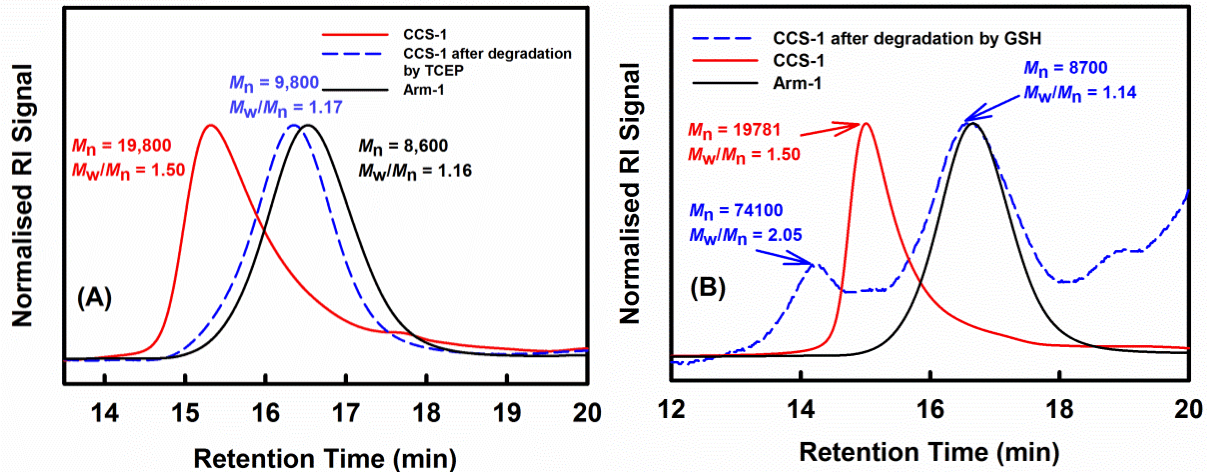


**Figure 3-8** GPC traces of CCS-1 before and after degradation by TCEP (A) and GSH (B), respectively

Since TCEP is not physiologically available, glutathione (GSH) was then chosen for the degradation of CCS-1. It has been reported that GSH is present in the human body at micromolar concentrations in blood plasma, ~10 mM in the cytosol, [53, 70] and at several times higher concentration in tumour cells than normal cells.[71, 72] As shown in Figure 3-8 (B), two peaks appeared after degradation with TCEP. To be more specific, the major peak with $M_n$ of 8700 was from the linear polymers after the degradation of the crosslinked core, while the minor peak with $M_n$ of 74100 was caused by the re-formation of disulfide groups due to the incomplete degradation of the core. As the core was comprised of hydrophobic DSDMA units that were poorly accessible for water and the GSH concentration was also relatively low, we propose that the degradation of CCS-1 using 10 mM GSH in PBS would take much longer time than the degradation by TCEP. Based on these results, we conclude that the as-synthesised CCS polymers were biodegradable.

### 3.3.5 $^{19}$F NMR Studies

In order to assess their potential as pH-responsive $^{19}$F MRI contrast agents, the CCS polymers were examined by $^{19}$F NMR in solutions with different values of pH. As displayed in Figure 3-9, only one peak at -72.6 ppm was observed in each spectrum of all the three samples, confirming a single $^{19}$F chemical environment in the CCS polymer structure. When the pH was raised, this peak became broader and the signal intensity decreased, as highlighted by the superimposed spectra in Figure 3-9 (D), (E) and (F). As discussed above, the particle size was dependent on pH owing to the presence of the pH-sensitive monomer DMAEMA. An increase in pH leads to the deprotonation of PDMAEMA, thus the P(TFEMA-co-DMAEMA) block becomes hydrophobic and tends to

aggregate in aqueous solution, reducing the mobility of $^{19}F$ nuclei. This leads to an increase in the NMR line width and a decrease in the $^{19}F$ signal intensity. In addition, it can be seen that the increase of $^{19}F$ content (from CCS-1 to CCS-3) also resulted in a considerable decrease in the signal intensity because of the increased likelihood of association of the $^{19}F$-containing segments. Overall, the $^{19}F$ NMR results indicated that the $^{19}F$ signal was dependent on both solution pH and $^{19}F$ content

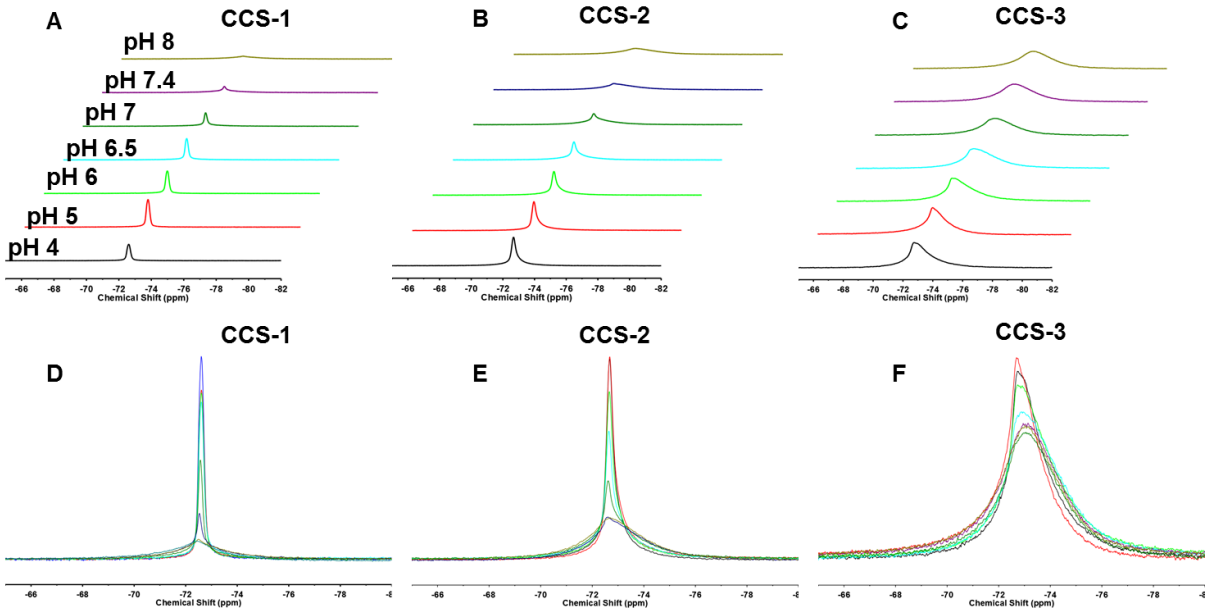


**Figure 3-9** $^{19}F$ NMR spectra of the CCS polymers in PBS/D2O (90/10, v/v) with 20 mg $mL^{-1}$ concentration at 25 $^{o}C$.

Spin-lattice ($T_1$) and spin-spin ($T_2$) relaxations times were also measured at different values of pH. In Figure 3-10, for CCS-1, the $T_2$ remained at around 35 ms when the pH was below pH 6.5 and then dropped drastically to less than 5 ms at pH 8. The $T_2$ at pH 9 could not be measured due to the greatly attenuated signal. Meanwhile the $T_1$ was not greatly affected by the change of pH, indicating that the spectral density of high MHz motions of the fluoroethyl segments is not greatly affected by the change in polymer dimensions. Similar conclusions were reached by Peng *et al.* in their study of the behaviour of linear block copolymers.[23, 25] For CCS-2, the $T_2$ was much lower than that of CCS-1, but it showed a similar behaviour with changes in pH. As before, the $T_2$ above pH 7 could not be measured, demonstrating the reduced mobility of the $^{19}F$ nuclei. The $T_2$ of CCS-3 could not be measured at all values of pH owing to the self-association of $^{19}F$-containing units and highly restricted motion, but was instead estimated from the width of the lines in the NMR spectra.

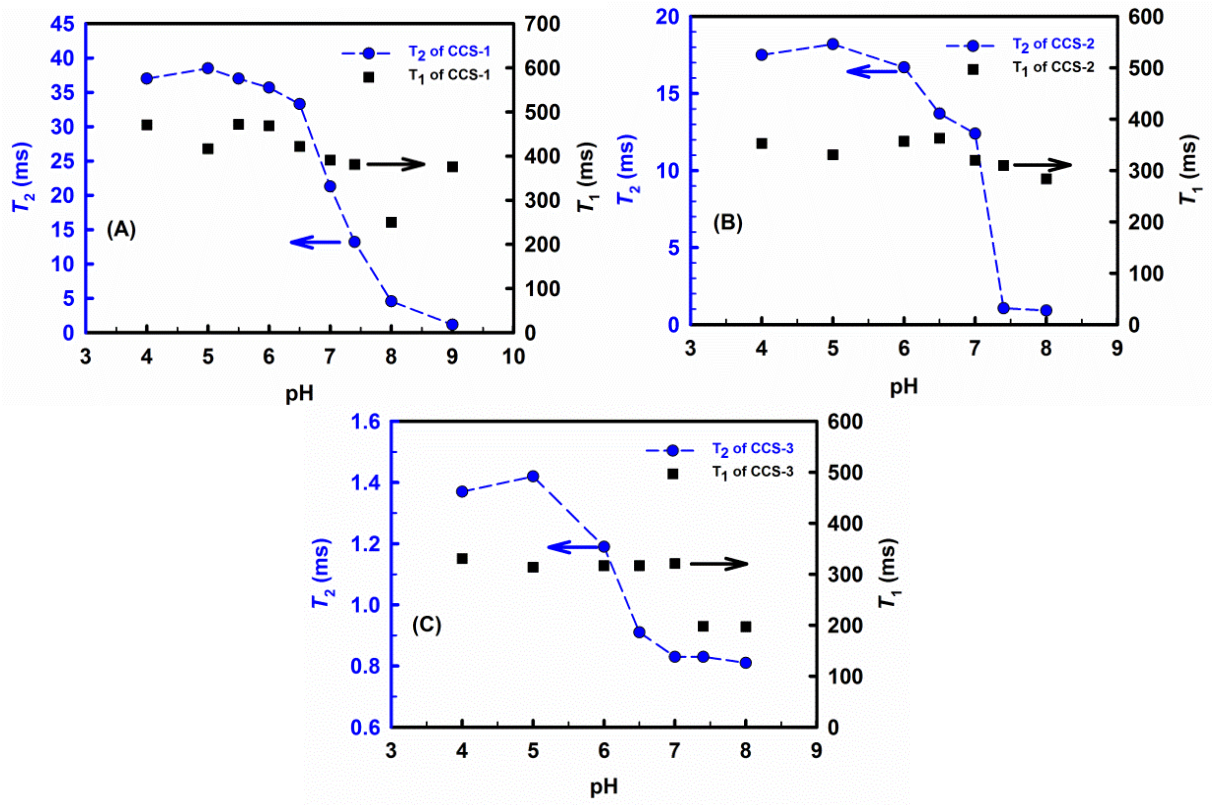


**Figure 3-10** Relaxation times of CCS-1 (A), CCS-2 (B) and CCS-3 (C) at different pH.

### 3.3.6 *In vitro* $^{19}$F MRI Evaluation

Following the $^{19}$F NMR study, the CCS polymers were evaluated for *in vitro* $^{19}$F MRI. As depicted in Figure 3-11 (A), $^{1}$H RARE images were taken to allow localisation of the sample vials (phantoms). The $^{19}$F MR images are shown on the right-hand side of Figure 3-11 (A). CCS-1 and CCS-2 showed a clear change in imaging performance at the four values of pH. Specifically, CCS-1 could be well visualised at pH 5, and the intensity decreased upon an increase of pH until being undetectable at pH 8. The figure demonstrates that CCS-2 was detected at pH 5 and 6.5 with poor signal-to-noise ratios, and exhibited no signal at pH 7.4 and 8. Unsurprisingly, CCS-3 could not be imaged at any pH owing to its very short $T_2$ relaxation times. As shown in Figure 3-11 (B), a decrease in signal-to-noise ratio (SNR) was confirmed on an increase in pH of the polymer solution. On the basis of this $^{19}$F MRI study, CCS-1 and CCS-2 showed better imaging performance at acidic pH. Thus it can be expected that these particles could be visualised only at acidic pH, and are thus potential candidates for the detection of tumour tissues that have acidic environments.

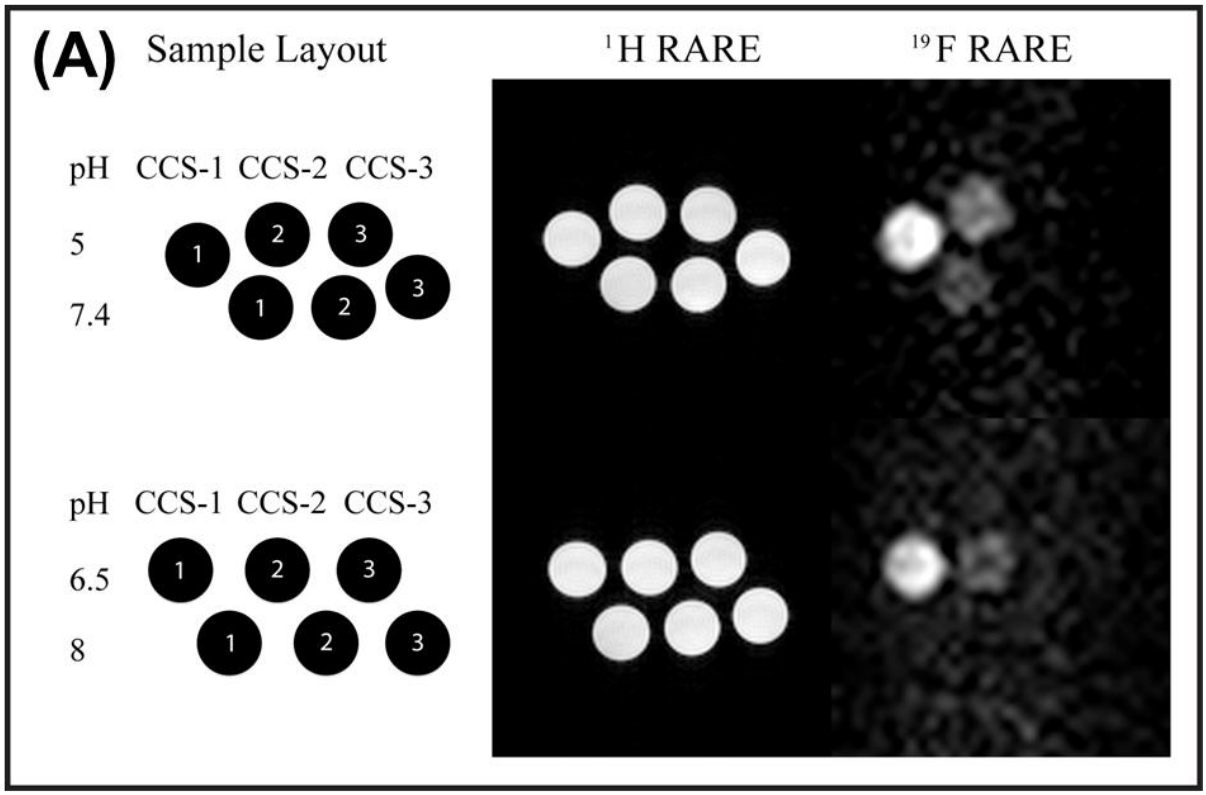


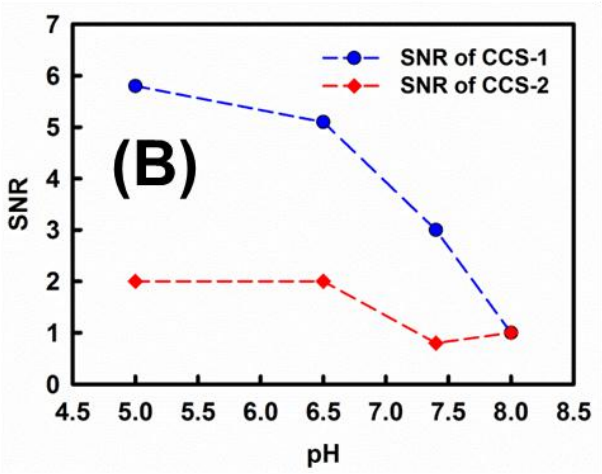


**Figure 3-11** (A) *In vitro* $^{1}$H and $^{19}$F MRI images of the CCS polymers in solutions at four values of pH. (B) Signal-to-noise ratio (SNR) of CCS-1 and CCS-2 at four pHs.

Our previous study of star polymers with fluorinated and DMAEMA units within the branched core also demonstrated a change in imaging performance with pH.[52] However, the best performing polymer in this current work (CCS-1) exhibited much better imaging performance at a comparable $^{19}$F content. For this reason the MRI scan time could be notably shortened to 1 hour 8 minutes from 9 hours 6 minutes. We hypothesise that this improvement is attributed to the greater flexibility of polymer chains around the core for the CCS polymer compared with the segments within the

relatively confined core-crosslinked structure.

## 3.4 Conclusions

In conclusion, CCS polymers were synthesised by RAFT dispersion polymerisation through the arm-first approach. The synthetic conditions were studied and optimised. The as-synthesised CCS polymer could form nanoparticles in aqueous solution and the particle size was dependent on pH. In addition, the CCS polymers were degradable due to the abundant disulfide bonds in the core. Moreover, $^{19}$F NMR confirmed that the $^{19}$F signal intensity was attenuated as the $T_2$ relaxation time decreased upon an increase of pH of the polymer solution. *In vitro* $^{19}$F MRI indicated that the CCS polymers could be imaged well at acidic pH while they had poor imaging performance above physiological pH, demonstrating that these CCS polymers are promising $^{19}$F MRI contrast agents for the selective imaging of tumour tissues.

Compared with the $^{19}$F MRI results in Chapter 2, the improved imaging performance presented in this Chapter suggests that the mobility of $^{19}$F nuclei can be improved by placing the fluorine units in the arms around the core instead of in a densely-crosslinked and relatively confined structure. Therefore this chapter reveals that the imaging properties can be influenced by the polymer architecture. This finding can be used for the future design of polymeric contrast agents for $^{19}$F MRI.

## 3.5 References


1. J. C. Knight, P. G. Edwards and S. J. Paisey, *Rsc Adv*, 2011, **1**, 1415-1425.
2. Z. X. Zhou and Z. R. Lu, *Wires Nanomed Nanobi*, 2013, **5**, 1-18.
3. Y. J. Liu and N. Zhang, *Biomaterials*, 2012, **33**, 5363-5375.
4. A. M. Mohs and Z. R. Lu, *Expert Opin Drug Del*, 2007, **4**, 149-164.
5. Z. R. Stephen, F. M. Kievit and M. Q. Zhang, *Mater Today*, 2011, **14**, 330-338.
6. A. K. Gupta and M. Gupta, *Biomaterials*, 2005, **26**, 3995-4021.
7. D. P. J. Pan, S. D. Caruthers, A. Senpan, A. H. Schmieder, S. A. Wickline and G. M. Lanza, *Wires Nanomed Nanobi*, 2011, **3**, 162-173.
8. M. F. Bellin, *Eur J Radiol*, 2006, **60**, 314-323.
9. A. P. Koretsky and A. C. Silva, *Nmr Biomed*, 2004, **17**, 527-531.
10. I. Aoki, S. Naruse and C. Tanaka, *Nmr Biomed*, 2004, **17**, 569-580.

11. H. J. Weinmann, W. Ebert, B. Misselwitz and H. Schmitt-Willich, *Eur J Radiol*, 2003, **46**, 33-44.
12. M. Bottrill, L. K. Nicholas and N. J. Long, *Chem Soc Rev*, 2006, **35**, 557-571.
13. D. D. Castelli, E. Gianolio, S. G. Crich, E. Terreno and S. Aime, *Coordin Chem Rev*, 2008, **252**, 2424-2443.
14. G. N. Holland, P. A. Bottomley and W. S. Hinshaw, *J Magn Reson*, 1977, **28**, 133-136.
15. J. Ruiz-Cabello, B. P. Barnett, P. A. Bottomley and J. W. Bulte, *Nmr Biomed*, 2011, **24**, 114-129.
16. J. X. Yu, V. D. Kodibagkar, W. N. Cui and R. P. Mason, *Curr Med Chem*, 2005, **12**, 819-848.
17. J. M. Janjic and E. T. Ahrens, *Wires Nanomed Nanobi*, 2009, **1**, 492-501.
18. S. Temme, F. Bonner, J. Schrader and U. Flogel, *Wires Nanomed Nanobi*, 2012, **4**, 329-343.
19. W. Liu and J. A. Frank, *Eur J Radiol*, 2009, **70**, 258-264.
20. M. M. Kaneda, S. Caruthers, G. M. Lanza and S. A. Wickline, *Ann Biomed Eng*, 2009, **37**, 1922-1933.
21. Y. Nose, *Artif Organs*, 2004, **28**, 807-812.
22. Z. X. Jiang, X. Liu, E. K. Jeong and Y. B. Yu, *Angew Chem Int Edit*, 2009, **48**, 4755-4758.
23. H. Peng, K. J. Thurecht, I. Blakey, E. Taran and A. K. Whittaker, *Macromolecules*, 2012, **45**, 8681-8690.
24. L. Nurmi, H. Peng, J. Seppala, D. M. Haddleton, I. Blakey and A. K. Whittaker, *Polym Chem*, 2010, **1**, 1039-1047.
25. H. Peng, I. Blakey, B. Dargaville, F. Rasoul, S. Rose and A. K. Whittaker, *Biomacromolecules*, 2009, **10**, 374-381.
26. M. M. Bailey, C. M. Mahoney, K. E. Dempah, J. M. Davis, M. L. Becker, S. Khondee, E. J. Munson and C. Berkland, *Macromol Rapid Comm*, 2010, **31**, 87-92.
27. S. Rossi, M. Benaglia, M. Ortenzi, E. Micotti, C. Perego and M. G. De Simoni, *Tetrahedron Lett*, 2011, **52**, 6581-6583.
28. M. M. Bailey, S. R. Kline, M. D. Anderson, J. L. Staymates and C. Berkland, *J Appl Polym Sci*, 2012, **126**, 1218-1227.
29. W. J. Du, A. M. Nystrom, L. Zhang, K. T. Powell, Y. L. Li, C. Cheng, S. A. Wickline and K. L. Wooley, *Biomacromolecules*, 2008, **9**, 2826-2833.
30. K. J. Thurecht, I. Blakey, H. Peng, O. Squires, S. Hsu, C. Alexander and A. K. Whittaker, *J Am Chem Soc*, 2010, **132**, 5336-5337.

31. M. Ogawa, H. Kataoka, S. Nitahara, H. Fujimoto, H. Aoki, S. Ito, M. Narazaki and T. Matsuda, *B Chem Soc Jpn*, 2012, **85**, 79-86.
32. M. Ogawa, S. Nitahara, H. Aoki, S. Ito, M. Narazaki and T. Matsuda, *Macromol Chem Phys*, 2010, **211**, 1602-1609.
33. M. Ogawa, S. Nitahara, H. Aoki, S. Ito, M. Narazaki and T. Matsuda, *Macromol Chem Phys*, 2010, **211**, 1369-1376.
34. J. M. Criscione, B. L. Le, E. Stern, M. Brennan, C. Rahner, X. Papademetris and T. M. Fahmy, *Biomaterials*, 2009, **30**, 3946-3955.
35. M. Oishi, S. Sumitani and Y. Nagasaki, *Bioconjugate Chem*, 2007, **18**, 1379-1382.
36. L. Josephson, M. F. Kircher, U. Mahmood, Y. Tang and R. Weissleder, *Bioconjugate Chem*, 2002, **13**, 554-560.
37. R. N. Muller, L. Vander Elst and S. Laurent, *J Am Chem Soc*, 2003, **125**, 8405-8407.
38. Y. T. Chang, C. M. Cheng, Y. Z. Su, W. T. Lee, J. S. Hsu, G. C. Liu, T. L. Cheng and Y. M. Wang, *Bioconjugate Chem*, 2007, **18**, 1716-1727.
39. M. F. Bennewitz, T. L. Lobo, M. K. Nkansah, G. Ulas, G. W. Brudvig and E. M. Shapiro, *Acs Nano*, 2011, **5**, 3438-3446.
40. G. L. Liang, J. Ronald, Y. X. Chen, D. J. Ye, P. Pandit, M. L. Ma, B. Rutt and J. H. Rao, *Angew Chem Int Edit*, 2011, **50**, 6283-6286.
41. D. Patel, A. Kell, B. Simard, B. Xiang, H. Y. Lin and G. H. Tian, *Biomaterials*, 2011, **32**, 1167-1176.
42. Y. Li, Y. Qian, T. Liu, G. Zhang and S. Liu, *Biomacromolecules*, 2012, **13**, 3877-3886.
43. B. A. Webb, M. Chimenti, M. P. Jacobson and D. L. Barber, *Nat Rev Cancer*, 2011, **11**, 671-677.
44. G. B. Giovenzana, R. Negri, G. A. Rolla and L. Tei, *Eur J Inorg Chem*, 2012, 2035-2039.
45. Y. Chen, Q. Yin, X. F. Ji, S. J. Zhang, H. R. Chen, Y. Y. Zheng, Y. Sun, H. Y. Qu, Z. Wang, Y. P. Li, X. Wang, K. Zhang, L. L. Zhang and J. L. Shi, *Biomaterials*, 2012, **33**, 7126-7137.
46. G. H. Gao, G. H. Im, M. S. Kim, J. W. Lee, J. Yang, H. Jeon, J. H. Lee and D. S. Lee, *Small*, 2010, **6**, 1201-1204.
47. T. Kim, E. J. Cho, Y. Chae, M. Kim, A. Oh, J. Jin, E. S. Lee, H. Baik, S. Haam, J. S. Suh, Y. M. Huh and K. Lee, *Angew Chem Int Edit*, 2011, **50**, 10589-10593.
48. S. H. Crayton and A. Tsourkas, *Acs Nano*, 2011, **5**, 9592-9601.
49. K. E. Lokling, S. L. Fossheim, J. Klaveness and R. Skurtveit, *J Control Release*, 2004, **98**, 87-95.

50. M. M. Ali, M. Woods, P. Caravan, A. C. L. Opina, M. Spiller, J. C. Fettinger and A. D. Sherry, *Chem-Eur J*, 2008, **14**, 7250-7258.
51. L. Barner, T. P. Davis, M. H. Stenzel and C. Barner-Kowollik, *Macromol Rapid Comm*, 2007, **28**, 539-559.
52. K. Wang, H. Peng, K. J. Thurecht, S. Puttick and A. K. Whittaker, *Polym Chem*, 2013, **4**, 4480.
53. G. Saito, J. A. Swanson and K. D. Lee, *Adv Drug Deliver Rev*, 2003, **55**, 199-215.
54. M. W. Jones, R. A. Strickland, F. F. Schumacher, S. Caddick, J. R. Baker, M. I. Gibson and D. M. Haddleton, *J Am Chem Soc*, 2012, **134**, 1847-1852.
55. A. W. Jackson and D. A. Fulton, *Macromolecules*, 2012, **45**, 2699-2708.
56. G. Moad, Y. K. Chong, A. Postma, E. Rizzardo and S. H. Thang, *Polymer*, 2005, **46**, 8458-8468.
57. Y. T. Li and S. P. Armes, *Macromolecules*, 2005, **38**, 8155-8162.
58. Q. Qiu, G. Y. Liu and Z. S. An, *Chem Commun*, 2011, **47**, 12685-12687.
59. X. F. Shi, W. Zhou, Q. Qiu and Z. S. An, *Chem Commun*, 2012, **48**, 7389-7391.
60. C. L. Zhang, M. Miao, X. T. Cao and Z. S. An, *Polym Chem*, 2012, **3**, 2656-2664.
61. X. F. Shi, M. Miao and Z. S. An, *Polym Chem*, 2013, **4**, 1950-1959.
62. J. Ferreira, J. Syrett, M. Whittaker, D. Haddleton, T. P. Davis and C. Boyer, *Polym Chem*, 2011, **2**, 1671-1677.
63. K. M. Yang, H. Liang and J. Lu, *J Mater Chem*, 2011, **21**, 10390-10398.
64. Z. M. Dong, X. H. Liu, H. W. Liu and Y. S. Li, *Macromolecules*, 2010, **43**, 7985-7992.
65. F. Cheng, E. M. Bonder, A. Doshi and F. Jakle, *Polym Chem*, 2012, **3**, 596-600.
66. A. Blencowe, J. F. Tan, T. K. Goh and G. G. Qiao, *Polymer*, 2009, **50**, 5-32.
67. F. H. Meng, W. E. Hennink and Z. Zhong, *Biomaterials*, 2009, **30**, 2180-2198.
68. A. H. Soeriyadi, G. Z. Li, S. Slavin, M. W. Jones, C. M. Amos, C. R. Becer, M. R. Whittaker, D. M. Haddleton, C. Boyer and T. P. Davis, *Polym Chem* 2011, **2**, 815-822.
69. M. Li, P. De, H. M. Li and B. S. Sumerlin, *Polym Chem*, 2010, **1**, 854-859.
70. G. Y. Wu, Y. Z. Fang, S. Yang, J. R. Lupton and N. D. Turner, *J Nutr*, 2004, **134**, 489-492.
71. R. R. Perry, J. Mazetta, M. Levin and S. C. Barranco, *Cancer*, 1993, **72**, 783-787.
72. A. Russo, W. Degraff, N. Friedman and J. B. Mitchell, *Cancer Res*, 1986, **46**, 2845-2848.

# Chapter 4
# Multifunctional Hyperbranched Polymers for CT/F-19 MRI Bimodal Molecular Imaging

## 4.1 Introduction

In recent decades clinical diagnosis has advanced rapidly owing to the emergence of modern imaging techniques, such as magnetic resonance imaging (MRI), computed tomography (CT), positron emission tomography (PET), single photon emission computed tomography (SPECT), optical imaging, ultrasonography, etc. Although these techniques are frequently employed in the clinic and in research, each modality has its own advantages and limitations. For instance, optical imaging has high sensitivity but poor tissue penetration, while MRI provides high spatial resolution and no tissue penetration limitations but suffers from low sensitivity and relatively long imaging time.[1] Therefore, in some cases a single modality cannot offer sufficiently comprehensive data required for accurate diagnosis. In recognition of this the combination of two or more modalities has been a trend in both research and clinic applications in recent years.[2-5] Compared to single modality imaging, complementary information can be obtained through multimodal imaging, such as PET/CT, PET/MRI and optical/MRI, facilitating accurate diagnosis as well as assisting treatment.

The development of nanotechnology has brought enormous possibilities for the design of nanoparticle (NP)-based molecular imaging agents. Owing to the unique physicochemical properties of NPs, NP-based agents have a number of advantages compared with their small molecule counterparts, e.g. longer circulation time, integration of different functionalities, controllable size and surface properties, etc.[2] In the past decade a significant range of NP-based multimodal imaging agents have been developed, and this has greatly bolstered the prospects of multimodal imaging techniques. [2, 6-8]

Magnetic resonance imaging (MRI) is a non-invasive and non-destructive imaging modality that can generate 3D anatomic images of patients with high resolution in particular for soft tissue. In contrast, X-ray CT can produce images with high spatial resolution for hard tissue but it has poor contrast for soft tissue. Therefore the synergetic application of MRI and CT is attractive as this can

enhance the imaging capability. In recent years, considerable attention has been paid to the design of CT/MRI contrast agents.[9-18] Most proposed agents have been based on liposomes, inorganic NPs or polymer-containing hybrid NPs. Surprisingly, CT/MRI agents based on dendritic polymers including hyperbranched polymers (HBPs) and dendrimers have not been reported to this date, regardless of their advantages for nanomedicine such as long blood retention time, 3D globular structure, multifunctional sites for functionalisation, intramolecular cavity for drug loading, biocompatibility, biodegradability, etc.[19-23]

Since the first study in 1977,[24] $^{19}$F MRI has been recognised as a promising complementary modality to $^{1}$H MRI, which is currently the dominant MRI in routine clinic scans. $^{19}$F MRI has a number of advantages, the most remarkable being the physiological rarity of $^{19}$F in the human body which can eliminate confounding background signals and thus generate selective $^{19}$F MRI images.[25] In the past few years, polymeric $^{19}$F MRI agents have attracted increasing attention. A wide range of $^{19}$F-containing polymers have been synthesised and evaluated as $^{19}$F MRI contrast agents, including linear polymers,[26-29] star polymers,[30, 31] hyperbranched and dendritic polymers,[32-38] nanogels,[39, 40] etc.

The combination of CT and $^{19}$F MRI can allow for the imaging for hard tissue as well as the visualising of imaging probes. To the best of our knowledge, there is no literature reporting the design of CT/$^{19}$F MRI molecular imaging agents. Herein we report the design of multifunctional hyperbranched polymers containing iodine and fluorine and their application as CT/$^{19}$F MRI bimodal imaging contrast agents. The synthetic route is described in Scheme 4-1. In the first step, a hyperbranched iodopolymer (HBIP) was synthesised via reversible addition-fragmentation chain transfer (RAFT) polymerisation based on a previously reported procedure.[41] Specifically, the iodine-containing monomer, 2-(2',3',5'-triiodobenzoyl)ethyl methacrylate (TIBMA), was incorporated to introduce iodine atoms to provide X-ray opacity. The macromonomer, poly(ethylene glycol) methyl ether methacrylate (PEGMA, MW = 475 g mol$^{-1}$), was copolymerised to provide hydrophilicity. The disulfide-containing bifunctional monomer, bis2-(methacryloyl)oxyethyl disulfide (DSDMA), was chosen as a crosslinker to form branching structures and to achieve biodegradability. In the second step, the as-synthesised HBIP was used as a macro chain transfer agent (macro-CTA) and was chain extended with 2,2,2-trifluoroethyl acrylate (TFEA) and PEGMA. Finally hyperbranched iodopolymers containing $^{19}$F (HBIPF) were obtained. According to the chemical structure, the iodine atoms were positioned within the branched inner part while the $^{19}$F nuclei were dispersed in the outer copolymer chains. Since the

polymers contained both iodine and fluorine, it was thus expect that they could be utilised as molecular imaging agents for CT/$^{19}$F MRI bimodal imaging.

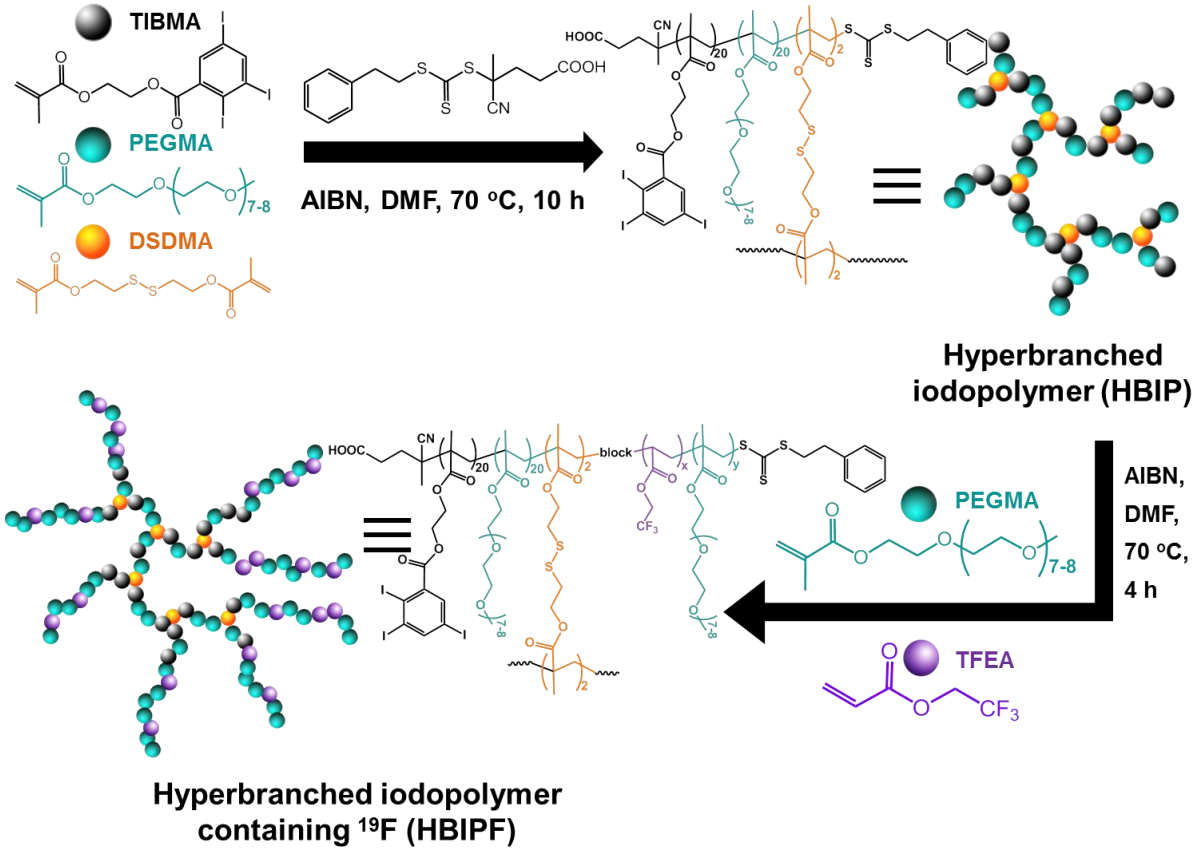


**Scheme 4-1** Schematic illustration of the synthesis of hyperbranched polymer containing iodine and fluorine.

## 4.2 Experimental Section

### 4.2.1 Materials

All chemicals were purchased from Sigma-Aldrich unless otherwise stated. Poly(ethylene) glycol methyl ether methacrylate (PEGMA, MW = 475 g mol$^{-1}$) and 2,2,2-trifluoroethyl acrylate (TFEA) were passed through basic alumina columns to remove inhibitors before use. 2,2'-Azobis(2-methylpropionitrile) (AIBN) was recrystallised twice from methanol prior to use. Bis(2-methacryloyl)oxyethyl disulfide (DSDMA) was synthesised following procedures published previously.[31, 42] The chain transfer agent (CTA), 4-cyano-4-(2-phenylethane sulfanylthiocarbonyl)

sulfanylpentanoic acid (PETTC), was synthesised according to a previously reported method.[43] 4-(Dimethylamino)pyridine (DMAP), tris(2-carboxyethyl)phosphine hydrochloride (TCEP) and reduced L-glutathione (GSH) were used as received. N,N'-dicyclohexylcarbodiimide (DCC) were ordered from Alfa Aesar. Milli-Q water with a resistivity of 18.4 MΩ $cm^{-1}$ was used for all the experiments that require water. Tetrahydrofuran (THF), dichloromethane (DCM) and N,N-dimethylformamide (DMF) were obtained from a solvent purification system (MB-SPS-800-Auto, Mbraun) and used directly. All other organic solvents were of analytical grade. Amicon ultra-15 centrifugal filter units (100k) were purchased from Merck Millipore.

## 4.2.2 Synthesis

### 4.2.2.1 Synthesis of 2-(2',3',5'-Triiodobenzoyl)ethyl Methacrylate (TIBMA)

TIBMA was prepared following an approach published elsewhere.[44, 45] Typically, 1,3,5-triiodobenzoic acid (10 g, 20 mmol), 2-hydroxyethyl methacrylate (5.2 g, 40 mmol) and DMAP (0.54 g, 4.4 mol) were mixed in 150 mL of DCM in a 500 mL flask. DCC (9.08 g, 44 mmol) in 50 mL of DCM was added dropwise to the above mixture over 10 min, and the solution was then stirred at room temperature for 24 h in the dark. After reaction, the mixture was filtered, and the filtrate was washed successively with HCl (2 M, 200 mL × 3) and saturated $NaHCO_3$ (200 mL × 3). Then the filtrate was dried over anhydrous $MgSO_4$, followed by filtration. The dark brown solution was collected and concentrated by rotary evaporation, then it was recrystallised from hexane/ethyl acetate (10/90, v/v) twice. Finally, the obtained pale soft powder was dried in vacuum at room temperature. Yield: 9.17 g, 75%. $^1$H NMR (500 MHz, $CDCl_3$, ppm): 8.43 and 7.80 (2H, d, phenyl protons), 6.12 and 5.75 (2H, s, vinyl protons), 4.55 and 4.47 (4H, m, COOC$\underline{H}_2$C$\underline{H}_2$), 1.94 (3H, s, C$\underline{H}_3$). $^{13}$C NMR (125 MHz, $CDCl_3$, ppm): 166.80, 148.71, 142.47, 136.80, 127.25, 115.36, 108.16, 96.19, 64.81, 62.97, 18.91.

### 4.2.2.2 Synthesis of Hyperbranched Iodopolymer (HBIP)

The HBIP was synthesised by RAFT polymerisation. In a typical experiment, TIBMA (3.672 g, 6 mmol), PEGMA (2.85 g, 6 mmol), DSDMA (0.174 g, 0.6 mmol), PETTC (0.102 g, 0.3 mmol) and AIBN (4.92 mg, 0.03 mmol) were dissolved in 7.12 mL of DMF in a 50 mL flask. Next the flask was sealed with a rubber septum and purged with argon for 30 min in an ice bath. Then the flask was placed in a 70 $^o$C oil bath and magnetically stirred for 10 h. After that the polymerisation was quenched by immersing the flask in ice bath and exposing it to air. The crude solution was

precipitated into cold diethyl ether three times. Finally a brown viscous solid was obtained after drying in vacuum at room temperature. Yield: 6 g, 88%. GPC MALLS: $M_n$ = 1.57 × $10^5$ g $mol^{-1}$, molar mass dispersity ($Đ_M$, $M_w/M_n$) = 2.2.

#### 4.2.2.3 Synthesis of Hyperbranched Iodopolymer Containing $^{19}F$ (HBIPF)

The HBIPF was prepared through chain extension of HBIPF with TFEA and PEGMA. By varying TFEA/PEGMA feed ratio, HBIPF-1, HBIPF-2 and HBIPF-3 with different compositions were synthesised. The synthesis of HBIPF-1 is described here as an example. HBIP (0.4 g, 2.55 ×$10^{-3}$ mmol, equivalent to 0.018 mmol of CTA), TFEA (0.055 g, 0.36 mmol), PEGMA (0.684 g, 1.44 mmol) and AIBN (0.59 mg, 0.0036 mmol) were dissolved in 3.6 mL DMF in a 25 mL flask, which was then sealed with a rubber septum and purged with argon for 20 min in ice bath. After that the flask was placed in 70 $^oC$ oil bath and stirred for 4 h. Then the polymerisation was cooled down using an ice bath and exposed to air. The crude solution was precipitated into cold diethyl ether three times, and the collected polymer was further purified by centrifugal filtration (Amicon Ultra-15, 100k). After lyophilisation, a yellowish viscous solid was obtained. According to $^1H$ NMR, the monomer conversions of TFEA and PEGMA were 30% and 52%, respectively. GPC MALLS: $M_n$ = 2.27 × $10^5$ g $mol^{-1}$, molar mass dispersity ($Đ_M$, $M_w/M_n$) = 2.0. Yield: 0.65 g, 84%.

#### 4.2.2.4 Degradation of HBIP Using Reducing Agents

In order to study the degradation using TCEP, HBIP (20 mg, 8.81 × $10^{-4}$ mmol) and TCEP (10.1 mg, 0.035 mmol) were dissolved in 1 mL methanol. The solution was purged with argon for 20 min and then stirred at room temperature for 24 h. An aliquot was sampled for GPC analysis.

For the treatment by GSH, HBIP (20 mg, 8.81 × $10^{-4}$ mmol) and GSH (21.6 mg, 0.07 mmol) were dissolved in 7 mL of PBS. The concentration of GSH was 10 mM. The solution was purged with argon for 20 min and then stirred at room temperature for 24 h. An aliquot was withdrawn and lyophilised for GPC analysis.

### 4.2.3 Characterisation

#### Gel Permeation Chromatography (GPC)

Molecular weights and molecular weight distributions were determined by GPC using a Waters Alliance 2690 Separations Module equipped with Waters 2414 Refractive Index (RI) Detector,

Waters 2489 UV/Visible Detector, Waters 717 Plus Autosampler and Waters 1515 Isocratic HPLC Pump. Samples were dissolved in THF and passed through 0.45 μm filters before each measurement. THF was used as the mobile phase at a flow rate of 1 mL min $^{-1}$. The system was calibrated using polystyrene (PS) standards, to which the number average molecular weight ($M_n$) and weight average molecular weight ($M_w$) were referenced. For measuring absolute molecular weights, a multi angle laser light scattering (MALLS) detector (DAWN 8+, Wyatt) was attached to the GPC, and the polymer solutions were eluted at a flow rate of 1 mg mL$^{-1}$ in THF. The refractive index increment (*dn/dc*) was determined by using ATAGO Pocket Refractometer at room temperature. Briefly, polymers were dissolved in THF at a range of concentrations from 10 to 300 mg mL$^{-1}$, and the refractive index of each solution was measured 5 times to get the average value. The *dn/dc* for each sample was calculated based on those values. The *dn/dc* values for HBIP and HBIPFs were 0.085 and 0.070, respectively.

**Nuclear Magnetic Resonance (NMR)**

$^{1}$H NMR and $^{13}$C NMR were performed on a Bruker Avance 500 MHz spectrometer equipped with a BBO5 probe at 25 $^{o}$C using an internal lock ($CDCl_3$) and referenced to the residual non-deuterated solvent ($CHCl_3$).

**Dynamic Light Scattering (DLS)**

DLS measurements were carried out on a Nanoseries Zetasizer (Malvern, UK) at 25 $^{o}$C. Sample solutions were prepared in PBS (1 mg mL$^{-1}$) at different pH values and passed through 0.45 μm filters prior to each measurement. Each hydrodynamic diameter was the average value of 5 measurements. To minimise the influence of large aggregates, number averaged diameters are reported.

**Transmission Electron Microscopy (TEM)**

TEM experiments were conducted on a JOEL JEM-1010 transmission electron microscope at 80 kV. Samples were prepared by dropping polymer solutions (5 mg mL$^{-1}$ in water) onto copper grids coated with glow discharged carbon, which were then left at room temperature overnight until dry. For each sample, a number of areas on the grid were examined and different magnifications were applied. Representative images are provided in this chapter.

### $^{19}$F Nuclear Magnetic Resonance ($^{19}$F NMR)

All $^{19}$F NMR spectra were acquired at 470.55 MHz without $^{1}$H decoupling on a Bruker Avance 500 spectrometer using a 5 mm broadband inverse probe (BBO5) for which the inner coil was double-tuned for $^{19}$F and $^{1}$H. The samples were prepared by dissolving the star polymers in PBS/$D_2O$ (90/10, v/v) at a concentration of 100 mg mL$^{-1}$. All measurements were performed at 25 $^{o}$C. A 90$^{o}$ pulse of 15.1 μs was used in all measurements, the relaxation delay was 2 s and the acquisition time was 0.7 s. Data were collected using a spectrum width of 23 kHz, 32k data points and 128 scans.

$^{19}$F spin-spin relaxation times ($T_2$) were measured using the Carr-Purcell-Meiboom-Gill (CPMG) pulse sequence at 25 $^{o}$C. The samples were dissolved in PBS/$D_2O$ (90/10, v/v) at a concentration of 100 mg mL$^{-1}$. The relaxation delay was 3 s and the acquisition time was 0.7 s. For each measurement, the echo times were from 2 to 770 ms and 15 points were collected, which could be described by exponential functions for the calculation of $T_2$. Only values for the major peaks are reported.

$^{19}$F spin-lattice ($T_1$) relaxation times were measured using the standard inversion-recovery pulse sequence. For each measurement, the recovery times were from 2 ms to 3 s and 15 points were acquired. Only values for the major peaks are reported.

### $^{19}$F Magnetic Resonance imaging ($^{19}$F MRI)

Images of phantoms containing the solutions of the HBIPF nanoparticles were acquired on a Bruker BioSpec 94/30 USR 9.4 T small animal MRI scanner. HBIPFs were dissolved in PBS/$D_2O$ (90/10,v/v) at different concentrations and were loaded in 30 × 8 mm clear vials， which were placed in a $^{1}$H/$^{19}$F dual resonator 40 mm volume coil. $^{1}$H images were acquired for localisation of the samples using a RARE sequence with an echo train length of 8 (TE = 28 ms, TR = 2 s, FOV = 40 × 40 × 1 mm, Matrix = 256 × 256 × 1). $^{19}$F images were acquired in the same stereotactic space as the $^{1}$H image using a RARE sequence with an echo train length of 8 (TE = 10 ms, effective TE = 40 ms, TR = 1 s, FOV = 40 × 40 × 10 mm, Matrix = 40 × 40 × 1, No. Averages = 256) and a total acquisition time of 21 minutes.

### Computed Tomography (CT)

Images of phantoms containing the solutions of the HBIPF nanoparticles were acquired on a Siemens Inveon Preclinical PET/CT scanner. HBPIFs were dissolved in PBS at different

concentrations and were loaded in 30 × 8 mm clear vials. Each sample was imaged individually to avoid the confound of X-ray attenuation across the sample space. Each sample was placed in the centre of the X-ray field and images were acquired using an X-ray source with the voltage set to 80 kV and the current set to 500 µA. Scans were performed using 360° rotation with 180 rotation steps with low magnification and a binning factor of 4. Exposure time was 230 ms with an effective voxel size of 106 µm. CT images were reconstructed using the Cobra software package (Siemens) and normalised to a phantom containing pure water where Hounsfield units were set to 0 for pure water and -1000 for air.

## 4.3 Results and Discussion

### 4.3.1 Synthesis of Partly-fluorinated Hyperbranched Iodopolymers

Since the pioneer work reported by Davy and co-workers,[44, 46] 2-(2',3',5'-triiodobenzoyl)ethyl methacrylate (TIBMA) has drawn much attention as a typical iodo-monomer for the synthesis of X-ray-opaque polymeric materials.[13, 45, 47-53] To date, most of the TIBMA-based polymeric agents have been microparticles prepared by conventional free radical polymerisation, whereas there are very few reports of TIBMA-based polymeric agents with hyperbranched or dendritic structures synthesised by controlled radical polymerisation.[54, 55] As introduced above, hyperbranched polymers possess a number of unique advantages, thus it is desirable to explore the synthesis of TIBMA-based hyperbranched polymers. These can be prepared via controlled polymerisation methods such as RAFT polymerisation,[56] which can be utilised for the synthesis of well-defined and complex architectures.[57, 58] As the TIBMA homopolymer is hydrophobic, it is important to increase the hydrophilicity by copolymerisation with PEGMA. This approach introduces polyethylene glycol side chains and has been widely used for preparing hydrophilic and biocompatible materials.[59] Furthermore, the crosslinker DSDMA used here contains a disulfide bond that can be cleaved in the presence of reducing agents,[60-62], facilitating the removal of the polymers from the body for *in vivo* applications.

The iodo-monomer TIBMA was synthesised by the esterification between 1,3,5-triiodobenzoic acid and 2-hydroxyethyl methacrylate, and was purified by recrystallisation (see Appendix C Figure A4.1 for $^{1}$H and $^{13}$C NMR spectra). The RAFT agents PETTC was chosen because of the well-resolved peaks of its two aromatic protons at 8.43 and 7.80 ppm, facilitating the determination of degree of polymerisation by $^{1}$H NMR (see Appendix C Figure A4.2 for $^{1}$H and $^{13}$C NMR spectra). Hyperbranched iodopolymers (HBIPs) were synthesised from the monomers TIBMA, PEGMA and

DSDMA via RAFT polymerisation. The feed ratio of TIBMA/PEGMA/DSDMA/PETTC/AIBN was set to be 20/20/2/1/0.1. During the polymerisation, the conversion of the three monomers was monitored by $^{1}$H NMR, and reached above 97% within 10 hours, indicating a fast rate of polymerisation. As listed in Table 4-1, the as-synthesised HBIP had an absolute $M_n$ of 157 kDa with a relatively low (for a hyperbranched structure) molar mass dispersity, $Đ_M$, of 2.2. For each HBIP molecule, the number of CTA functionalities ($N_{CTA}$) was calculated to be 7, confirming the highly branched structure of the HBIP.

The HBIP was then used as a macro-CTA and chain extended with TFEA and PEGMA for the synthesis of hyperbranched iodopolymers containing $^{19}$F (HBIPF). To investigate the effect of fluorine content on the $^{19}$F MRI performance, three feed ratios of TFEA/PEGMA/CTA were used, i.e. 20/80/1, 40/80/1 and 80/80/1. The polymerisations were allowed to proceed for 4 hours, and the conversions of TFEA and PEGMA were approximately 30% and 52%, respectively. The resultant HBIPF samples with different TFEA/PEGMA compositions were denoted as HBIPF-1, HBIPF-2 and HBIPF-3, respectively. As shown in Table 4-1, all the HBIPFs had larger $M_n$ than the HBIP macro-CTA, meanwhile the $Đ_M$ still kept low at 2.0, demonstrating successful chain extension of HBIP via RAFT polymerisation.

**Table 4-1** GPC and $^{1}$H NMR data for the HBIP and HBIPFs

| Sample | TIBMA/PEGMA /DSDMA in 1st block[a] | TFEA/PEGMA in 2nd block[a] | $M_n$ (each chain, kDa)[b] | Absolute $M_n$ (kDa)[c] | $Đ_M$[c] | $N_{CTA}$[d] |
|---|---|---|---|---|---|---|
| HBIP | 20/20/2 | — | 22.7 | 157 | 2.2 | 7 |
| HBIPF-1 | 20/20/2 | 10/45 | 45.6 | 227 | 2.0 | 5 |
| HBIPF-2 | 20/20/2 | 10/34 | 40.4 | 238 | 2.0 | 6 |
| HBIPF-3 | 20/20/2 | 37/52 | 53.0 | 207 | 2.0 | 4 |

[a] Degree of polymerisation (DP) was obtained from $^{1}$H NMR results. [b] $M_n$ for each chain was calculated based on $^{1}$H NMR. [c] Absolute molecular weight was measured by GPC MALLS. [d] Number of CTA functionalities per each molecule was estimated through the equation ($N_{CTA}$) = $M_n$ (GPC MALLS)/$M_n$ ($^{1}$H NMR),[32, 63] presuming that the branched structure was formed by inter-chain reaction rather than intra-chain cyclisation.

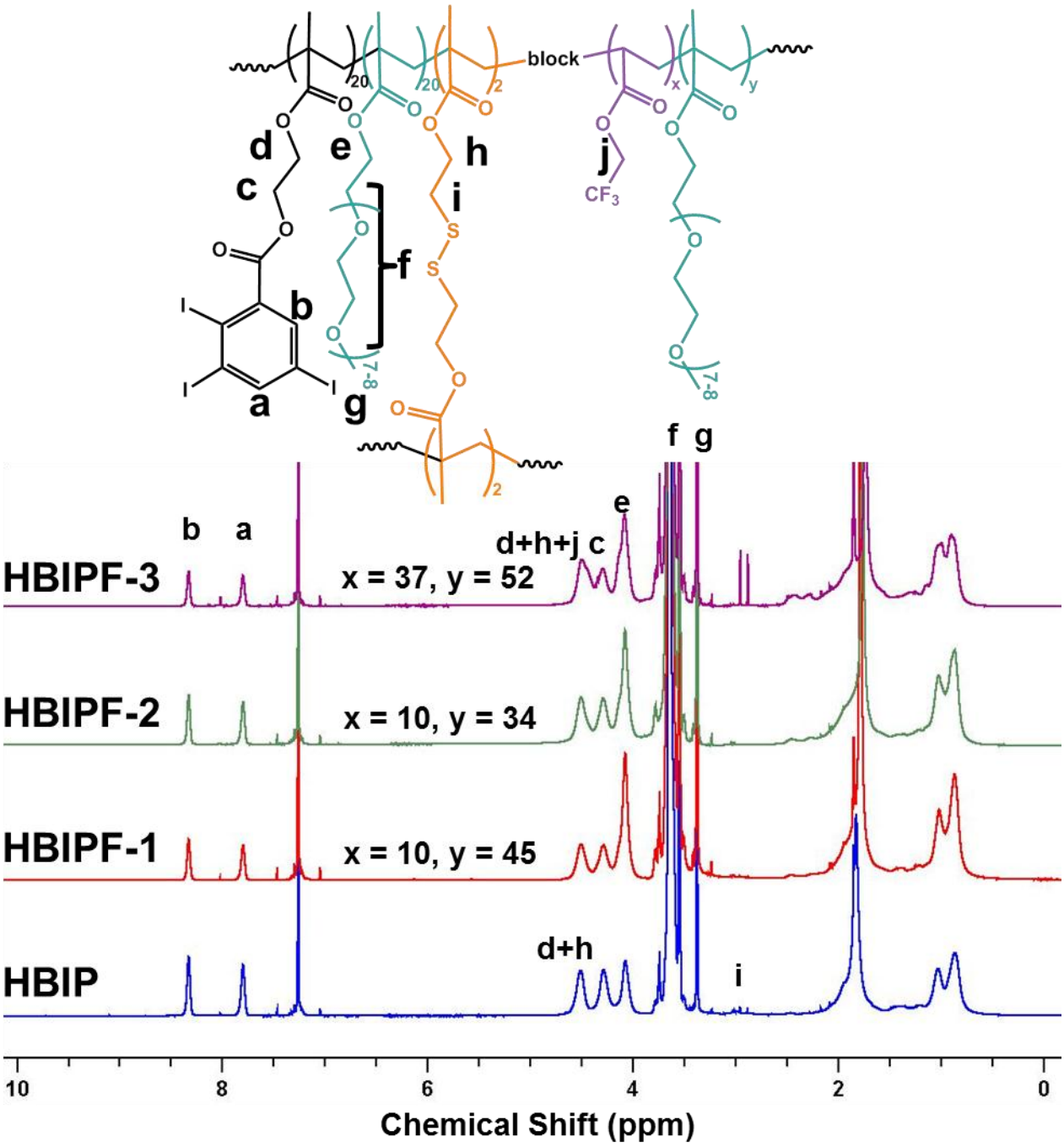


**Figure 4-1** $^{1}$H NMR spectra of HBIP and HBIPFs in $CDCl_3$ at 25 $^{o}$C.

As displayed in Figure 4-1, the chemical structures of HBIP and HBIPFs were characterised by $^{1}$H NMR. Specific peaks in the spectra were assigned to protons of TIBMA, PEGMA and DSDMA, as shown in the spectra. For all the samples, the protons of the aromatic ring were observed at 7.8 and 8.3 ppm, respectively. In addition, for the samples after chain extension, the peak of the two protons in the methylene group adjacent to -$CF_3$ was found to be overlapped with the peaks at 4.4~4.7 ppm, however the integral of this peak became larger with increasing TFEA/PEGMA feed ratio,

suggesting an increasing amount of TFEA incorporated into the second block. Therefore, $^{1}$H NMR results revealed the chemical structures of the samples and confirmed the successful chain extension of HBIP. Based on $^{1}$H NMR results, the DP of each polymer chain was calculated and the content of iodine and fluorine was obtained. As listed in Table 4-2, the iodine content of HBIPFs was relatively constant at 17 ± 2.5 wt%. The weight percentages of $^{19}$F of both the polymer and the 2$^{nd}$ block were also provided in Table 4-2. The fluorine content of the polymer is required for the determination of $^{19}$F concentration for $^{19}$F MRI. However, the fluorine content of the 2$^{nd}$ block is crucial for the study of $^{19}$F NMR properties of the polymers because it can directly affect the mobility of $^{19}$F nuclei in aqueous solution.

**Table 4-2** Properties of HBIP and HBIPFs

| Sample | I wt%[a] of each molecule | $^{19}$F wt%[a] of each molecule | $^{19}$F wt%[a] of the 2$^{nd}$ block | $T_1$ (ms)[b] | $T_2$ (ms)[b] | $D_h$ (nm)[c] |
|---|---|---|---|---|---|---|
| HBIP | 33.6 | 0 | - | - | - | 12.24±2.31 |
| HBIPF-1 | 17.0 | 1.3 | 2.5 | 405 | 61 | 13.49±1.05 |
| HBIPF-2 | 19.0 | 1.4 | 3.2 | 374 | 38 | 13.09±1.28 |
| HBIPF-3 | 14.4 | 4.0 | 6.9 | 102 | 11 | 12.45±1.03 |

[a] Iodine and fluorine weight percentages were calculated based on $^{1}$H NMR results. [b] $T_1$ and $T_2$ of $^{19}$F were determined by $^{19}$F NMR. [c] Hydrodynamic diameter ($D_h$) was measured by DLS in water at 25 $^{o}$C.

### 4.3.2 Examination of $^{19}$F NMR Properties

The HBIPFs were also characterised by $^{19}$F NMR. As shown in Figure 4-2, the peaks at -72~-74.4 ppm confirmed the presence of $^{19}$F in the HBIPFs. The bimodal nature of the peaks indicated that there are possibly two chemical environments for the $^{19}$F nuclei. We propose that this is due to different sequence distributions caused by the largely different reactivity ratios of TFEA/PEGMA (0.22 and 2.46, respectively).[64] Hence, segments of PTFEA homopolymer and P(TFEA-co-PEGMA) statistical copolymer co-existed in the second block, resulting in two $^{19}$F resonances. Furthermore, the peak width also increased with $^{19}$F content, indicating that the $^{19}$F nuclei are experiencing stronger dipolar coupling at higher $^{19}$F content. The spin-lattice relaxation time ($T_1$) and spin-spin relaxation time ($T_2$), which are two important parameters for $^{19}$F MRI, were also

determined by $^{19}$F NMR. As displayed in Table 4-2, when the fluorine content was increased from 0.6 to 4.0 wt%, $T_2$ dropped from 61 to 11 ms. We previously reported that $T_2$ could be significantly affected by the $^{19}$F content of similar polymers because of the hydrophobic nature of the fluorinated segments.[28, 30, 31] To be more specific, in aqueous solution, a high fluorine content can induce aggregation of these units, which reduces the mobility of the $^{19}$F nuclei resulting in short $T_2$ values. In Chapter 2 and 3, it was observed that $T_1$ was not greatly affected by the change in polymer dimensions. However, in this work, the $T_1$ of HBIPF-3 was measured to be 102 ms, which is much shorter than those of HBIPF-1 and 2. This is not surprising because $T_1$ generally decreases with $T_2$ in a certain range of correlation time in a fixed magnetic field.[65] We thus assume that $T_1$ could be significantly related to the composition or tacticity of the copolymer chain. Since long $T_2$ and short $T_1$ relaxation times are preferred for spin-echo imaging,[27] it is essential to not only achieve high fluorine content but also prevent the fluorine nuclei from associating strongly.

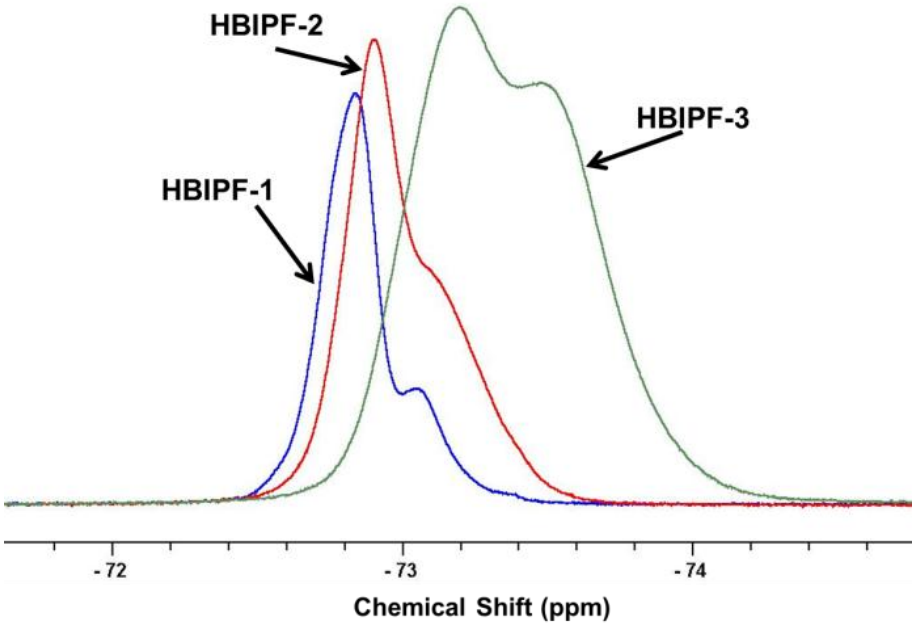


**Figure 4-2** $^{19}$F NMR spectra of HBIPFs.

### 4.3.3 Studies of Morphology

Owing to the incorporation of significant concentrations of hydrophilic PEGMA monomer units, the as synthesised HBIP and HBIPFs were water soluble. Nanoparticles could be formed by direct dissolution of the polymers in water (1 mg mL$^{-1}$), and the particle size was measured by dynamic light scattering (DLS) at 25 $^{o}$C. As shown in Table 4-2, the number-averaged diameter of all three HBIPFs was approximately 13 nm, which was slightly larger than that of the HBIP, indicating an

increased size after chain extension. The size and morphology were also studied by transmission electron microscopy (TEM) (Figure 4-3), and the majority of HBIPF-1 nanoparticles exhibited a size of ~6 nm, which was smaller than the size provided by DLS. This is because DLS determines the hydrodynamic diameter of the nanoparticles in aqueous solution, which is generally larger than the size of dehydrated samples observed by TEM experiments.[66] Moreover, a number of large particles (~12 nm) were also found in the TEM images. We propose that a small amount of aggregations were formed owing to the hydrophobic nature of fluorine and iodine units. Hence it could be concluded that the HBPIFs could form nanoparticles with size of ~13 nm in aqueous solution.

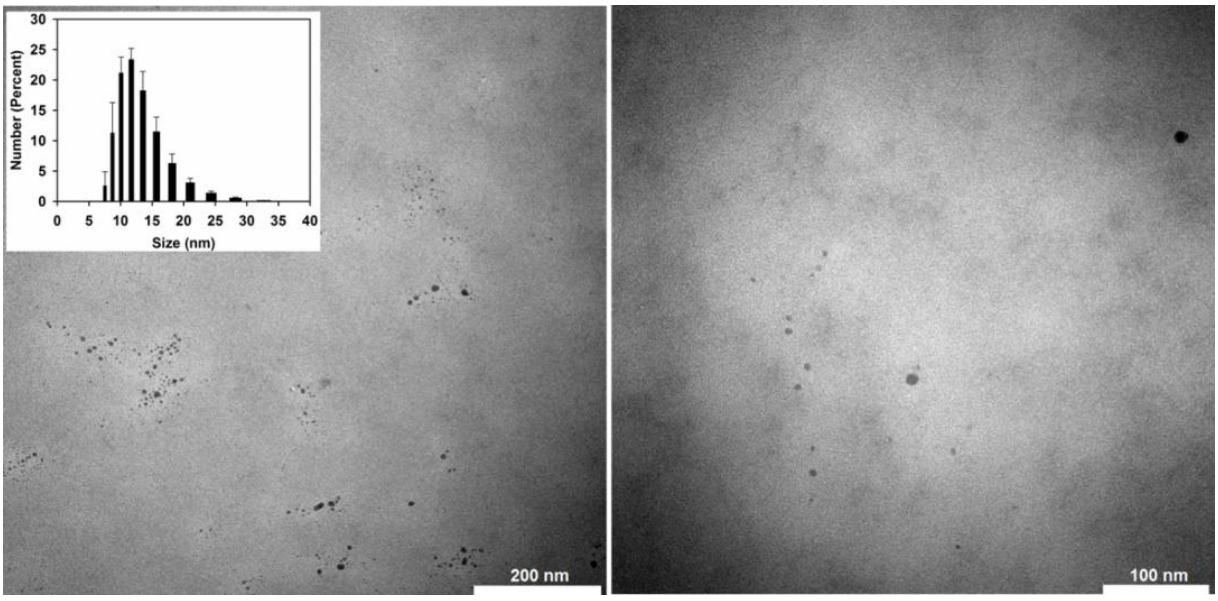


**Figure 4-3** Representative TEM images of HBIPF-1 nanoparticles in water. Inset is the number-averaged size statistics graph acquired by DLS.

### 4.3.4 Degradation of HBIP in Reducing Environment

As mentioned above, the crosslinker DSDMA contains a disulfide bond that is cleavable in the presence of reducing agents. Therefore the HBIP and HBIPFs are expected to be biodegradable. Test of the degradability were carried out by using either TCEP or GSH as reducing agents, and the resultant polymers were characterised by GPC. As shown in Figure 4-4, the original HBIP showed bimodal GPC peaks with retention times of 14.4 and 15.6 min, which is a typical characteristic of hyperbranched polymers synthesised by controlled radical polymerisation in the presence of crosslinkers.[41, 67, 68] After being treated with TCEP in methanol for 24 h, the peak at shorter retention time (14.4 min) almost disappeared, and only a single peak at longer retention time (15.6

min) was observed, demonstrating degradation of the hyperbranched structure via cleavage of disulfide bonds. Similarly, the HBIP was also treated with GSH at a physiological concentration (10 mM)[69] in PBS for 24 h, and the majority of the hyperbranched polymers were degraded. It should be noted that the small peak at 13.2 min arises from polymers formed by re-formation of inter-molecular disulphide bonds on the degraded fragments. We assume that the lower degradation efficiency of GSH was caused by the relatively low concentration of reducing agent. Overall, the GPC results confirmed that incorporation of the crosslinker DSDMA can impart biodegradability to the hyperbranched polymers.

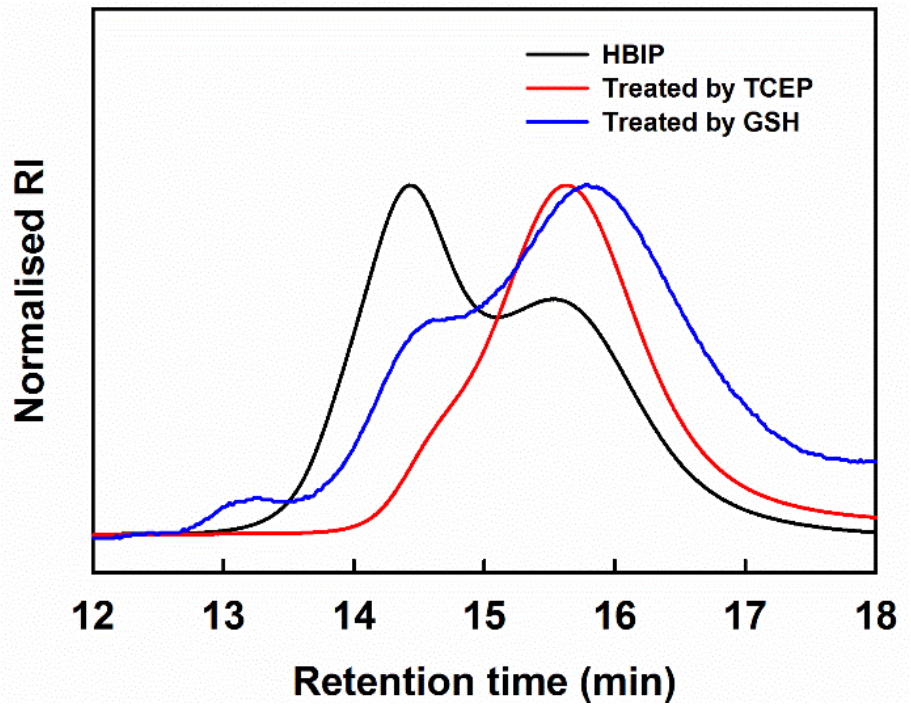


**Figure 4-4** GPC traces for HBIP before and after treatment by TCEP and GSH.

### 4.3.5 Imaging Performance: X-ray CT and $^{19}$F MRI

The imaging performance of the HBIPFs was evaluated by *in vitro* X-ray CT and $^{19}$F MRI experiments. Each sample was dissolved in PBS at four different concentrations and loaded in clear glass vials (8 × 30 mm, 0.75 mL) for imaging tests. The detailed concentrations and results are listed in Table 4-3.

**Table 4-3** Sample concentrations, CT values and signal-to-noise ratio (SNR) of $^{19}$F MRI.

| Sample | [Polymer] | [I] | | [F] | | CT values | $^{19}$F MRI |
|---|---|---|---|---|---|---|---|
| | mg mL$^{-1}$ | mg mL$^{-1}$ | M | mg mL$^{-1}$ | M | (HU) | SNR |
| HBIPF-1 | 11.2 | 1.9 | 0.015 | 0.07 | 0.004 | 18.8±32.3 | 1.96 |
| | 22.4 | 3.8 | 0.030 | 0.14 | 0.008 | 66.3±30.4 | 2.55 |
| | 56 | 9.5 | 0.075 | 0.36 | 0.019 | 278.3±30.3 | 7.77 |
| | 112 | 19 | 0.150 | 0.72 | 0.038 | 571.9±30.9 | 10.83 |
| HBIPF-2 | 10 | 1.9 | 0.015 | 0.10 | 0.005 | 33.6±28.8 | 2.30 |
| | 20 | 3.8 | 0.030 | 0.20 | 0.010 | 90.6±28.5 | 23.23 |
| | 50 | 9.5 | 0.075 | 0.50 | 0.025 | 304±29.8 | 9.82 |
| | 100 | 19 | 0.150 | 1.00 | 0.050 | 591.6±30.4 | 15.29 |
| HBIPF-3 | 13.2 | 1.9 | 0.015 | 0.53 | 0.028 | 2.6±30.4 | 2.67 |
| | 26.4 | 3.8 | 0.030 | 1.06 | 0.056 | 46.3±32.8 | 4.21 |
| | 52.8 | 7.6 | 0.060 | 2.11 | 0.111 | 167.1±31.3 | 9.07 |
| | 105.6 | 15.2 | 0.120 | 4.22 | 0.222 | 333.1±30.9 | 14.75 |

Owing to the high atomic number, and hence high x-ray cross-section of iodine, iodine-based materials have been extensively studied for CT molecular imaging.[70] In recent years, iodine-containing particles and polymers have drawn much attention, such as liposomes,[71, 72] emulsion particles,[73-75] block copolymer micelles,[55] coordination polymers,[76] etc. However, data on dendritic polymer-based agents is scarce. In this work, the radio-opacity of the HBIPFs was evaluated by *in vitro* CT experiments using an Inveon PET/CT scanner (Siemens). As shown in Figure 4-5 (A), all the sample solutions exhibited X-ray opacity, which increased with the polymer concentration. In addition, the CT attenuation (in Hounsfield units) of the region of interest (ROI) showed a linear relationship with iodine concentration (Figure 4-5 (B)).

In a previous report, iodinated polymeric nanoparticles (58 wt% Iodine) were prepared using the same iodine-containing monomer by emulsion polymerisation.[51] The radio-opacification was measured to be 362±1 HU for the nanoparticle dispersion at16 mg mL$^{-1}$ in water (equals to 9.28 mg mL$^{-1}$ iodine). In another paper, an emulsion based on iodinated oils was fabricated and stabilised by block copolymers.[75] These nanoparticles were utilised for *in vivo* CT and tested using mouse models. The CT values for blood, spleen and liver were measured after injection. It was observed that the CT value was proportional to the iodine concentration in the organs, which was calculated

from the change in the CT values. For example, the CT values for iodine concentrations of 10 and 20 mg $ml^{-1}$ were 310±20 and ~620±40 HU, respectively. In our work, the CT values for the sample with 9.5 mg $mL^{-1}$ iodine were 278.3±30.3 HU and 304±29.8 HU for HBIPF-1 and HBIPF-2, respectively, while the CT values for the sample with 19 mg $mL^{-1}$ iodine were measured to be 571.9±30.9 HU and 591.6±30.4 HU for HBIPF-1 and HBIPF-2, respectively. Because the CT values for specific iodine concentrations were close to those reported in the literatures, we suggest that the radio-opacity of the iodinated polymers was only related to the iodine concentration, and was not significantly affected by the architecture, morphology or composition of the polymeric materials. Notably, the CT values of *in vitro* and *in vivo* studies were relatively close, similarly suggesting that the radio-opacity was not affected by the physiological environment. Therefore these results confirm that the HBIPFs have the potential for application as *in vivo* CT agents.

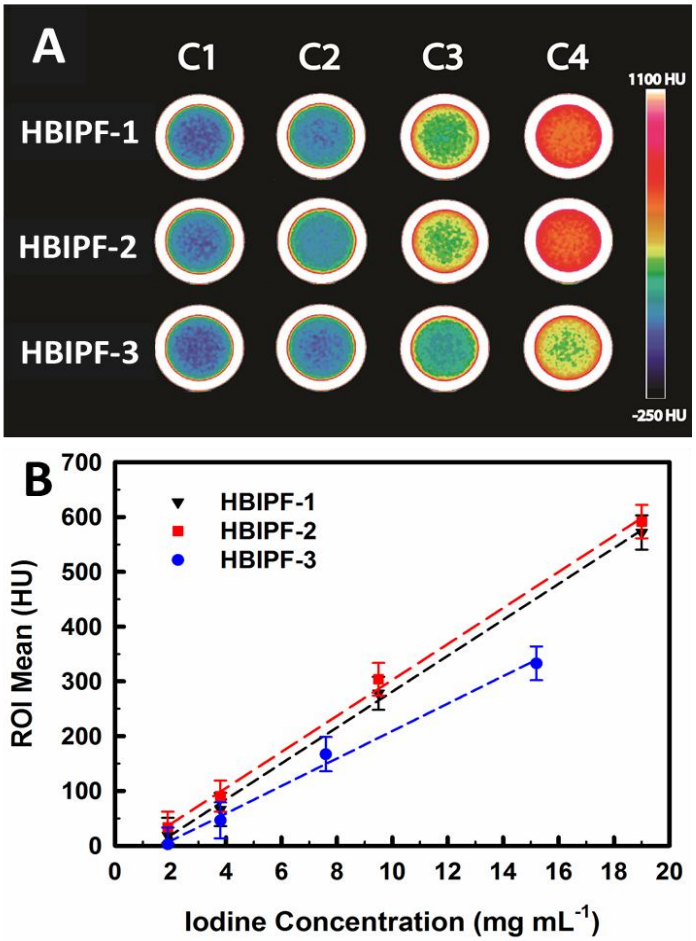


**Figure 4-5** (A) *In vitro* CT phantom images of HBIPFs aqueous solutions with different iodine concentrations. For HBIPF-1 and HBIPF-2, C1 = 0.015 M, C2 = 0.030 M, C3 = 0.075 M, C4 = 0.150 M. For HBIPF-3, C1 = 0.015 M, C2 = 0.030 M, C3 = 0.060 M, C4 = 0.120 M. (B) The corresponding CT values of ROI as a function of iodine concentration.

The NMR detectable $^{19}F$ nuclei were confirmed by $^{19}F$ NMR, indicating that the HBIPFs developed here could have potential as contrast agents for $^{19}F$ MRI. The same solutions of HBIPFs examined by x-ray CT were assessed by $^{19}F$ MRI. As depicted in Figure 4-6 (A), the HBIPF nanoparticles provided positive signals at all concentrations. When the fluorine concentration was relatively high (C3 and C4 for all the samples), the nanoparticles could be particularly well imaged. From Figure 4-6 (B), one can see that the signal-to-noise ratio (SNR) was directly proportional to fluorine content. Moreover, the SNR for HBIPF-2 was slightly higher than that of HBIPF-1 because of the increase in fluorine content from 0.64% to 1%. However, the SNR for HBIPF-3 was significantly lower than for the other samples. This can be explained by the considerably increased fluorine content (4%) causing aggregation of fluorine nuclei in water and thus resulting in greatly shortened $T_2$ relaxation times, as was revealed by $^{19}F$ NMR.

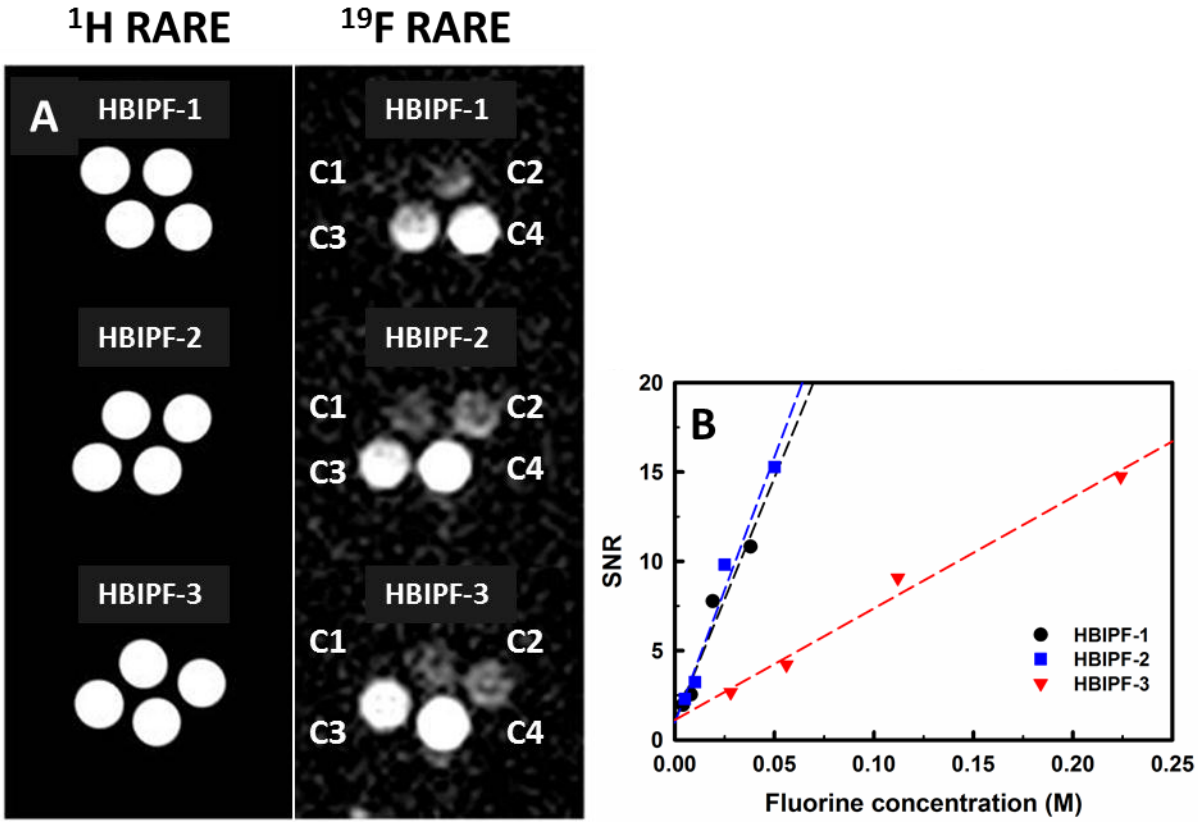


**Figure 4-6** (A) *In vitro* $^{19}F$ MRI phantom images of aqueous solutions of HBIPFs at different fluorine concentrations. The concentrations are the same as those in Figure 4-5. Note: $^{1}H$ RARE images were used for the localisation of the field of view. (B) Signal-to-noise ratio (SNR) in $^{19}F$ MRI as a function of fluorine concentration.

As studied in Chapter 2 and Chapter 3, the $T_2$ relaxation time was shortened with the increase of $^{19}$F content of the polymers due to the increased association of $^{19}$F segments in aqueous solution. For example, at pH 4~7.4, the $T_2$s of the sample CCS-2 (3.9 wt% of $^{19}$F) were nearly half of those of the sample CCS-1 (2.3 wt% of $^{19}$F), indicating the dramatically increased aggregation of $^{19}$F units at higher $^{19}$F content. Consequently, the $^{19}$F MRI SNR of CCS-2 was significantly lower than that of CCS-1.[31] In this Chapter, similar results were obtained. The observation of lowest SNR of HBIPF-3 is in accord with previous findings, supporting that long $T_2$s (mobile $^{19}$F nuclei) are preferred for spin-echo imaging. However, the SNR of HBIPF-2 (1 wt% of $^{19}$F, $T_2$ = 38 ms) was slightly higher than that of HBIPF-1 (0.6 wt% of $^{19}$F, $T_2$ = 61 ms), confirming that $^{19}$F concentration was also another crucial factor for $^{19}$F MRI. Therefore both high $^{19}$F content and long $T_2$ are prerequisite for the design of $^{19}$F MRI CAs with high efficiency.

## 4.4 Conclusions

In conclusion, multifunctional hyperbranched polymers containing iodine and fluorine were synthesised via RAFT polymerisation. The content of iodine and fluorine could be tuned by varying the monomer feed ratio for the chain extension reaction. The HBIPFs could be degraded by treatment of reducing agents such as GSH and TCEP, and thus the polymer would be likely excreted *in vivo*. By direct dissolution of the HBIPFs in water, nanoparticles were formed with diameters between 10~15 nm. In aqueous solution, the radio-opacity of these nanoparticles was confirmed by *in vitro* CT experiments. In addition, solutions of the nanoparticles could be visualised by $^{19}$F MRI. These results suggest that the HBIPFs are promising molecular imaging agents for CT/$^{19}$F MRI bimodal imaging.

## 4.5 References

1. J. K. Willmann, N. van Bruggen, L. M. Dinkelborg and S. S. Gambhir, *Nat Rev Drug Discov*, 2008, **7**, 591-607.
2. D. E. Lee, H. Koo, I. C. Sun, J. H. Ryu, K. Kim and I. C. Kwon, *Chem Soc Rev*, 2012, **41**, 2656-2672.
3. L. E. Jennings and N. J. Long, *Chem Commun*, 2009, 3511-3524.
4. S. R. Cherry, *Annu Rev Biomed Eng*, 2006, **8**, 35-62.
5. A. Y. Louie, *Chem Rev*, 2010, **110**, 3146-3195.

6. G. Bao, S. Mitragotri and S. Tong, *Annual Review of Biomedical Engineering, Vol 15*, 2013, **15**, 253-282.
7. P. A. Jarzyna, A. Gianella, T. Skajaa, G. Knudsen, L. H. Deddens, D. P. Cormode, Z. A. Fayad and W. J. M. Mulder, *Wires Nanomed Nanobi*, 2010, **2**, 138-150.
8. J. Cheon and J. H. Lee, *Accounts Chem Res*, 2008, **41**, 1630-1640.
9. M. Lijowski, S. Caruthers, G. Hu, H. Y. Zhang, M. J. Scott, T. Williams, T. Erpelding, A. H. Schmieder, G. Kiefer, G. Gulyas, P. S. Athey, P. J. Gaffney, S. A. Wickline and G. M. Lanza, *Invest Radiol*, 2009, **44**, 15-22.
10. J. Z. Zheng, J. B. Liu, M. Dunne, D. A. Jaffray and C. Allen, *Pharm Res-Dordr*, 2007, **24**, 1193-1201.
11. D. Kim, M. K. Yu, T. S. Lee, J. J. Park, Y. Y. Jeong and S. Jon, *Nanotechnology*, 2011, **22**.
12. S. W. Chou, Y. H. Shau, P. C. Wu, Y. S. Yang, D. B. Shieh and C. C. Chen, *J Am Chem Soc*, 2010, **132**, 13270-13278.
13. A. Hagit, B. Soenke, B. Johannes and M. Shlomo, *Biomacromolecules*, 2010, **11**, 1600-1607.
14. L. J. Wang, H. Y. Xing, S. J. Zhang, Q. G. Ren, L. M. Pan, K. Zhang, W. B. Bu, X. P. Zheng, L. P. Zhou, W. J. Peng, Y. Q. Hua and J. L. Shi, *Biomaterials*, 2013, **34**, 3390-3401.
15. M. Beija, Y. Li, H. T. Duong, S. Laurent, L. Vander Elst, R. N. Muller, A. B. Lowe, T. P. Davis and C. Boyer, *J Mater Chem*, 2012, **22**, 21382-21386.
16. S. Narayanan, B. N. Sathy, U. Mony, M. Koyakutty, S. V. Nair and D. Menon, *Acs Appl Mater Inter*, 2012, **4**, 251-260.
17. C. Alric, J. Taleb, G. Le Duc, C. Mandon, C. Billotey, A. Le Meur-Herland, T. Brochard, F. Vocanson, M. Janier, P. Perriat, S. Roux and O. Tillement, *J Am Chem Soc*, 2008, **130**, 5908-5915.
18. D. P. Cormode, T. Skajaa, M. M. van Schooneveld, R. Koole, P. Jarzyna, M. E. Lobatto, C. Calcagno, A. Barazza, R. E. Gordon, P. Zanzonico, E. A. Fisher, Z. A. Fayad and W. J. M. Mulder, *Nano Lett*, 2008, **8**, 3715-3723.
19. Y. F. Zhou, W. Huang, J. Y. Liu, X. Y. Zhu and D. Y. Yan, *Adv Mater*, 2010, **22**, 4567-4590.
20. H. B. Jin, W. Huang, X. Y. Zhu, Y. F. Zhou and D. Y. Yan, *Chem Soc Rev*, 2012, **41**, 5986-5997.
21. S. Sevenson and D. A. Tomalia, *Adv Drug Deliver Rev*, 2012, **64**, 102-115.
22. C. M. Paleos, D. Tsiourvas, Z. Sideratou and L. A. Tziveleka, *Expert Opin Drug Del*, 2010, **7**, 1387-1398.

23. C. M. Paleos, L. A. Tziveleka, Z. Sideratou and D. Tsiourvas, *Expert Opin Drug Del*, 2009, **6**, 27-38.
24. G. N. Holland, P. A. Bottomley and W. S. Hinshaw, *J Magn Reson*, 1977, **28**, 133-136.
25. J. Ruiz-Cabello, B. P. Barnett, P. A. Bottomley and J. W. Bulte, *Nmr Biomed*, 2011, **24**, 114-129.
26. H. Peng, K. J. Thurecht, I. Blakey, E. Taran and A. K. Whittaker, *Macromolecules*, 2012, **45**, 8681-8690.
27. H. Peng, I. Blakey, B. Dargaville, F. Rasoul, S. Rose and A. K. Whittaker, *Biomacromolecules*, 2009, **10**, 374-381.
28. L. Nurmi, H. Peng, J. Seppala, D. M. Haddleton, I. Blakey and A. K. Whittaker, *Polym Chem*, 2010, **1**, 1039-1047.
29. X. N. Huang, G. Huang, S. R. Zhang, K. Sagiyama, O. Togao, X. P. Ma, Y. G. Wang, Y. Li, T. C. Soesbe, B. D. Sumer, M. Takahashi, A. D. Sherry and J. M. Gao, *Angew Chem Int Edit*, 2013, **52**, 8074-8078.
30. K. W. Wang, H. Peng, K. J. Thurecht, S. Puttick and A. K. Whittaker, *Polym Chem*, 2013, **4**, 4480-4489.
31. K. Wang, H. Peng, K. J. Thurecht, S. Puttick and A. K. Whittaker, *Polym Chem*, 2014, **5**, 1760.
32. K. J. Thurecht, I. Blakey, H. Peng, O. Squires, S. Hsu, C. Alexander and A. K. Whittaker, *J Am Chem Soc*, 2010, **132**, 5336-5337.
33. M. Ogawa, S. Nitahara, H. Aoki, S. Ito, M. Narazaki and T. Matsuda, *Macromol Chem Phys*, 2010, **211**, 1369-1376.
34. M. Ogawa, S. Nitahara, H. Aoki, S. Ito, M. Narazaki and T. Matsuda, *Macromol Chem Phys*, 2010, **211**, 1602-1609.
35. W. J. Du, A. M. Nystrom, L. Zhang, K. T. Powell, Y. L. Li, C. Cheng, S. A. Wickline and K. L. Wooley, *Biomacromolecules*, 2008, **9**, 2826-2833.
36. W. J. Du, Z. Q. Xu, A. M. Nystrom, K. Zhang, J. R. Leonard and K. L. Wooley, *Bioconjugate Chem*, 2008, **19**, 2492-2498.
37. J. M. Criscione, B. L. Le, E. Stern, M. Brennan, C. Rahner, X. Papademetris and T. M. Fahmy, *Biomaterials*, 2009, **30**, 3946-3955.
38. C. Porsch, Y. N. Zhang, A. Ostlund, P. Damberg, C. Ducani, E. Malmstrom and A. M. Nystrom, *Part Part Syst Char*, 2013, **30**, 381-390.
39. M. Oishi, S. Sumitani and Y. Nagasaki, *Bioconjugate Chem*, 2007, **18**, 1379-1382.

40. M. M. Bailey, C. M. Mahoney, K. E. Dempah, J. M. Davis, M. L. Becker, S. Khondee, E. J. Munson and C. Berkland, *Macromol Rapid Comm*, 2010, **31**, 87-92.
41. B. L. Liu, A. Kazlauciunas, J. T. Guthrie and S. Perrier, *Macromolecules*, 2005, **38**, 2131-2136.
42. Y. T. Li and S. P. Armes, *Macromolecules*, 2005, **38**, 8155-8162.
43. M. Semsarilar, V. Ladmiral, A. Blanazs and S. P. Armes, *Langmuir*, 2012, **28**, 914-922.
44. K. W. M. Davy, M. R. Anseau, M. Odlyha and G. M. Foster, *Polym Int*, 1997, **43**, 143-154.
45. A. Galperin and S. Margel, *J Polym Sci Pol Chem*, 2006, **44**, 3859-3868.
46. K. W. M. Davy, M. R. Anseau and C. Berry, *J Dent*, 1997, **25**, 499-505.
47. K. Saralidze, Y. B. J. Aldenhoff, M. L. W. Knetsch and L. H. Koole, *Biomacromolecules*, 2003, **4**, 793-798.
48. A. Artola, M. Gurruchaga, B. Vazquez, J. San Roman and I. Goni, *Biomaterials*, 2003, **24**, 4071-4080.
49. C. Zaharia, T. Zecheru, M. F. Moreau, F. Pascaretti-Grizon, G. Mabilleau, B. Marculescu, R. Filmon, C. Cincu, G. Staikos and D. Chappard, *Acta Biomater*, 2008, **4**, 1762-1769.
50. H. Aviv, S. Bartling, F. Kieslling and S. Margel, *Biomaterials*, 2009, **30**, 5610-5616.
51. A. Galperin, D. Margel, J. Baniel, G. Dank, H. Biton and S. Margel, *Biomaterials*, 2007, **28**, 4461-4468.
52. A. Galperin and S. Margel, *Biomacromolecules*, 2006, **7**, 2650-2660.
53. A. Galperin and S. Margel, *J Biomed Mater Res B*, 2007, **83B**, 490-498.
54. J. Ma, G. Sun, N. S. Lee, W. J. Du, K. L. Wooley, C. L. Kahakachchi, W. D. McGhee, J. McDonald, T. E. Rogers and D. A. Moore, *Abstr Pap Am Chem S*, 2010, **239**.
55. Z. Y. Wang, T. Chang, L. Hunter, A. M. Gregory, M. Tanudji, S. Jones and M. H. Stenzel, *Aust J Chem*, 2014, **67**, 78-84.
56. J. Chiefari, Y. K. Chong, F. Ercole, J. Krstina, J. Jeffery, T. P. T. Le, R. T. A. Mayadunne, G. F. Meijs, C. L. Moad, G. Moad, E. Rizzardo and S. H. Thang, *Macromolecules*, 1998, **31**, 5559-5562.
57. A. Gregory and M. H. Stenzel, *Prog Polym Sci*, 2012, **37**, 38-105.
58. C. Boyer, M. H. Stenzel and T. P. Davis, *J Polym Sci Pol Chem*, 2011, **49**, 551-595.
59. J. F. Lutz, *J Polym Sci Pol Chem*, 2008, **46**, 3459-3470.
60. L. Tao, J. Q. Liu, B. H. Tan and T. P. Davis, *Macromolecules*, 2009, **42**, 4960-4962.
61. L. Zhang, W. G. Liu, L. Lin, D. Y. Chen and M. H. Stenzel, *Biomacromolecules*, 2008, **9**, 3321-3331.

62. F. H. Meng, W. E. Hennink and Z. Zhong, *Biomaterials*, 2009, **30**, 2180-2198.
63. D. J. Coles, B. E. Rolfe, N. R. B. Boase, R. N. Veedu and K. J. Thurecht, *Chem Commun*, 2013, **49**, 3836-3838.
64. C. Zhang, H. Peng and A. K. Whittaker, *J Polym Sci Pol Chem*, 2014, **52**, 2375-2385.
65. N. Bloembergen, E. Purcell and R. Pound, *Phys Rev*, 1948, **73**, 679-712.
66. H. Yan, L. He, C. Ma, J. Li, J. Yang, R. Yang and W. Tan, *Chem Commun (Camb)*, 2014, **50**, 8398-8401.
67. J. H. Tan, N. A. J. McMillan, E. Payne, C. Alexander, F. Heath, A. K. Whittaker and K. J. Thurecht, *J Polym Sci Pol Chem*, 2012, **50**, 2585-2595.
68. T. Y. Zhao, Y. Zheng, J. Poly and W. X. Wang, *Nat Commun*, 2013, **4**.
69. G. Y. Wu, Y. Z. Fang, S. Yang, J. R. Lupton and N. D. Turner, *J Nutr*, 2004, **134**, 489-492.
70. M. Shilo, T. Reuveni, M. Motiei and R. Popovtzer, *Nanomedicine*, 2012, **7**, 257-269.
71. C. T. Badea, K. K. Athreya, G. Espinosa, D. Clark, A. P. Ghafoori, Y. F. Li, D. G. Kirsch, G. A. Johnson, A. Annapragada and K. B. Ghaghada, *Plos One*, 2012, **7**.
72. C. Y. Kao, E. A. Hoffman, K. C. Beck, R. V. Bellamkonda and A. V. Annapragada, *Acad Radiol*, 2003, **10**, 475-483.
73. X. Li, N. Anton, G. Zuber, M. J. Zhao, N. Messaddeq, F. Hallouard, H. Fessi and T. F. Vandamme, *Biomaterials*, 2013, **34**, 481-491.
74. F. Hallouard, S. Briancon, N. Anton, X. Li, T. Vandamme and H. Fessi, *Eur J Pharm Biopharm*, 2013, **83**, 54-62.
75. A. de Vries, E. Custers, J. Lub, S. van den Bosch, K. Nicolay and H. Grull, *Biomaterials*, 2010, **31**, 6537-6544.
76. K. E. Dekrafft, Z. G. Xie, G. H. Cao, S. Tran, L. Q. Ma, O. Z. Zhou and W. B. Lin, *Angew Chem Int Edit*, 2009, **48**, 9901-9904.

# Chapter 5

# Segmented Highly-Branched Copolymers: Rationally Designed Macromolecules for Improved $^{19}$F MRI

## 5.1 Introduction

Magnetic resonance imaging (MRI), which was developed in the 1970s,[1] has advanced rapidly in recent decades. Due to the advantages of non-invasiveness, relatively high resolution, rich information content and lack of radiation burden,[2, 3] MRI has become an indispensable diagnosis technique in both the clinic and in medical research. As a leading MRI modality, $^{1}$H MRI has been dominant in clinical scans because it can generate 3D anatomical images with high penetration depth especially for soft tissues.[4] However, contrast agents are often required to enhance the imaging contrast through affecting the relaxation times of the protons in surrounding tissues. Emerging only four years later than $^{1}$H MRI,[5] $^{19}$F MRI has been recognised as a promising modality to complement $^{1}$H MRI. The most significant feature of $^{19}$F MRI is the physiological rarity of detectable $^{19}$F in the body, which minimises confounding background signal during imaging.[6, 7] Therefore $^{19}$F MRI is more advantageous in quantification and tracking, such as measurement of the partial pressure of oxygen ($pO_2$), cell labelling, cell tracking, etc.[8, 9]

$^{19}$F MRI highly relies on the use of contrast agents (CAs), which introduce exogenous $^{19}$F to the body. A successful $^{19}$F MRI CA should fulfil the following two basic criteria: (1) a single and narrow $^{19}$F resonance for maximum sensitivity and reduced chemical shift imaging artefacts;[10, 11] (2) a short spin-lattice ($T_1$) relaxation time for reduced scan time and long spin-spin ($T_2$) relaxation time for increased image intensity in the case of the spin-echo pulse sequence.[10] In recent years, polymer-based CAs have attracted increasing attention for $^{19}$F MRI owing to the diverse functionalities and architectures possible with polymers.[12, 13] A variety of partly-fluorinated polymeric CAs have been reported, including linear polymers,[14-18] star polymers,[19, 20] dendritic polymers,[21-24] hyperbranched polymers (HBPs),[25-29] polymer nanogels,[30-32] etc. Among them, HBPs have been considered to be excellent candidates for $^{19}$F MRI, in particular the HBPs synthesised via reversible addition-fragmentation chain transfer (RAFT) polymerisation.[25, 26, 29] Specifically, these

novel HBPs that consist of fluoro monomer and PEG-based monomer possess quite a number of prominent properties. First, a high $^{19}F$ payload (up to 20 mol% fluoro monomer) can be achieved while the water solubility is still maintained. Second, the strong tendency of $^{19}F$ aggregation in aqueous solution can be prevented by positioning $^{19}F$ segments within a 3D hyperbranched structure, leading to high $^{19}F$ mobility and strong signal intensity. Third, the abundant functionalities (alkyne and trithiocarbonate groups) can be utilised for conjugation reactions to attach targeting/drug molecules as well as other imaging moieties. Therefore, RAFT synthesised HBPs represent a straightforward approach for the design of $^{19}F$ MRI CAs.

Generally, the RAFT synthesis of HBPs requires the use of bifunctional monomers (or crosslinkers).[33] Under optimised experimental conditions, well-defined HBPs with reasonably narrow molar mass dispersity can be obtained.[34-37] Nevertheless, the structure of the resultant HBPs can be influenced by a number of factors related to the crosslinker (e.g., crosslinker type, crosslinker/CTA ratio, crosslinker concentration), and sometimes unwanted macroscopic gelation occurs.[38-40] Other than using crosslinkers, self-condensing vinyl polymerisation (SCVP), which utilises initiator monomers (inimers), is another method for the synthesis of HBPs by free radical polymerisation.[41] When the inimer is copolymerised with other conventional vinyl monomers, the degree of branching (DB) is dependent on the comonomer/inimer ratio ($\gamma$) and monomer conversion. In the past decade, RAFT-mediated SCVP (RAFT SCVP) has been developed for the controlled synthesis of HBPs with a myriad of branched architectures and functionalities.[42-53] It is also worth noting that RAFT SCVP is a robust strategy for the design of segmented branched polymers, which are composed of linear polymer chains and thus possess unique properties due to chain entanglement.[54] Benefitting from the RAFT technique,[55] the HBPs synthesised by RAFT SCVP have controllable topologies, multifunctional groups and relatively narrow molar mass dispersity. For example, by using a polymerisable trithiocarbonate chain transfer agent (CTA), Gao and co-workers synthesised segmented hyperbranched polymers (SHBPs) of poly(glycidyl methacrylate), which beared highly-dense and hetero-functional groups and served as a versatile platform for a collection of standard click chemistries.[50] Zhao and co-workers explored RAFT SCVP for the synthesis of hyperbranched and star polymers via one or two steps.[46] Methyl methacrylate (MMA), styrene (St), methyl acrylate (MA) and tert-butyl acrylate (tBA) were selected to copolymerise with a polymerisable CTA (S-(4-vinyl)benzyl S'-propyltrithiocarbonate). The DB and branch length of HBPs were tuneable, and the arm length of star polymers was

controllable, confirming that RAFT SCVP is a robust approach to synthesise hyperbranched and star polymers with desired segmental and arm composition.

Although a number of HBP-based CAs have been developed for $^{19}$F MRI, more detailed investigations are needed to understand how imaging properties are regulated by the hyperbranched molecular structure. However, it would be challenging to examine HBPs synthesised by using crosslinker as a model because of the complexity of this approach. As a comparable analogue, partly-fluorinated SHBPs synthesised by RAFT SCVP offer a simpler model for a systematic study due to the facile control over polymer structure as well as chain tacticity. To date such polymers have not been reported for application in $^{19}$F MRI. In this work we report the synthesis of water-soluble and partly-fluorinated SHBPs via RAFT SCVP using a polymerisable trithiocarbonate CTA. By taking advantage of RAFT SCVP, SHBPs with different degree of branching and sequence distribution are prepared. A robust methodology is thus established for the design of SHBPs with targeted branched structure and composition. Both acrylate and methacrylate comonomers are used to examine the effect of flexibility of statistical copolymer chains in water. One particular aim is to determine how the hyperbranched structure, sequence distribution and composition affect the $^{19}$F NMR properties. This understanding will allow the synthesis of partly-fluorinated SHBPs with tailored structure and properties for selective and tuneable $^{19}$F MRI.

## 5.2 Experimental Section

### 5.2.1 Materials

All chemicals were purchased from Sigma-Aldrich unless otherwise stated. Poly(ethylene glycol) methyl ether methacrylate (PEGMA, MW = 475), poly(ethylene glycol) methyl ether acrylate (PEGA, MW = 480), 2,2,2-trifluoroethyl methacrylate (TFEMA), 2,2,2-trifluoroethyl methacrylate (TFEA), and 2-hydroxyethyl methacrylate (HEMA) were passed through basic alumina columns to remove inhibitors prior to use. The initiator, 2,2'-azobis(2-methylpropionitrile) (AIBN), was recrystallised from ethanol twice before use. 4-(Dimethylamino)pyridine (DMAP) and N,N'-dicyclohexylcarbodiimide (DCC, purchased from Alfa Aesar) were used as received. The trithiocarbonate RAFT agent, 4-cyano-4-(dodecylsulfanylthiocarbonyl)sulfanyl pentanoic acid was synthesised and purified according to a previously reported method.[56] Milli-Q water with a resistivity of 18.4 MΩ cm$^{-1}$ was used for the relevant experiments. Tetrahydrofuran (THF) and

dichloromethane (DCM) were obtained from a solvent purification system (MB-SPS-800-Auto, Mbraun) and used directly. All other solvent were of analytical grade.

## 5.2.2 Synthesis

### 5.2.2.1 Synthesis of the Polymerisable CTA, (S)-2-(Methacryloyloxy)ethyl 4-cyano-4-(((propylthio)carbonothioyl)thio)pentanoate (MECP)

4-Cyano-4-(dodecylsulfanylthiocarbonyl)sulfanyl pentanoic acid (8.07 g, 0.02 mol), HEMA (5.21 g, 0.04 mol) and DMAP (0.489 g, 0.004 mol) were dissolved in 200 mL of DCM in a 500 mL round bottom flask immersed in an ice bath. DCC (5.25 g, 0.04 mol) in 50 mL DCM was added dropwise to the above solution. The resulted mixture was stirred at 0 $^{o}$C for 1 h and then at room temperature for 24 h. After reaction, the mixture was filtered to remove the insoluble dicyclohexylurea by-product. The filtrate was washed with 1 M HCl solution (200 mL × 3) and saturated $NaHCO_3$ aqueous solution (200 mL × 3), and then dried over anhydrous $MgSO_4$ overnight in a freezer. After that the solution was filtered again and concentrated by rotary evaporation. The crude product was purified by flash column chromatography (Silica gel, 230-400 mesh) using petroleum spirit (40-60)/ethyl acetate mixture (gradient from 9/1 to 7/3) as eluent. After removal of the solvents, a red oil was obtained and stored in a freezer away from light. Yield: 7.15 g, 69%. $^{1}$H NMR (500 MHz, $CDCl_3$, ppm): 6.13 and 5.6 (s, 2H, C$H_2$($CH_3$)C), 4.36 (m, 4H, COOC$H_2$C$H_2$), 3.32 (t, 2H, $CH_2$C$H_2$S), 2.36-2.56 (m, 4H, C$H_2$C$H_2$COO), 1.95 (s, 3H, $CH_2$C(C$H_3$)COO), 1.87 (s, 3H, SC$H_3$C(CN)$CH_2$), 1.69 (m, 2H, C$H_2$$CH_2$S), 1.26-1.40 (m, 18H, $CH_3$(C$H_2$)$_9$$CH_2CH_2$S), 0.88 (t, 3H, C$H_3$($CH_2$)$_9$$CH_2CH_2$S). $^{13}$C NMR (125 MHz, $CDCl_3$, ppm): 217.22, 176.61, 167.43, 136.22, 126.54, 119.30, 63.08, 62.54, 46.67, 37.43, 34.16, 32.26, 30.02, 29.96, 29.89, 29.76, 29.68, 29.41, 29.28, 28.02, 25.22, 23.03, 18.63.

### 5.2.2.2 Synthesis of Segmented Highly Branched Polymers via RAFT SCVP

A typical polymerisation is described as follows. PEGMA (1.43 g, 3 mmol), TFEMA (0.336 g, 2 mmol), MECP (51.6 mg, 0.1 mmol) and AIBN (3.28 mg, 0.02 mmol) were dissolved in 1 mL of 1,4-dioxane in a 10 mL tube placed with a magnetic stir bar. PEGMA/TFEMA/MECP/AIBN = 30/20/1/0.2, and the comonomer/MECP ratio ($\gamma$) = 50. Then the tube was sealed with a rubber septum and purged with argon for 15 min, followed by immersing in a 70 $^{o}$C oil bath for 24 h. The polymerisation was then quenched by immersing the flask in an ice bath and exposing to air. The conversions of PEGMA, TFEMA and MECP were found to be all above 97% according to $^{1}$H

NMR. The crude solution was diluted with THF and precipitated in cold hexane three times. A yellowish viscous oil was collected after drying at 35 $^{o}$C in vacuum for 24 h. Yield: 1.46 g, 80%.

Following this procedure, a series of SHBPs was synthesised under the same conditions by varying the comonomer type and comonomer/MECP ratio. The polymer characteristics are listed in Table 5-1.

#### 5.2.2.3 Synthesis of Linear Statistical Copolymer Poly(TFEA-co-PEGA)

PEGA (1.44 g, 3 mmol), TFEA (0.308 g, 2 mmol), 4-cyano-4-(dodecylsulfanylthiocarbonyl)sulfanyl pentanoic acid (40.4 mg, 0.1 mmol) and AIBN (3.28 mg, 0.02 mmol) were dissolved in 1 mL of 1,4-dioxane in a 10 mL tube placed with a magnetic stir bar. After purging with argon for 15 min, the tube was placed in a 70 $^{o}$C oil bath for 24 h. The polymerisation was then quenched by immersing the flask in an ice bath and exposing to air. The crude sample was diluted with THF and precipitated in cold hexane three times. The collected sample was dried at 35 $^{o}$C in vacuum for 24 h. A yellowish viscous oil was obtained. Yield: 1.1 g, 62%.

### 5.2.3 Characterisation

#### Gel Permeation Chromatography (GPC)

Molecular weights and molecular weight distributions were determined by GPC using a Waters Alliance 2690 Separations Module equipped with Waters 2414 Refractive Index (RI) Detector, Waters 2489 UV/Visible Detector, Waters 717 Plus Autosampler and Waters 1515 Isocratic HPLC Pump. Samples were dissolved in THF and passed through 0.45 µm filters before each measurement. THF was used as the mobile phase at a flow rate of 1 mL min$^{-1}$. The system was calibrated using polystyrene (PS) standards, to which the number average molecular weight ($M_n$) and weight average molecular weight ($M_w$) were referenced. For measuring absolute molecular weights, a multi angle laser light scattering (MALLS) detector (DAWN 8+, Wyatt) was attached to the GPC, and the polymer solutions were eluted at a flow rate of 1 mg mL$^{-1}$ in THF. The refractive index increment ($dn/dc$) was determined by using ATAGO Pocket Refractometer at room temperature. Briefly, polymer/THF solutions were prepared with concentrations from 10 to 300 mg mL$^{-1}$, then the refractive index of each solution was measured 5 times to get an average value.

Refractive index as a function of polymer concentration was plotted, and the slope was calculated as the *dn/dc* for each sample. It was found that the *dn*/*dc* for all samples was approximately 0.04 ml $g^{-1}$ in THF at 25 $^{o}$C.

### $^{1}$H and $^{13}$C Nuclear Magnetic Resonance (NMR)

$^{1}$H NMR and $^{13}$C NMR were performed on Bruker Avance 500 MHz and 700 MHz spectrometer at 25 $^{o}$C using an internal lock ($CDCl_3$ or $D_2O$) and referenced to the residual non-deuterated solvent ($CHCl_3$ or $H_2O$). $^{1}$H-$^{13}$C heteronuclear multiple-bond correlation ($^{1}$H-$^{13}$C HMBC) and $^{1}$H-$^{13}$C heteronuclear single quantum coherence ($^{1}$H-$^{13}$C HSQC) spectra were recorded on a Bruker Avance 700 MHz using $CDCl_3$ as solvent at 25 $^{o}$C.

### Dynamic Light Scattering (DLS)

DLS measurements were carried out on a Nanoseries Zetasizer (Malvern, UK) at 25 $^{o}$C. Polymers were dissolved in PBS at a concentration of 1 mg $mL^{-1}$ and passed through 0.45 μm filters to remove dust particles prior to each measurement. Each hydrodynamic diameter was the average value of 5 measurements. To minimise the possible influence of large aggregates, number-averaged diameters are reported.

### UV-Vis Spectroscopy

UV-Vis spectra were recorded on a Cary 4000 UV-Vis spectrophotometer. Samples were dissolved in acetonitrile at given concentrations at 25 $^{o}$C.

### Differential Scanning Calorimetry (DSC)

DSC analyses were carried out on a Mettler Toledo DSC1 Star System calorimeter. Samples (5~9 mg) were heated from 25 to 150 $^{o}$C at a heating/cooling rate of 10 $^{o}$C $min^{-1}$ in nitrogen atmosphere. The glass transition temperature was determined from the midpoint of the change in capacity in the second heating cycle (-100 to 150 $^{o}$C).

### $^{19}$F Nuclear Magnetic Resonance ($^{19}$F NMR)

All $^{19}$F NMR spectra were acquired at 659 MHz on a Bruker Avance 700 spectrometer. The samples were prepared by dissolving the polymers in PBS/$D_2O$ (90/10, v/v) at a concentration of 20 mg $mL^{-1}$. All measurements were performed at 25 $^{o}$C. A 90$^{o}$ pulse of 15.1 μs was used in all

measurements, the relaxation delay was 2 s and the acquisition time was 0.18 s. Data were collected using a spectrum width of 46 kHz, 16k data points and 64 scans.

$^{19}$F spin-spin relaxation times ($T_2$) were measured using the Carr-Purcell-Meiboom-Gill (CPMG) pulse sequence at 25 $^{o}$C. The samples were dissolved in PBS/$D_2O$ (90/10, v/v) at a concentration of 20 mg mL$^{-1}$. The relaxation delay was 2.3 s and the acquisition time was 0.18 s. For each measurement, the echo times were from 2 to 770 ms and 15 points were collected, which could be described by exponential functions for the calculation of $T_2$. For the samples that have broad and unsymmetrical $^{19}$F peaks, the $T_2$s were calculated by SigmaPlot software using nonlinear regression function (exponential decay, double, 4 parameters). For some samples, three $T_2$ measurements were conducted, and the standard errors were found to be negligible (< 1%).

$^{19}$F spin-lattice ($T_1$) relaxation times were measured using the standard inversion-recovery pulse sequence. The relaxation delay was 2.5 s and the acquisition time was 0.18 s. For each measurement, the recovery times were from 2 ms to 3 s and 15 points were acquired.

**$^{19}$F Magnetic Resonance Imaging ($^{19}$F MRI)**

Images of phantoms containing the polymer solutions were acquired on a Bruker BioSpec 94/30 USR 9.4 T small animal MRI scanner. SHBPs solutions (100 mg mL$^{-1}$ in pure water) were loaded in 30 × 8 mm clear glass vials, which were placed in a $^{1}$H/$^{19}$F dual resonator 40 mm volume coil. $^{1}$H were acquired for localisation of the samples using a RARE sequence with an echo train length of 8 (TE = 28 ms, TR = 2 s, FOV = 40 × 40 × 1 mm, Matrix = 96 × 96 × 1). $^{19}$F images were acquired in the same stereotactic space as the $^{1}$H image using fast low-angle shot (FLASH) and rapid acquisition with relaxation enhancement (RARE) sequence with an echo train length of 8. The detailed experimental parameters are given as follows.

$^{19}$F FLASH: TE = 3.72 ms, TR = 30 ms, Flip Angle = 20 degrees, NEX = 1024, FOV = 40 × 40 mm, MAT = 96 × 96, Measurement time = 47 minutes.

$^{19}$F RARE-8: Rare Factor = 8, TE = 10 ms, Effective TE = 40 ms, TR = 1 s, NEX = 512, FOV = 40 × 40 mm, MAT = 96 × 96, Measurement time = 1 h and 46 minutes.

$^{19}$F RARE-32: Rare Factor = 32, TE = 10 ms, Effective TE = 160 ms, TR = 1 s, NEX = 512, FOV = 40 × 40 mm, MAT = 96 × 96, Measurement time = 52 minutes.

## 5.3 Results and Discussion

### 5.3.1 Polymerisation Mechanism and Molecular Design

The aim of this work is to study the use of RAFT SCVP for the synthesis of segmented highly branched polymers (SHBPs) that are partly-fluorinated and water-soluble for $^{19}$F MRI applications. A polymerisable RAFT agent, (S)-2-(methacryloyloxy)ethyl 4-cyano-4-(((propylthio)carbonothioyl)thio)pentanoate (MECP), was synthesised by the standard DCC/DMAP esterification between 4-cyano-4-(dodecylsulfanylthiocarbonyl)sulfanyl pentanoic acid and HEMA. As shown in Figure 5-1, MECP is a typical AB*-type inimer for SCVP, in which B* is a trithiocarbonate function for the RAFT polymerisation of the vinyl group A and other comonomers. Therefore, MECP can be exploited for controlled polymerisation via the RAFT process as well as the simultaneous formation of branching points through the A groups.

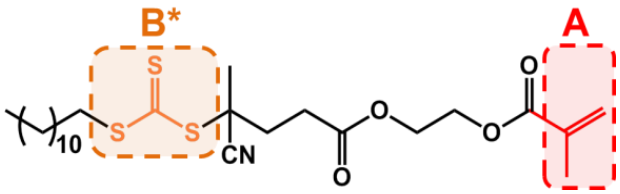


**Figure 5-1** Chemical structure of the polymerisable CTA.

As illustrated in Scheme 5-1, the polymerisation process follows the typical reaction mechanism of a SCVP.[54] In the scheme the lower case letter, b and M refer to the reacted monomers. Upon initiation through the decomposition of AIBN, A-b-M* is generated through the chain transfer of propagating radicals of comonomers M at a rate constant of $K_{BM}$, while A-b-A*-B* is formed by the chain transfer of propagating radicals of inimer A-B* at a rate constant of $K_{BA}$. Then A-b-M* can undergo two possible reactions through the addition of either inimer or comonomers at rate constants of $K_{MA}$ and $K_{MM}$, respectively. Meanwhile, through similar monomer additions, A-b-A*-B* can be reacted with inimer and comonomers in six routes at its two activated sites A* and B*, resulting in the formation of the six depicted structures at rate constants of $K_{AA}$, $K_{AM}$, $K_{BA}$, and $K_{BM}$. As the polymerisation proceeds, highly branched macromolecules composed of linear chains are gradually produced via these reactions. According to the nature of the RAFT process, the equilibrium between the active propagating radicals and dormant thiocarbonylthio compound is very fast. Hence the chain growth progresses in a controlled fashion, yielding polymer segments with narrow molar mass distribution as well as the formation of branching structures. [57]

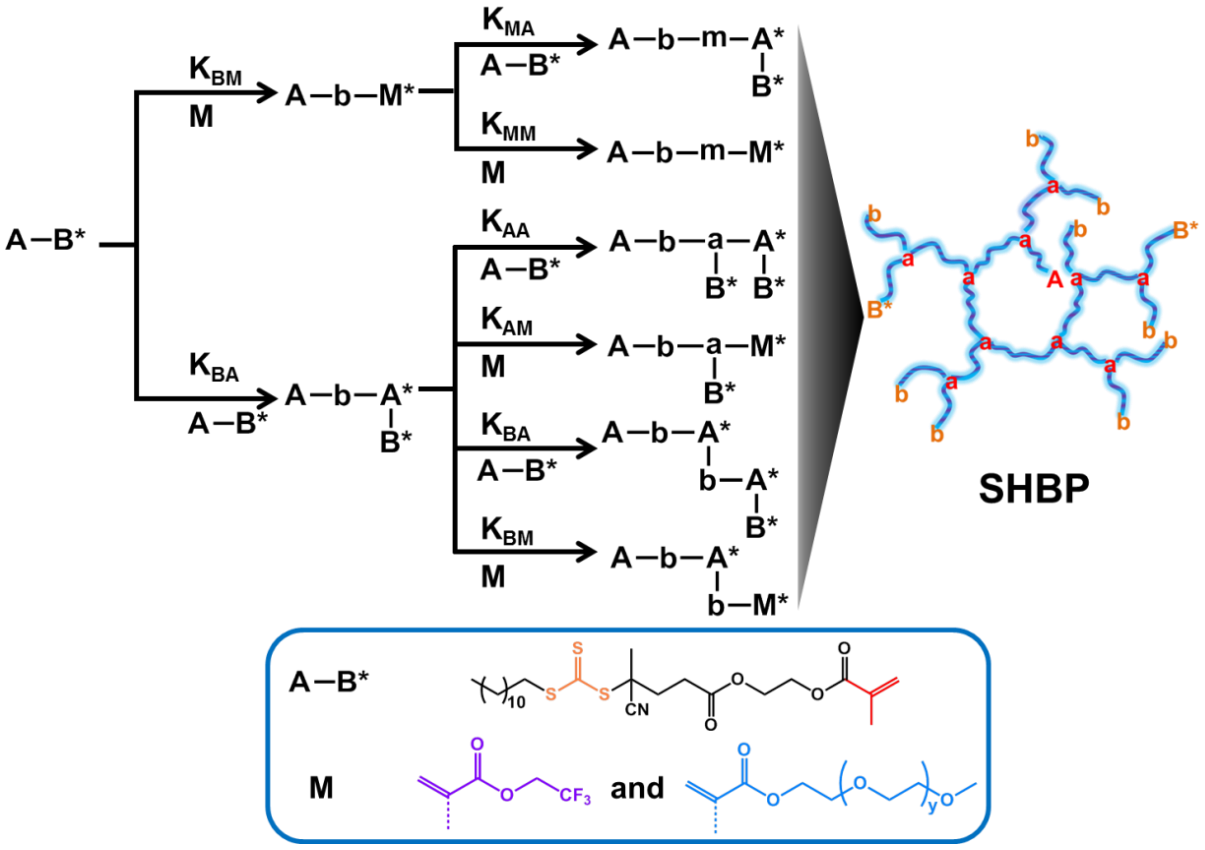


**Scheme 5-1** Reaction mechanism for RAFT SCVP. A: vinyl group of MECP. B: trithiocarbonate function of MECP. M: comonomers TFE(M)A and PEG(M)A. Lowercase letters 'a' and 'b' stand for reacted A and B, respectively. Asterisks represent activated sites for the addition of monomers and inimer.

The detailed synthetic route is described in Scheme 5-2. 2,2,2-Trifluoroethyl methacrylate (TFEMA) and 2,2,2-trifluoroethyl acrylate (TFEA) were selected as fluoro monomers, while poly(ethylene glycol) methyl ether methacrylate (PEGMA) and poly(ethylene glycol) methyl ether acrylate (PEGA) were chosen as PEG-based oligomers. Through RAFT SCVP using a polymerisable trithiocarbonate CTA (MECP), segmented highly branched p(TFE(M)A-co-PEG(M)A) were prepared. According to the mechanism, each SHBP macromolecule contains an unreacted vinyl group and numerous trithiocarbonate end-groups. As described above, these SHBPs are intended for $^{19}$F MRI as CAs. A number of previous publications have pointed out that high $^{19}$F segmental mobility is of importance for achieving long spin-spin relaxation ($T_2$) times, which are preferred for $^{19}$F MRI.[15, 17] To achieve high $^{19}$F mobility in water, the $^{19}$F segments should be hydrated and separated from each other to avoid association. One strategy is to design statistical copolymers composed of units of fluoro monomers and hydrophilic PEG-based oligomers such as

PEGMA and PEGA. Consequently, two issues are to be addressed. First, the choice of monomers needs to be examined. As reported before,[14, 15] tapered or block copolymers could cause $^{19}$F aggregation in water. In addition, the type of monomer (acrylates or methacrylates) can affect the segmental motion. Thus certain monomers with close reactivity ratios are required for the synthesis of statistical copolymers that have highly flexible polymer backbones. Second, the $^{19}$F content should be maximised. A high $^{19}$F payload is preferred for reducing scan time as well as improving image quality, but may lead to aggregation of $^{19}$F-containing units (short $T_2$) and decreased water solubility. Hence the relationship of $^{19}$F payload and $^{19}$F mobility needs to be investigated. Following these findings, the next goal is to understand the influence of branched structure on the $^{19}$F NMR properties before $^{19}$F MRI evaluation.

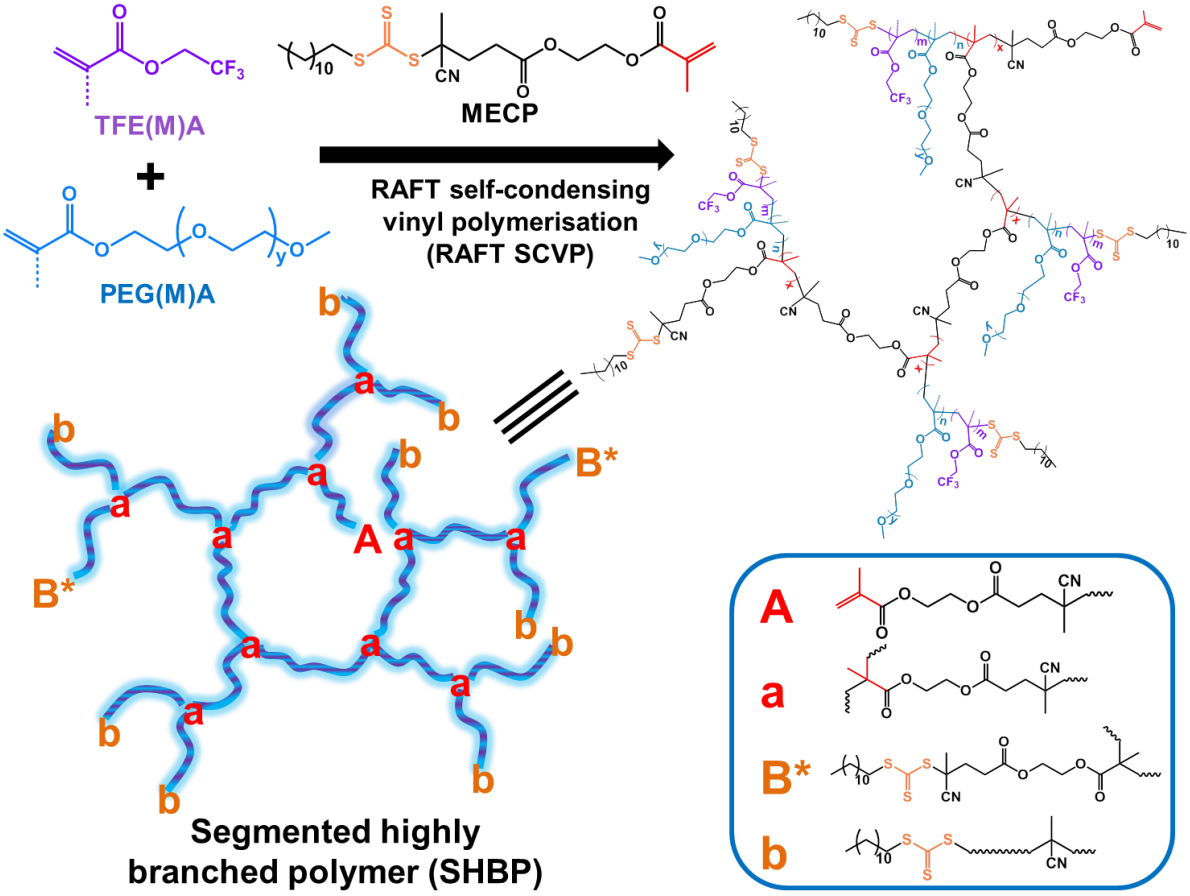


**Scheme 5-2** Illustration of the synthesis of SHBPs via RAFT SCVP. Lowercase letters 'a' and 'b' stand for reacted A and B, respectively. 'A' refers to unreacted vinyl groups in MECP, and 'B*' denotes to trithiocarbonate groups that have not engaged in the RAFT process.

### 5.3.2 Synthesis of SHBPs via RAFT SCVP

The RAFT SCVP of TFEMA and PEGMA using MECP as CTA was carried out in 1,4-dioxane at 70 $^{o}$C. The influence of reaction time was first studied by GPC and $^{1}$H NMR. As shown in Figure 5-2, from 2 to 48 h, the GPC traces measured by RI detector evolved toward higher molecular weight with increasing monomer conversions evidenced by $^{1}$H NMR. Meanwhile, owing to the RAFT process, the molar mass dispersity ($Đ_w$, $M_w/M_n$) remained relatively low at 1.25~1.81. In addition, the monomer conversion reached ~90% after 6 h with MW of ~$10^4$ g mol$^{-1}$, indicating a rapid polymerisation rate. A shoulder peak appeared after 6 h with MW of ~ $10^5$ g mol$^{-1}$, suggesting the formation of highly branched macromolecules via the polymerisation of vinyl groups of MECP. Nevertheless, the conversion of MECP could not be identified precisely by $^{1}$H NMR because its characteristic peaks were significantly overlapped with those of PEGMA units. According to the GPC results, the RAFT SCVP exhibited hybrid chain-growth/step-growth behaviour that could be described by two steps.[54] In the first step (0-6 h), due to the much higher concentration of TFEMA and PEGMA compared with MECP, RAFT-mediated chain growth proceeded with rapidly increasing monomer conversions, yielding lightly branched polymers (macroinimers) with narrow molar mass distribution. In the second step (6-48 h), after the consumption of most comonomers, the macroinimers started to react with each other through the A group sites, resulting in highly branched polymers with dramatically increased MW as evidenced by the bimodal GPC curves. In fact, these two processes occur simultaneously, but each step dominates at different stages.[54] Similar results were also reported by others.[44, 45]

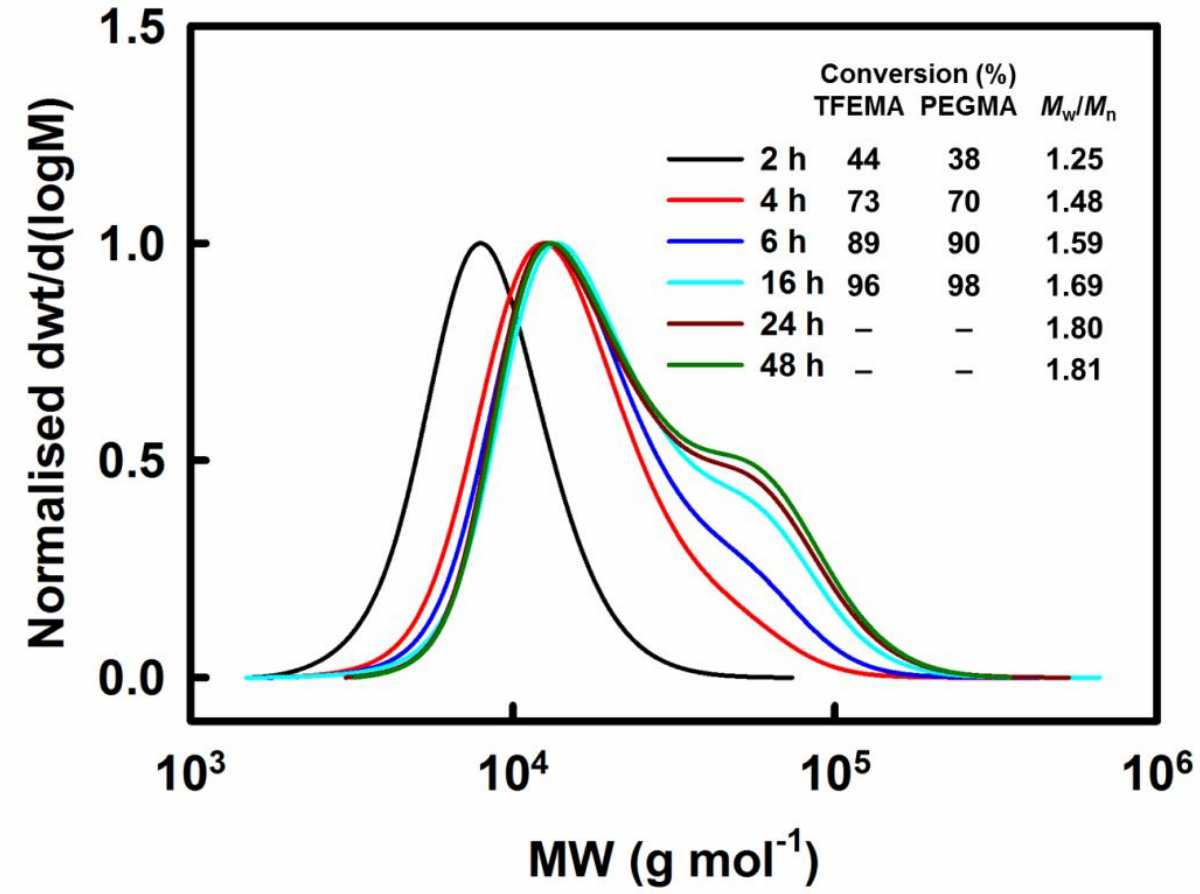


**Figure 5-2** GPC traces of the samples withdrawn at different time intervals during a RAFT SCVP. Inset gives the monomer conversions determined by $^{1}$H NMR. Polymerisation conditions: [PEGMA]/[TFEMA]/[MECP]/[AIBN] = 40/10/1/0.2, [monomer] = 1 M, 70 $^{o}$C.

The effect of monomer concentration was investigated next. As displayed in Figure 5-3 (A), single GPC peaks with low MW and narrow $Đ_w$ were observed for the polymerisation performed at low monomer concentration (0.25 and 0.5 M). When the monomer concentration was above 1 M, bimodal GPC curves were obtained with a peak becoming more pronounced at MW of ~ $10^5$ g mol$^{-1}$, suggested that highly branched macromolecules were only produced at relatively high monomer concentrations instead of dilute conditions. We thus assume that a high monomer concentration increased the probability of condensation of macroinimers, facilitating the formation of polymers with highly branched structures. It was also found that an increase of the ratio [comonomer]/[MECP] (γ) resulted in polymers with higher MW mainly due to the longer chain length between two branching points (Figure 5-3 (B)).

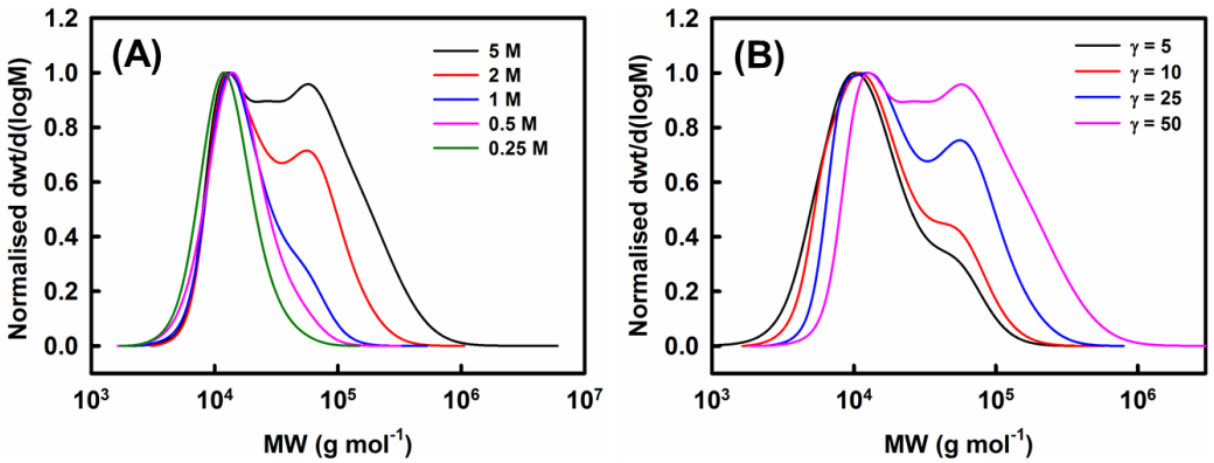


**Figure 5-3** GPC traces of RAFT SCVP at different monomer concentrations (A) and [comonomer]/[MECP] ratios. Condition for (A): [PEGMA]/[TFEMA]/[MECP]/[AIBN] = 40/10/1/0.2, 70 $^{o}$C, 24 h. Condition for (B): [PEGMA]/[TFEMA] = 4/1, [MECP]/[AIBN] = 5/1, [monomer] = 5 M, 70 $^{o}$C, 24 h.

Based on these results, a series of SHBPs were synthesised via RAFT SCVP using a monomer concentration of 5 M. For an in-depth study, both methacrylates and acrylates were chosen to vary the polymer compositions. In addition, different [comonomer]/[MECP] ratios were selected for the synthesis of SHBPs with various degree of branching. The details of the SHBPs are summarised in Table 5-1.

**Table 5-1** Molecular characteristics of the SHBPs synthesised by RAFT SCVP.

| Sample | PEG(M)A:TFE(M)A:CTA[a] | $M_n$ [a] | $M_n$ (kDa)[b] | $Đ_M$[b] | DB[c] | RB[c] | $N_{CTA}$[d] |
|---|---|---|---|---|---|---|---|
| SHBP-1 | 52:7:1 (PEGMA+TFEMA) | 26400 | 1440 | 2.2 | 0.033 | 30 | 55 |
| SHBP-2 | 47:12:1 (PEGMA+TFEMA) | 24900 | 690 | 3.6 | 0.033 | 30 | 28 |
| SHBP-3 | 35:17:1 (PEGMA+TFEMA) | 20000 | 1030 | 2.3 | 0.037 | 27 | 51 |
| SHBP-4 | 30:22:1 (PEGMA+TFEMA) | 18400 | 820 | 2.6 | 0.037 | 27 | 45 |
| SHBP-5 | 25:26:1 (PEGMA+TFEMA) | 16800 | 510 | 3.8 | 0.038 | 26 | 30 |
| SHBP-6 | 16:26:1 (PEGMA+TFEMA) | 12500 | 440 | 3.6 | 0.045 | 22 | 35 |
| SHBP-7 | 45:13:1 (PEGMA+TFEA) | 23900 | 1030 | 2.5 | 0.033 | 30 | 43 |
| SHBP-8 | 48:15:1 (PEGA+TFEMA) | 26100 | 430 | 1.8 | 0.036 | 28 | 16 |
| SHBP-9 | 39:12:1 (PEGA+TFEA) | 20600 | 370 | 1.6 | 0.038 | 26 | 18 |
| SHBP-10 | 37:17:1 (PEGA+TFEA) | 20400 | 230 | 2.1 | 0.036 | 28 | 11 |
| SHBP-11 | 34:22:1 (PEGA+TFEA) | 19700 | 210 | 2.0 | 0.034 | 29 | 11 |
| SHBP-12 | 24:35:1 (PEGA+TFEA) | 16900 | 130 | 2.0 | 0.033 | 30 | 8 |
| SHBP-13 | 4:3:1 (PEGA+TFEA) | 2900 | 140 | 1.7 | 0.219 | 5 | 49 |
| SHBP-14 | 7:5:1 (PEGA+TFEA) | 4600 | 160 | 1.2 | 0.142 | 7 | 35 |
| SHBP-15 | 14:11:1 (PEGA+TFEA) | 8900 | 270 | 1.2 | 0.074 | 14 | 31 |
| LP-11 | 39:23:1 (PEGA+TFEA) | 22700 | 13[e] | 1.43[e] | 0 | - | 1 |

[a] Degree of polymerisation (DP) was determined by $^1$H NMR. $M_n$ ($^1$H NMR) of a single polymer chain was calculated by using the equation $M_n = MW_{PEG(M)A} \times DP_{PEG(M)A} + MW_{TFE(M)A} \times DP_{TFE(M)A} + MW_{MECP}$, assuming the polymerisations completely followed the RAFT process. [b] Absolute MW and $Đ_M$ were measured by GPC MALLS. [c] Degree of branching (DB) was calculated by the equation introduced in the main text. Repeating unit per branch (RB) = 1/DB. [d] Number of trithiocarbonate functionality per SHBP ($N_{CTA}$) = $M_n$ (GPC MALLS)/$M_n$ ($^1$H NMR). [e] Measured by GPC RI detector. All the SHBPs were synthesised in 1,4-dioxane at 70 $^o$C for 24 h with [monomer] = 5 M and [MECP]/[AIBN] = 5/1.

One benefit of SCVP is that the degree of branching (DB) of the resultant HBPs can be predicted at given [comonomer]/[MECP] ratio and monomer conversion. In our study, the DBs of SBHPs can be calculated by the following equations.[54]

$$\mathrm{DB} = \frac{2\left(1 - e^{-(\gamma+1)x_M}\right)\left(x_M - \frac{1 - e^{-(\gamma+1)x_M}}{\gamma + 1}\right)}{\gamma x_M + 1 - (1 - x_M)(2 - e^{-(\gamma+1)x_M})} \quad (5\text{-}1)$$

$$\mathrm{DB} = \frac{2\left(1 - e^{-(\gamma+1)}\right)\left(\gamma + e^{-(\gamma+1)}\right)}{(\gamma + 1)^2} \quad (5\text{-}2)$$

In Equations 5-1 and 5-2, γ and $x_M$ refer to [comonomer]/[MECP] ratio and monomer conversion, respectively. Because nearly full monomer conversion was achieved, Equation 5-1 can be simplified to Equation 5-2. Accordingly, the degree of branching was calculated to be between 0.033 and 0.219 (Table 5-1). It should be stressed that the degree of branching is solely dependent on γ at fixed monomer conversions (e.g. 100%). Hence it is feasible to obtain targeted DBs by simply using a stoichiometric [comonomer]/[MECP] ratio. This feature is especially advantageous for the synthesis of SHBPs with tailored compositions and degrees of branching.[54] As reported by Sumerlin and Vogt, highly-branched poly(N-isopropylacrylamide) with different degrees of branching were prepared through RAFT SCVP by varying ratios of monomer to CTA.[48]

### 5.3.3 Characterisation of Structure and End Functionality of SHBPs

The chemical structure of the SHBPs was characterised by NMR spectroscopy. SHBP-4 was chosen as a typical sample for detailed NMR analysis. As displayed in Figure 5-4 (A), all the characteristic peaks of TFEMA, PEGMA were found and assigned. Specifically, the peaks at 4.3 and 4.0 ppm are from $CH_2$ adjacent to the ester bonds of TFEMA and PEGMA units, respectively. The dominant peak at 4.5~4.7 ppm can be ascribed to the $CH_2CH_2O$ repeating units of PEGMA segments. Noticeably, the peaks of MECP were also identified, confirming the retention of CTA functionality. The presence of peaks from vinyl bonds is in accord with the aforementioned RAFT SCVP mechanism that each SHBP retains an unreacted vinyl group of MECP. According to $^1$H NMR, the measured ratio of PEGMA/TFEMA/MECP in the SHBP-4 was calculated to be 30/22/1, which is very close to the feed ratio 30/20/1. Therefore the $M_n$ for a single polymer chain was calculated to be 18400 g mol$^{-1}$ using the equation $M_n = MW_{PEGMA} \times DP_{PEGMA} + MW_{TFEMA} \times DP_{TFEMA} + MW_{MECP}$. In addition, $^{13}$C NMR (Figure 5-4 (B)) verified the chemical structure with all the relevant carbon peaks being observed, such as at 221.8 ppm (trithiocarbonate groups), 175.3~177.4 ppm (carbonyl groups), 126.0 and 107.9 ppm (vinyl groups), 128.2 (CN groups), 121.0~125.7 ppm ($CF_3$ groups), etc. Both $^1$H and $^{13}$C NMR confirmed the successful incorporation of TFEMA, PEGMA and MECP units into the SHBPs via RAFT SCVP.

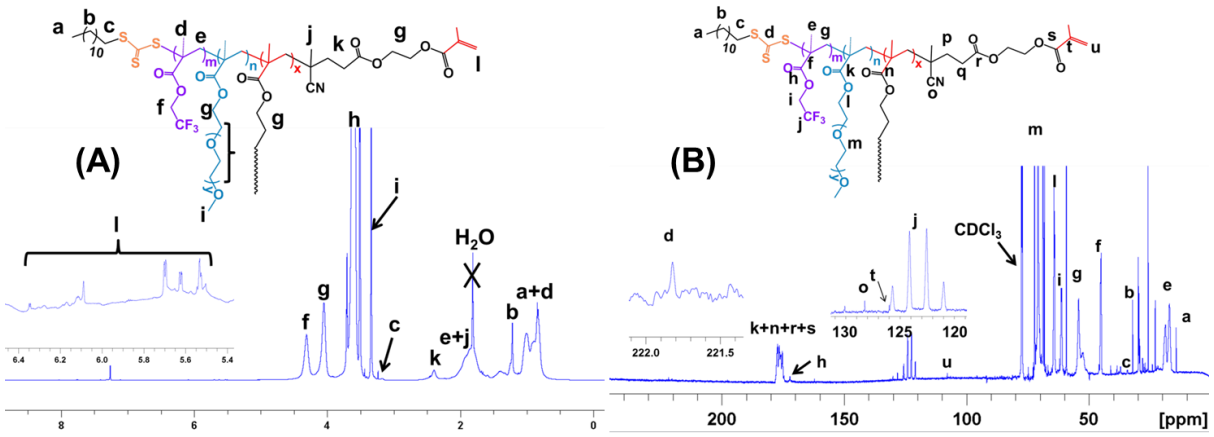


**Figure 5-4** NMR spectra of SHBP-4 in $CDCl_3$. (A) $^{1}H$ NMR spectrum, inset is the expanded area of 5.4~6.4 ppm. (B) $^{13}C$ NMR spectrum, insets are expanded areas of 221.5~222 ppm and 120~130 ppm.

To get more detailed information, SHBP-4 was characterised by $^{1}H$-$^{13}C$ 2D NMR. $^{1}H$-$^{13}C$ HSQC can be used to confirm the direct attachment of $^{1}H$ atoms to $^{13}C$ atoms through displaying correlations between resonances of $^{1}H$ and $^{13}C$ nuclei with one-bond C-H couplings ($^{1}J_{CH}$). In Figure 5-5 (A) the characteristic protonated carbons are labelled with numbers, and they can be assigned to the related cross-peaks. For example, the cross-peak 4 ($\delta_H$ = 4.3 ppm, $\delta_C$ = 60.9 ppm) is from the correlation of resonances of $CH_2$ connected to the ester bond in TFEMA units, while cross-peak 5 ($\delta_H$ = 4.0 ppm, $\delta_C$ = 64.3 ppm) is from $CH_2$ next to the ester bond in PEGMA units. It is worth mentioning that the $CH_2$ adjacent to trithiocarbonate was also evidenced by two cross-peaks (red circle; see Appendix D Figure A5.1 for the enlarged spectrum). Thee spectrum also confirms retention of trithiocarbonate functionalities in the SHBPs crucial for either further bioconjugation or chain extension. To be more specific, cross-peak 1 ($\delta_H$ = 3.2 ppm, $\delta_C$ = 37.1 ppm) is from the $CH_2$ next to the reacted trithiocarbonate groups that engaged in the RAFT process, while cross-peak 1' ($\delta_H$ = 3.3 ppm, $\delta_C$ = 37.2 ppm) can be attributed to the neighbouring $CH_2$ of unreacted trithiocarbonate groups that did not participate in the RAFT process. Hence, the coexistence of both reacted and unreacted RAFT species in the highly branched structure, a typical characteristic of RAFT SCVP, was elucidated by the $^{1}H$-$^{13}C$ HSQC spectrum. In addition, the correlations of $CH_2$ in vinyl groups can also be confirmed by several cross-peaks (see Appendix D Figure A5.2), indicating different chemical environments of double bonds existing in the complicated highly branched structure.

To further study the structure, SHBP-4 was also analysed by $^{1}$H-$^{13}$C HMBC experiments, which can provide information about long distance connectivity between $^{1}$H and $^{13}$C atoms in particular the three-bond scalar coupling ($^{3}J_{CH}$) as well as occasional observation of $^{2}J_{CH}$ and $^{4}J_{CH}$. As shown in Figure 5-5 (B), the correlations of major characteristic $^{1}$H-$^{13}$C pairs were detected and labelled accordingly. The cross-peaks highlighted by a red circle are related to the correlations of $^{1}$H atoms in $CH_2$ and $^{13}$C atoms in the neighbouring trithiocarbonate groups, providing further proof for the trithiocarbonate functionality in SHBP macromolecules.

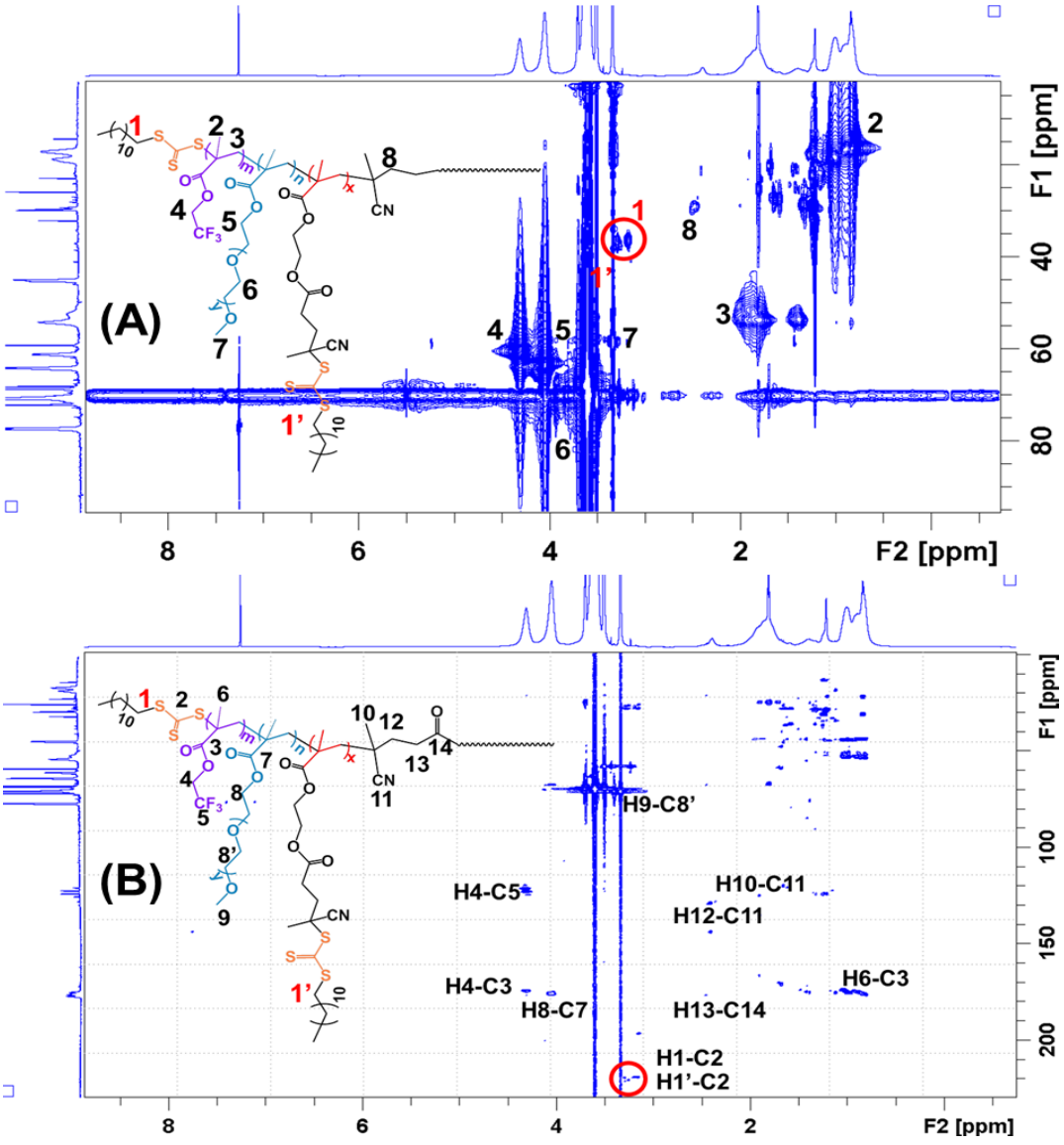


**Figure 5-5** $^{1}$H-$^{13}$C HSQC spectrum (A) and $^{1}$H-$^{13}$C HMBC spectrum (B) of SHBP-4 in $CDCl_3$. The red circles highlight the correlations that are related to trithiocarbonate group and its neighbouring $CH_2$.

In addition to NMR analysis, the presence of trithiocarbonate was also confirmed by UV-Vis spectroscopy and the UV detector of GPC at wavelength of ~306 nm (see Appendix D Figure A5.3).

### 5.3.4 Characterisation of Chain Sequence Distribution

As stated in the Introduction, one design priority for $^{19}F$ MRI polymeric CAs is to achieve a single $^{19}F$ NMR resonance with strong signal intensity. Therefore the choice of monomers should be carefully considered as it directly determines the $^{19}F$ NMR properties of the resulting polymers. In this study, hydrophobic TFEA and TFEMA were selected as fluoro monomers to provide the $^{19}F$ NMR signal. Both of these monomers have moderate $^{19}F$ contents that can possibly generate strong $^{19}F$ signal while avoiding association of the fluorinated segments in water. In addition, both monomers have only one $^{19}F$ chemical structure ($CF_3$) and so is expected to produce a single $^{19}F$ NMR resonance. PEG-based hydrophilic oligomers, PEGA and PEGMA, were copolymerised with TFE(M)A to obtain water-soluble polymers. SHBPs consisting of a range of compositions were synthesised, including TFEA/PEGA, TFEA/PEGMA, TFEMA/PEGA and TFEMA/PEGMA pairs (see Table 5-1 for details). $^{1}H$ NMR was used for the investigation of the chain composition and sequence. In Figure 5-6 $^{1}H$ NMR spectra of SHBP-2, 7, 8 and 9 having relatively close TFE(M)A/PEG(M)A ratios are compared particularly within the chemical shift of 4~5 ppm to highlight several differences. For the sample contained TFEA and PEGMA, two peaks ‘a’ and ‘b’ (in solid box) were observed from 4.25 to 4.60 ppm, which could be assigned to the resonances of protons in $CH_2$ adjacent to ester bond in TFEA, as further evidenced by the $^{1}H$-$^{13}C$ HSQC spectrum (see Appendix D Figure A5.4). In addition, a shoulder peak c (in dash box) was also found in the peak (4.07 ppm) for $CH_2$ next to ester bond in PEGMA. These results imply that both TFEA and PEGMA segments exist in different chemical environments.

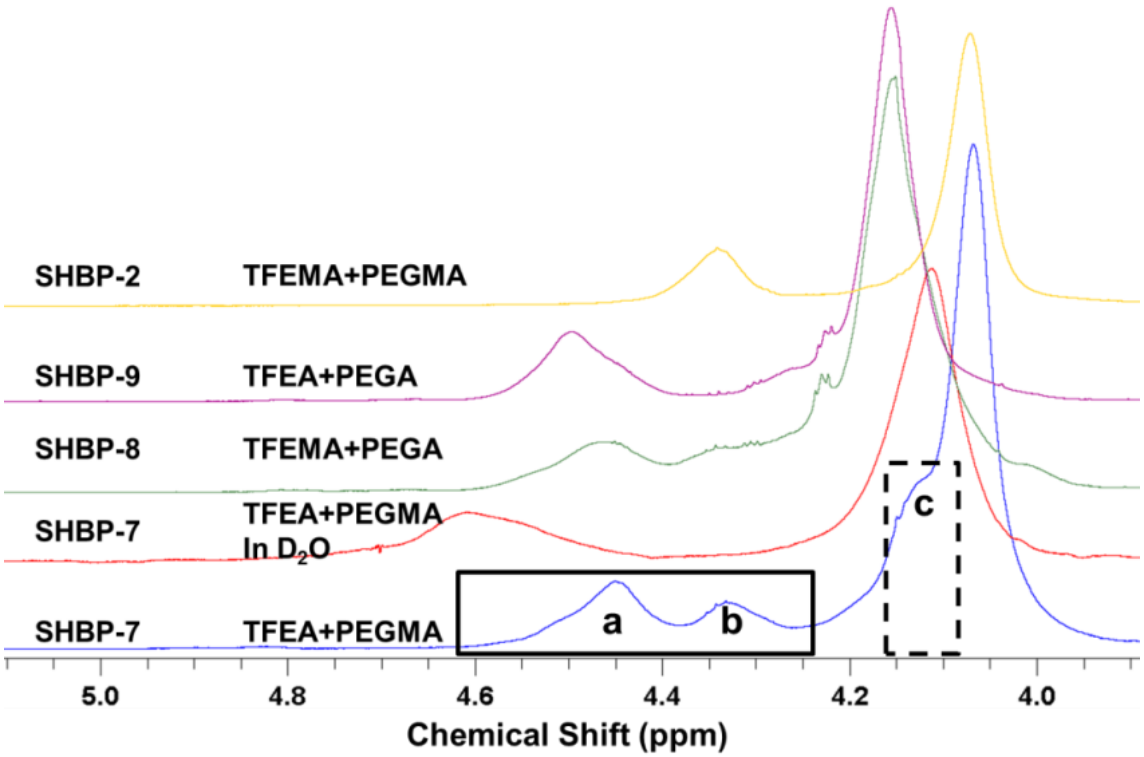


**Figure 5-6** $^{1}$H NMR spectra of 4 selected SHBPs with expanded region between 4~5 ppm. All spectra were recorded using $CDCl_3$ except that SHBP-7 was additionally characterised in $D_2O$.

To get more details, SHBP-7 was also analysed in $D_2O$ using the diffusion NMR technique (1D double-stimulated echo experiment) that suppressed the water signal at 4.7 ppm. Compared with the spectrum in $CDCl_3$, only one peak of $CH_2$ in TFEA was found and it was shifted to 4.6 ppm, while a single peak due to the $CH_2$ adjacent to the ester bond in PEGMA appeared at 4.1 ppm without the previous shoulder peak. The $^{1}$H NMR spectrum in $D_2O$ indicates that the peaks 'b' and 'c' could be attributed to the hydrophobic segments in the polymer. In our previous paper, the reactivity ratios of PEGMA and TFEA were determined to be 2.46 and 0.22, respectively, suggesting a tendency of forming gradient copolymers.[58] Based on these observations, we propose that SHBP-7 was constructed of poly(TFEA-co-PEGMA) gradient copolymer chains, which had TFEA-rich sequences (hydrophobic) and PEGMA-rich sequences (hydrophilic). Therefore the gradient incorporation of TFEA and PEGMA results in different chemical environments of TFEA and PEGMA units, as reflected by the changes in the $^{1}$H NMR spectra. On the basis of the $^{1}$H NMR results, the water-insoluble TFEA segments in SHBP-7 account for 40% of TFEA units, judged by comparing the integration of peaks 'b' and peak 'a', indicating a considerable loss of effective $^{19}$F loading. This may have implications for $^{19}$F MRI performance.

The $^{1}$H NMR spectrum of SHBP-8 (24 mol% of TFEMA and 76 mol% of PEGA) was quite similar to that of SHBP-7. This may be due to the large differences in reactivity ratios of TFEMA and PEGA. However, for SHBP-9 and 2, a single peak for $CH_2$ was found for both TFEA and PEGMA, illustrating that near-ideal copolymers were prepared owing to the close reactivity ratios of TFEA/PEGA and TFEMA/PEGMA. We suggest that statistical copolymers (poly(TFEA-co-PEGA) or poly(TFEMA-co-PEGMA) are more preferable than gradient copolymers (poly(TFEA-co-PEGMA) or poly(TFEMA-co-PEGA) (see Figure 5-7) for $^{19}$F MRI because the latter would not only reduce the effective of $^{19}$F loading but also cause potential multiple peaks in the $^{19}$F NMR spectrum.

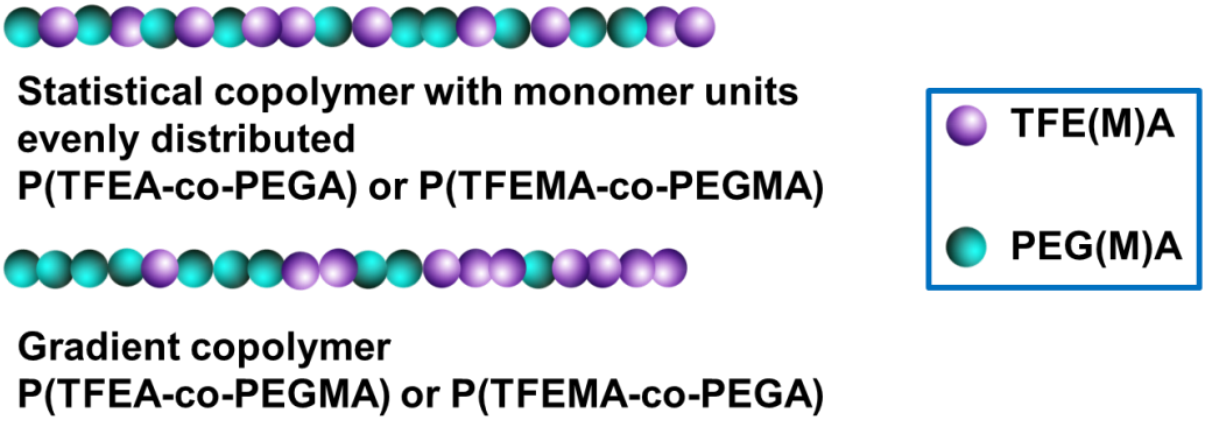


**Figure 5-7** Illustration of the structures of copolymers with different sequence distribution.

### 5.3.5 $^{19}$F NMR Studies

In order to evaluate their potential as $^{19}$F MRI CAs, the SHBPs were examined by $^{19}$F NMR. Samples were dissolved in PBS/$D_2O$ (90/10, v/v) at a concentration of 20 mg $mL^{-1}$. The SHBPs could form nanoparticles with diameters of 4~8 nm in PBS by direct dissolution (see Table 5-2). It should be mentioned that all the SHBPs were water-soluble even with incorporation of fluorinated units up to 60 mol% due to the excellent hydrophilicity of the PEG-based oligomers. As can be seen in Figure 5-8 (A), all the $^{19}$F NMR spectra exhibited a single peak at -73.1~-72.6 ppm. The small triplet at -76.6 ppm could be ascribed to residual fluorinated compounds, including monomer. Clearly, the peaks become broader when the $^{19}$F content increases, indicating the decreasing signal intensity caused by the elevated chance of $^{19}$F association at higher $^{19}$F content. This can also be concluded from the relevant values of half width listed in Table 5-2.

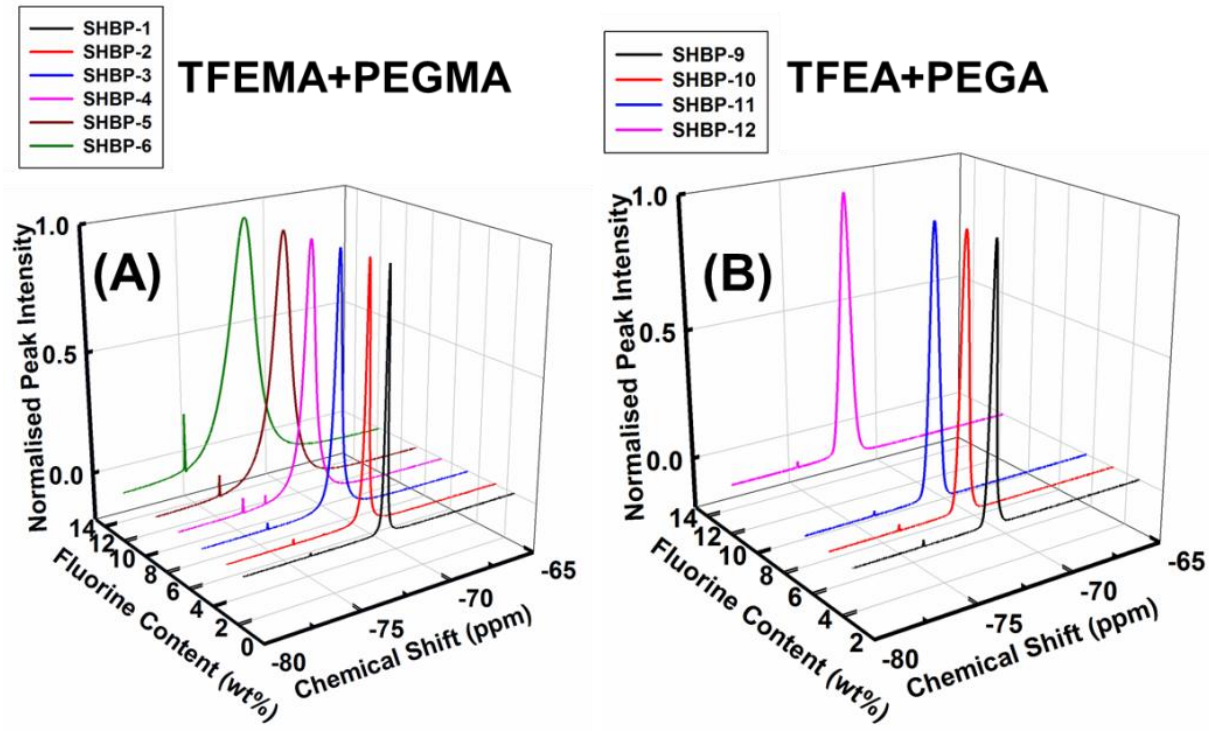


**Figure 5-8** Stacked $^{19}$F NMR spectra of the SHBPs in PBS/$D_2O$(90/10, v/v) at 20 mg $mL^{-1}$ at 25 $^{o}$C. (A) Samples consisted of P(TFEMA-co-PEGMA) copolymer chains. (B) Samples composed of P(TFEA-co-PEGA) copolymer chains. Note: the peak intensities have been normalised to the same value (1.0).

**Table 5-2** Physical and $^{19}$F NMR properties of the SHBPs.

| Sample | $D_h$[a] | F% (wt%)[b] | $T_2$ (ms)[c] | $T_1$ (ms)[c] | Half width (Hz)[c] | $T_g$ ($^o$C) | $^{19}$F MRI Intensity[d] |
|---|---|---|---|---|---|---|---|
| SHBP-1 | 7.90±0.65 | 1.5 | 17.9 | 291.4 | 119.4 | -65.8 | 1.33 |
| SHBP-2 | 7.52±1.1 | 2.8 | 11.3 | 288.0 | 161.7 | -60.7 | 0.65 |
| SHBP-3 | 6.24±0.51 | 4.8 | 6.5 | 282.4 | 288.9 | -59.3 | 0.07 |
| SHBP-4 | 7.42±0.79 | 6.8 | 4.7 | 282.4 | 310.8 | -57.9 | 0.01 |
| SHBP-5 | 5.89±0.50 | 8.8 | 3.6 | 284.4 | 783.7 | -53.3 | 0.0009 |
| SHBP-6 | 8.12±0.42 | 11.9 | 3.0 | 291.4 | 1115.8 | -51.6 | 0.0001 |
| SHBP-7 | 6.45±0.22 | 3.1 | 44.0 | 308.5 | 200.6 | -60.9 | 10.62 |
| SHBP-8 | 6.29±0.24 | 3.3 | 33.9 | 302.3 | 248.0 | -62.1 | 8.59 |
| SHBP-9 | 6.31±0.36 | 3.3 | 87.1 | 345.4 | 223.9 | -61.2 | 17.59 |
| SHBP-10 | 6.07±0.31 | 4.8 | 51.7 | 330.0 | 320.5 | -59.3 | 18.69 |
| SHBP-11 | 5.62±0.08 | 6.4 | 35.3 | 317.7 | 373.4 | -57.7 | 17.34 |
| SHBP-12 | 5.56±0.06 | 11.8 | 20.3 | 308.5 | 422.2 | -48.7 | 13.61 |
| SHBP-13 | 5.12±0.02 | 5.9 | 17.6 | 307.4 | 349.7 | – | 4.50 |
| SHBP-14 | 4.09±0.06 | 6.1 | 24.4 | 309.1 | 333.7 | – | 9.88 |
| SHBP-15 | 4.52±0.21 | 6.7 | 33.1 | 318.1 | 355.6 | – | 16.80 |
| LP-11 | 3.95±0.15 | 5.8 | 43.9 | 319.3 | 371.2 | – | 19.72 |

[a] Hydrodynamic diameters were measured in PBS (1 mg mL$^{-1}$) by DLS at 25 $^o$C, and number-averaged diameters are reported here. [b] $^{19}$F payloads were calculated based on $^1$H NMR results. [c] $^{19}$F NMR spectra and measurements of relaxation times were performed by $^{19}$F NMR at 659 MHz in PBS/$D_2O$ (90/10, v/v) at 25 $^o$C. [c] Half width is the peak width at half height.

To study the effect of copolymer composition and sequence on the $^{19}$F NMR spectra, SHBP-2, 7, 8 and 9 were selected for comparison as these samples have similar fluorine contents of approximately ~3.0 wt%. From Figure 5-9 (A) one can see that SHBP-9 has the highest $^{19}$F NMR signal intensity, while SHBP-7 has the lowest intensity. At a given fluorine concentration, the signal intensity is dependent on mobility of the fluorinated segments, which can be affected by the flexibility of the polymer chains. As reported in our previous study,[15] the fluorinated units connected to acrylate backbones have higher local mobility compared to those in methacrylate backbones. Therefore acrylate monomers are favoured for achieving high $^{19}$F signal intensity. The ratios of peak integral to fluorine concentration were calculated based on $^{19}$F NMR spectra. In

Figure 5-9 (B), the samples consisting of acrylate monomers exhibit higher ratios of peak integral to fluorine concentration, indicating that they have higher $^{19}F$ signal intensity at a given $^{19}F$ concentration. It is noteworthy that SHBP-7 shows a considerably low intensity because it contained 40% of '$^{19}F$ NMR-invisible' $^{19}F$, as revealed by $^{1}H$ NMR spectrum. In the normalised spectra (see Appendix D Figure A5.5), SHBP-7 displays an unsymmetrical peak, which was caused by multiple $^{19}F$ chemical environments in the gradient copolymers. In contrast, the statistical copolymer chains in SHBP-2 and 9 resulted in relatively symmetrical peaks. This is in good agreement with the $^{1}H$ NMR results shown in Figure 5-6.

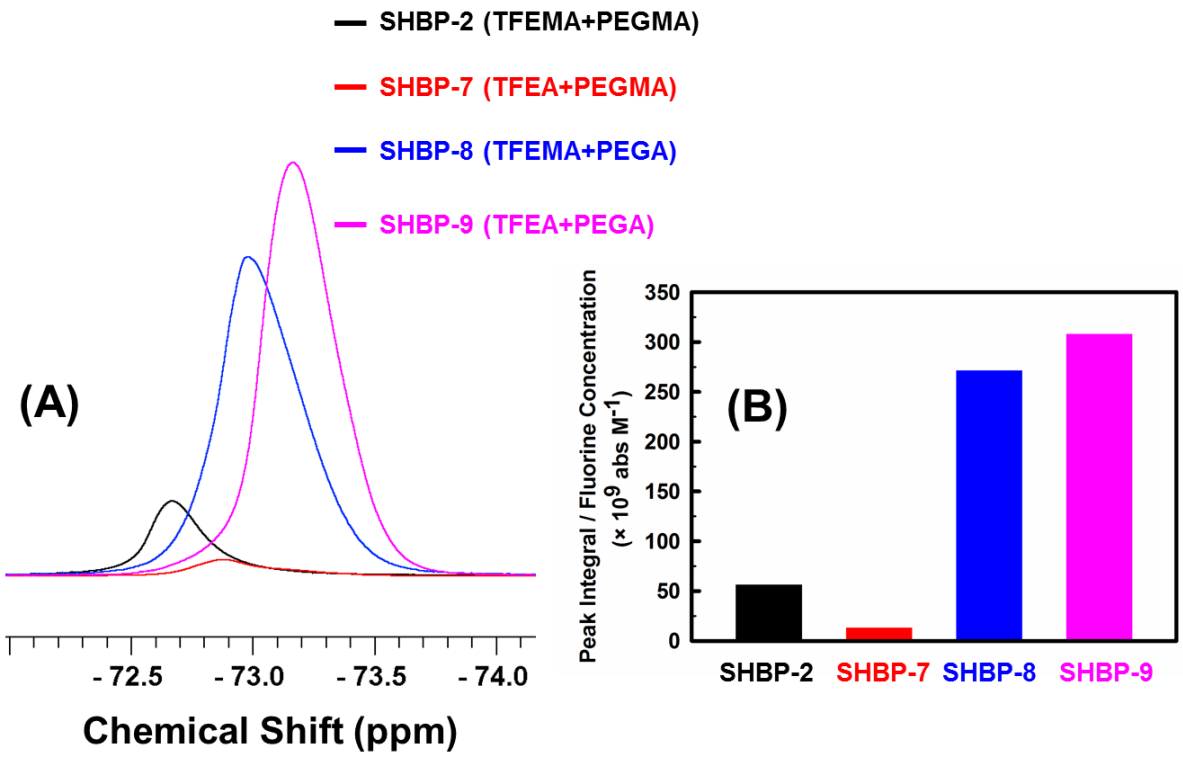


**Figure 5-9** $^{19}F$ NMR results of four SHBPs. (A) Stacked $^{19}F$ NMR spectra of SHBP-2, 7, 8 and 9. (B) The ratios of peak integral to fluorine concentration. Samples were dissolved in PBS/$D_2O$(90/10, v/v) at 20 mg $mL^{-1}$ at 25 $^{o}C$.

Spin-lattice ($T_1$) and spin-spin ($T_2$) relaxation times, which are two important parameters for $^{19}F$ MRI, were measured by $^{19}F$ NMR. Generally, highly mobile fluorine nuclei experience reduced dipolar couplings which can result in narrow $^{19}F$ peaks and long $T_2$ relaxation times. As depicted in Figure 5-10, it is clear that samples composed of acrylates have much longer $T_2$ relaxation times

than their methacrylate counterparts, providing further evidence that fluorine atoms in acrylate backbones are more mobile. In addition, the sample with TFEA/PEGMA (SHBP-7) units exhibit a slightly longer $T_2$ than the polymer consisting of TFEMA/PEGA (SHBP-8). Considering the gradient in sequence of the chains in SHBP-7, we assume that the $^{19}$F NMR-detectable nuclei were mainly from its PEGMA-rich sequences, where the $^{19}$F units were loosely dispersed, affording comparably higher mobility and longer $T_2$ relaxation times than SHBP-8. Furthermore, when the $^{19}$F content increases, $T_2$ decreases dramatically. For example, the $T_2$ of samples with TFEA/PEGA dropped by 76% when $^{19}$F content was increased from 3.3 wt% to 11.8 wt%. This tendency confirms that the $^{19}$F mobility is becoming restricted at higher $^{19}$F contents due to the significantly increasing association in an aqueous environment. Compared with $T_2$, the $T_1$ values stayed relatively short at ~300 ms, implying that the spectral density of motions in the range of 700 MHz was not much affected by the change in polymer conformation. Similar results were observed in previous reports.[19, 20]

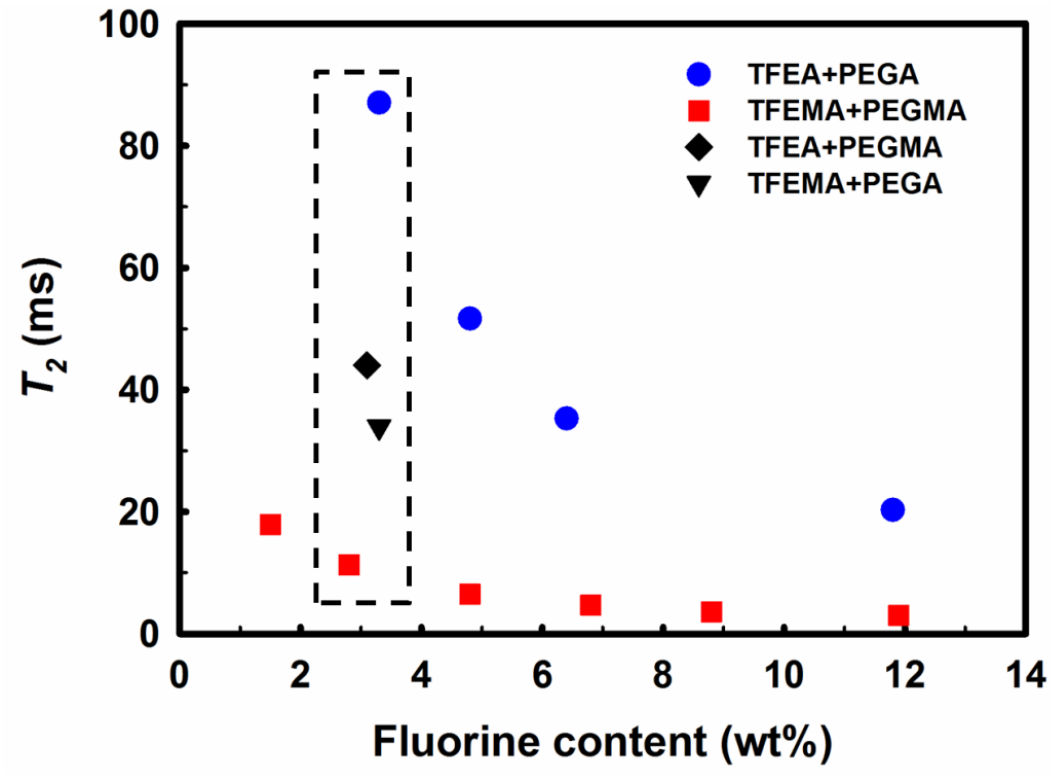


**Figure 5-10** $T_2$ relaxation times of the SHBPs. Samples were dissolved in PBS/$D_2O$(90/10, v/v) at 20 mg mL$^{-1}$ at 25 $^{o}$C.

The glass transition temperature ($T_g$) of the SHBPs is also a measure of the molecular mobility of the main chains, and can be related to the NMR properties. The $T_g$ of the homopolymers PTFEA

and PTFEMA were reported to be 2 and 60 °C,[59, 60] respectively, whereas the $T_g$ of PPEGA and PPEGMA were in the range of -70 ~ -65 °C.[61-63] As listed in Table 5-2, for the SHBPs consisting of TFEMA and PEGMA (from SHBP-1 to 6), $T_g$ increases gradually with the molar fraction of TFEMA from -65.8 to -51.6 °C. The same trend was also noted for SHBPs composed of TFEA and PEGA (from SHBP-9 to 12), as evidenced by the stack of DSC curves (see Appendix D Figure A5.6). In addition, the $T_g$ values were predicted by using the Fox equation based on the composition determined by $^1$H NMR. In Appendix D Figure A5.7, the experimental $T_g$ values are generally in agreement with the curve fitted by Fox equation. The deviation is reasonable as the Fox equation inherently gives the assumed $T_g$ values. It could be expected that the segmental flexibility was more restricted for samples with higher $T_g$, and it is not surprising that longer $T_2$ relaxation times were observed for the samples with lower $T_g$ values because of the enhanced averaging of the dipole-dipole and chemical shift interactions.[15] Therefore, PEG-based oligomers are ideal monomers for the copolymerisation with fluoro monomers to yield copolymers with low $T_g$ and good water-solubility.

As discussed before, the degree of branching (DB) of the SHBPs can be adjusted by varying the [comonomer]/[MECP] ratio. In this work, SHBPs with different DBs and close [TFEA]/[PEGA] ratios were synthesised for the study on the relationship between DB and relaxation times. A linear analogue of SHBP-11 (LP-11, DB = 0) was also prepared for comparison. As displayed in Figure 5-11, a remarkable decrease of $T_2$ from 43.9 to 17.6 ms was observed with an increase of DB, implying poor $^{19}$F mobility for samples with high degrees of branching. This result suggests that samples with high DBs are more compact, leading to the increased rigidity, restricted macromolecular motion and reduced segmental flexibility. The change in macromolecular compactness was also confirmed by GPC MALLS, which revealed that samples with higher DBs showed larger absolute MWs at the same retention time (see Appendix D Figure A5.8). However, the spin-lattice relaxation time $T_1$ was relatively constant at ~310 ms, indicating the little effect of chain motion at a frequency of 700 Hz.

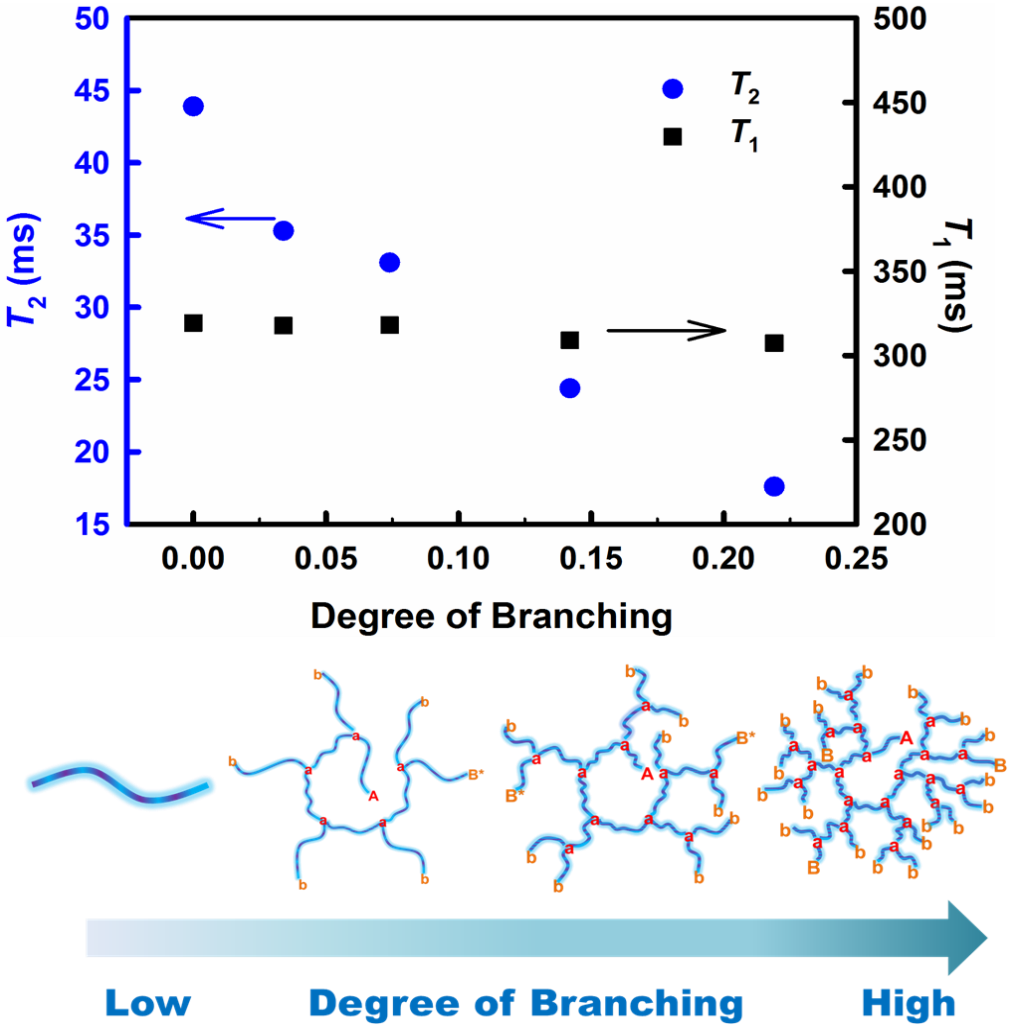


**Figure 5-11** $^{19}$F $T_1$ and $T_2$ relaxation times of SHBPs with different degrees of branching and similar $^{19}$F contents of ~ 3 wt%. DB from low to high: LP-11, SHBP-11, SHBP-13, SHBP-14, and SHBP-15.

### 5.3.6 $^{19}$F MRI Studies

The ultimate aim of this work was to exploit the SHBPs as contrast agents for $^{19}$F MRI. Following $^{19}$F NMR characterisation, the imaging performance was evaluated by *in vitro* $^{19}$F MRI. For comparison, SHBP-2, 7, 8 and 9 were selected for imaging as they possess different compositions but similar $^{19}$F content (~3 wt%). Samples were dissolved in pure water at a concentration of 100 mg mL$^{-1}$, and the solutions were loaded in 30 × 8 mm clear glass vials, of which the cross-sections were shown in phantom images. The vials in the resonator were localised using the $^{1}$H RARE sequence, then the samples were imaged using $^{19}$F FLASH which is a $T_1$-weighted gradient echo sequence with a short scan time.[64] As depicted in Figure 5-12, all four samples were effectively

visualised using $^{19}$F FLASH (repetition time TR = 30 ms) within 47 min. The signal-to-noise ratios (SNRs) for the images are displayed in Figure 5-12 (bottom right). Since the samples have different spin-spin relaxation times, $T_2$-weighted imaging was then conducted using the RARE spin-echo pulse sequence. As shown in Figure 5-12, using the RARE sequence with an echo time TE of 41 ms, SHBP-7, 8 and 9 that have $T_2$s above 30 ms were all well imaged, while SHBP-2 having a short $T_2$ of 11.3 ms exhibited a poor SNR. Notably, SHBP-9 with the longest $T_2$ showed the brightest image. When the TE was increased to 157 ms, only SHBP-9 could be imaged, while SHBP- 7 and 8 were detected with fairly low SNRs. SHBP-2 was found to be hardly visualised owing to its very short $T_2$, affording a dark field. The $^{19}$F MRI results demonstrate that the SHBPs can be selectively imaged by making use of the differences in $T_2$ values and selection of the appropriate pulse sequences.

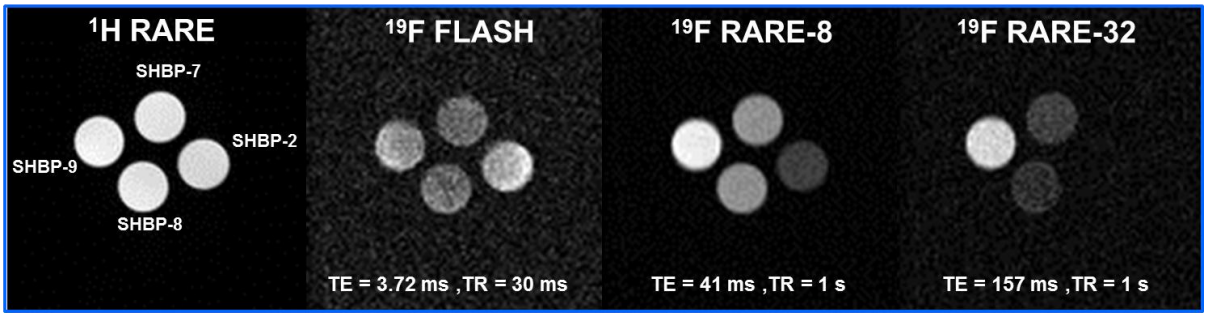


| Sample | [$^{19}$F] (mM) | $T_1$ (ms) | $T_2$ (ms) |
|---|---|---|---|
| SHBP-2 | 147 | 288.0 | 11.3 |
| SHBP-7 | 163 | 308.5 | 44.0 |
| SHBP-8 | 174 | 302.3 | 33.9 |
| SHBP-9 | 174 | 345.4 | 87.1 |

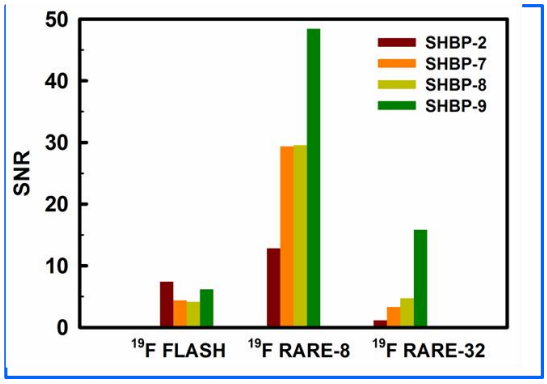


**Figure 5-12** $^{19}$F MRI results for four selected SHBPs. Top: phantom images of the samples using different sequences. Note that $^{1}$H RARE was performed to localise the sample vials. Bottom left: concentrations and $^{19}$F NMR profiles of the samples. Bottom right: signal-to-noise ratios for the imaging experiments.

For $^{19}$F MRI using a spin-echo pulse sequence, the imaging intensity can be described as the following equation.[65]

$$I \approx N(F)\, exp\left(\frac{-TE}{T_2}\right)\left[1 - 2exp\left(\frac{-\left(TR - \frac{TE}{2}\right)}{T_1}\right) + exp\left(\frac{-TR}{T_1}\right)\right] \quad (5\text{-}3)$$

In Equation (5-3), I is the imaging intensity, N(F) is a measure of the number of fluorine nuclei in the sensitive volume of the imaging coil, and TR and TE are the pulse sequence repetition time and echo delay times, respectively. According to this equation, high fluorine content, long $T_2$ and short $T_1$ are required for the design of efficient contrast agents. The $^{19}$F MRI intensity values were estimated using Equation (5-3) using the parameters for the RARE-8 pulse sequence (TE = 41 ms, TR = 1 s, sample concentration = 100 mg mL$^{-1}$). As listed in Table 5-2, the calculated imaging intensity generally decreases with the $T_2$ relaxation time. It is not surprising that the SHBPs consisting of P(TFEA-co-PEGA) exhibit considerably higher imaging intensities compared to those containing P(TFEMA-co-PEGMA). In addition, the calculated imaging intensity decreases with the increase of DB, providing further evidence that SHBPs with low DBs are preferred for $^{19}$F MRI. Besides, the fluorine content plays an important role in imaging intensity. Compared with SHBP-9 (3.3 wt%), SHBP-10 (4.8 wt%) has a shorter $T_2$ relaxation time but a slightly higher imaging intensity due to the increased fluorine content.

These results suggest that SHBPs consisting of P(TFEA-co-PEGA) with low DB are excellent candidates as $^{19}$F MRI contrast agents.

## 5.4 Conclusions

Segmented and highly-branched polymers were successfully synthesised by RAFT SCVP of TFE(M)A, PEG(M)A and a polymerisable trithiocarbonate CTA. By varying monomer type and [comonomer]/[MECP] ratio, SHBPs with desired compositions and degree of branching were prepared. The structure of the SHBPs was thoroughly characterised by a range of different analytical techniques. Statistical copolymers were obtained using TFEA/PEGA or TFEMA/PEGMA, while gradient copolymers were produced with monomers having largely different reactivity ratios. The $^{19}$F NMR properties were affected by both chain composition and monomer sequence. Higher $^{19}$F mobility (longer $T_2$) was achieved in statistical copolymers consisting of acrylate units due to greater segmental flexibility. In addition, the $^{19}$F mobility was greatly restricted for the samples with higher $^{19}$F contents due to increased association of the fluorinated segments. A shortened $T_2$ was also observed with an increase in degree of branching, which caused increased compactness, rigidity, and restricted segmental motion. For gradient

copolymers, the $^{19}F$ signal intensity was significantly reduced by the loss of solubilised $^{19}F$ units in the chains. The relationship between $T_2$ and chain flexibility was also revealed by thermal analysis, and longer $T_2$ relaxation times were observed for the samples with lower glass temperatures, $T_g$. The imaging performance of the SHBPs was confirmed by $^{19}F$ MRI. All the samples could be well imaged by $T_1$-weighted imaging, while they could be selectively visualised using a $T_2$-weighted sequence using different echo times.

In summary, we have demonstrated therefore a robust concept for the controlled design of polymeric $^{19}F$ MRI contrast agents. By tailoring the branched structure and composition, the imaging properties of the agents can be effectively controlled, enabling the realisation of selective and tuneable $^{19}F$ MRI agents. Furthermore, this work provides useful guidance for the future design of polymeric CAs with high $^{19}F$ content, long $T_2$ and short $T_1$ for effective $^{19}F$ MRI

## 5.5 References

1. P. C. Lauterbur, *Nature*, 1973, 242, 190-191.
2. M. Bottrill, L. K. Nicholas and N. J. Long, *Chem Soc Rev*, 2006, 35, 557-571.
3. M. F. Bellin, *Eur J Radiol*, 2006, 60, 314-323.
4. Z. R. Stephen, F. M. Kievit and M. Q. Zhang, *Mater Today*, 2011, 14, 330-338.
5. G. N. Holland, P. A. Bottomley and W. S. Hinshaw, *J Magn Reson*, 1977, 28, 133-136.
6. J. Ruiz-Cabello, B. P. Barnett, P. A. Bottomley and J. W. Bulte, *Nmr Biomed*, 2011, 24, 114-129.
7. J. C. Knight, P. G. Edwards and S. J. Paisey, *Rsc Adv*, 2011, 1, 1415-1425.
8. J. J. Chen, G. M. Lanza and S. A. Wickline, *Wires Nanomed Nanobi*, 2010, 2, 431-440.
9. M. Srinivas, A. Heerschap, E. T. Ahrens, C. G. Figdor and I. J. M. de Vries, *Trends Biotechnol*, 2010, 28, 363-370.
10. J. M. Janjic and E. T. Ahrens, *Wires Nanomed Nanobi*, 2009, 1, 492-501.
11. Y. B. Yu, *Wires Nanomed Nanobi*, 2013, 5, 646-661.
12. K. J. Thurecht, *Macromol Chem Phys*, 2012, 213, 2567-2572.
13. N. R. B. Boase, I. Blakey and K. J. Thurecht, *Polym Chem*, 2012, 3, 1384-1389.
14. L. Nurmi, H. Peng, J. Seppala, D. M. Haddleton, I. Blakey and A. K. Whittaker, *Polym Chem*, 2010, 1, 1039-1047.
15. H. Peng, I. Blakey, B. Dargaville, F. Rasoul, S. Rose and A. K. Whittaker, *Biomacromolecules*, 2009, 10, 374-381.

16. X. N. Huang, G. Huang, S. R. Zhang, K. Sagiyama, O. Togao, X. P. Ma, Y. G. Wang, Y. Li, T. C. Soesbe, B. D. Sumer, M. Takahashi, A. D. Sherry and J. M. Gao, *Angew Chem Int Edit*, 2013, 52, 8074-8078.
17. H. Peng, K. J. Thurecht, I. Blakey, E. Taran and A. K. Whittaker, *Macromolecules*, 2012, 45, 8681-8690.
18. H. G. Lu, F. Y. Su, Q. Mei, Y. Q. Tian, W. J. Tian, R. H. Johnson and D. R. Meldrum, *J Mater Chem*, 2012, 22, 9890-9900.
19. K. W. Wang, H. Peng, K. J. Thurecht, S. Puttick and A. K. Whittaker, *Polym Chem*, 2013, 4, 4480-4489.
20. K. Wang, H. Peng, K. J. Thurecht, S. Puttick and A. K. Whittaker, *Polym Chem*, 2014, 5, 1760.
21. M. Ogawa, S. Nitahara, H. Aoki, S. Ito, M. Narazaki and T. Matsuda, *Macromol Chem Phys*, 2010, 211, 1602-1609.
22. J. M. Criscione, B. L. Le, E. Stern, M. Brennan, C. Rahner, X. Papademetris and T. M. Fahmy, *Biomaterials*, 2009, 30, 3946-3955.
23. C. Porsch, Y. N. Zhang, A. Ostlund, P. Damberg, C. Ducani, E. Malmstrom and A. M. Nystrom, *Part Part Syst Char*, 2013, 30, 381-390.
24. Z. H. Huang, R. S. Sengar, A. Nigam, M. C. Abadjian, D. M. Potter, D. B. Grotjahn and E. C. Wiener, *Invest Radiol*, 2010, 45, 641-654.
25. B. E. Rolfe, I. Blakey, O. Squires, H. Peng, N. R. B. Boase, C. Alexander, P. G. Parsons, G. M. Boyle, A. K. Whittaker and K. J. Thurecht, *J Am Chem Soc*, 2014, 136, 2413-2419.
26. K. J. Thurecht, I. Blakey, H. Peng, O. Squires, S. Hsu, C. Alexander and A. K. Whittaker, *J Am Chem Soc*, 2010, 132, 5336-5337.
27. W. J. Du, A. M. Nystrom, L. Zhang, K. T. Powell, Y. L. Li, C. Cheng, S. A. Wickline and K. L. Wooley, *Biomacromolecules*, 2008, 9, 2826-2833.
28. W. J. Du, Z. Q. Xu, A. M. Nystrom, K. Zhang, J. R. Leonard and K. L. Wooley, *Bioconjugate Chem*, 2008, 19, 2492-2498.
29. D. J. Coles, B. E. Rolfe, N. R. B. Boase, R. N. Veedu and K. J. Thurecht, *Chem Commun*, 2013, 49, 3836-3838.
30. M. Oishi, S. Sumitani and Y. Nagasaki, *Bioconjugate Chem*, 2007, 18, 1379-1382.
31. M. M. Bailey, C. M. Mahoney, K. E. Dempah, J. M. Davis, M. L. Becker, S. Khondee, E. J. Munson and C. Berkland, *Macromol Rapid Comm*, 2010, 31, 87-92.

32. M. M. Bailey, S. R. Kline, M. D. Anderson, J. L. Staymates and C. Berkland, *J Appl Polym Sci*, 2012, 126, 1218-1227.
33. B. L. Liu, A. Kazlauciunas, J. T. Guthrie and S. Perrier, *Macromolecules*, 2005, 38, 2131-2136.
34. B. L. Liu, A. Kazlauciunas, J. T. Guthrie and S. Perrier, *Polymer*, 2005, 46, 6293-6299.
35. M. Luzon, C. Boyer, C. Peinado, T. Corrales, M. Whittaker, L. Tao and T. P. Davis, *J Polym Sci Pol Chem*, 2010, 48, 2783-2792.
36. K. J. Thurecht, I. Blakey, H. Peng, O. Squires, S. Hsu, C. Alexander and A. K. Whittaker, *J Am Chem Soc*, 2010, 132, 5336-5337.
37. Y. Wang, C. Y. Hong and C. Y. Pan, *Biomacromolecules*, 2012, 13, 2585-2593.
38. J. Rosselgong, S. P. Armes, W. Barton and D. Price, *Macromolecules*, 2009, 42, 5919-5924.
39. J. Rosselgong, S. P. Armes, W. R. S. Barton and D. Price, *Macromolecules*, 2010, 43, 2145-2156.
40. R. Wang, Y. W. Luo, B. G. Li and S. P. Zhu, *Macromolecules*, 2009, 42, 85-94.
41. J. M. J. Frechet, M. Henmi, I. Gitsov, S. Aoshima, M. R. Leduc and R. B. Grubbs, *Science*, 1995, 269, 1080-1083.
42. Y. Y. Zhuang, Y. Su, Y. Peng, D. L. Wang, H. P. Deng, X. D. Xi, X. Y. Zhu and Y. F. Lu, *Biomacromolecules*, 2014, 15, 1408-1418.
43. M. J. Zhang, H. H. Liu, W. Shao, C. N. Ye and Y. L. Zhao, *Macromolecules*, 2012, 45, 9312-9325.
44. A. P. Vogt, S. R. Gondi and B. S. Sumerlin, *Aust J Chem*, 2007, 60, 396-399.
45. J. Han, S. P. Li, A. J. Tang and C. Gao, *Macromolecules*, 2012, 45, 4966-4977.
46. C. B. Zhang, Y. A. Zhou, Q. A. Liu, S. X. Li, S. Perrier and Y. L. Zhao, *Macromolecules*, 2011, 44, 2034-2049.
47. X. B. Zhou, J. Zhu, M. Y. Xing, Z. B. A. Zhang, Z. P. Cheng, N. A. C. Zhou and X. L. Zhu, *Eur Polym J*, 2011, 47, 1912-1922.
48. A. P. Vogt and B. S. Sumerlin, *Macromolecules*, 2008, 41, 7368-7373.
49. S. P. Li and C. Gao, *Polym Chem*, 2013, 4, 4450-4460.
50. S. P. Li, J. Han and C. Gao, *Polym Chem*, 2013, 4, 1774-1787.
51. S. Carter, S. Rimmer, R. Rutkaite, L. Swanson, J. P. A. Fairclough, A. Sturdy and M. Webb, *Biomacromolecules*, 2006, 7, 1124-1130.
52. S. Carter, S. Rimmer, A. Sturdy and M. Webb, *Macromol Biosci*, 2005, 5, 373-378.
53. S. Carter, B. Hunt and S. Rimmer, *Macromolecules*, 2005, 38, 4595-4603.

54. D. Yan, C. Gao and H. Frey, *Hyperbranched polymers: synthesis, properties, and applications*, John Wiley & Sons, 2011.
55. J. Chiefari, Y. K. Chong, F. Ercole, J. Krstina, J. Jeffery, T. P. T. Le, R. T. A. Mayadunne, G. F. Meijs, C. L. Moad, G. Moad, E. Rizzardo and S. H. Thang, *Macromolecules*, 1998, 31, 5559-5562.
56. G. Moad, Y. K. Chong, A. Postma, E. Rizzardo and S. H. Thang, *Polymer*, 2005, 46, 8458-8468.
57. R. M. England and S. Rimmer, *Polym Chem*, 2010, 1, 1533-1544.
58. C. Zhang, H. Peng and A. K. Whittaker, *J Polym Sci Pol Chem*, 2014, 52, 2375-2385.
59. P. Spahn, C. E. Finlayson, W. M. Etah, D. R. E. Snoswell, J. J. Baumberg and G. P. Hellmann, *J Mater Chem*, 2011, 21, 8893-8897.
60. O. Chiantore, M. Lazzari, M. Aglietto, V. Castelvetro and F. Ciardelli, *Polym Degrad Stabil*, 2000, 67, 461-467.
61. Y. Q. Zhang, Z. H. Xu, Z. K. Wang, Y. S. Ding and Z. G. Wang, *Rsc Adv*, 2014, 4, 20582-20591.
62. J. Rolland, J. Brassinne, J. P. Bourgeois, E. Poggi, A. Vlad and J. F. Gohy, *J Mater Chem A*, 2014, 2, 11839-11846.
63. H. Q. Lin, B. D. Freeman, S. Kalakkunnath and D. S. Kalika, *J Membrane Sci*, 2007, 291, 131-139.
64. A. Haase, J. Frahm, D. Matthaei, W. Hanicke and K. D. Merboldt, *J Magn Reson*, 1986, 67, 258-266.
65. R. E. Hendrick, *Magn Reson Imaging*, 1987, 5, 31-37.

# Chapter 6 Partly-Fluorinated Star Polymers with a POSS core for F-19 MRI

## 6.1 Introduction

Owing to the rapidly advancing field of nanotechnology, the emergence of nanomedicine, which refers to the technologies for the diagnosis, treatment and prevention of diseases using nanomaterials, has revolutionised the biomedical field with a new generation of medicines.[1, 2] In recent years, theranostic nanomedicine that combines therapy and diagnosis has drawn considerable attention.[3, 4] Being integrated with functions such as drug loading, targeted drug delivery and imaging, theranostic agents can be utilised not only for drug delivery and localising but also for biomedical imaging, greatly enhancing cancer diagnosis and treatment. A vast library of nanomaterials have been exploited as potential platforms for the development of theranostic nanomedicine, including liposomes, micelles, polymer nanoparticles, inorganic nanoparticles, hybrid nanoparticles, etc.[3, 5] To impart multifunctionality to a nanoparticle-based system, the convergence of both organic and inorganic components are often required, resulting in hybrid theranostic nanoparticles.[6-8]

Polyhedral oligomeric silsesquioxanes (POSS) are a class of silsesquioxanes that have the general formula, $(RSiO_{1.5})_n$.[9] The chemical structure of the most studied and exploited POSS can be described as $(RSiO_{1.5})_8$, in which one Si atom has three stable Si-O bonds and a Si-C bond for the attachment of diverse functionalities. Therefore, as a type of organic/inorganic hybrid nanomaterial, POSS has been utilised as an excellent platform for the design of nanomedicine owing to its symmetrical cage-like structure, small particle size (0.53~1.5 nm), biological stability, low cytotoxicity, high density of functional moieties and commercial availability.[9-12] In the past decade, great effort has been devoted to the fabrication of POSS/polymer hybrid nanomaterials, which have a number of benefits as therapeutic and diagnostic agents. First, the cage-like structure of POSS has been proven to be advantageous for entrapping various drug/gene/dye molecules.[13-18] Second, the

introduction of polymers can facilitate diverse architectures (micellar, star-like, hyperbranched and dendritic structures) and functionalities (fluorescence agents, targeting ligands, stimuli-responsive properties, etc).[19-24] Third, due to the well-defined structure of POSS molecules, POSS/polymer hybrid nanomaterials can be readily designed to have controlled structure and composition with narrow polydispersity, which are essential for building up robust platforms.[10] According to the $(RSiO_{1.5})_8$ structure, POSS possesses eight potentially-functionalisable sites. Hence, they have been extensively employed as core materials for the synthesis of star polymers which are constructed of a central core and multiple arms.[25-28] Star polymers have been recognised as an important class of polymers for the development of nanomedicine owing to their 3D globular architecture and multifunctional arms.[29] Recently, the synthesis of star polymers with POSS cores via controlled radical polymerisation (CRP) has attracted increasing attention. A number of such star polymers have been prepared by atom transfer radical polymerisation (ATRP)[14, 25, 30-32] and reversible addition-fragmentation chain transfer (RAFT) polymerisation.[33, 34] However, there are still very few reports utilising the RAFT-mediated approach compared with ATRP, despite the versatility and robustness of RAFT technique for the synthesis of star polymers.[35-37] As a typical example, Ye and co-workers explored the 'grafting from' synthesis of star polymers with POSS cores using RAFT polymerisation.[34] Azide-functionalised POSS was conjugated with an alkyne-terminated chain transfer agent (CTA) via click chemistry (copper (I)-catalysed [2+3] Huisgen cycloaddition), resulting in a macroCTA anchored with eight CTA moieties. Then the macroCTA was used for the RAFT polymerisation of methyl methacrylate (MMA), yielding star polymers with a POSS core and PMMA arms. Confirmation of the controlled nature of the RAFT polymerisation was achieved by etching the core with HF, after which the PMMA arms were found to have narrow molar mass dispersity (1.15) by gel permeation chromatography (GPC).[38] While the POSS-initiated polymerisation exhibited controlled characteristics, it was noteworthy that bimodal GPC traces were observed for the star polymers, indicating that the formation of star polymers was accompanied by a parallel polymerisation of linear analogues. This distribution of products is typically observed for star polymers synthesised via the 'R-group' approach.[35]

Magnetic resonance imaging (MRI) is an indispensable modern diagnostic technique. It features non-invasive and radiation-free imaging and can provide 3D anatomic images at high resolution.[39] Although $^{1}H$ is the dominant nuclei studied in MRI, $^{19}F$ MRI has also been considered as a promising MRI modality in the past few decades because $^{19}F$ has comparable nuclear magnetic resonance (NMR) properties to $^{1}H$. More importantly, the lack of detectable $^{19}F$ in the body can ensure minimal background signal, highlighting the quantitative capability of $^{19}F$ MRI. Very

recently, the development of polymeric agents for $^{19}$F MRI has been an active research field. Owing to the abundant architectures and functionalities present in polymeric systems, a wide range of partly-fluorinated polymers have been developed as contrast agents (CAs) for $^{19}$F MRI, including linear polymers,[40-43] star polymers,[44, 45] hyperbranched polymers,[46-51] dendrimers,[52-54] etc. These studies have pointed out that successful $^{19}$F MRI CAs should possess high fluorine content as well as highly mobile $^{19}$F nuclei. In Chapter 3, core crosslinked (CCS) star polymers were evaluated to be excellent candidates as $^{19}$F MRI agents. The positioning of $^{19}$F in flexible and water-soluble arms resulted in improved $^{19}$F mobility in aqueous solution compared with those in a hyperbranched core. Inspired by this finding, we propose that star polymers with a POSS core and partly-fluorinated arms could be utilised as efficient $^{19}$F MRI CAs and potential drug carriers.

In this chapter, we aim to synthesise star polymers with a POSS core and partly-fluorinated arms. Octavinyl POSS with eight vinyl groups was selected as the starting material, and functionalised with eight hydroxyl groups via UV-induced thiol-ene reaction. Then a macroCTA with eight CTA moieties on the POSS core was prepared through the esterification between hydroxyl-functionalised POSS and a carboxyl-terminated CTA. The macroCTA was used for the RAFT polymerisation of a fluoro monomer and PEG-based oligomer, affording star polymers with a POSS core. Owing to the presence of highly-mobile $^{19}$F units and a POSS cage with the potential for loading with a drug molecule, it is expected that these star polymers have the potential to be theranostic agents for $^{19}$F MRI and drug delivery.

## 6.2 Experimental Section

### 6.2.1 Materials

Octavinyl POSS was purchased from Hybrid Plastics. Poly(ethylene glycol) methyl ether acrylate (PEGA, MW = 480) and 2,2,2-trifluoroethyl methacrylate (TFEA) were purchased from Sigma-Aldrich and passed through basic alumina columns to remove inhibitors prior to use. 2-Mercaptoethanol and 2,2-dimethoxy-2-phenylacetophenone (DMPA) were obtained from Sigma-Aldrich and used as received. 2,2'-Azobis(2-methylpropionitrile) (AIBN), was recrystallised from ethanol twice before use. 1,1'-Azobis(cyclohexanecarbonitrile) (VAZO-88) was purchased from Sigma-Aldrich and used as received. 4-(Dimethylamino)pyridine (DMAP) and N,N'-dicyclohexylcarbodiimide (DCC, purchased from Alfa Aesar) were used as received. The trithiocarbonate chain transfer agent, 4-cyano-4-(((phenethylthio)carbonothioyl)thio)pentanoic acid (denoted as 'CTA') was synthesised and purified according to a previously reported method.[55]

Milli-Q water with a resistivity of 18.4 MΩ $cm^{-1}$ was used for the relevant experiments. Tetrahydrofuran (THF) and dichloromethane (DCM) were obtained from a solvent purification system (MB-SPS-800-Auto, Mbraun) and used directly. All other solvent were of analytical grade.

## 6.2.2 Synthesis

### 6.2.2.1 Synthesis of Hydroxyl-functionalised POSS (POSS-$(OH)_8$

Octavinyl POSS (5 g, 7.9 mmol), 2-mercaptoethanol (7.41 g, 0.095 mol) and the photoinitiator DMAP (0.243 g, 0.95 mmol) were mixed in 50 mL of THF in a 100 mL flask. Then the flask was sealed with a silicon septum and covered with aluminium foil, followed by purging with argon for 20 min. The flask was subsequently exposed to UV irradiation (SunRay 600 UV flood curing system, UVitron) for 40 min at a constant power of 0.61 mW $cm^{-2}$. After cooling to room temperature, the crude solution was concentrated by rotary evaporation and purified by precipitating in diethyl ether three times. A pale powder was obtained after drying in vacuum at room temperature for 24 h. Yield: 6.8 g, 68%. $^1$H NMR (700 MHz, DMSO-$d_6$, ppm): 4.72 (t, $^1$H, $CH_2O\underline{H}$), 3.51 (q, 2H, $C\underline{H_2}OH$), 2.55 (q, 4H, $C\underline{H_2}SC\underline{H_2}$), 0.97 (t, 2H, $SiC\underline{H_2}CH_2S$). $^{13}$C NMR (125 MHz, DMSO-$d_6$, ppm): 61.72 ($\underline{C}H_2OH$), 34.58 ($\underline{C}H_2CH_2OH$), 26.29 ($SiCH_2\underline{C}H_2S$), 13.55 ($Si\underline{C}H_2CH_2S$).

### 6.2.2.2 Synthesis of POSS-based macroCTA (POSS-$(CTA)_8$)

POSS-$(OH)_8$ (1.15 g, 0.92 mmol), CTA (3.7 g, 11 mmol) and DMAP (0.28 g, 2.31 mmol) were dissolved in 75 mL of THF, which was then purged with argon for 20 min in an ice bath. DCC (4.76 g, 23.1 mmol) in 25 mL of THF was injected to the flask over 10 min under argon atmosphere. The reaction was stirred at 0 $^o$C for 1 h and then room temperature for 24 h. After reaction, the crude solution was filtered to remove the insoluble dicyclohexylurea precipitates. The filtrate was concentrated by rotary evaporation and purified by precipitating in hexane three times. After drying under high vacuum, a scarlet viscous oil was obtained. Yield: 3.17 g, 90%. $^1$H NMR (700 MHz, $CDCl_3$, ppm): at 7.23-7.31 (m, 5H, $C_6\textit{H}_5$ from the phenyl group), 4.24 (t, 2H, $SCH_2C\underline{H_2}O$), 3.57 (t, 2H, $S(C{=}S)SC\underline{H_2}CH_2$), 2.98 (t, 2H, $S(C{=}S)SCH_2C\underline{H_2}$), 2.77 (t, 2H, $SC\underline{H_2}CH_2O$), 2.65 ($SiCH_2C\underline{H_2}S$), 2.38-2.52 (m, 4H, $C\underline{H_2}C\underline{H_2}COO$), 1.88 (s, 3H, $SCC\underline{H_3}(CN)(CH_2)$), 1.05 (t, 2H, $SiC\underline{H_2}CH_2S$). $^{13}$C NMR (125 MHz, $CDCl_3$, ppm): at 216.84 (carbon of trithiocarbonate group), 171.54 ($\underline{C}OOCH_2$), 139.46 (the substituted carbon of phenyl group), 129.00, 128.87, 127.16 (rest five carbons in phenyl group), 119.22 ($\underline{C}N$), 63.77 ($COO\underline{C}H_2$), 46.80 ($\underline{C}(CH_3)(CN)(CH_2)$) 38.27 ($PhCH_2\underline{C}H_2S$), 34.35 ($Ph\underline{C}H_2CH_2S$), 34.14 ($\underline{C}H_2\underline{C}H_2COO$), 30.47

(S<u>C</u>H$_2$CH$_2$OOC), 30.03 (<u>C</u>H$_2$<u>C</u>H$_2$COO), 26.45 (SiCH$_2$<u>C</u>H$_2$), 25.18 (<u>C</u>H$_3$C(CN)(CH$_2$)), 13.29 (Si<u>C</u>H$_2$CH$_2$).

#### 6.2.2.3 Synthesis of Star Polymers

In a typical experiment, POSS-(CTA)$_8$ (96 mg, 0.025 mmol), TFEA (0.462 g, 3 mmol), PEGA (3.36 g, 7 mmol) and AIBN (6.56 mg, 0.04 mmol) were dissolved in 10 mL of 1,4-dioxane in a 50 mL flask. Feed ratio: [TFEA]/[PEGA]/[CTA]/[AIBN] = 15/35/1/0.2. The flask was then sealed with a rubber septum and purged with argon for 15 min before immersing in a 70 $^{o}$C oil bath for 2 h. According to $^{1}$H NMR, the conversions of TFEA and PEGA were 73% and 60%, respectively. After polymerisation, ~1 mL of the crude solution was collected for characterisation, and the remainder was diluted to 30 mL in water and dialysed against water for 2 days using dialysis tubing with molecular-weight-cut-off (MWCO) of 100 kDa (Spectrum Laboratories Inc.). After lyophilisation, a yellowish viscous oil was obtained. Yield: 0.56 g, 22%. This sample was denoted as SP-1.

Two additional samples were synthesised by varying the monomer to CTA ratios under the same conditions, and purified using the same procedure. For the sample SP-2 synthesised using a feed ratio of [TFEA]/[PEGA]/[CTA]/[AIBN] = 30/70/1/0.2, the conversions of TFEA and PEGA were 68% and 55%, respectively. Yield: 0.97 g, 44%. For the sample SP-3 synthesised using a feed ratio of [TFEA]/[PEGA]/[CTA]/[AIBN] = 45/105/1/0.2, the conversions of TFEA and PEGA were 65% and 52%, respectively. Yield: 0.73 g, 35%.

### 6.2.3 Characterisation

#### Gel Permeation Chromatography (GPC)

Molecular weights and molecular weight distributions were determined by GPC using a Waters Alliance 2690 Separations Module equipped with Waters 2414 Refractive Index (RI) Detector, Waters 2489 UV/Visible Detector, Waters 717 Plus Autosampler and Waters 1515 Isocratic HPLC Pump. Samples were dissolved in THF and passed through 0.45 μm filters before each measurement. THF was used as the mobile phase at a flow rate of 1 mL min$^{-1}$. The system was calibrated using polystyrene (PS) standards, to which the number average molecular weight ($M_n$) and weight average molecular weight ($M_w$) were referenced.

### Fourier Transform Infrared (FTIR) Spectroscopy

FTIR spectra were recorded on a Nicolet 5700 FTIR spectrometer (Thermo Electron Corporation) equipped with a Nicolet Smart Orbit ATR accessory having a diamond internal reflection element. Spectra were collected in the range of 4500 – 525 $cm^{-1}$ with a scan number of 64 and resolution of 4 $cm^{-1}$.

### $^{1}H$ and $^{13}C$ Nuclear Magnetic Resonance (NMR)

$^{1}H$ NMR and $^{13}C$ NMR were performed on a Bruker Avance 700 MHz spectrometer at 25 $^{o}C$ using an internal lock ($CDCl_3$ or DMSO-$d_6$) and referenced to the residual non-deuterated solvent. $^{1}H$-$^{1}H$ Correlation spectroscopy (COSY), $^{1}H$-$^{13}C$ heteronuclear multiple-bond correlation ($^{1}H$-$^{13}C$ HMBC), $^{1}H$-$^{13}C$ heteronuclear single quantum coherence ($^{1}H$-$^{13}C$ HSQC) and distortionless enhancement by polarisation transfer (DEPT) $^{13}C$ NMR spectra were recorded on a Bruker Avance 700 MHz using $CDCl_3$ as solvent at 25 $^{o}C$.

### Dynamic Light Scattering (DLS)

DLS measurements were carried out on a Nanoseries Zetasizer (Malvern, UK) at 25 $^{o}C$. Star polymers were dissolved in PBS at a concentration of 1 mg $mL^{-1}$ and passed through 0.45 μm filters to remove dust particles prior to each measurement. Each hydrodynamic diameter was the average value of 3 measurements. To minimise the possible influence of large aggregates, number-averaged diameters are reported.

### $^{19}F$ Nuclear Magnetic Resonance ($^{19}F$ NMR)

All $^{19}F$ NMR spectra were acquired at 659 MHz on a Bruker Avance 700 MHz spectrometer. The samples were prepared by dissolving the polymers in PBS/$D_2O$ (90/10, v/v) at a concentration of 20 mg $mL^{-1}$. All measurements were performed at 25 $^{o}C$. A 90$^{o}$ pulse of 15.1 μs was used in all measurements, the relaxation delay was 2 s and the acquisition time was 0.18 s. Data were collected using a spectrum width of 46 kHz, 16k data points and 64 scans.

$^{19}F$ spin-spin relaxation times ($T_2$) were measured using the Carr-Purcell-Meiboom-Gill (CPMG) pulse sequence at 25 $^{o}C$. The samples were dissolved in PBS/$D_2O$ (90/10, v/v) at a concentration of 20 mg $mL^{-1}$. The relaxation delay was 2.3 s and the acquisition time was 0.18 s. For each measurement, the echo times were from 2 to 770 ms and 15 points were collected, which could be described by exponential functions for the calculation of $T_2$.

$^{19}$F spin-lattice ($T_1$) relaxation times were measured using the standard inversion-recovery pulse sequence. The relaxation delay was 2.5 s and the acquisition time was 0.18 s. For each measurement, the recovery times were from 2 ms to 3 s and 15 points were acquired.

## 6.3 Results and Discussion

### 6.3.1 Design Concept

The aim of this work was to synthesise star polymers with a POSS core and partly-fluorinated and water-soluble arms for potential applications as theranostic agents. The synthetic route is described in Figure 6-1. Vinyl-functionalised POSS was first reacted with 2-mercaptoethanol via UV-induced thiol-ene reaction to introduce hydroxyl groups to the POSS. Then CTA-functionalised POSS, a macroCTA, was synthesised through the standard DCC/DMAP esterification between hydroxyl-functionalised POSS and carboxyl-terminated CTA molecules. The macroCTA was utilised for the RAFT copolymerisation of 2,2,2-trifluoroethyl methacrylate (TFEA) and poly(ethylene glycol) methyl ether acrylate (PEGA), yielding star polymers with a POSS core and P(TFEA-co-PEGA) arms. As reported in Chapter 5, P(TFEA-co-PEGA) copolymers are excellent candidates as contrast agents for $^{19}$F MRI because of the high mobility of the fluorine units in the polymer chain even with high molar fractions of TFEA. Therefore the multifunctional star polymers can be used for MRI and drug delivery. To be more specific, the arms are expected to be $^{19}$F MRI visible, while the POSS core has the potential to load drug molecules.

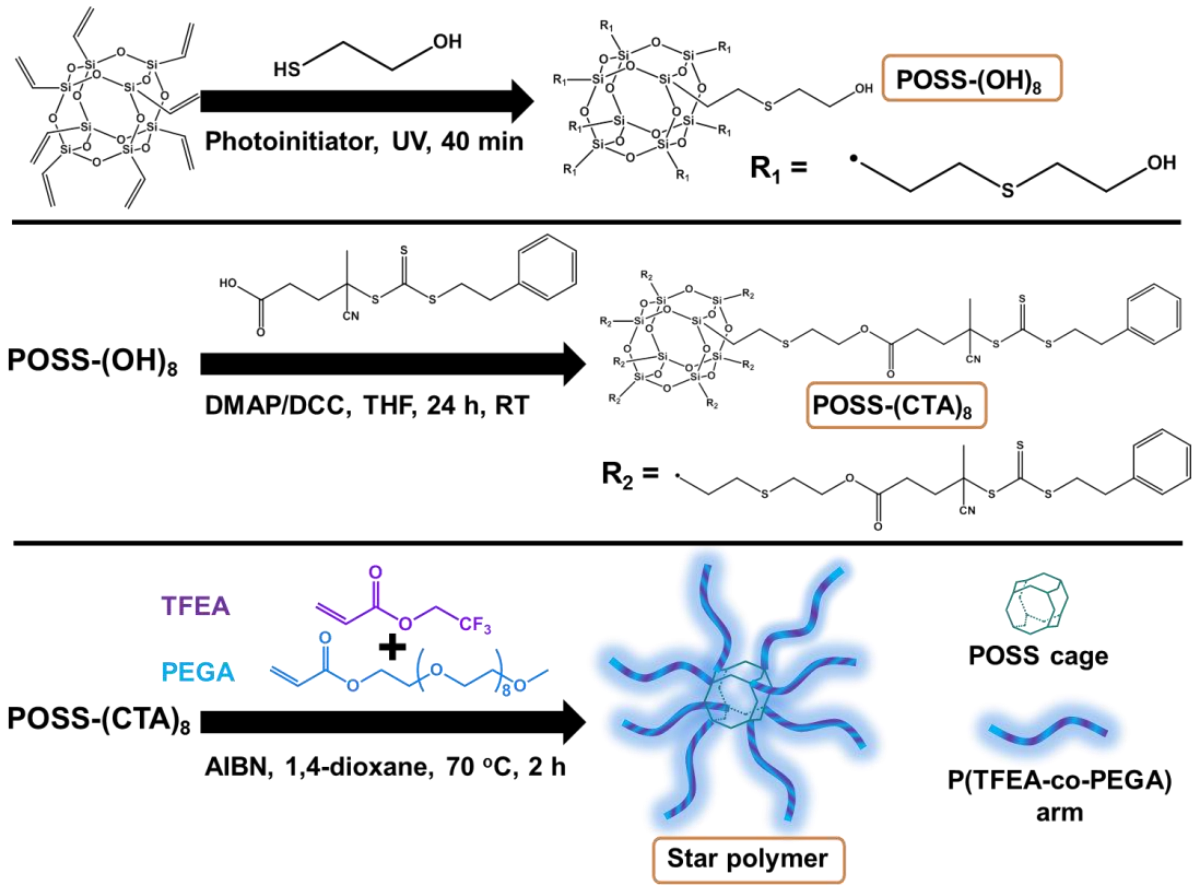


**Figure 6-1** Schematic illustration of the synthesis of hydroxyl-functionalised POSS (POSS-$(OH)_8$), CTA-functionalised POSS (POSS-$(CTA)_8$) and star polymers with a POSS core and P(TFEA-co-PEGA) copolymer arms.

### 6.3.2 Synthesis of POSS-$(OH)_8$ and POSS-$(CTA)_8$

Octavinyl POSS was reacted with 2-mercaptoethanol in THF by UV-mediated thiol-ene chemistry. The conversion was monitored by $^1$H NMR, and the samples were characterised by $^1$H and $^{13}$C NMR. In Figure 6-2 (A), multiple peaks of vinyl protons were found at 6.0~6.2 ppm for octavinyl POSS, and these peaks disappeared after 40 minutes of UV radiation, indicating the high efficiency of UV-induced thiol-ene reaction. The absence of vinyl peaks was also revealed by the spectrum of POSS-$(OH)_8$, implying that all the eight vinyl groups were functionalised (see enlarged $^1$H NMR spectra in Appendix E Figure A6.1). In addition, all the characteristic proton peaks of POSS-$(OH)_8$ can be assigned in the spectrum (Figure 6-2 (A)) and the integrals matched the chemical structure (see Appendix E Figure A6.1). The $^{13}$C NMR spectrum in Figure 6-2 (B) further confirmed the chemical structure of POSS-$(OH)_8$ with all the carbons assigned. The chemical structure was also verified by the relevant correlations in $^1$H-$^1$H COSY spectrum ((see Appendix E Figure A6.1)).

These combined NMR results indicate the efficient functionalisation of octavinyl POSS with 2-mercaptoethanol by UV-induced thiol-ene reaction.

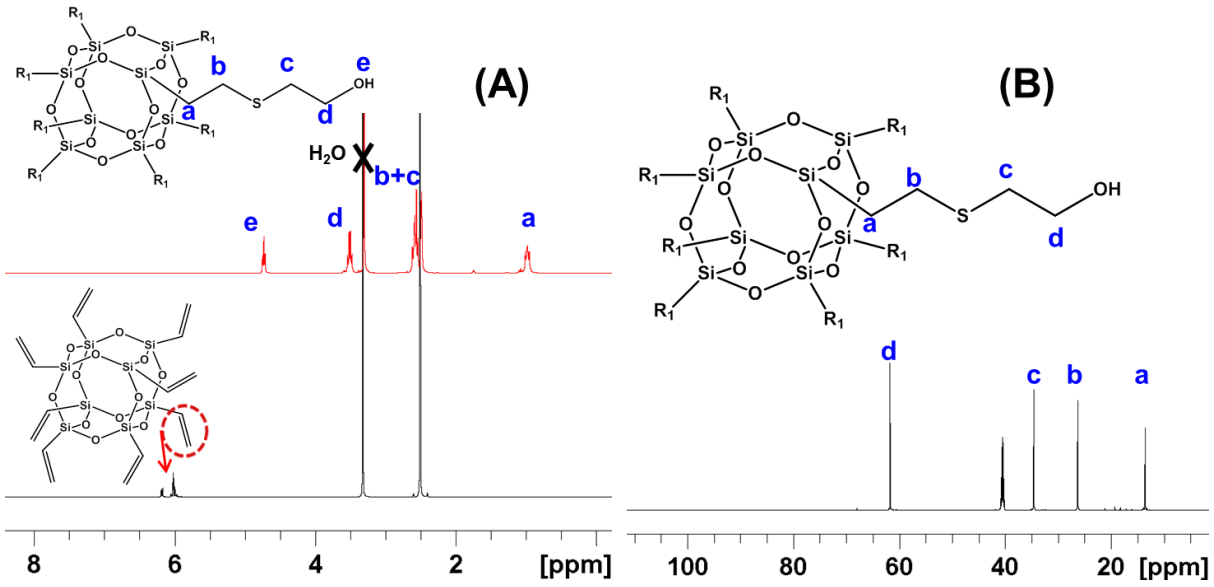


**Figure 6-2** $^{1}$H NMR (A) and $^{13}$C NMR (B) spectra of octavinyl POSS and POSS-$(OH)_8$ in DMSO-$d_6$ at 25 $^{o}$C.

In the next step, the POSS-$(OH)_8$ was further reacted with 4-cyano-4-(((phenethylthio)carbonothioyl)thio)pentanoic acid, which is a trithiocarbonate chain transfer agent (CTA) for RAFT polymerisation. The esterification was carried out in THF in the presence of DMAP/DCC at room temperature for 24 h. The resultant product was characterised by NMR techniques. In Figure 6-3 (A), the disappearance of the peak of hydroxyl group proton at 4.72 ppm was monitored, suggesting the successful attachment of eight CTA moieties to a POSS core by esterification. Owing to the complexity of the structure, the assignment of the NMR peaks was assisted by DEPT $^{13}$C NMR and 2D NMR ($^{1}$H-$^{1}$H COSY and $^{1}$H-$^{13}$C HSQC) spectra (see Appendix E Figure A6.2 and 6.3). As shown in Figure 6-3 (A), all the characteristic peaks were found and assigned in $^{1}$H NMR spectrum, including the peaks of POSS-$(OH)_8$ and CTA units. For example, the multiple peaks at 7.23~7.31 ppm are attributed to the protons of the phenyl group, and the peak at 1.05 is ascribed to the $CH_2$ adjacent to the Si atom. In addition, the integral ratios were calculated to be in accord with the illustrated chemical structure. In Figure 6-3 (B), the $^{13}$C NMR spectrum is in good agreement with the $^{1}$H NMR results with all the relevant peaks assigned, such as the peaks at 216.84 (trithiocarbonate carbon), 171.54 (carbonyl carbon), 119.22 (CN group) and 13.29 ppm (the carbon adjacent to Si). The NMR results confirmed the successful synthesis of POSS-$(CTA)_8$ macroCTA with the targeted chemical structure and high yield (90%).

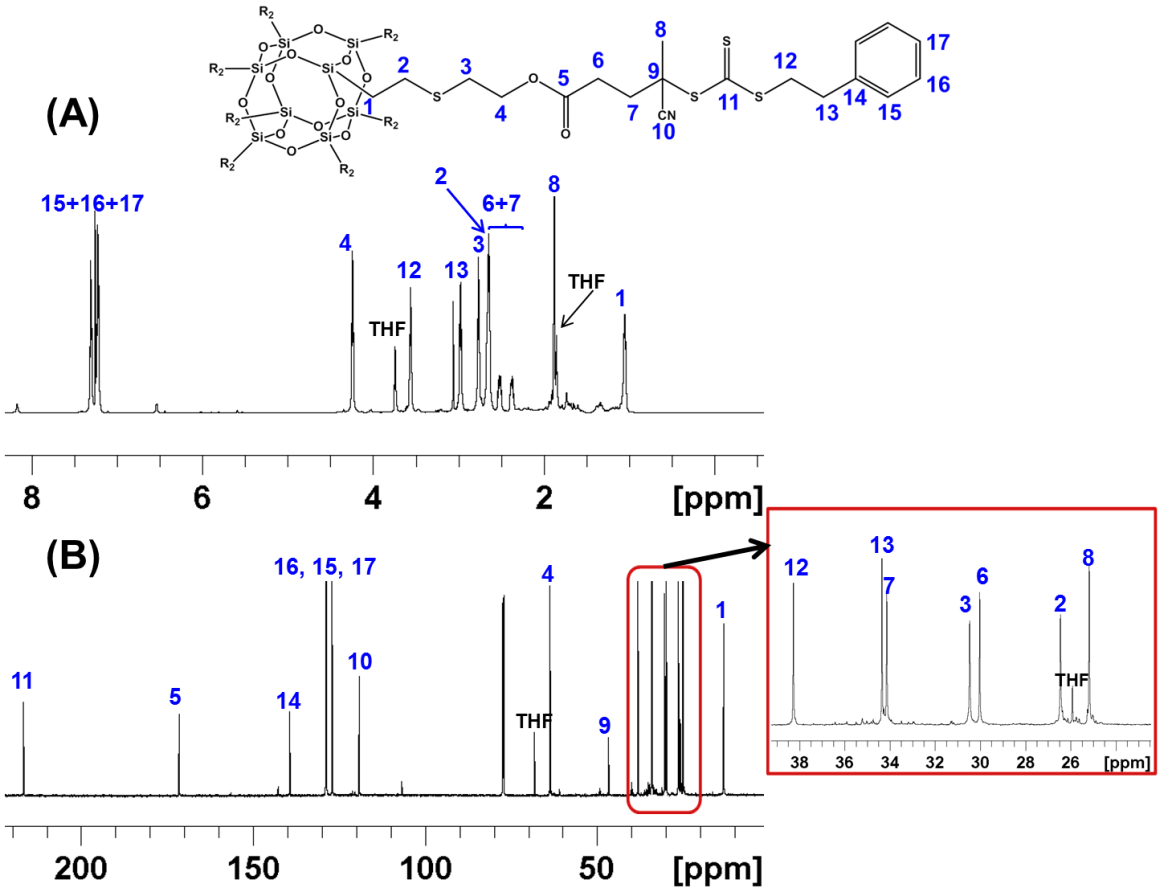


**Figure 6-3** $^{1}$H NMR (A) and $^{13}$C NMR (B) spectra of POSS-(CTA)$_8$ in $CDCl_3$ at 25 $^{o}$C.

### 6.3.3 Synthesis of Star Polymers using POSS-(CTA)$_8$ as a MacroCTA

The POSS-(CTA)$_8$ was used as a macroCTA for the RAFT copolymerisation of 2,2,2-trifluoroethyl methacrylate (TFEA) and poly(ethylene glycol) methyl ether acrylate (PEGA) monomers, resulting in star polymers with a POSS core and eight P(TFEA-co-PEGA) copolymer arms. As the CTA molecules were connected to the POSS core via the R-group, this synthetic route can be classified as an R-group approach for the synthesis of star polymer by RAFT polymerisation and a "grafting from" method for the surface functionalisation. The detailed mechanism is illustrated in Scheme 6-1.[35, 38, 56] A propagating radical ($P_n$•) is formed after initiation process, then it transfers to the macroCTA to form a new radical anchored on the POSS core and a linear polymer with thiocarbonylthio group. This step implies that the synthesis of star polymer by R-group approach is accompanied by the generation of linear polymers. The new radical reacts with monomers to produce a new propagating radical ($P_n$•) located on the POSS core, which can continue to react with either macroCTA or linear polymer with thiocarbonylthio group during the chain equilibration, forming the targeted star polymers with thiocarbonylthio functionalities. As the chain equilibration between propagating radicals and dormant compounds is very fast, the arms and linear polymers are

growing with identical compositions and narrow molar mass distributions, and the degree of radical-radical termination is minimised as well. Generally, the polymerisation can be terminated by radical-radical termination between linear chains. However, due to the presence of multiple radicals on a core, star-star and star-linear couplings are also possible terminations, broadening the molar mass distribution of the final product.

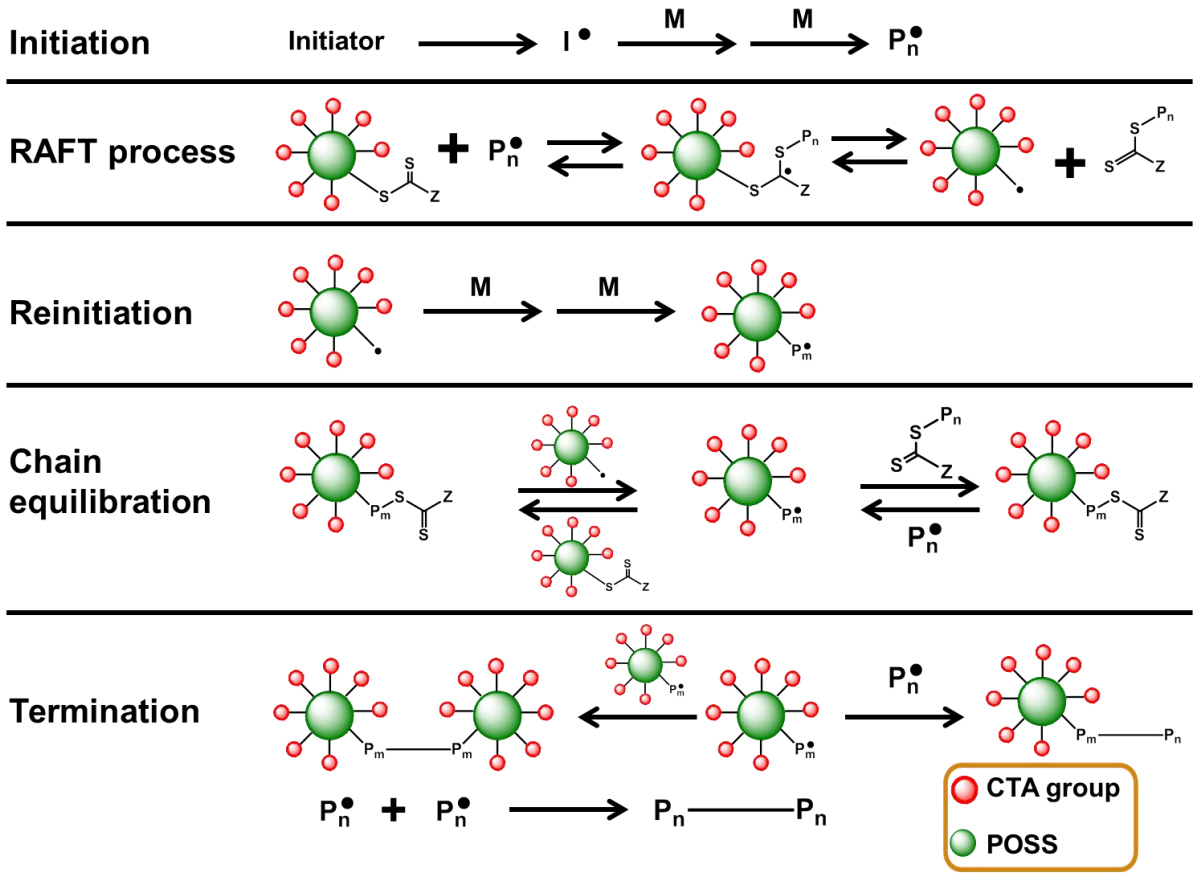


**Scheme 6-1** Mechanism for the synthesis of star polymers using R-group approach by RAFT polymerisation.

According to the mechanism of R-group approach, the final product contains the targeted star polymer as well as those unwanted by-products formed by star-star, star-linear and linear-linear terminations. The increase of star polymer yield can be achieved by minimising the termination reactions, including: (1) using low initiator concentration, (2) reducing arm number, (3) introducing a stable intermediate as a 'radical storage reservoir, and (4) using monomers that have fast propagating rates.[35, 57] In addition, high temperature may be beneficial for increasing star polymer yield because it can shorten the polymerisation time by accelerating the propagating rate of monomer at a low radical concentration.[35] Moreover, stopping the reaction at low monomer conversion is another common option as this can minimise the termination reactions.[36]

We first attempted to synthesise star polymers in 1,4-dioxane using AIBN as initiator at 70 °C. The polymerisation kinetics were studied by analysing the samples withdrawn at given time intervals using GPC and $^1$H NMR. In Figure 6-4 (A), both TFEA and PEGA were consumed at similar rates, indicating the formation of P(TFEA-co-PEGA) arms with azeotropic composition. The low monomer conversions (< 20%) in the first three hours could be attributed to a low initiator concentration (1/10 of CTA) and a possible inhibition time. As shown in Figure 6-4 (B), the ln([$M_0$]/[M]) was almost linear with time from 2 to 7 h, indicating a reasonable 'controlled' polymerisation by RAFT process. However, the deviation from linearity revealed that the radical concentration was not ideally constant due to radical-radical termination reactions.

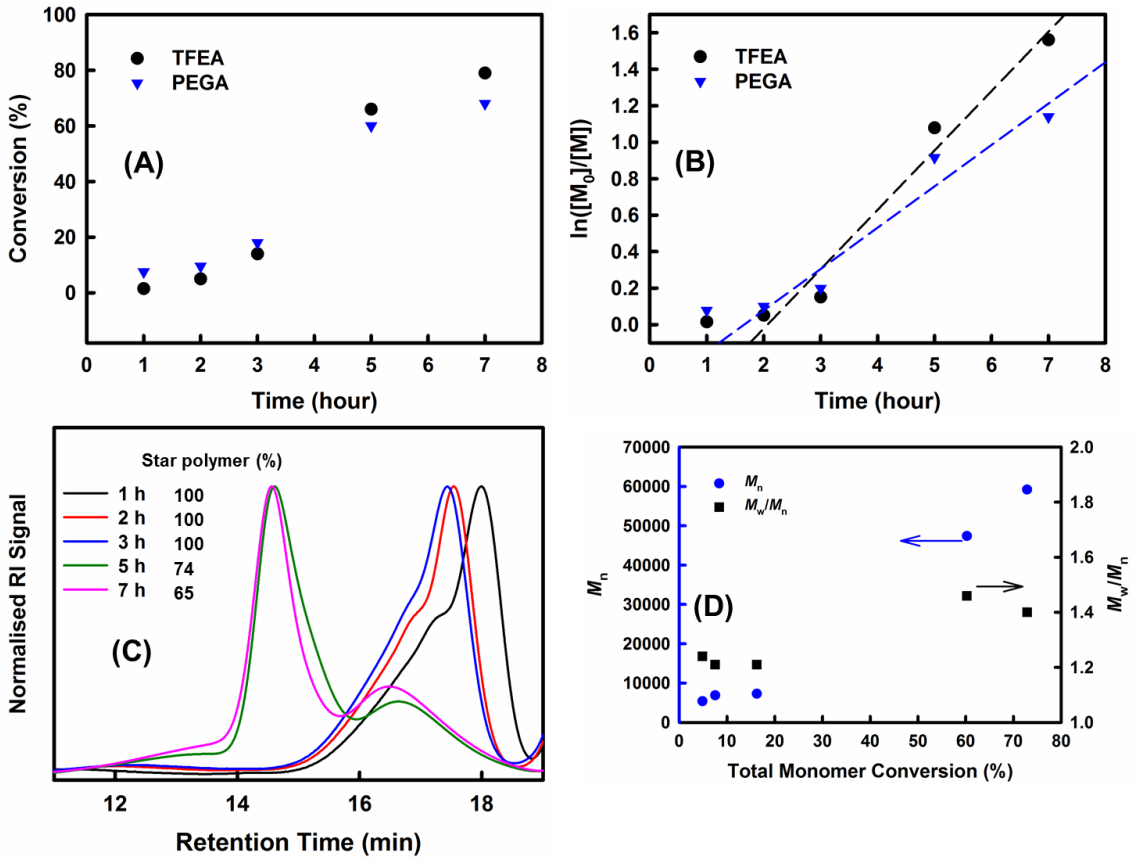


**Figure 6-4** GPC traces of the samples withdrawn at different time intervals using AIBN as initiator. Condition: POSS-$(CTA)_8$/TFEA/PEGA/AIBN = 1/200/200/0.8, [monomer] = 1 M in 1,4-dioxane, 70 °C. The percentage of star polymer in the polymer mixture was estimated by the deconvolution of GPC curves.

In Figure 6-4 (C), the GPC curve evolves toward short retention (high molecular weight) with polymerisation time. Notably, the curves for 5 and 7 h display multiple peaks. To be more specific, the peaks at ~16.5 min can be ascribed to the linear polymers produced during the RAFT

polymerisation, as illustrated in Scheme 6-1. The narrow peaks at ~14.5 min are due to the presence of star polymers, while the broad peaks at 12~14 min can be presumably attributed to the polymers formed by star-star coupling. The star polymer yield was estimated to be 74% and 65% after 5 and 7 h, respectively, by the deconvolution of GPC curves. As shown in Figure 6-4 (D), the molar mass distribution ($Đ_M$) was narrow (< 1.5), confirming the relatively well-defined structure by RAFT polymerisation. It should be noted that the molecular weights measured by GPC were found to be underestimates. Compared to linear polymers, star polymers were more compact and had different hydrodynamic volumes. Therefore conventional GPC, which was referenced to linear polystyrene standards, generated underestimated results. We suggest that $^1$H NMR was suitable for the estimation of the absolute molecular of the star polymers due to the relatively well-defined structure (eight arms).

A parallel experiment was also carried out using 100% larger concentration of AIBN (1/5 of CTA) to study the effect of initiator concentration. As shown Figure A6.4 in Appendix E, the monomer conversions reached 69% and 58% after 2 h for TFEA and PEGA, respectively, indicating an accelerated polymerisation by increased radical concentration. Star polymers with a yield of 72% and $Đ_M$ of 1.55 were obtained. These results suggest that the increase of AIBN from 1/10 to 1/5 of CTA increased the polymerisation rate while it had little effect to the star polymer yield or molar mass distribution.

In an attempt to increase the star polymer yield, VAZO-88 was then selected as initiator for the synthesis of star polymers at 90 $^o$C. VAZO-88 is a well-known radical initiator that has relatively high decomposition temperature.[58] The half-life time of VAZO-88 at 90 $^o$C was calculated to be 7.6 h using activation energy decomposition $E_a$ = 149.1 kJ mol$^{-1}$ and Arrhenius pre-exponential factor A = 7.1 × 10$^{16}$ s$^{-1}$, while the half-life time of AIBN at 70 $^o$C was calculated to be 5.0 h using activation energy decomposition $E_a$ = 131.7 kJ mol$^{-1}$ and Arrhenius pre-exponential factor A = 4.31 × 10$^{15}$ s$^{-1}$.[58] By using VAZO-88 at 90 $^o$C, the polymerisation time is expected to be shortened due to the increased propagating rates of the monomers, although the radical concentration was reduced compared to the polymerisation using AIBN . Thus the star polymers could be synthesised at a low radical concentration, which can possibly minimise radical-radical terminations. The polymerisation kinetics were investigated by motoring the polymerisation progress using GPC and $^1$H NMR. In Figure 6-5 (A), unlike the use of AIBN at 70 $^o$C, both TFEA and PEGA were consumed very rapidly, reaching monomer conversions at ~80% within 3 h and ~90% after 6 h. This result indicates that the increase of polymerisation temperature greatly increased the propagating rates of

monomers. In addition, the polymerisation exhibited pseudo-first-order kinetics (Figure 6-5 (B)), suggesting a well-controlled RAFT polymerisation. The formation of star polymers was evidenced by the GPC results shown in Figure 6-5 (C) and (D). The molecular weight increased with polymerisation time, and the GPC traces were multimodal. The peaks of star polymers were found to be at 14.6~15.3 min with narrow $Đ_M$ (< 1.6), while the generation of linear polymers was confirmed by the peaks at ~17 min. In addition, the star-star termination is observed by the peaks at 12~14 min. However, compared to the polymerisation using AIBN at 70 °C, the star-star coupling here is much less significant. We thus propose that the star-star termination was suppressed owing to the reduced radical concentration by using VAZO-88 at 90 °C.

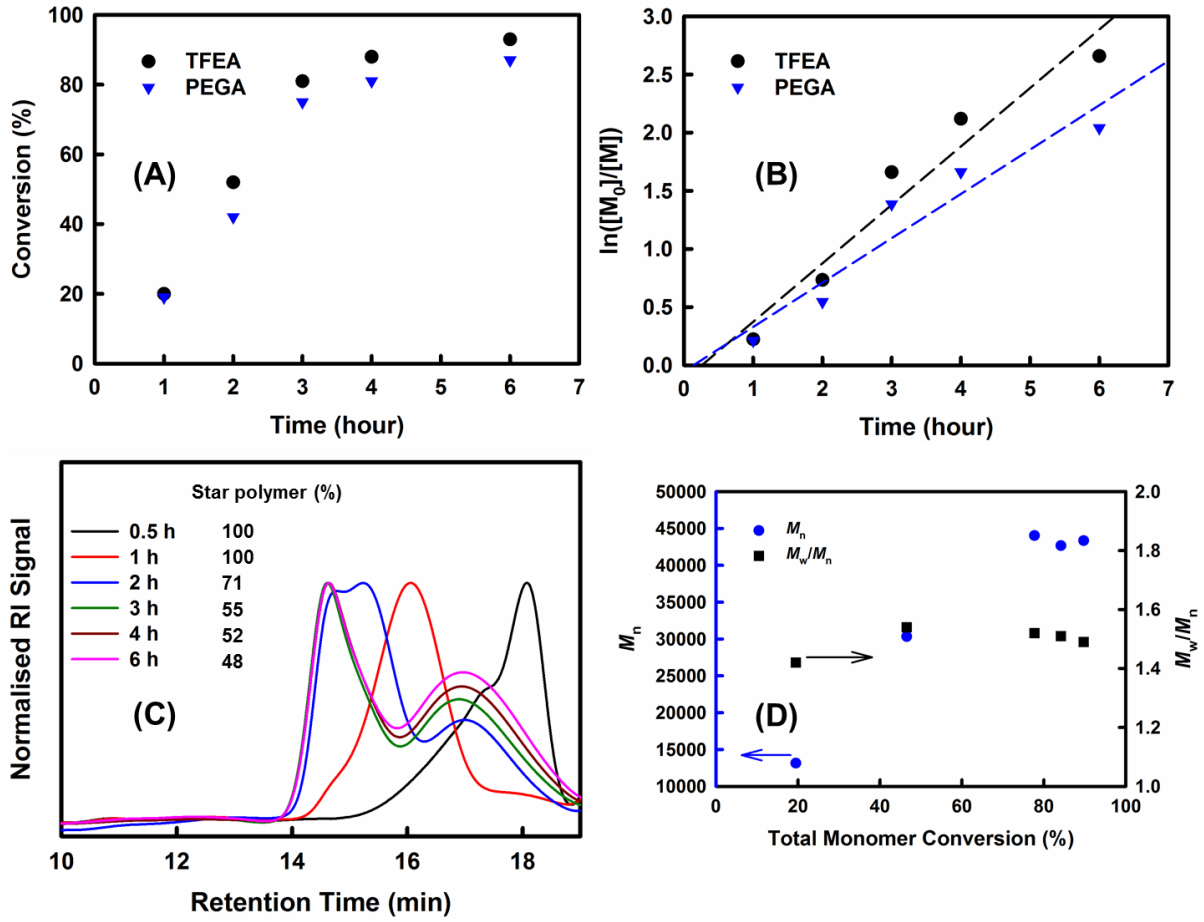


**Figure 6-5** GPC traces of the samples withdrawn at different time intervals using VAZO-88 as initiator. Condition: POSS-$(CTA)_8$/TFEA/PEGA/VAZO-88 = 1/200/200/0.8, [monomer] = 1 M in 1,4-dioxane, 90 °C. The percentage of star polymer in the polymer mixture was estimated by the deconvolution of GPC curves.

The synthesis of star polymers was also conducted using different ratios of monomer to CTA. In Figure 6-6, the molecular weight of star polymers were increased by increasing the

[monomer]/[CTA] ratio from 25/1 to 100/1. However, the yield of star polymers was reduced from 91% to 61%. We suggest that the chain equilibrations between the active propagating radicals on the POSS core and dormant thiocarbonylthio functionalities in linear and star intermediates were hampered owing to the increased steric hindrance around the POSS core, leading to the decreased star polymer yield. The copolymer arms have brush-like structure because of PEGA units, and hence the chain equilibrations are likely to be more restricted by the shielding effect of polymer brushes as the polymerisation proceeds. As reported by Perrier and Zhao, the introduction of free CTA was significantly beneficial to the control of molecular weight and dispersity during the grafting of polymers onto silica particles using Z-group approach.[59] Very recently, Müller and co-workers reported in a similar manner that the active free radicals were entrapped in the synthesis of well-defined cylindrical polymer brushes, and that this could be overcome by addition of free CTA molecules to the polymerisation as shuttles to transport radicals.[60]

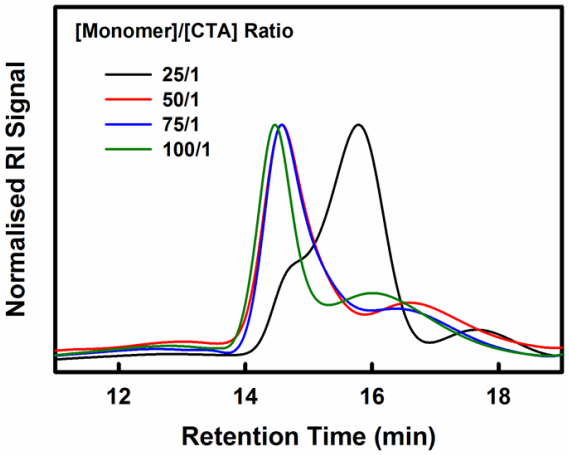


| Ratio | $M_n$ | $M_w/M_n$ | Star polymer (%) |
|---|---|---|---|
| 25/1 | 20200 | 1.48 | 91 |
| 50/1 | 51400 | 1.55 | 75 |
| 75/1 | 46600 | 1.52 | 77 |
| 100/1 | 76200 | 1.35 | 61 |

**Figure 6-6** GPC traces (left) and GPC details (right) of the samples synthesised using different [monomer]/[CTA] ratios. Condition: POSS-$(CTA)_8$/TFEA/PEGA/AIBN = 1/100-400/100-400/1.6, [monomer] = 1 M in 1,4-dioxane, 70 $^{o}$C, 2 h.

Three star polymers having different arm length were synthesised using different monomer to CTA ratios, and the molecular details are summarised in Table 6-1. Star polymers with narrow $Đ_M$ (~1.4) were obtained. The increase of monomer to CTA feed ratio resulted in the increase of degree of polymerisation (by $^1$H NMR) and $M_n$ (by GPC). In addition, the molar fraction of TFEA (~33%) was consistent with the TFEA/PEGA feed ratio (3/7) for all the three samples, implying that the TFEA and PEGA were polymerised at close rates. Nanoparticles were formed with diameters between 8.63 and 10.13 nm and measured using DLS following direct dissolution of the star

polymers in pure water. The increase of hydrodynamic diameter was in agreement with the increase of arm length and molecular weight.

**Table 6-1** Characteristics of the three star polymers.

| Sample[a] | Composition[b] (TFEA:PEGA:CTA) | $M_n$[b] ($^1$H NMR) | $M_n$[c] (GPC) | $M_w/M_n$[c] | $D_h$ (nm)[d] |
|---|---|---|---|---|---|
| SP-1 | 25:52:1 | 234k | 71k | 1.44 | 8.63±0.34 |
| SP-2 | 34:69:1 | 311k | 87k | 1.39 | 9.17±0.19 |
| SP-3 | 54:107:1 | 481k | 102k | 1.39 | 10.13±0.34 |

[a] Polymerisation condition: POSS-$(CTA)_8$/TFEA/PEGA/AIBN = 1/120/280/1.6 for SP-1, POSS-$(CTA)_8$/TFEA/PEGA/AIBN = 1/240/560/1.6 for SP-2, POSS-$(CTA)_8$/TFEA/PEGA/AIBN = 1/360/840/1.6 for SP-3, [monomer] = 1 M in 1,4-dioxane, 70 $^oC$, 2 h. [b] The degree of polymerisation was determined by $^1$H NMR. $M_n$ ($^1$H NMR) = ($MW_{PEGA} \times DP_{PEGA} + MW_{TFEA} \times DP_{TFEA}$) × 8+ $MW_{macroCTA}$. [c] Measured by GPC. [d] Hydrodynamic diameter ($D_h$) was analysed by DLS in pure water at 25 $^oC$, and number-averaged diameters are reported.

The star polymers were purified by dialysing against water for two days using dialysis tubing with 100 kDa molecular-weight-cut-off (MWCO). In Figure 6-7, the GPC curve for the purified sample indicates that most of the linear polymer impurities were removed by dialysis. In addition, the peak of the by-products formed by star-star coupling almost disappeared. Indeed, the dialysis using membrane with MWCO as large as 100 kDa removed polymers with a wide range of molecular weights, including linear polymers, targeted star polymers and by-products with higher molecular weights. This was revealed to some extent by the relatively low yield after dialysis (22% for SP-1, 44% for SP-2 and 35% for SP-3). Star polymers SP-2 and SP-3 were also purified using the same procedure (see Appendix E Figure A6.5 for GPC curves).

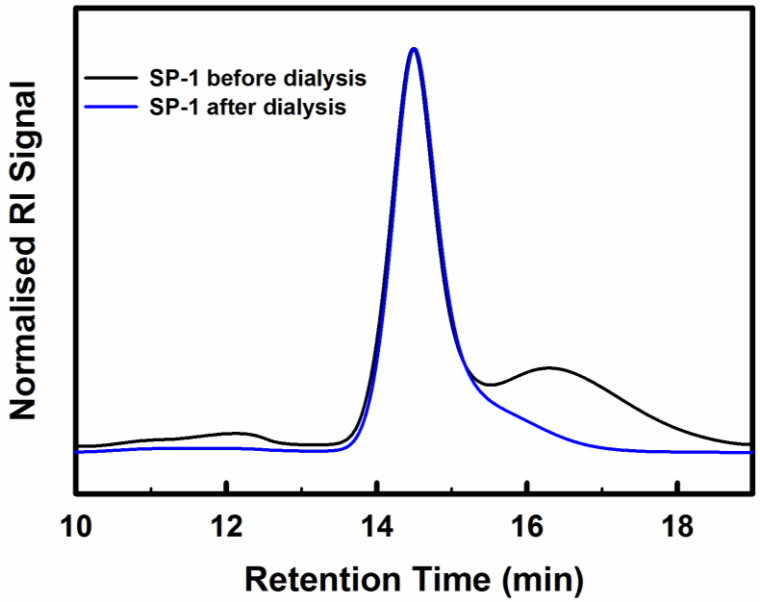


**Figure 6-7** GPC curves of SP-1 before and after dialysis using dialysis tubings with 100 kDa MWCO.

The POSS-based precursors and purified star polymers were characterised by ATR-FTIR spectroscopy, and the resultant spectra are displayed in Figure 6-8. For the original octavinyl POSS, the characteristic peaks can be found at ~3000 $cm^{-1}$ (C-H stretching vibration), 1603 $cm^{-1}$ (C=C stretching vibration) and 1097 $cm^{-1}$ (Si-O-Si stretching vibration). In the spectrum of POSS-$(OH)_8$, the hydroxyl functionalisation was confirmed by the peak at 3354 $cm^{-1}$ (-OH stretching vibration) and absence of the C=C peak at 1603 $cm^{-1}$. In the spectrum of POSS-$(CTA)_8$, the peak at 3354 $cm^{-1}$ for -OH groups disappeared, indicating the complete esterification between POSS-$(OH)_8$ and CTA. In addition, the attachment of CTA to POSS was also revealed by a number of characteristic peaks at 3000~3100 $cm^{-1}$ (aromatic C-H stretching vibration), 2115~2230 $cm^{-1}$ (C≡N stretching vibration), 1734 $cm^{-1}$ (C=O stretching vibration), 1600~1640 $cm^{-1}$ (aromatic ring stretching vibration), etc. In the spectra for the star polymers, the peaks assigned to the copolymer arms can be clearly seen, such as the peaks at ~2860 $cm^{-1}$ (C-H stretching vibration), 1450 $cm^{-1}$ ($CH_3$ anti-symmetric deformation), 1350 $cm^{-1}$ (C-F stretching vibration) and 1100 $cm^{-1}$ (C-O-C stretching vibration). Moreover, the peaks of POSS-$(CTA)_8$ were also found in the spectra of star polymers. The FTIR spectra provided additional evidence for the successful functionalisation of octavinyl POSS and the synthesis of star polymers using a POSS-based macroCTA.

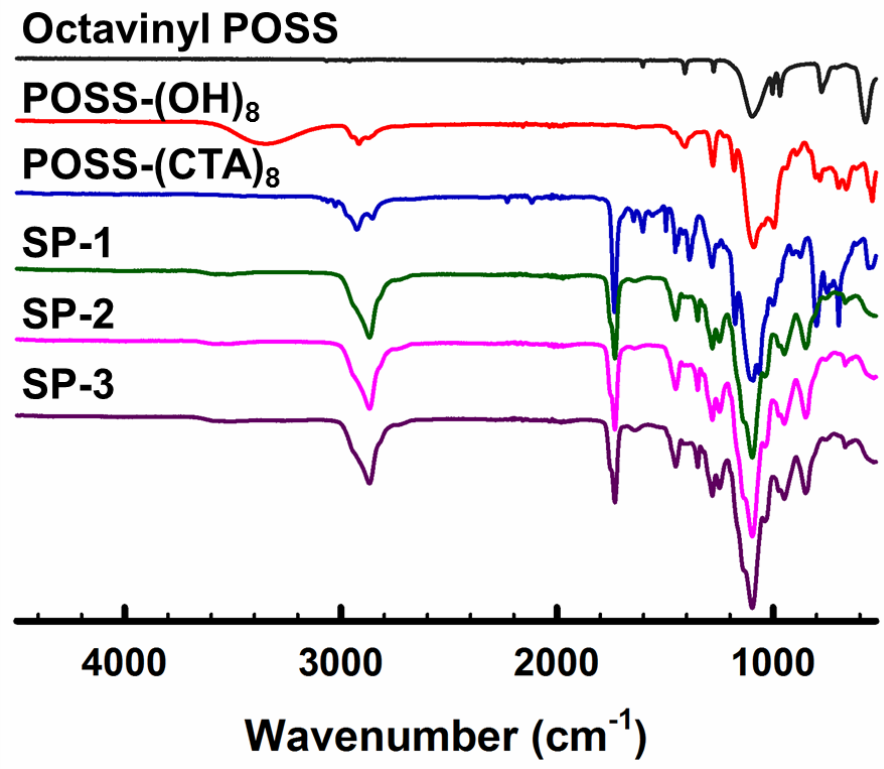


**Figure 6-8** FTIR spectra of the POSS-based precursors and star polymers.

The macroCTA and purified star polymers were analysed by $^{1}$H NMR. In Figure 6-9, the peaks of TFEA and PEGA units can be found in the spectra of star polymers, such as peaks at 4.51 ppm ($CH_2$ adjacent to $C_{F3}$), 4.18 ppm (neighbouring $CH_2$ of COO in PEGA), 3.38 ppm ($CH_3$ end group of PEGA), 1.6~2.3 ppm (protons in polymer backbone), etc. In addition, the characteristic peaks of CTA moieties are also identified, including peaks at 7.24~7.32 ppm (protons in phenyl group), 2.99 ($CH_2$ connected to the phenyl group), 1.04 ppm ($CH_2$ adjacent to Si), and those peaks highlighted by the blue circle. Moreover, the peaks at 4.51 (for TFEA) and 4.18 ppm (for PEGA) were relatively symmetric, implying a single chemical environment due to the even distribution of TFEA and PEGA in the statistical copolymers. This is because TFEA and PEGA have the possibly close reactivity ratios. In Chapter 5, we have reported that gradient copolymers were obtained on the polymerisation of TFEA and poly(ethylene glycol) methyl ether methacrylate (PEGMA), which possess largely different reactivity ratios, and multiple chemical environments of TFEA and PEGMA were detected by both $^{1}$H and $^{19}$F NMR. The existence of peaks attributed to the CTA end-group confirmed the retention of CTA functionalities in the star polymers. Furthermore, the small single peak at 4.86 ppm could be assigned to the methine proton in TFEA back bone adjacent to the trithiocarbonate group, as evidenced by $^{1}$H-$^{13}$C HSQC and HMBC spectra (see Appendix E Figure A6.6). Similar observation has also been reported in a recent paper.[51] According to the integral ratio

of the peak at 4.86 to the peak at 4.51 ppm, the P(TFEA-co-PEGA)arms in which there are TFEA units directly connected to the trithiocarbonate account for 76% of the total arms, indicating the preference of TFEA units being positioned directly to trithiocarbonate during the copolymerisation.

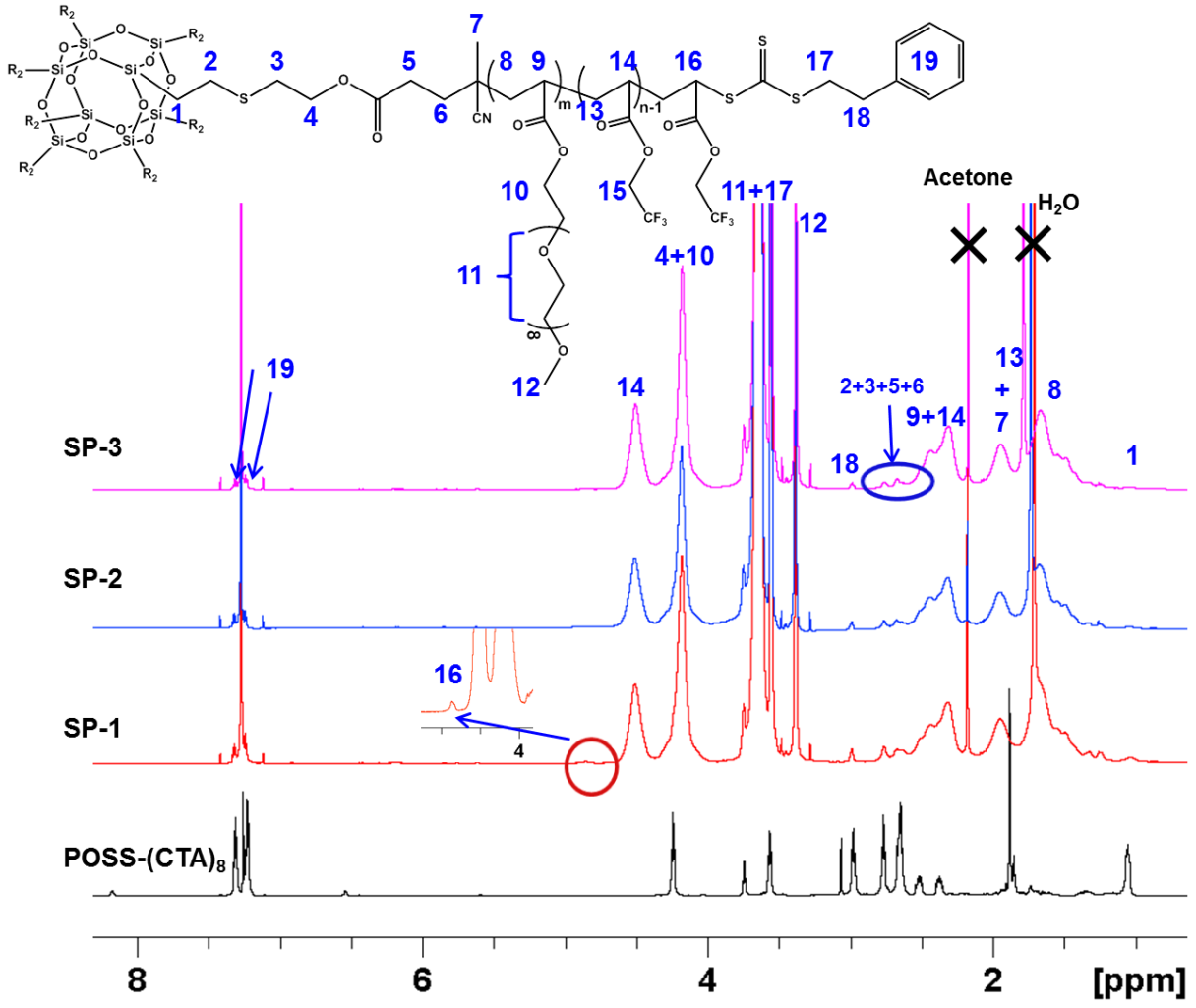


**Figure 6-9** $^{1}$H NMR spectra of the POSS-$(CTA)_8$ and star polymers in $CDCl_3$ at 25 $^{o}$C.

### 6.3.4 $^{19}$F NMR Studies

One aim of this study was to utilise the star polymers as contrast agents for $^{19}$F MRI. As discussed in Chapter 5, P(TFEA-co-PEGA) copolymers are advantageous for $^{19}$F MRI because of the evenly distributed fluorine units in the copolymers, resulting in a single and strong $^{19}$F signal even with high $^{19}$F content. The star polymers were dissolved in PBS/$D_2O$ (90/10, v/v) at 20 mg $mL^{-1}$ and evaluated by $^{19}$F NMR at 25 $^{o}$C. As shown in Figure 6-10, a strong and symmetric peak was observed at around -73.4 ppm for all three star polymers, suggesting an identical chemical environment of the fluorine units.

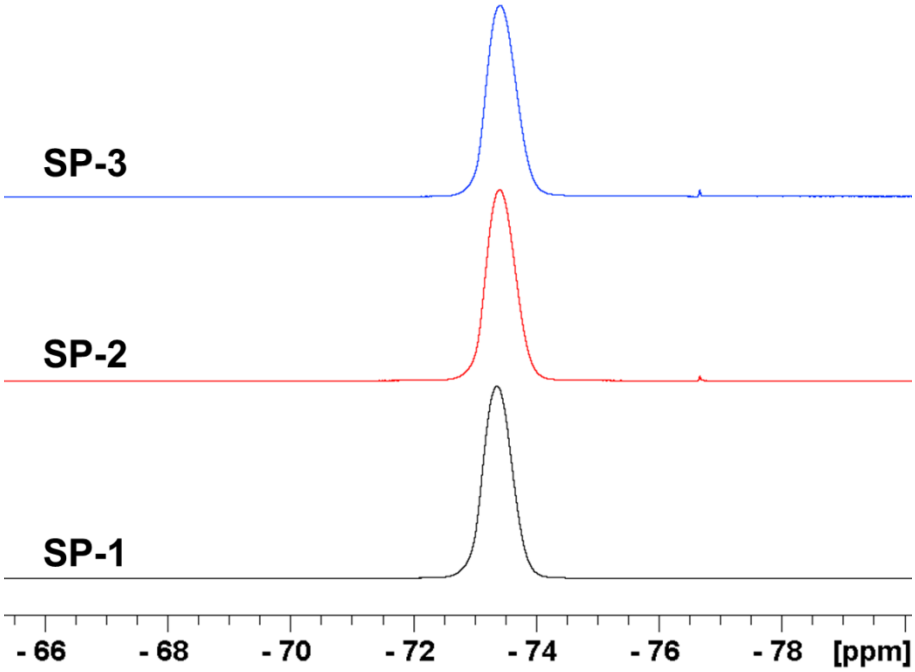


**Figure 6-10** $^{19}$F NMR spectra of the star polymers.

The $^{19}$F NMR properties of the star polymers are listed in Table 6-2. All the three star polymers possess a close fluorine atom content of ~5.0 wt%, indicating a close TFEA/PEGA ratio in the copolymers. The spin-spin ($T_2$) and spin-lattice ($T_1$) relaxation times were measured by $^{19}$F NMR at 659 MHz using a Bruker Avance 700 MHz spectrometer. The $T_2$ is determined by the strength of the dipolar coupling of the $^{19}$F nuclei with the surrounding fluorine and proton nuclei, and hence is sensitive to the chemical environment of the $^{19}$F nuclei and their relative mobility. The $T_2$ relaxation time was increased slightly with the arm length, indicating that longer arms had higher segmental flexibility and fluorine mobility. Meanwhile, the $T_1$ relaxation time showed minimal variation between samples, suggesting that the spectral density of the $^{19}$F motion in the range of 700 MHz was not significantly affected by the change in arm length.

**Table 6-2** $^{19}$F NMR properties of the star polymers.

| Sample | $^{19}$F wt%[a] | $T_2$ (ms)[b] | $T_1$ (ms)[b] | Half width (Hz)[c] | $^{19}$F MRI Intensity[d] |
|---|---|---|---|---|---|
| SP-1 | 4.9 | 37.0 (37.7)[d] | 328.6 (328.3)[e] | 345 | 13.93 |
| SP-2 | 5.0 | 42.1 | 329.6 | 353 | 16.24 |
| SP-3 | 5.1 | 44.7 | 331.8 | 358 | 17.52 |

[a] Fluorine content was determined by $^1$H NMR. [b] Spin-spin ($T_2$) and spin-lattice ($T_1$) relaxation times were measured by $^{19}$F NMR using Carr-Purcell-Meiboom-Gill (CPMG) and inversion-recovery pulse sequences, respectively. [c] The peak width at half height was obtained from the $^{19}$F NMR spectra. [d] $^{19}$F MRI Intensity was calculated using Equation (6-1). [e] The relaxation times in the brackets were measured for SP-1 before dialysis.

The relaxation times of SP-1 before dialysis (denoted as 'crude SP-1') were also examined to study the influence of linear impurities on $^{19}$F NMR properties. As provided in the brackets in Table 6-2, the $T_2$ relaxation time of crude SP-1 was measured to be 37.7 ms, slightly higher than that of the dialysed sample, revealing higher average fluorine mobility. Since the percentage of by-products formed by star-star coupling is negligible (~2 wt% by GPC), we suggest that the longer $T_2$ of crude SP-1 could be mainly attributed to the presence of linear polymers, which was likely to have higher fluorine mobility than their counterparts connected to a rigid POSS core. Such explanation can be supported by the results studied in Chapter 5, in which the linear analogue possessed a longer $T_2$ than the highly-branched polymers having same composition and fluorine content. As expected, $T_1$ was nearly constant, implying the little effect of polymer architecture on $T_1$.

In Chapter 5, a segmented highly-branched polymer (SHBP-10) was synthesised and it was constructed of P($TFEA_{17}$-co-$PEGA_{37}$) chains, which had the same components and a very close fluorine content (4.8%) to the arms of the star polymers in this work. The $T_2$ and $T_1$ of SHBP-10 were measured under the same conditions and found to be 51.7 and 330.0 ms, respectively. This implies that the copolymers in a highly-branched structure with low degree of branching are more segmentally flexible than those anchored on the POSS core. We thus speculate that the fluorine units in the arms of star polymers are less mobile than those positioned in a highly-branched architecture owing to a possibly more confined environment around the core. In addition, the little

effect of polymer architecture on $T_1$ relaxation time was further proved by the very small variation of $T_1$ values.

For $^{19}$F MRI using a spin-echo pulse sequence, the imaging intensity can be calculated using the following equation.[61]

$$I \approx N(F)\, exp\left(\frac{-TE}{T_2}\right)\left[1 - 2exp\left(\frac{-\left(TR - \frac{TE}{2}\right)}{T_1}\right) + exp\left(\frac{-TR}{T_1}\right)\right] \qquad (6\text{-}1)$$

In Equation (6-1), I is the imaging intensity, N(F) is a measure of the number of fluorine nuclei in the sensitive volume of the imaging coil, and TR and TE are the pulse sequence repetition time and echo delay times, respectively. According to this equation, an efficient contrast agent for $^{19}$F MRI should possess high fluorine content, long $T_2$ and short $T_1$. The $^{19}$F MRI intensity values were estimated using Equation (6-1). The parameters used in Chapter 5 for the RARE-8 pulse sequence were adopted for the simulation, i.e, TE = 41 ms, TR = 1 s, sample concentration = 100 mg mL$^{-1}$. The intensity values were calculated to be from 13.93 to 17.52, increasing with the fluorine content and $T_2$. These intensity values are relatively close to that of SHBP-9 (17.6) in Chapter 5. As studied in Chapter 5, SHBP-9 was well imaged using several pulse sequences (FLASH, RARE-8 and RARE-32). For example, the signal-to-noise ratio (SNR) was calculated to be as high as 48.42 using RARE-8 spin-echo pulse sequence with a scan time of 1 h and 46 minutes. Therefore we expect that the star polymers have the comparable imaging property as SHBP-9 because they have the similar copolymer chains as well as relatively close theoretical MRI intensities. The favourable $^{19}$F NMR properties of these star polymers are in agreement with the observations in Chapter 5, and thus further confirmed that P(TFEA-co-PEGA) copolymers are excellent materials for the fabrication of $^{19}$F MRI agents based on star and hyperbranched polymers owing to the highly mobile $^{19}$F nuclei and high fluorine content.

## 6.4 Conclusions

This chapter reports the synthesis of star polymers with a POSS core as potential theranostic agents. Octavinyl POSS was functionalised with hydroxyl groups by the UV-induced thiol-ene reaction. The macroCTA having eight CTA moieties on a POSS core was synthesised through the esterification between hydroxyl-functionalised POSS and carboxyl-terminated CTA. Star polymers consisting of eight partly-fluorinated copolymer arms and a POSS core were synthesised by the RAFT copolymerisation of fluoro monomer and PEG-based monomer using the POSS-based macroCTA. The synthesis of star polymers was accompanied by the formation of linear polymers

and polymers formed by star-star terminations, as was evidenced by the kinetics study. Star polymers with different arm length were synthesised by varying the feed ratio of monomer to CTA, and were purified by extensive dialysis in water. The evenly distributed fluorine units in the arms were observed by $^{1}$H NMR. Nanoparticles with diameters of 8~10 nm were formed by dissolving the star polymers in water, and the particle size increased with arm length. The single fluorine chemical environment was confirmed by a single peak in the $^{19}$F NMR spectra. The $T_2$ relaxation time was increased with arm length. The $T_2$s were shorter than those of linear (main impurities in this Chapter) and highly-branched (polymers in Chapter 5) analogues, indicating that the fluorine nuclei were less mobile in the arms of star polymers because of the possibly confined environment around the POSS core. The theoretical values of $^{19}$F MRI intensity were estimated, and confirmed that the star polymers showed potential for use as $^{19}$F MRI agents with high imaging intensity.

As stated in the Introduction, the POSS core has the potential to be exploited for encapsulating drug/gene/dye molecules. In addition, the trithiocarbonate could be utilised for conjugation reactions after aminolysis, as demonstrated previously.[51] Therefore these multifunctional star polymers with a POSS core and partly-fluorinated arms are promising theranostic agents for cancer diagnosis and treatment.

## 6.5 References


1. S. M. Moghimi, A. C. Hunter and J. C. Murray, *Faseb J*, 2005, **19**, 311-330.
2. K. Riehemann, S. W. Schneider, T. A. Luger, B. Godin, M. Ferrari and H. Fuchs, *Angew Chem Int Edit*, 2009, **48**, 872-897.
3. T. Lammers, S. Aime, W. E. Hennink, G. Storm and F. Kiessling, *Accounts Chem Res*, 2011, **44**, 1029-1038.
4. B. Sumer and J. M. Gao, *Nanomedicine*, 2008, **3**, 137-140.
5. L. Y. Rizzo, B. Theek, G. Storm, F. Kiessling and T. Lammers, *Curr Opin Biotech*, 2013, **24**, 1159-1166.
6. M. J. Sailor and J. H. Park, *Adv Mater*, 2012, **24**, 3779-3802.
7. J. E. Lee, N. Lee, T. Kim, J. Kim and T. Hyeon, *Accounts Chem Res*, 2011, **44**, 893-902.
8. W. T Al-Jamal and K. Kostarelos, *Nanomedicine*, 2007, **2**, 85-98.
9. D. B. Cordes, P. D. Lickiss and F. Rataboul, *Chem Rev*, 2010, **110**, 2081-2173.
10. F. K. Wang, X. H. Lu and C. B. He, *J Mater Chem*, 2011, **21**, 2775-2782.

11. H. Ghanbari, B. G. Cousins and A. M. Seifalian, *Macromol Rapid Comm*, 2011, **32**, 1032-1046.
12. K. Tanaka and Y. Chujo, *J Mater Chem*, 2012, **22**, 1733-1746.
13. K. Tanaka, K. Inafuku, K. Nakab and Y. Chujo, *Org Biomol Chem*, 2008, **6**, 3899-3901.
14. X. J. Loh, Z. X. Zhang, K. Y. Mya, Y. L. Wu, C. B. He and J. Li, *J Mater Chem*, 2010, **20**, 10634-10642.
15. Y. Bai, L. P. Yang, C. L. Toh, C. B. He and X. H. Lu, *Macromol Chem Phys*, 2013, **214**, 396-404.
16. D. D. Liu, B. Yu, X. S. Jiang and J. Yin, *Langmuir*, 2013, **29**, 5307-5314.
17. Z. L. Su, B. Yu, X. S. Jiang and J. Yin, *Macromolecules*, 2013, **46**, 3519-3528.
18. B. P. Nair, D. Vaikkath and P. D. Nair, *Langmuir*, 2014, **30**, 340-347.
19. K. Y. Pu and B. Liu, *Adv Funct Mater*, 2011, **21**, 3408-3423.
20. J. Liu, K. Li, J. L. Geng, L. Zhou, P. Chandrasekharan, C. T. Yang and B. Liu, *Polym Chem*, 2013, **4**, 1517-1524.
21. K. Li, Y. T. Liu, K. Y. Pu, S. S. Feng, R. Y. Zhan and B. Liu, *Adv Funct Mater*, 2011, **21**, 287-294.
22. J. Liu, G. X. Feng, D. Ding and B. Liu, *Polym Chem*, 2013, **4**, 4326-4334.
23. P. A. Ledin, I. M. Tkachenko, W. N. Xu, I. Choi, V. V. Shevchenko and V. V. Tsukruk, *Langmuir*, 2014, **30**, 8856-8865.
24. H. Yuan, K. Luo, Y. S. Lai, Y. J. Pu, B. He, G. Wang, Y. Wu and Z. W. Gu, *Mol Pharmaceut*, 2010, **7**, 953-962.
25. Y. Y. Yang, X. Wang, Y. Hu, H. Hu, D. C. Wu and F. J. Xu, *Acs Appl Mater Inter*, 2014, **6**, 1044-1052.
26. Y. J. Pu, L. G. Zhang, H. Zheng, B. He and Z. W. Gu, *Polym Chem*, 2014, **5**, 463-470.
27. Y. J. Pu, L. G. Zhang, H. Zheng, B. He and Z. W. Gu, *Macromol Biosci*, 2014, **14**, 289-297.
28. C. H. Ni, G. Wu, C. P. Zhu and B. L. Yao, *J Phys Chem C*, 2010, **114**, 13471-13476.
29. H. F. Gao, *Macromol Rapid Comm*, 2012, **33**, 722-734.
30. H. Hussain, B. H. Tan, C. S. Gudipati, Y. Xaio, Y. Liu, T. P. Davis and C. B. He, *J Polym Sci Pol Chem*, 2008, **46**, 7287-7298.
31. Y. Bai, J. Wei, L. P. Yang, C. B. He and X. H. Lu, *Colloid Polym Sci*, 2012, **290**, 507-515.
32. Z. S. Ge, D. Wang, Y. M. Zhou, H. W. Liu and S. Y. Liu, *Macromolecules*, 2009, **42**, 2903-2910.
33. L. Wang, C. Y. Zhang, H. L. Cong, L. Li, S. X. Zheng, X. H. Li and J. Wang, *J Phys Chem B*, 2013, **117**, 8256-8268.

34. Y. S. Ye, W. C. Shen, C. Y. Tseng, J. Rick, Y. J. Huang, F. C. Chang and B. J. Hwang, *Chem Commun*, 2011, **47**, 10656-10658.
35. A. Gregory and M. H. Stenzel, *Prog Polym Sci*, 2012, **37**, 38-105.
36. C. Barner-Kowollik, T. P. Davis and M. H. Stenzel, *Aust J Chem*, 2006, **59**, 719-727.
37. M. H. Stenzel, *Macromol Rapid Comm*, 2009, **30**, 1603-1624.
38. J. Chiefari, Y. K. Chong, F. Ercole, J. Krstina, J. Jeffery, T. P. T. Le, R. T. A. Mayadunne, G. F. Meijs, C. L. Moad, G. Moad, E. Rizzardo and S. H. Thang, *Macromolecules*, 1998, **31**, 5559-5562.
39. M. Srinivas, A. Heerschap, E. T. Ahrens, C. G. Figdor and I. J. M. de Vries, *Trends Biotechnol*, 2010, **28**, 363-370.
40. L. Nurmi, H. Peng, J. Seppala, D. M. Haddleton, I. Blakey and A. K. Whittaker, *Polym Chem*, 2010, **1**, 1039-1047.
41. H. Peng, I. Blakey, B. Dargaville, F. Rasoul, S. Rose and A. K. Whittaker, *Biomacromolecules*, 2009, **10**, 374-381.
42. H. Peng, K. J. Thurecht, I. Blakey, E. Taran and A. K. Whittaker, *Macromolecules*, 2012, **45**, 8681-8690.
43. X. N. Huang, G. Huang, S. R. Zhang, K. Sagiyama, O. Togao, X. P. Ma, Y. G. Wang, Y. Li, T. C. Soesbe, B. D. Sumer, M. Takahashi, A. D. Sherry and J. M. Gao, *Angew Chem Int Edit*, 2013, **52**, 8074-8078.
44. K. Wang, H. Peng, K. J. Thurecht, S. Puttick and A. K. Whittaker, *Polym Chem*, 2014, **5**, 1760.
45. K. W. Wang, H. Peng, K. J. Thurecht, S. Puttick and A. K. Whittaker, *Polym Chem*, 2013, **4**, 4480-4489.
46. B. E. Rolfe, I. Blakey, O. Squires, H. Peng, N. R. B. Boase, C. Alexander, P. G. Parsons, G. M. Boyle, A. K. Whittaker and K. J. Thurecht, *J Am Chem Soc*, 2014, **136**, 2413-2419.
47. D. J. Coles, B. E. Rolfe, N. R. B. Boase, R. N. Veedu and K. J. Thurecht, *Chem Commun*, 2013, **49**, 3836-3838.
48. W. J. Du, Z. Q. Xu, A. M. Nystrom, K. Zhang, J. R. Leonard and K. L. Wooley, *Bioconjugate Chem*, 2008, **19**, 2492-2498.
49. W. J. Du, A. M. Nystrom, L. Zhang, K. T. Powell, Y. L. Li, C. Cheng, S. A. Wickline and K. L. Wooley, *Biomacromolecules*, 2008, **9**, 2826-2833.
50. K. J. Thurecht, I. Blakey, H. Peng, O. Squires, S. Hsu, C. Alexander and A. K. Whittaker, *J Am Chem Soc*, 2010, **132**, 5336-5337.
51. A. Ardana, A. K. Whittaker and K. J. Thurecht, *Macromolecules*, 2014, **47**, 5211-5219.

52. M. Ogawa, S. Nitahara, H. Aoki, S. Ito, M. Narazaki and T. Matsuda, *Macromol Chem Phys*, 2010, **211**, 1369-1376.
53. C. Porsch, Y. N. Zhang, A. Ostlund, P. Damberg, C. Ducani, E. Malmstrom and A. M. Nystrom, *Part Part Syst Char*, 2013, **30**, 381-390.
54. Z. H. Huang, R. S. Sengar, A. Nigam, M. C. Abadjian, D. M. Potter, D. B. Grotjahn and E. C. Wiener, *Invest Radiol*, 2010, **45**, 641-654.
55. M. Semsarilar, V. Ladmiral, A. Blanazs and S. P. Armes, *Langmuir*, 2012, **28**, 914-922.
56. A. Blencowe, J. F. Tan, T. K. Goh and G. G. Qiao, *Polymer*, 2009, **50**, 5-32.
57. H. Chaffey-Millar, M. H. Stenzel, T. P. Davis, M. L. Coote and C. Barner-Kowollik, *Macromolecules*, 2006, **39**, 6406-6419.
58. G. Moad and D. H. Solomon, *The chemistry of radical polymerization*, Elsevier, 2005.
59. Y. L. Zhao and S. Perrier, *Macromolecules*, 2006, **39**, 8603-8608.
60. Z. C. Zheng, J. Ling and A. H. E. Muller, *Macromol Rapid Comm*, 2014, **35**, 234-241.
61. R. E. Hendrick, *Magn Reson Imaging*, 1987, **5**, 31-37.

# Chapter 7
# Conclusions

## 7.1 Overall Conclusions

This thesis focuses on the design, synthesis and evaluation of multifunctional polymer nanoparticles as next-generation contrast agents for $^{19}$F MRI. The development of highly–efficient contrast agents is crucial for the maturing and popularisation of $^{19}$F MRI for biomedical diagnosis. In addition, a molecular level understanding is required for the design and applications of polymeric $^{19}$F MRI agents. Therefore this thesis aimed to develop multifunctional polymers with various architectures for $^{19}$F MRI-related applications and ultimately build a fundamental understanding of the relationship between molecular structure and imaging property.

The initial work was started by the design of star-like hyperbranched polymers as pH-responsive contrast agents for selective $^{19}$F MRI, as detailed in Chapter 2. The aim was to study how the $^{19}$F mobility could be tuned using a pH-responsive hyperbranched structure. Star-like hyperbranched polymers were synthesised using the arm-first approach by reversible addition-fragmentation chain transfer (RAFT) polymerisation. In those water-soluble molecules, the pH-responsive hyperbranched core consisted of TFEA and DMAEMA units, while the hydrophilic arms were composed of PPEGMA brush-like polymers. Nanoparticles were formed by dissolving the star-like polymers in aqueous solution, and the particle size was found to be highly dependent on the pH. The $^{19}$F signal intensity was dramatically decreased when the solution pH was above the p*K*a of DMAEMA. The spin-spin ($T_2$) relaxation time was strongly related to both the $^{19}$F content and the change in particle conformation. A strong $^{19}$F signal and long $T_2$ were only achieved under acidic conditions (pH < 6.5) owing to the enhanced mobility of the fluorinated segments. In contrast, the $T_2$ relaxation time was significantly reduced above the p*K*a. The $T_1$ relaxation time was not affected significantly by the change in solution pH. A strong dependence of imaging performance on pH was confirmed by *in vitro* $^{19}$F MRI, suggesting potential applications of these polymeric CAs for selective $^{19}$F MRI in the diagnosis of cancer tissue.

To study the effect of placement of $^{19}$F nuclei in the arms of star polymers, CCS polymers were synthesised by RAFT dispersion polymerisation and evaluated as $^{19}$F MRI agents, as reported in Chapter 3. The densely-crosslinked core contained disulfide bonds, and the partly-fluorinated arms

were comprised of PPEGMA-b-P(TFEMA-co-DMAEMA) block copolymers. The synthetic conditions were studied and optimised. Nanoparticles of the CCS polymers were formed in aqueous solution by direct dissolution, and the particle size was dependent on pH owing to the presence of the pH-responsive DMAEMA units. The biodegradability was confirmed by treatment with reducing agents. The $^{19}$F signal intensity and $T_2$ relaxation time decreased with an increase of pH of the polymer solution. As revealed by *in vitro* $^{19}$F MRI, the CCS polymers could be imaged well at acidic pH while they had poor imaging performance above the p*K*a of DMAEMA, demonstrating that these CCS polymers are promising $^{19}$F MRI contrast agents for the selective imaging of tumour tissues. Compared to the star-like polymers described in Chapter 2, one of the CCS polymers (CCS-1) had a close $^{19}$F content but could be imaged in greatly shortened time (from 9 h 6 min to 1 h 8 min), suggesting that the mobility of the $^{19}$F nuclei in a star polymer architecture could be enhanced by placing the fluorine segments in the flexible arms rather than in a relatively confined crosslinked (or hyperbranched) structure. It should be stressed that CCS polymers contained TFEMA segments that have a higher glass transition temperature than TFEA units, and thus are less preferable for $^{19}$F imaging agents due to the restricted $^{19}$F motion and shortened $T_2$ relaxation time. However, the imaging performance of CCS polymers was none-the-less improved compared with its counterparts consisting of TFEA units, implying that the polymer architecture played an important role in the imaging properties.

In Chapter 4, multifunctional hyperbranched polymers containing iodine and fluorine (HBIPFs) were designed for CT/$^{19}$F MRI bimodal imaging. Hyperbranched polymers consisting of iodo-monomer and PEGMA units were prepared by RAFT polymerisation, and then chain extended with TFEA and PEGMA. HBIPFs with different contents of iodine and fluorine were obtained by varying the monomer feed ratio. The HBIPFs could be degraded by treatment with reducing agents such as GSH and TCEP. Nanoparticles were formed with diameters between 10~15 nm by direct dissolution of the HBIPFs in water. The radio-opacity of these nanoparticles in aqueous solution was confirmed by *in vitro* CT experiments, while the solutions of the nanoparticles could be visualised by $^{19}$F MRI. These results suggest that hyperbranched polymer is a promising platform for the design of molecular imaging agents for CT/$^{19}$F MRI bimodal imaging.

The effect of polymer architecture on imaging performance was evidenced by the study on star and hyperbranched polymers. An in-depth understanding on the molecular level was pursued in Chapter 5. Segmented and highly-branched polymers (SHBPs), which were synthesised by RAFT SCVP of TFE(M)A, PEG(M)A and a polymerisable CTA, were chosen as a model to systematically

study the effect of molecular structure on the imaging performance. SHBPs with desired compositions and degree of branching (DB) were prepared by varying monomer type and [comonomer]/[MECP] ratio. The structure of the SHBPs was thoroughly characterised by a range of different analytical techniques. Statistical copolymers with fluorine units evenly distributed were obtained using TFEA/PEGA or TFEMA/PEGMA, while gradient copolymers were produced using monomers having largely different reactivity ratios. The $^{19}$F NMR properties were affected by both chain composition and monomer sequence. Higher $^{19}$F mobility (longer $T_2$) was achieved in statistical copolymers consisting of acrylate units due to greater segmental flexibility. In addition, the $^{19}$F mobility was greatly restricted for the samples with higher $^{19}$F contents due to the increased association of the fluorinated segments in aqueous solution. Moreover, a shortened $T_2$ was observed with an increase in DB, which caused increased compactness, rigidity, and restricted segmental motion. The $^{19}$F signal intensity of the SHBPs consisting of gradient copolymers was significantly reduced by the loss of solubilised $^{19}$F units in the chains. The relationship between $T_2$ and chain flexibility was also revealed by thermal analysis, and longer $T_2$ relaxation times were observed for the samples with lower glass transition temperatures in the bulk. The imaging performance of the SHBPs was confirmed by $^{19}$F MRI. All the samples could be well imaged by $T_1$-weighted imaging, while they could be selectively visualised using a $T_2$-weighted sequence using different echo times. Therefore the imaging performance could be regulated by tailoring the branched structure and composition of the SHPBs, enabling the selective and tuneable $^{19}$F MRI.

Theranostic agents combined with $^{19}$F MRI function are advantageous for monitoring drug delivery and quantitative diagnosis due to the high sensitivity and high-resolution capabilities of $^{19}$F MRI. Chapter 6 explored the fabrication of POSS-based star polymers for potential $^{19}$F MRI and drug delivery. Star polymers consisting of eight partly-fluorinated copolymer arms and a POSS core were synthesised by the RAFT copolymerisation of TFEA and PEGA using a POSS-based macroCTA. The synthetic mechanism was revealed by kinetic study, and the existence of linear polymers and polymers formed by star-star terminations was evidenced as the characteristics of the R-group approach. Star polymers with different arm length were synthesised by varying the feed ratio of monomer to CTA, and were purified by extensive dialysis in water. The evenly distributed fluorine units in the arms were observed by $^{1}$H NMR. Nanoparticles with diameters of 8~10 nm were formed by dissolving the star polymers in water, and the particle size increased with arm length. A single fluorine chemical environment was confirmed by a single peak in the $^{19}$F NMR spectra, and it was noted that the $T_2$ relaxation time was increased with increasing arm length. However, the $T_2$s were shorter than those of linear and highly-branched (polymers in Chapter 5)

analogues, indicating that the fluorine nuclei were less mobile in the arms of star polymers because of the possibly more confined environment around the POSS core. Nevertheless, the fluorine mobility was higher than that of hyperbranched structures having high DBs. The theoretical values of $^{19}$F MRI intensity were estimated, confirming that the star polymers could be used for $^{19}$F MRI with potentially high imaging intensity. These multifunctional star polymers with drug encapsulating capability imparted by the POSS and the possibility of conjugation by the trithiocarbonate functionality are promising theranostic agents for $^{19}$F MRI-enabled cancer diagnosis and treatment.

## 7.2 Comparison of the as-designed polymeric agents

Partly-fluorinated polymers with various star and hyperbranched structures were synthesised in this thesis for $^{19}$F MRI-related applications. The molecular details and $^{19}$F NMR properties of the representative samples are listed in Table 7-1.

**Table 7-1** Comparison of the partly-fluorinated polymers developed in this thesis.

| Polymer Type | Representative Sample | Polymer Chain[a] | $M_n$ (kDa)[b] | $Đ_M$[b] | $^{19}F$ wt%[c] | $T_1$ (ms)[d] | $T_2$ (ms)[d] | $D_h$ (nm)[e] | $^{19}F$ MRI Intensity[f] | Application |
|---|---|---|---|---|---|---|---|---|---|---|
| Star-like hyperbranched polymers | Star-1 | PPEGMA-b-P(TFEA-co-DMAEMA) | 225 | 1.6 | 1.4 | 420-471[g] | 7-40[g] | 10-25[h] | 0.85 | Selective $^{19}F$ MRI |
| Core corsslinked star polymers | CCS-1 | PPEGMA-b-P(TFEMA-co-DMAEMA) | 653 | 1.2 | 2.3 | 250-472[g] | 1-39[g] | 18.3-23.7[g] | 1.43 | Selective $^{19}F$ MRI |
| Hyperbranched polymers | HBIPF-1 | P(TFEA-co-PEGMA) | 227 | 2.0 | 1.3 | 405 | 61 | 13.5 | 1.20 | CT/$^{19}F$ MRI bimodal imaging |
| Segmented highly-branched polymers | SHBP-9 | P(TFEA-co-PEGA) | 370 | 1.6 | 3.3 | 345 | 87 | 6.3 | 3.86 | Improved and tuneable $^{19}F$ MRI |
| Star polymers with a POSS core | SP-1 | P(TFEA-co-PEGA) | 234[i] | 1.4[i] | 4.9 | 329 | 37 | 8.6 | 3.06 | $^{19}F$ MRI and drug delivery |

[a] The copolymer chains in which the fluorine segments were distributed. [b] Absolute molecular weight and $Đ_M$ were measured by GPC MALLS or triple detection GPC. [c] Fluorine content was determined by $^1H$ NMR. [d] $T_1$ and $T_2$ relaxation times were measured by $^{19}F$ NMR in PBS/D2O(90/10, v/v) at 25 $^oC$. [e] Hydrodynamic diameter was measured by DLS (1 mg $mL^{-1}$ in PBS) at 25 $^oC$, and number-averaged diameters were reported. [f] The intensity of $^{19}F$ MRI using spin-echo pulse sequence (e.g., RARE-8) was simulated by using the Equation (2-1). Supposed parameters: TE = 41 ms, TR = 1 s, polymer concentration = 20 mg $mL^{-1}$ in water. [g] $T_1$ and $T_2$ relaxation times and $D_h$ were measured at different pH from 4 to 9. [h] Determined by cryo-TEM at pH 6 and 9. [i] $M_n$ was calculated by $^1H$ NMR, and $Đ_M$ was measured by a GPC RI detector.

In this thesis, the highest mobility of $^{19}F$ nuclei was achieved by statistical copolymers P(TFEA-co-PEGA) owing to the close reactivity ratios and resultant evenly distributed fluorinated units along the polymer chain. Polymers consisting of P(TFEA-co-PEGA) segments possessed high fluorine contents (up to 11.8%), a single and strong $^{19}F$ signal resonance, long $T_2$ relaxation times (up to 87 ms) and short $T_1$ relaxation times (~350 ms), and hence they displayed significantly improved $^{19}F$ MRI performance compared to their counterparts containing other polymer chains such as P(TFEA-co-DMAEMA), P(TFEMA-co-DMAEMA), P(TFEA-co-PEGMA), P(TFEMA-co-PEGA) and P(TFEMA-co-PEGMA)).

The mobility of fluorine segments was decreased with an increase in degree of branching (DB) for the hyperbranched structure. In addition, the placement of $^{19}F$ nuclei in a hyperbranched structure with a low DB is more advantageous for improving $^{19}F$ mobility than positioning the $^{19}F$ in the arms of star polymer. Moreover, the $^{19}F$ nuclei were more mobile in in arms of the star polymer than in a hyperbranched structures having high degree of branching. Furthermore, the flexibility of the fluorinated segments in the arms of star polymers could be enhanced by increasing the arm length.

Therefore we conclude that low-DB hyperbranched polymers consisting of P(TFEA-co-PEGA) segments and star polymers having P(TFEA-co-PEGA) arms are promising candidates for $^{19}F$ MRI-related applications due to the excellent imaging performance as well as the architectural advantages.

In summary, multifunctional polymers with a range of architectures and compositions have been synthesised using the RAFT technique and evaluated as contrast agents for $^{19}F$MRI-related applications. The molecular level understanding gained in this thesis provides useful guidance for the future design of highly-efficient contrast agents for $^{19}F$ MRI-based molecular imaging and therapy.

## Appendix A, Supporting Information for Chapter 2

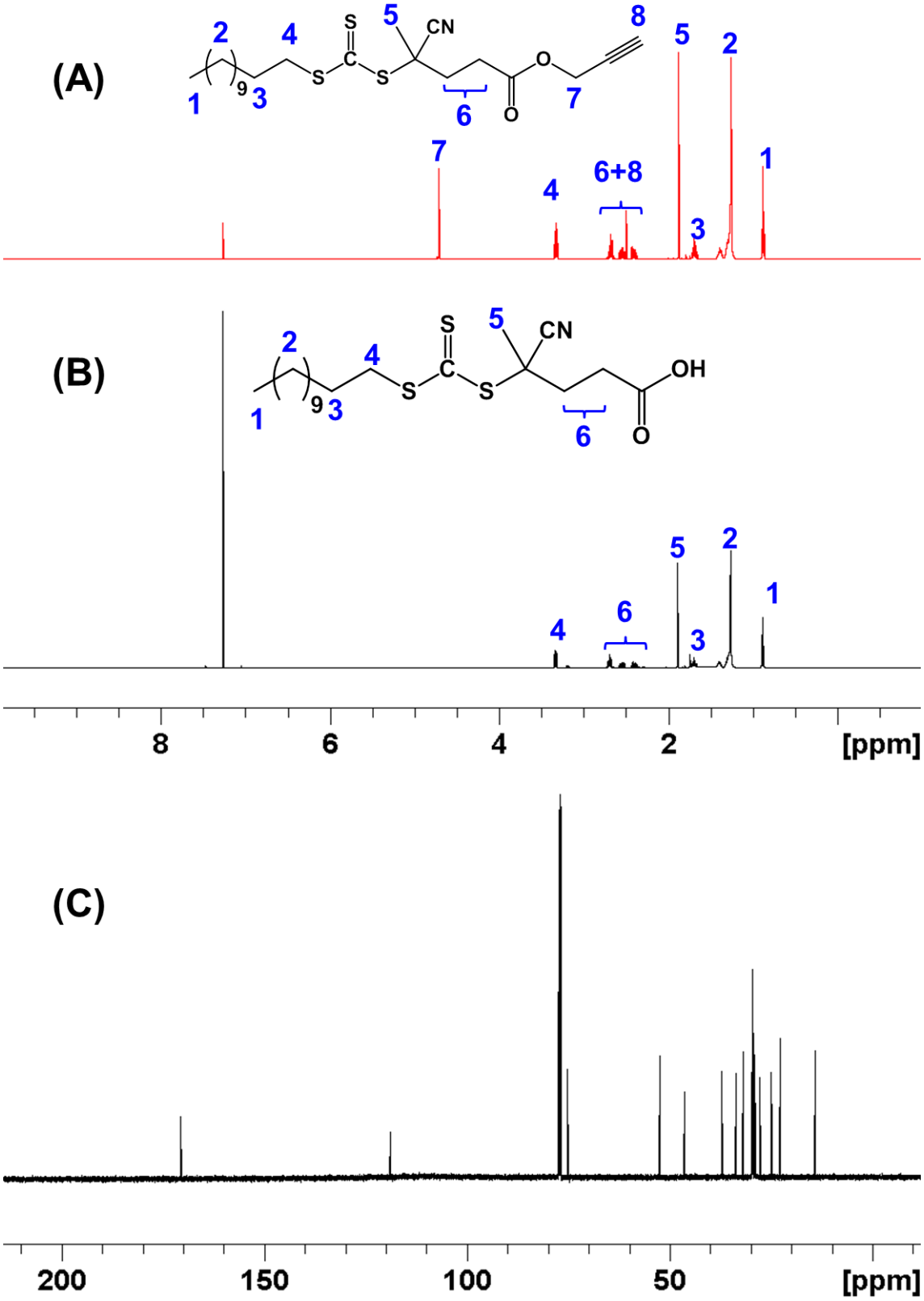


**Figure A2.1** $^{1}$H NMR spectra of alkyne-CTA (A) and original CTA (A), and $^{13}$C NMR spectrum of alkyne-CTA. All spectra were recorded using $CDCl_3$ at 25 $^{o}$C.

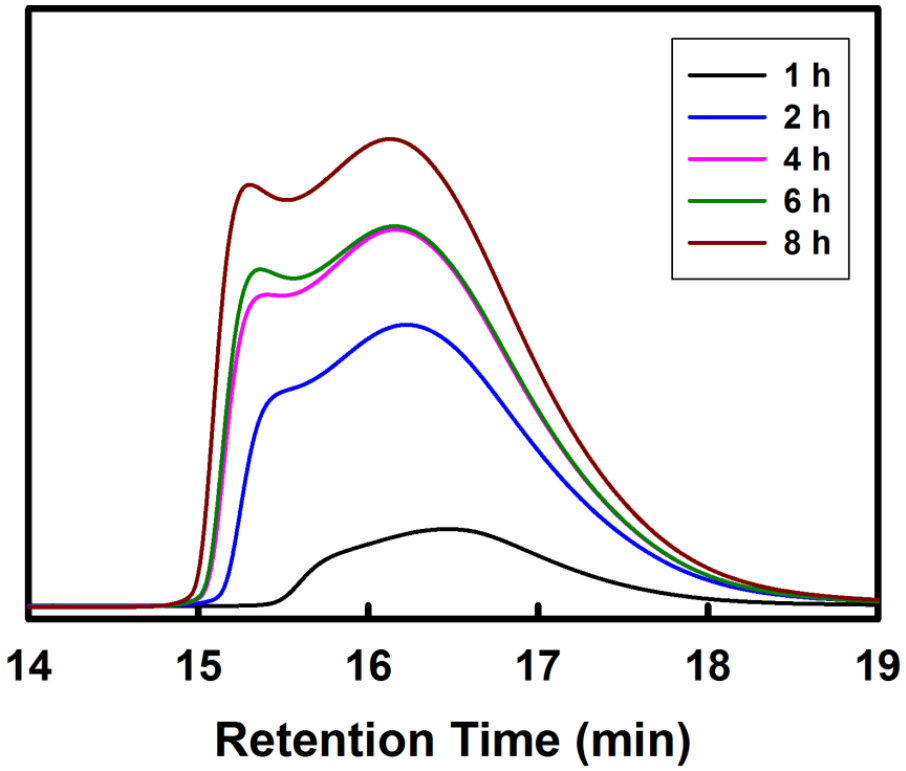


**Figure A2.2** GPC curves of the synthesis of PPEGMA using S-1-dodecyl-S'-(α,α'-dimethyl-α"-acetic acid) trithiocarbonate as CTA. [PEGMA]:[CTA]:[AIBN] = 50:1:0.1, [PEGMA] = 1 M in toluene, 70 $^{o}$C.

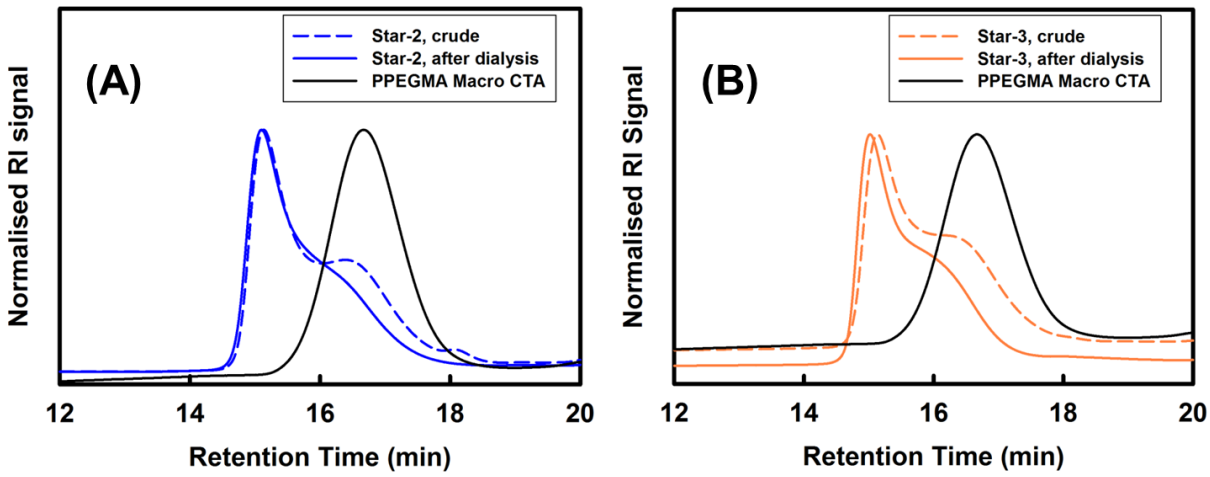


**Figure A2.3** GPC traces of Star-2 (A) and Star-3 (B) before and after dialysis. [Macro-CTA]:[TFEA]:[DMAEMA]:[EGDMA]:[AIBN] = 1:8:24:8:0.2 and 1:16:16:8:0.2 for Star-2 and Star-3, respectively. Polymerised in THF at 70 $^{o}$C for 24 h, [monomer] = 0.5 M.

# Appendix B, Supporting Information for Chapter 3

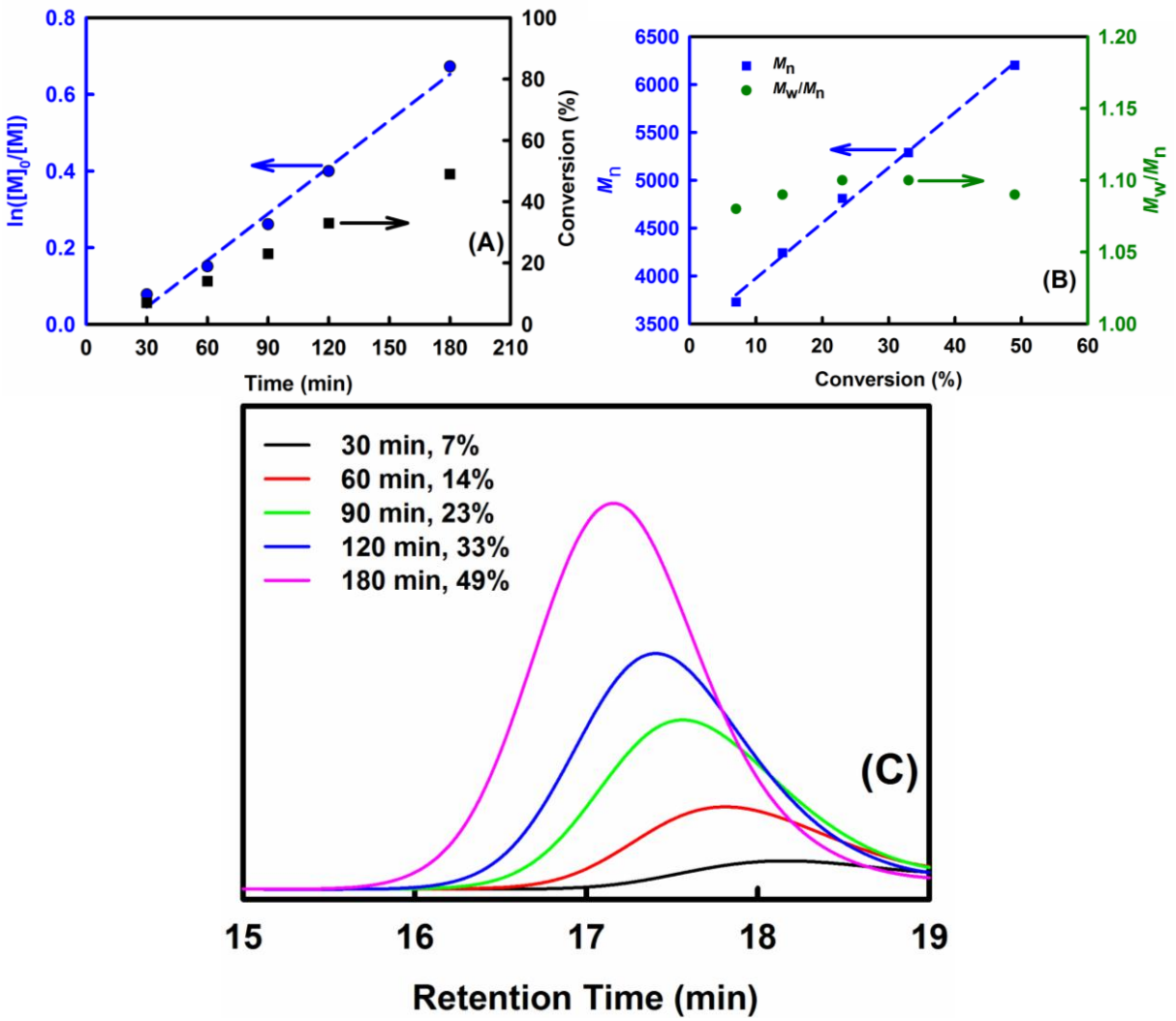


**Figure A3.1** RAFT polymerisation of PEGMA using alkyne-CTA. (A) Pseudo-first-order kinetic plot of the polymerisation. (B) Dependence of number-average molecular weight ($M_n$, determined by GPC) and molar-mass dispersity ($Đ_M$) on monomer conversion. (C) GPC traces during the polymerisation.

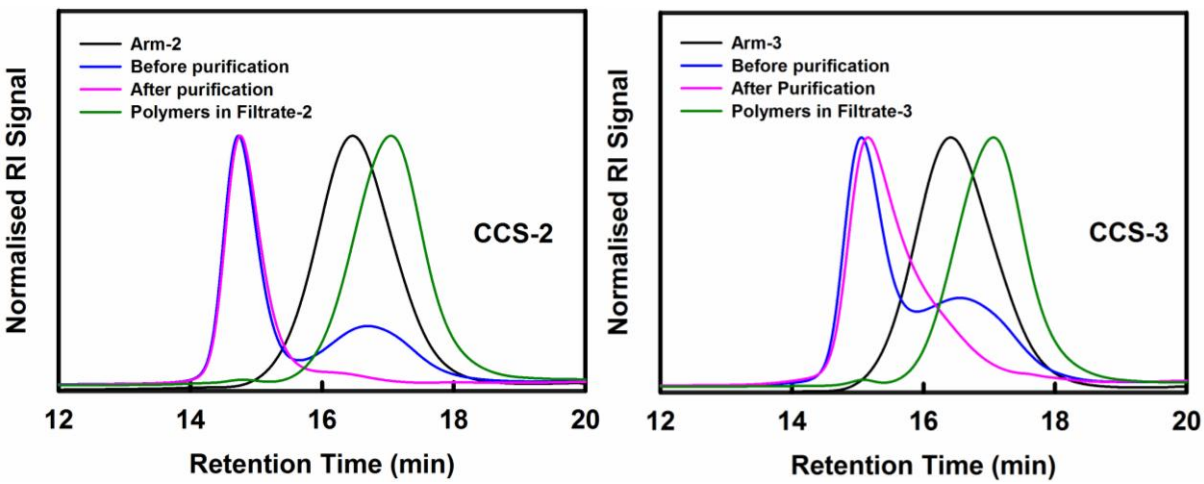


**Figure A3.2** GPC traces of the polymers related to the synthesis of CCS-2 and CCS-3.

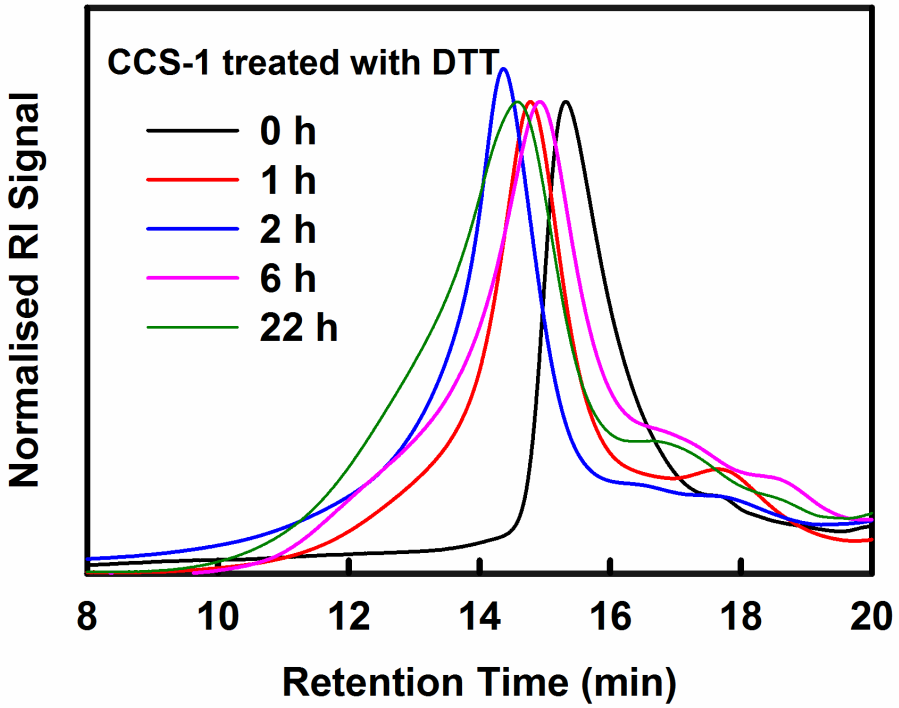


**Figure A3.3** GPC traces during the degradation of CCS-1 using DTT in THF. [DTT] = 50 mM, [CCS-1] = $1.15 \times 10^{-3}$ mM. Note that the sample solutions were exposed to air during the measurements.

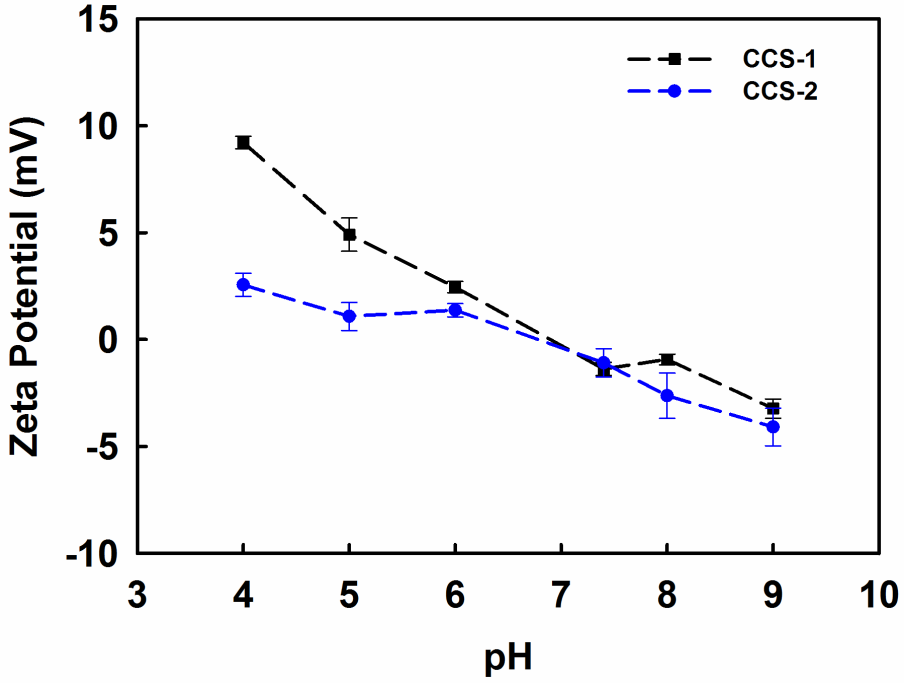


**Figure A3.4** Zeta potential of CCS-1 and CCS-2 at different pH in PBS (1 mg $mL^{-1}$) at 25 °C.

## Calculation of arm number

The arm number can be calculated according to the previously published methods. [1, 2]

First, the weight fractional of arms in CCS polymer can be calculated using Equation (A3-1).

$$WF_{arm} = \frac{m_{arm} \times X_{arm}}{m_{arm} \times X_{arm} + m_{CL} \times X_{CL}} \quad \text{(A3-1)}$$

In which $WF_{arm}$ is the weight fractional of arms in CCS polymer, $m_{arm}$ is the mass of arms, $X_{arm}$ is the conversion of arms that are incorporated into CCS polymer, $m_{CL}$ is the mass of crosslinker, and $X_{CL}$ is the conversion of crosslinker. We assume that the conversion of crosslinker is 100% because of the high polymerisation rate in a RAFT dispersion polymerisation.

Then the arm number can be obtained by Equation (A3-2).

$$f = \frac{M_{w(CCS)} \times WF_{arm}}{M_{w(arm)}} \quad \text{(A3-2)}$$

In which *f* is arm number, $M_{w(CCS)}$ is weight-average molecular weight of CCS polymer and $M_{w(arm)}$ is weight-average molecular weight of arms.

The details are listed in the following table.

**Table A3.1** Details for the calculation of arm numbers.

| **Sample** | $\mathbf{m_{arm}}$ **(g)** | $\boldsymbol{X_{arm}}$ | $\mathbf{m_{CL}}$ | $\boldsymbol{X_{CL}}$ | $\boldsymbol{M_{w(CCS)}}$ | $\boldsymbol{M_{w(arm)}}$[a] | $\mathbf{WF_{arm}}$ | $\boldsymbol{f}$ |
|---|---|---|---|---|---|---|---|---|
| CCS-1 | 2.16 | 0.74 | 0.58 | 1 | 764400 | 10500 | 0.734 | 53 |
| CCS-2 | 0.39 | 0.65 | 0.1 | 1 | 516300 | 11300 | 0.717 | 33 |
| CCS-3 | 0.53 | 0.6 | 0.139 | 1 | 785500 | 11700 | 0.713 | 49 |

[a] $M_n$ ($^1$H NMR) was used for $M_{w(arm)}$

**References**

1. A. Blencowe, J. F. Tan, T. K. Goh and G. G. Qiao, *Polymer*, 2009, **50**, 5-32.

2. X. F. Shi, W. Zhou, Q. Qiu and Z. S. An, *Chem Commun*, 2012, **48**, 7389-7391.

# Appendix C, Supporting Information for Chapter 4

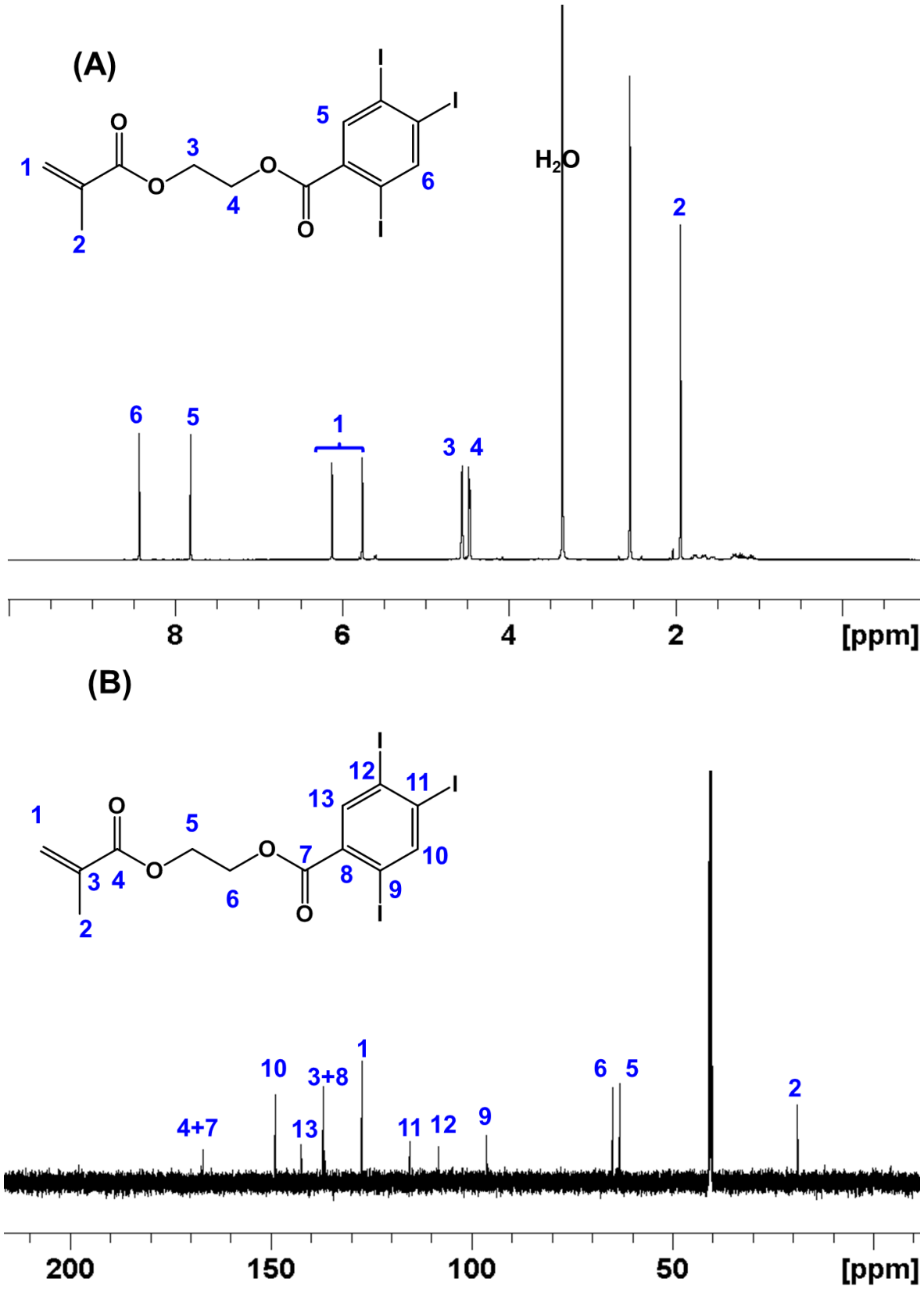


**Figure A4.1** $^{1}H$ and $^{13}C$ NMR spectra of the iodo-monomer TIBMA in DMSO-$d_6$ at 25 $^{o}C$.

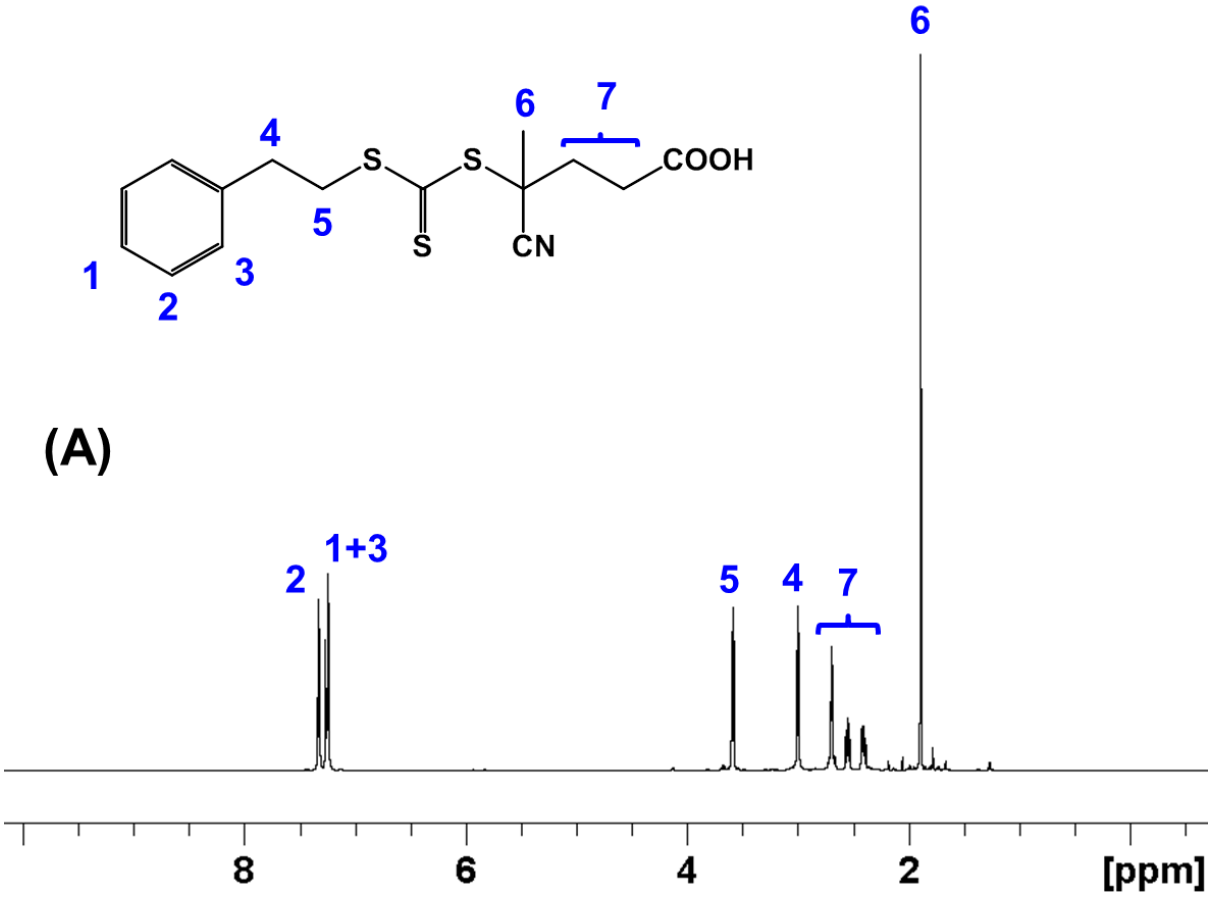
6
7
4
S
S
COOH
5
S
CN
1
3
2
(A)
1+3
2
5
4
7
8
6
4
2
[ppm]

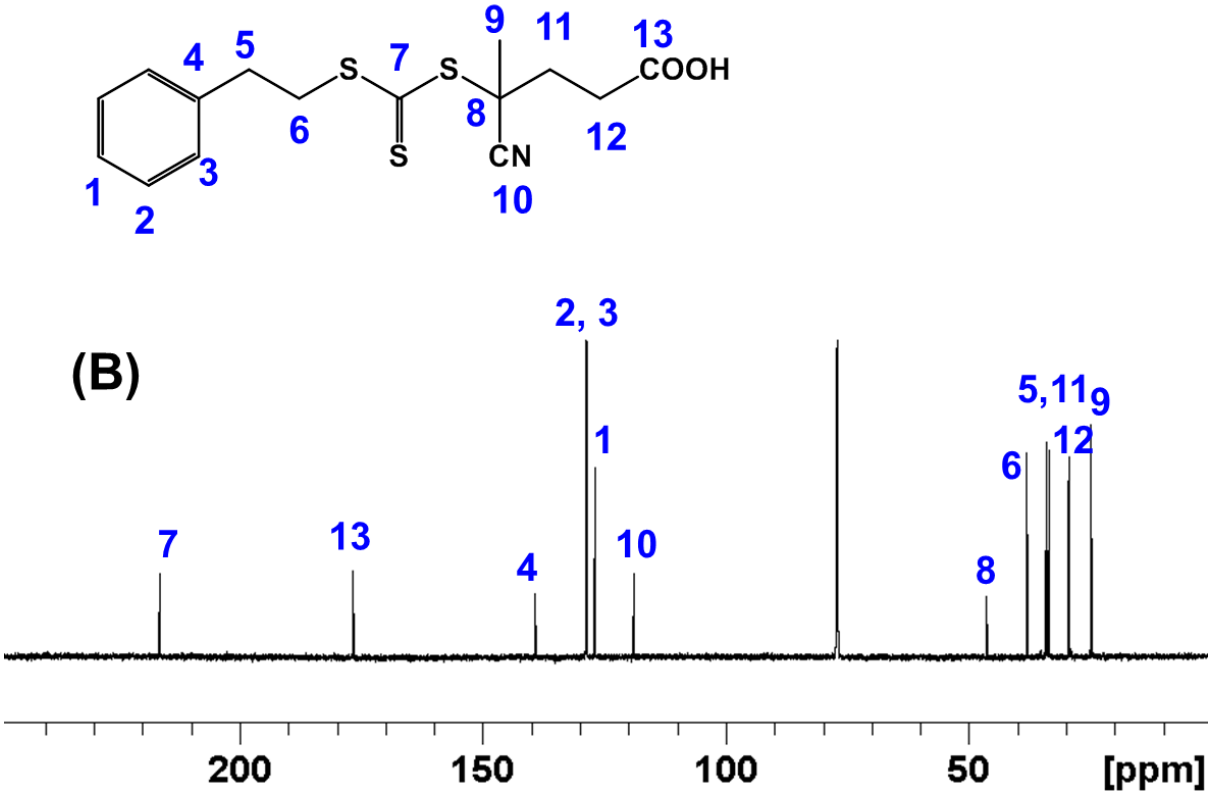
9
11
13
4
5
S
7
S
COOH
6
8
12
S
CN
1
3
10
2
(B)
2, 3
5,11
9
1
12
6
7
13
10
4
8
200
150
100
50
[ppm]

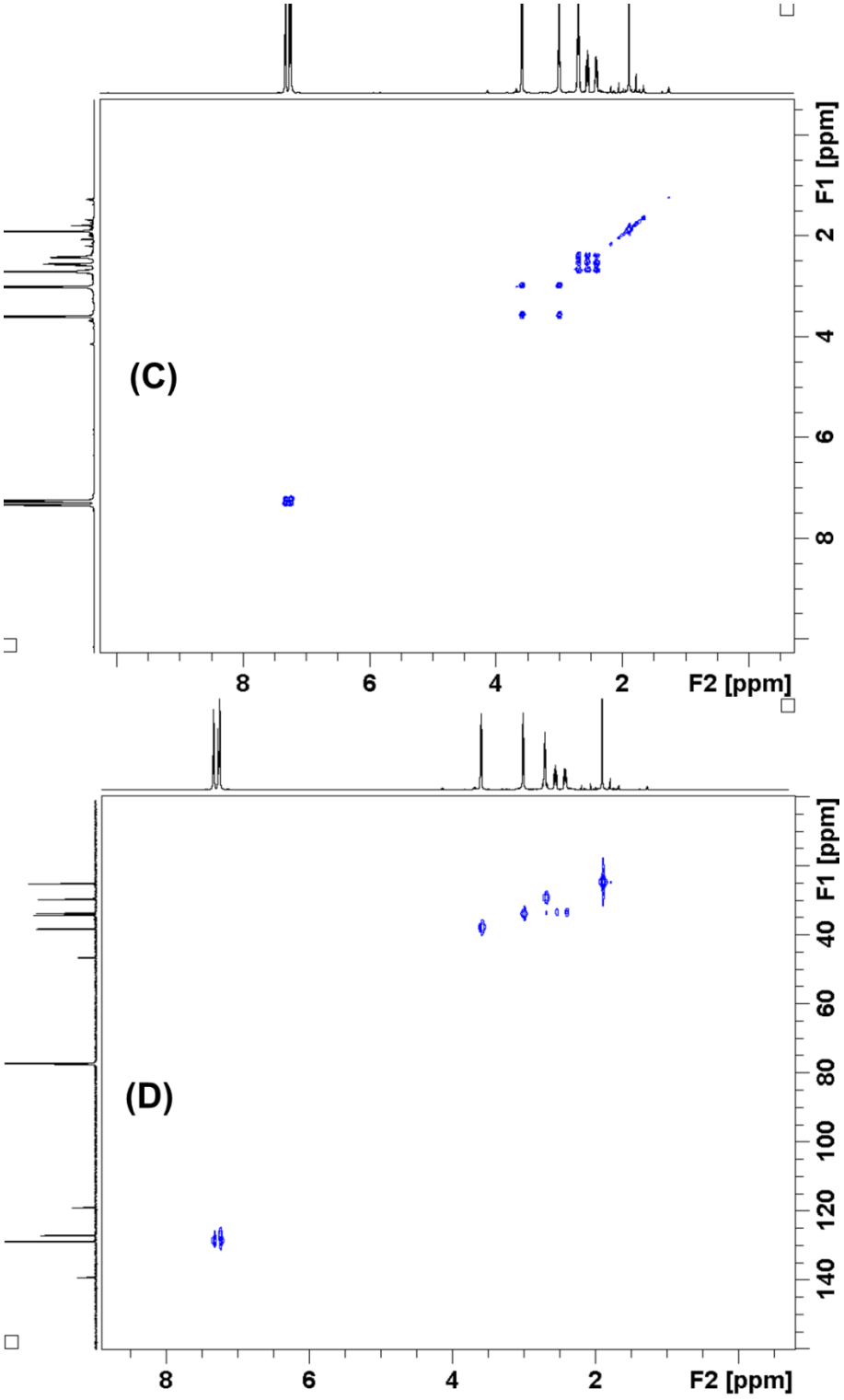


**Figure A4.2** $^{1}$H NMR (A), $^{13}$C NMR (B), $^{1}$H-$^{1}$H-COSY (C), $^{1}$H-$^{13}$C-HSQC (D) spectra of the RAFT agent PETTC in $CDCl_3$ at 25 $^{o}$C.

# Appendix D, Supporting Information for Chapter 5

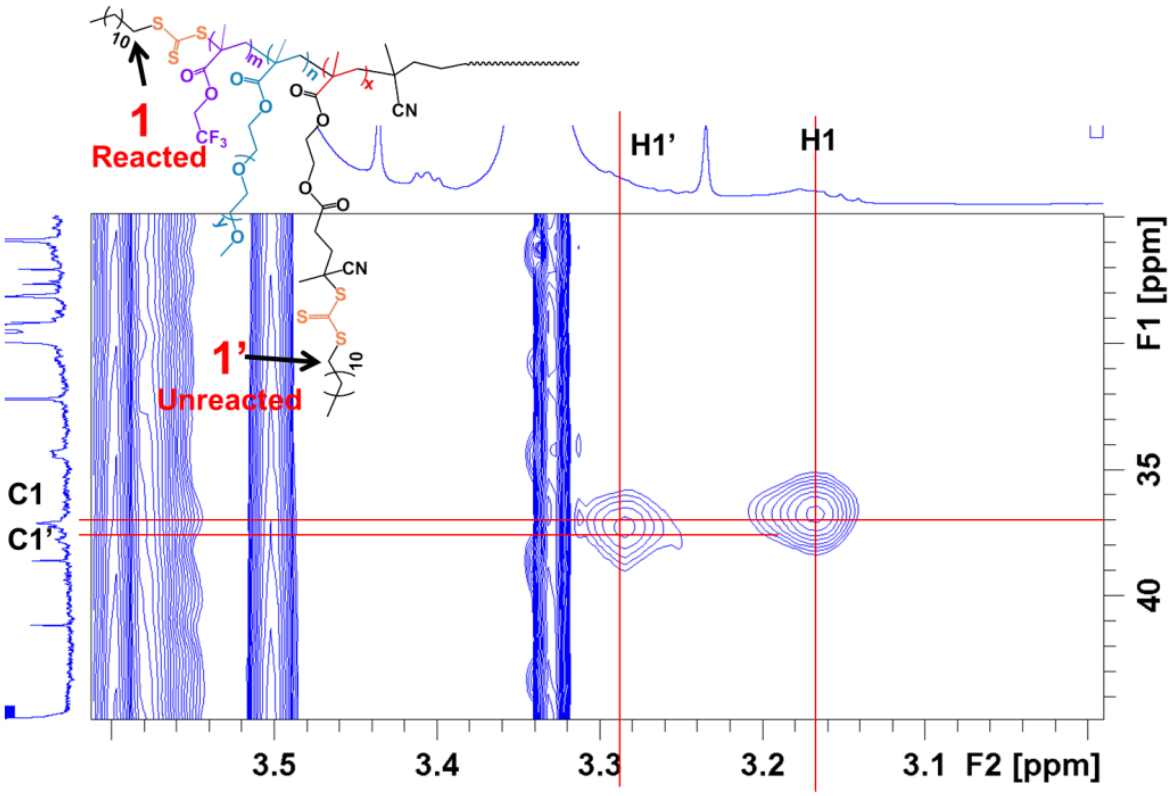


**Figure A5.1** Enlarged area of the $^{1}H$-$^{13}C$ HSQC spectrum of SHBP-4. The two cross-peaks for two different types of $CH_2$ adjacent to the trithiocarbonate can be clearly distinguished.

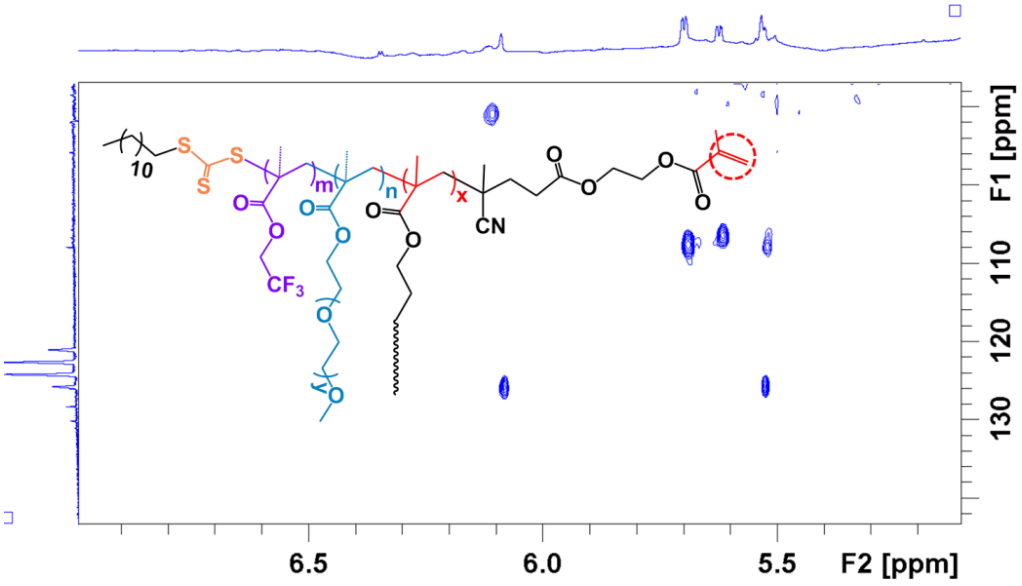


**Figure A5.2** Enlarged area of the $^{1}H$-$^{13}C$ HSQC spectrum of SHBP-4. The relevant cross-peaks for the $CH_2$ of the vinyl group are identified.

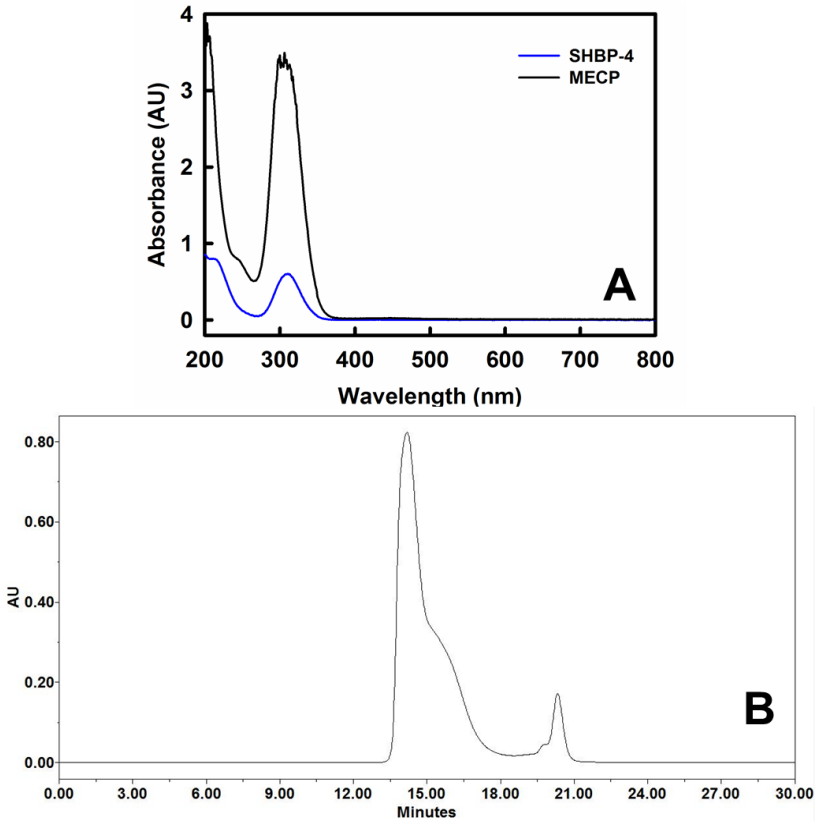


**Figure A5.3** (A) UV-vis spectra of SHBP-4 and MECP showing the characteristic absorbance of trithiocarbonate compounds at 306 nm. (B) GPC trace given by UV detector monitoring the wavelength of 306 nm.

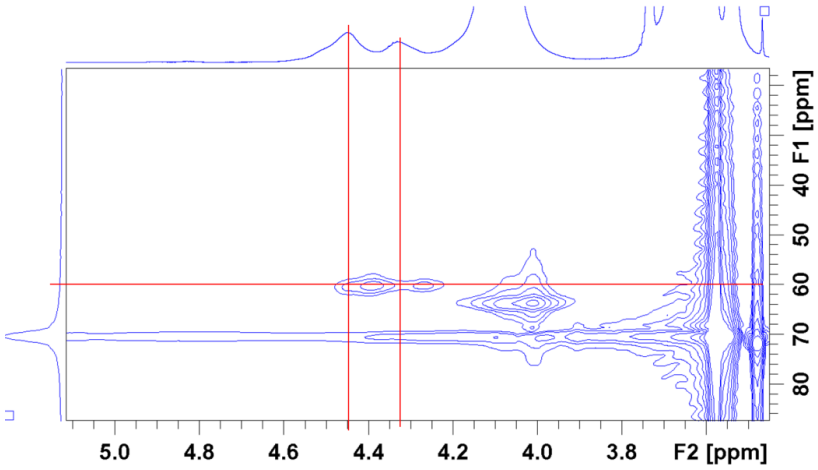


**Figure A5.4** Enlarged area of the $^{1}H$-$^{13}C$ HSQC spectrum of SHBP-7. The two highlighted cross-peaks can be assigned to the $CH_2$ adjacent to the ester bond in TFEA within different chemical environments.

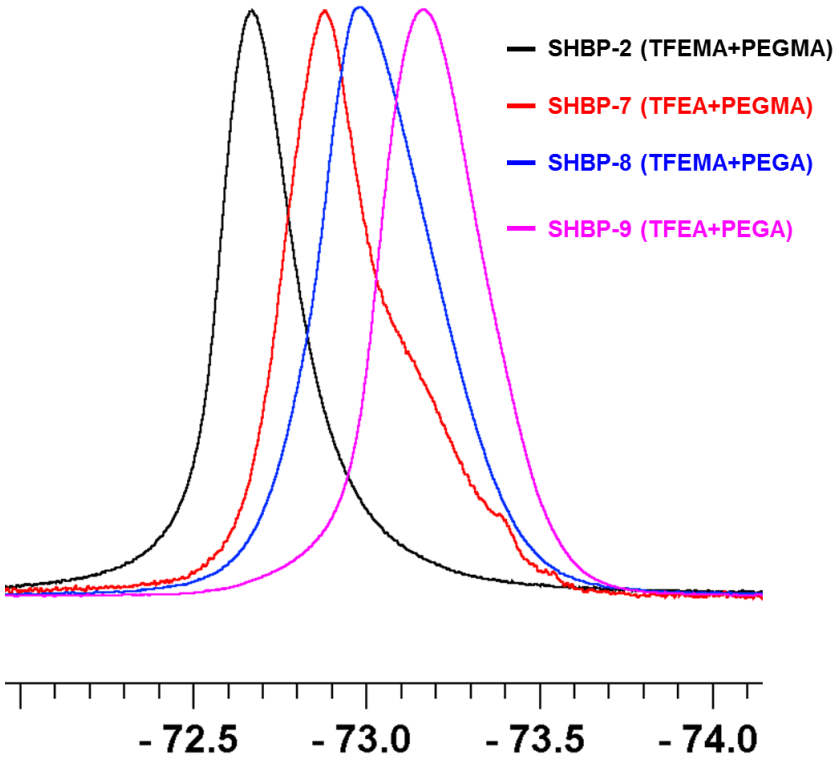


**Figure A5.5** Normalised $^{19}F$ NMR spectra of SHBP-2, 7, 8 and 9. Samples were dissolved in PBS/$D_2O$(90/10, v/v) at 20 mg $mL^{-1}$ at 25 $^oC$.

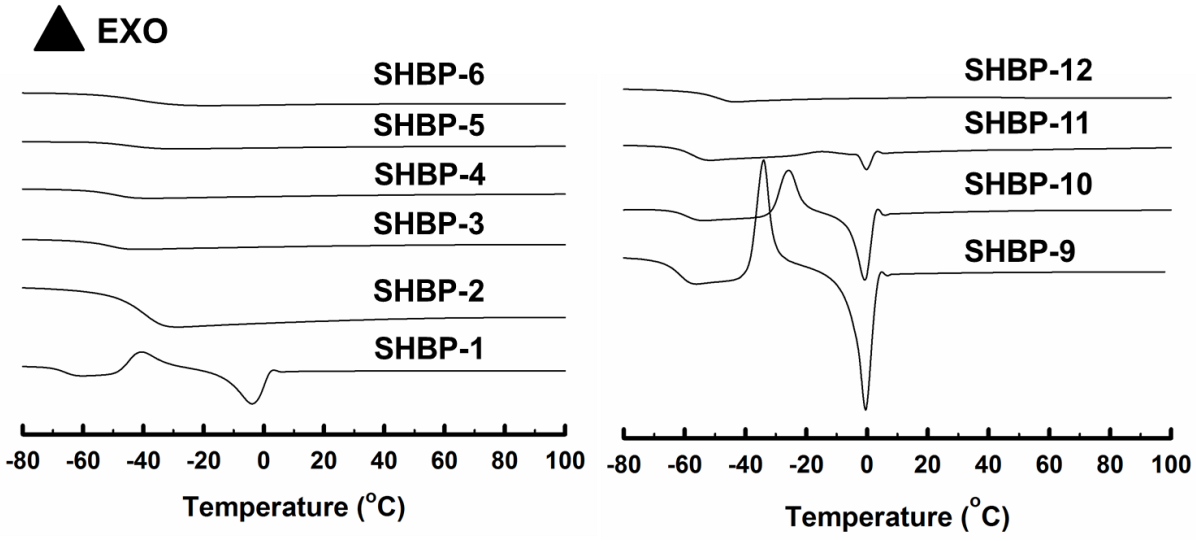


**Figure A5.6** Stacked DSC curves for the SHBPs. Samples (5~9 mg) were heated from 25 to 150 $^oC$ at a heating/cooling rate of 10 $^oC$ $min^{-1}$ in nitrogen atmosphere. The glass transition temperature was determined from the midpoint of the change in capacity in the second heating cycle (-100 to 150 $^oC$).

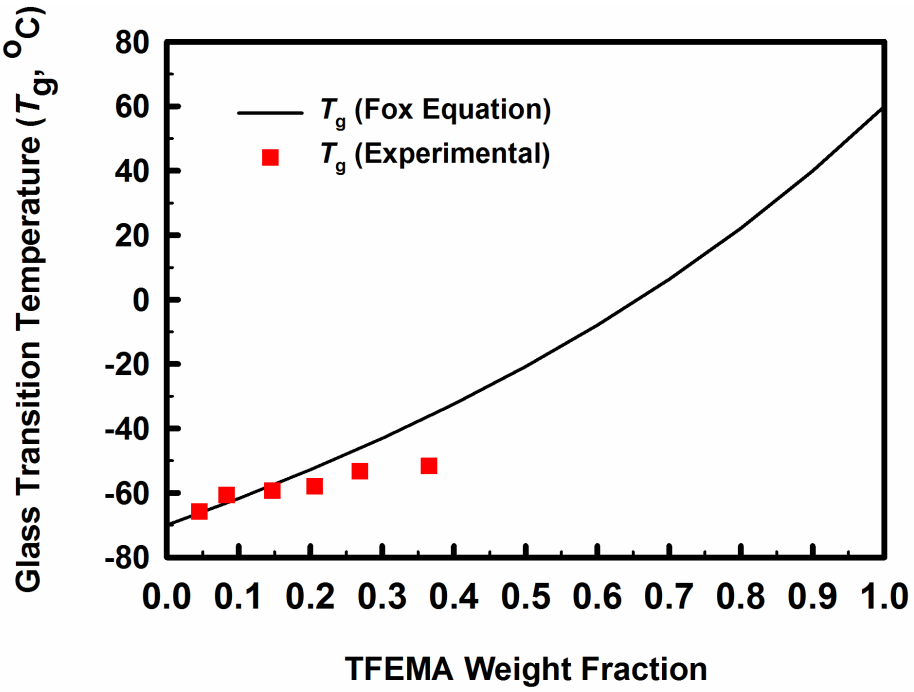


**Figure A5.7** Comparison of experimental and theoretical (calculated using the Fox Equation) $T_g$ values of samples consisting of TFEMA and PEGMA units with different weight fractions of TFEMA.

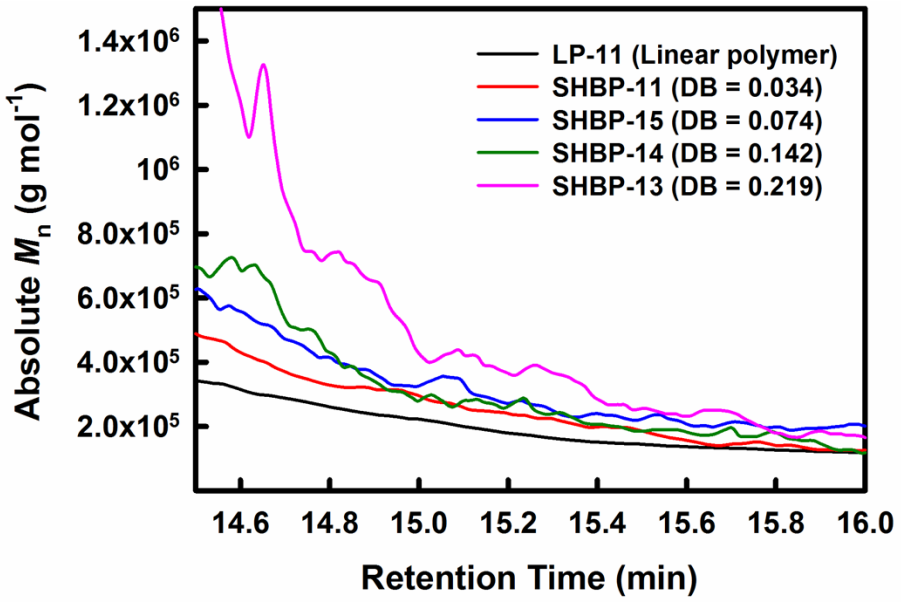


**Figure A5.8** Absolute MW versus retention time measured by GPC MALLS in THF for the polymers with various degrees of branching (DB).

# Appendix E, Supporting Information for Chapter 6

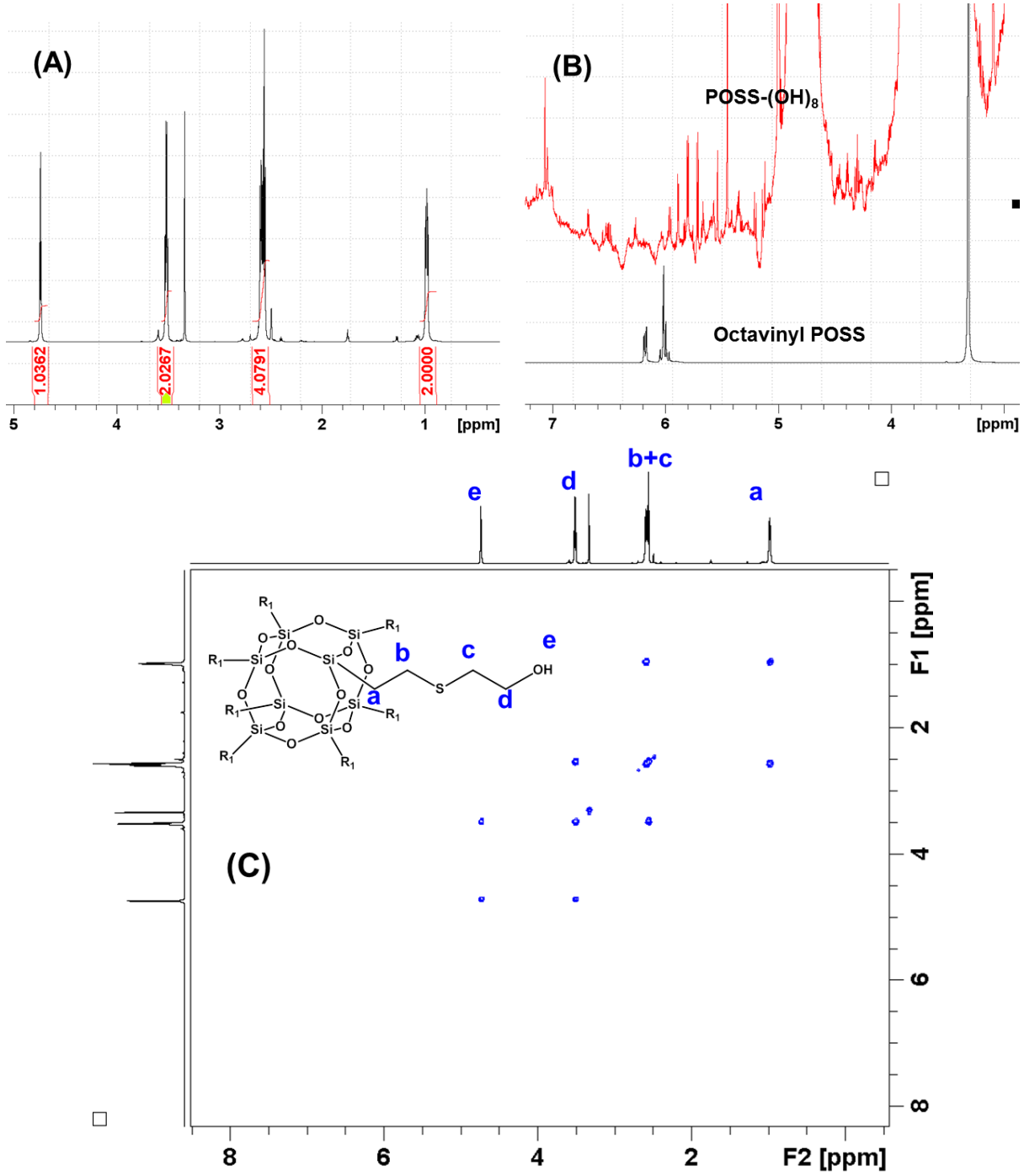


**Figure A6.1 (A)** $^{1}$H NMR spectrum of POSS-$(OH)_8$ with integrals displayed. (B) Comparison of the spectra of Octavinyl POSS and POSS-$(OH)_8$ in the region where the peaks of vinyl protons are. (C) $^{1}$H-$^{1}$H COSY NMR spectrum of POSS-$(OH)_8$. All spectra were recorded in DMSO-$d_6$ at 25 $^{o}$C.

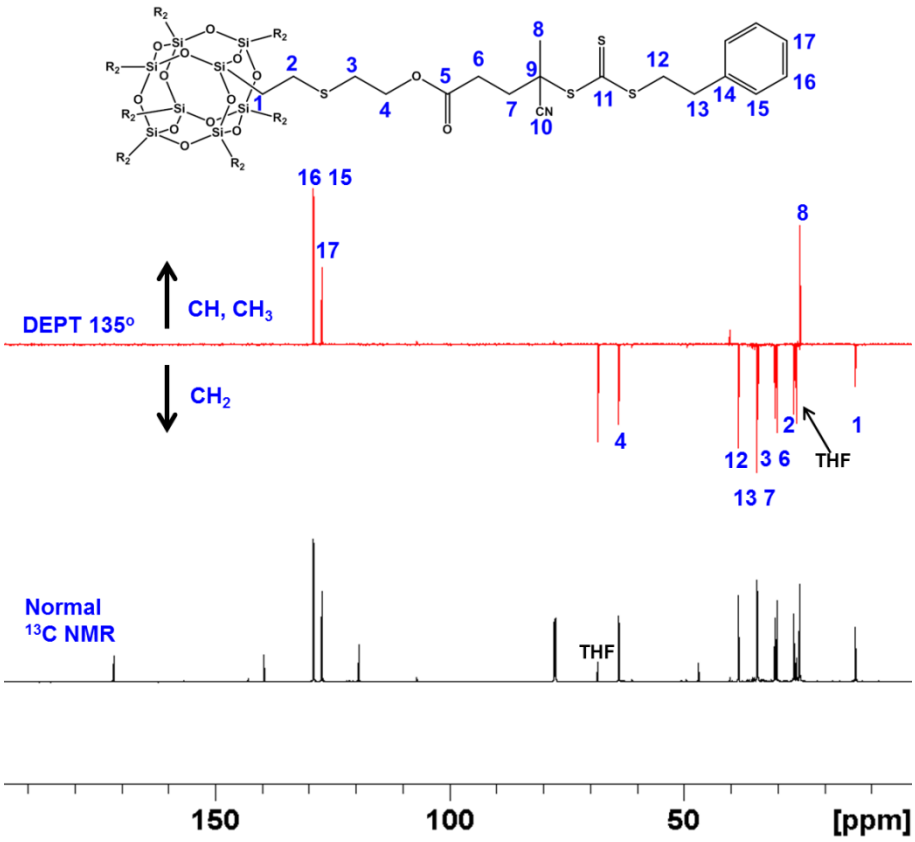


**Figure A6.2** Normal and DEPT $^{13}C$ NMR spectra of POSS-(CTA)$_8$ in $CDCl_3$ at 25 $^{o}C$.

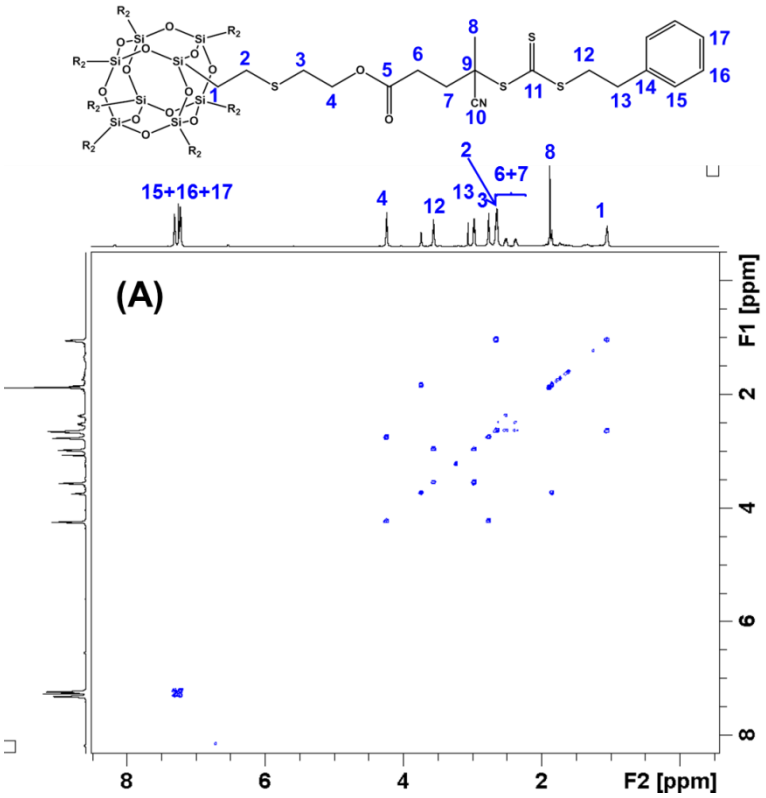

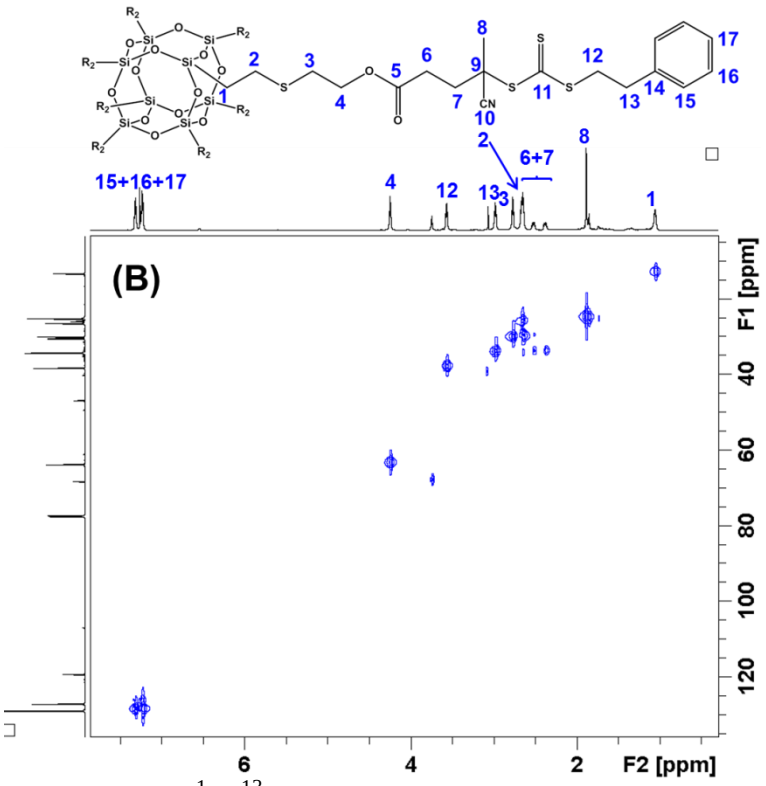


**Figure A6.3** $^{1}$H-$^{1}$H COSY (A) and $^{1}$H-$^{13}$C HSQC NMR spectra of POSS-(CTA)$_8$ in $CDCl_3$ at 25 $^{o}$C.

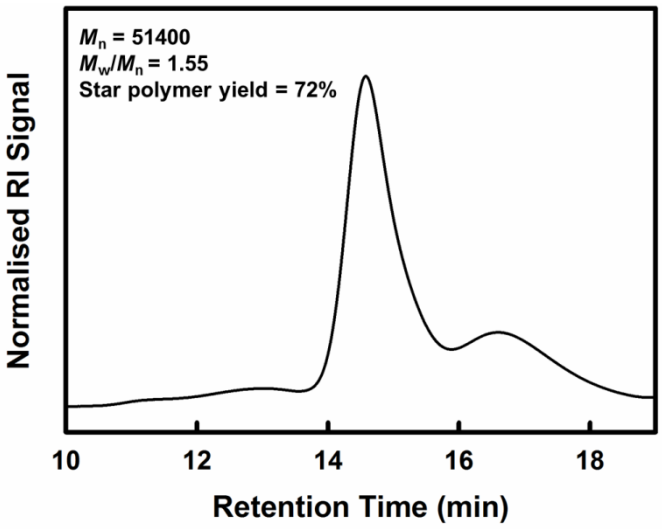


**Figure A6.4** GPC trace of the sample synthesised using an increased AIBN concentration (1/5 of CTA). Condition: POSS-(CTA)$_8$/TFEA/PEGA/AIBN = 1/200/200/1.6, [monomer] = 1 M in 1,4-dioxane, 70 $^{o}$C. The percentage of star polymer in the polymer mixture was estimated by the deconvolution of GPC curves. The conversions of TFEA and PEGA were 69% and 58%, respectively, as determined by $^{1}$H NMR.

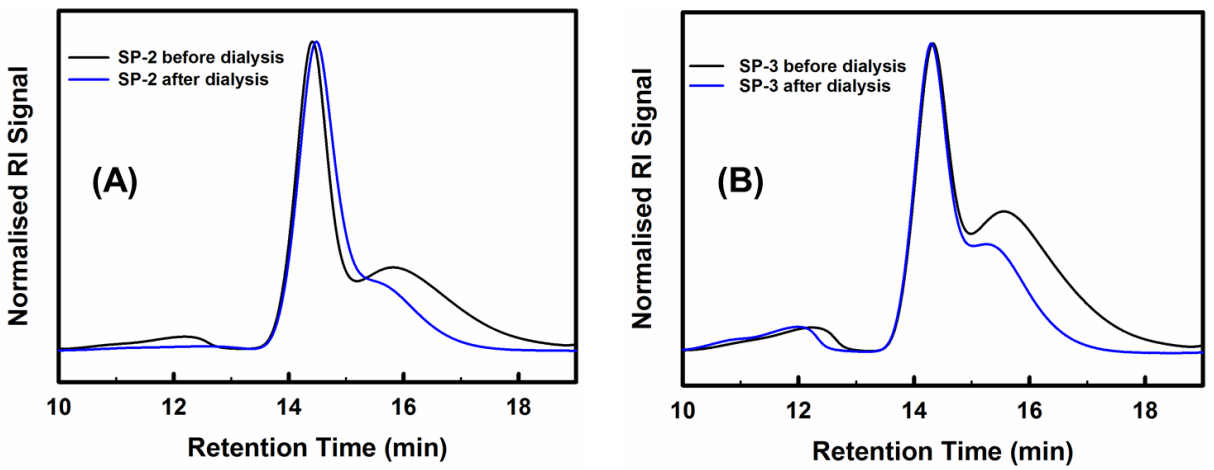


**Figure A6.5** GPC curves of SP-2 (A) and SP-3 (B) before and after purification using dialysis tubing of 100 kDa MWCO.

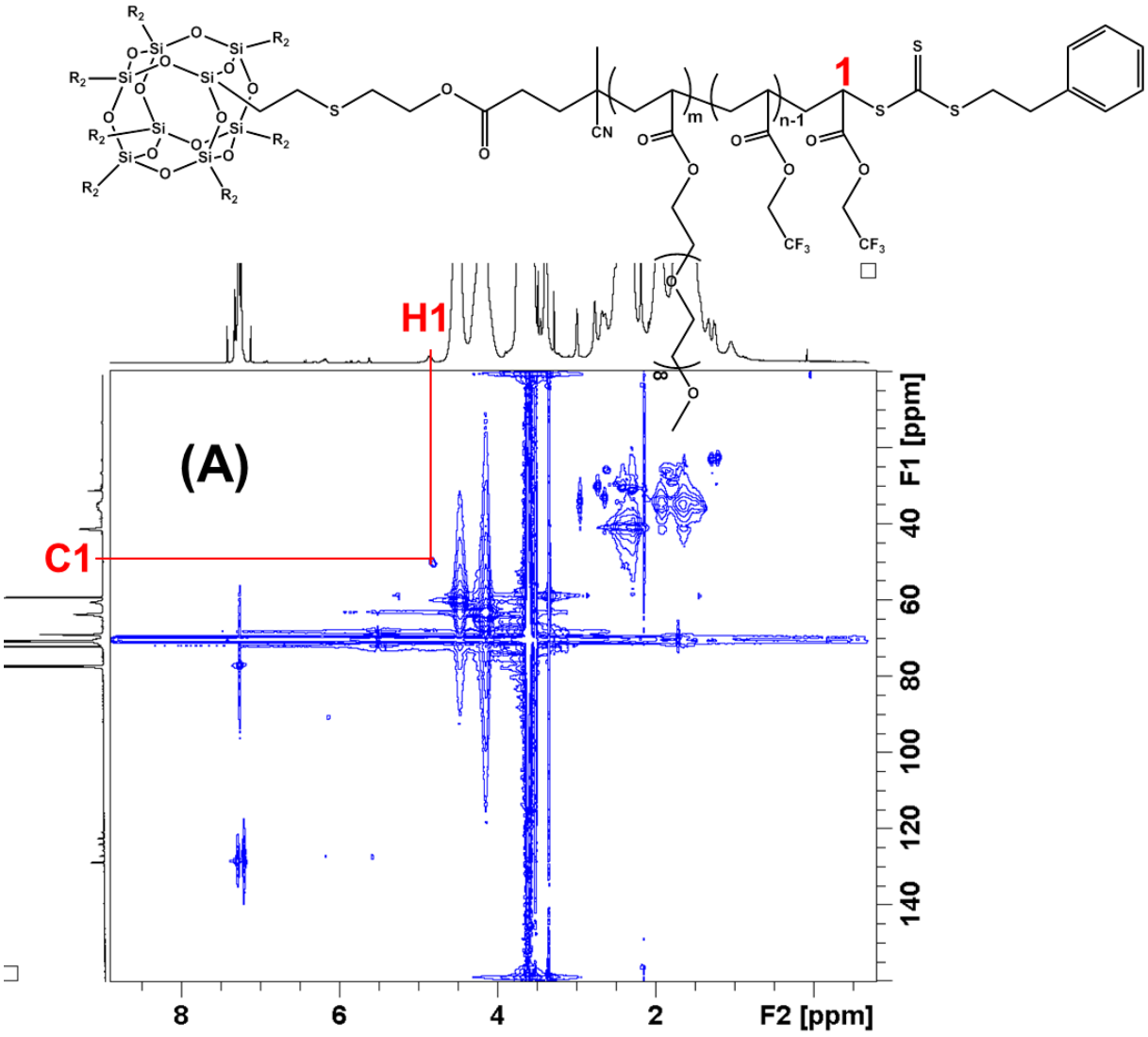

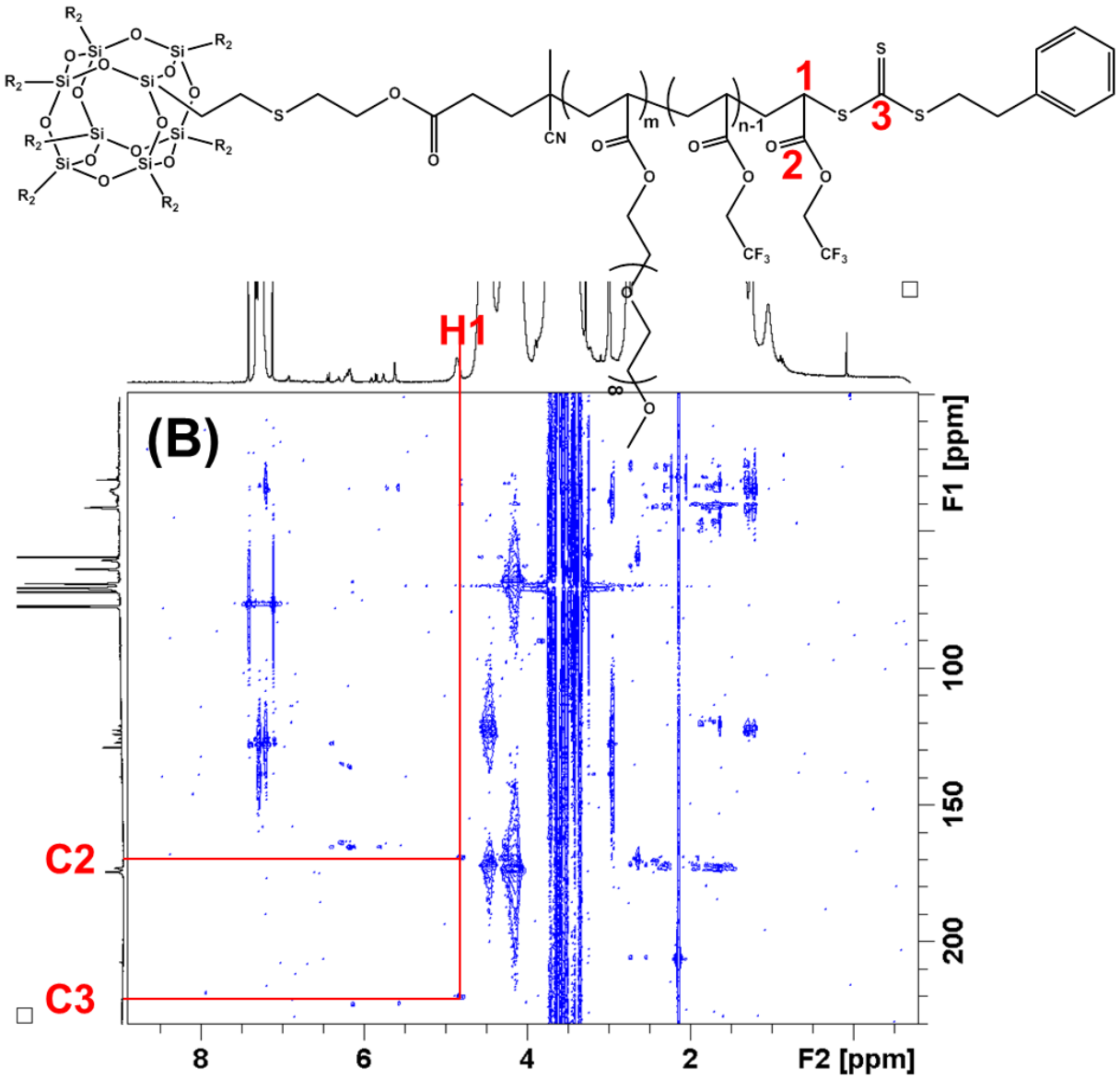


**Figure A6.6** $^{1}H$-$^{13}C$ HSQC (A) and HMBC (B) spectra of SP-1 in $CDCl_3$ at 25 $^{o}C$.

*"When it is obvious that the goals cannot be reached, do not adjust the goals, adjust the action steps."*

—Confucius